E-Plane Parallel Coupled Resonators for Waveguide Bandpass Filter Applications

Raúl López-Villarroya

A thesis submitted for the degree of Doctor of Philosophy

Heriot-Watt University

April 2012

Abstract

High skirt selectivity and extended out-of-band rejection is a major challenge for the successful progress of in-line microwave filters. This thesis presents novel filter realizations with improved performance, compatible with the standard single thin all-metal insert in a split-block housing and therefore maintaining the low-cost fabrication characteristics. In addition, significant filter performance improvement is achieved.

The synthesis procedure implemented for the filter concept consists of a few steps. Some preliminary steps are a rigorous characterization of a double-ridge coaxial waveguide, and the modelling of an equivalent circuit model for the parallel coupled ridge waveguide devised in the filter concept. From these elements, a full wave electromagnetic analysis shows that parallel-coupled asymmetric ridge waveguides produce strongly dispersive coupling which introduces a transmission zero. Later on this property is extended to parallel-coupled asymmetric ridge waveguide resonators, where it is demonstrated that it is possible to independently control the coupling coefficient and the frequency of the transmission zero. This allows the realization of pseudo-elliptic narrowband in-line bandpass filters in E-plane technology. A general synthesis procedure for high order filters is outlined and numerical and experimental results are presented for validation.

The elements employed for the synthesis procedure of the bandpass prototypes are also applied to investigate structures suitable for different applications. In particular, stopband and dual stopband filters are presented with numerical and experimental results. Finally, the study of a microwave chemical/biochemical sensing device for the characterization and detection of cells in chemical substances and cells in solution in micro-litre volumes is also reported.

Acknowledgements

I would like to express my gratitude for the guidance, encouragement and support provided by my supervisors Jiasheng Hong and George Goussetis. I thank the help provided by Professor Benito Gimeno, from University of Valencia, Professor Vicente Boria, from Universidad Politécnica de Valencia, and Professor Jose Luis Tornero from Universidad Politécnica de Cartagena for their generous guidance and collaboration support.

I apreciate the collaboration held by the technitians from the EPS workshop for the fabrication of the designed E-plane inserts. I am grateful to the Engineering and Physical Research council (EPSRC) and the school of Engineers and Physical Sciences for the funding this project.

Finally I would like to express my appreciation to my colleagues and friends within the Microwaves and Microsystems Engineering Group for their support, advice and assistance in the course of my research.

Raúl López-Villarroya

April 2012

To Gosia

Alius in aliis rebus est praestantior
Publilius Syrus

Glossary

3-D: Three dimensional

Al: Aluminium

BioMEMS: Biological MicroElectroMechanical Systems

Bw: Bandwidth

C: Capacitance

CAD: Computer Aided Design

CO_2: Carbon Dioxide

CPW: Coplanar Waveguide

Cu: Copper

CWG: Coaxial Waveguide

dB: Decibels

EBG: Electromagnetic Band Gap

E-plane: Electric Plane

EM Fields: Electromagnetic Fields

F: Frequency

F_{even}: Frequency of the even mode

F_{odd}: Frequency of the odd mode

FEM: Finite Element Method

FM: Field Matching

GHz: GigaHertz

HFSS: High Frequency Structure Simulator

Hz: Hertz

H-plane: Magnetic field plane

I: Current

Kc:Cutoff Wavenumber

L: Inductance

LOC: Lab-on-a-chip

LTCC: Low Temperature Co-fired Ceramic

MEMS: MicroElectroMechanical Systems

MHz: MegaHertz

nE: Normal component of the Electric Field

Non-TEM: Non Transverse ElectroMagnetic

PBS: Phosphate Buffer Saline

PMMA: Polymethylmethacrylate

PCR: Polymerase Chain Reaction

Q: Quality factor

Q_L: Loaded Quality factor

Q_U: Unloaded Quality factor

RCWG: Ridge Coaxial Waveguide

TE: Transverse Electric

RF: Radio Frequency

TEM: Transverse ElectroMagnetic

THz: TeraHertz

TL: Transmission line

TLM: Transmission line modelling

TM: Transverse Magnetic

LOC: Lab-On-a-Chip

TR: Transverse Resonance

TZ: Transmission Zero

Unloaded Q: Unloaded Quality factor

V: Voltage

VNA: Vector Network Analyzer

W-Band: 75 to 110 GHz frequency Band

WG: Waveguide

X-Band: 8 to 12 GHz Frequency Band

Y_{ep}: Admitance of the p TM mode

Z: Impedance

Z_0: Characteristic Impedance

Z_{hq}: Impedance of the q TE mode

Z_L: Impedance of the Load

Mathematical Formulation

α: Atenuation Coefficient

β: Propagation of the mode

δ_{om}: Kronecker delta

φ: Escalar Electromagnetic potential solution of the Laplace equation

θ_e: Electrical length of the even mode

θ_o: Electrical length of the odd mode

ω_0: Resonant frequency of a resonator

$\Delta\omega_{3dB}$: 3dB bandwidth of a resonator

A_{qm}^{a}: Fourier expansion series coefficient m of the TE q mode in region a

B_{pl}^{a}: Fourier expansion series coefficient l of the TM p mode in region a

E_x: Cartesian component of the Electric Field

F_m^{a}: Fourier expansion series coefficient m of the TEM mode in region a

H_x: Cartesian component of the Magnetic Field

$(J_{hTEM})_q$: Coupling integral of the TE q mode and the TEM mode

$(J_{eTEM})_q$: Coupling integral of the TM q mode and the TEM mode

$(J_{he})_{pq}$: Coupling integral of the TE p mode and the TM q mode

$(J_{hh})_{pq}$: Coupling integral of the TE p mode and the TE q mode

$(J_{ee})_{pq}$: Coupling integral of the TM p mode and the TM q mode

K_c: Cutoff Wavenumber

K_x: Wavenumber cartesian component x

K_{zqm}: Wavenumber cartesian component z of the TE/TM mode qm

M_a: Number of terms to expand the Fourier Series in region a

$S_{11:}$ Reflection coefficient

S_{12}: Transmission coefficient

T(x,y): Magnetic type of vector potential

$T_{hq}^{a}(x,y)$: Magnetic Hertzian type of vector potential of the mode TE q mode in region a

$T_{ep}^{a}(x,y)$: Electric Hertzian type of vector potential of the mode TM p mode in region a

Z_{11}: Impedance matrix element

Z_{1a}^{4port}: Impedance parameter a found in the first row of the general four-port network

List of figures

List of Tables

Contents

Publications

1. R. Lopez-Villarroya, G.Goussetis, J.-S. Hong, S. A. Kosmopoulos, “E-Plane Filter Design For Space Applications With Advanced And Stringent Performance Requirement”, *ESA Microwave Technology and Techniques Workshop 2008*, May 2008.
2. R. Lopez-Villarroya, G. Goussetis, J.S. Hong, J.L. Gomez-Tornero, "E-plane Filters with Selectively Located Transmission Zeros", *38th European Microwave Conference Proc.*, pp.733-736, Octobre 2008.
3. R. Lopez Villarroya, S.K. Pavuluri, G. Goussetis, M.P.Y. Desmulliez, D.M. Kavanagh, E. McKeever, “Novel RF microfluidic sensor for particle-cell detection", *IEEE-CPMT Proceedings of IMPAS-UK MicroTech*, April 2009.
4. R. Lopez-Villarroya, G. Goussetis, "Novel topology for low-cost dual-band stopband filters," *Asia-Pacific Microwaves Conference 2009*, pp. 933-936, December 2009.
5. E. McKeever, S.K. Pavuluri, R. Lopez-Villarroya, G. Goussetis, D.M. Kavanagh, M.I. Mohammed, M.P.Y. Desmulliez, "Label-free chemical/biochemical sensing device based on an integrated microfluidic channel within a waveguide resonator," *3rd Electronic System-Integration Technology Conference (ESTC)*, pp. 1-3, 13-16, September 2010.
6. G. Goussetis, R. Lopez-Villarroya, E. Doumanis, O.S. Arowolo, J.-S. Hong, "Quality factor of E-plane periodically loaded waveguide resonators and filter applications," *IET Microwaves, Antennas & Propagation*, vol. 5, no. 7, pp. 818-822, May 2011.

Award

2010 Finalist Certificate as a participant in the MTT-11 Contest on “Creativity and Originality in Microwave Measurements” awarded by the IEEE Microwave Theory and Techniques Society.

CHAPTER 1

Introduction

1.1 BACKGROUND AND MOTIVATION

Since the first configuration appeared back in 1974 [1] but particularly over the last two decades, waveguide E-plane filters have been a widely employed solution in order to meet the increasingly demanding requirements of modern RF/Microwave applications. The benefits of E-plane filter technology are well known among the microwave filter community such us easy design procedures and low-cost of fabrication [2-3]. Despite that, a major drawback has arisen after the large variety of filter configurations presented over the last two decades, namely the stopband performance. Good isolation at stopband, however, is required in many broadband front-ends to avoid cross-talk. Devoted research efforts have been put in this direction and some E-Plane Filters which do provide attenuation slopes have been investigated [4-5], however those configurations often imply higher order realisations, resulting in bulky filter realizations and making them not suitable for applications where the final size of the filter is an important concern. As being depicted in section 1.2, it is indeed among the main motivations of this project to contribute towards overcoming that important handicap of the E-Plane Filters. A novel filter concept which aims to provide high skirt selectivity but without going into higher order designs, then providing reduced size when compared with previous configurations, is investigated in this project. Steps forward considered to investigate and validate the novel filter concept are introduced along section 1.2.

A variety of numerical techniques for electromagnetic analysis as well as more efficient Computer Aided Design (CAD) tools developed mainly back in the 80s are main factors to explain the rich progress on novel microwave components and subsystems over the recent past, which has been of benefit for the waveguide E-Plane filters research community. Particularly and closely related to the analytical contents of this project, rectangular or circular waveguides with ridges have attracted special attention due to the practical applications they can be employed for such as dual-mode filters [6], [7], [8] but essentially

they are well known solutions to reduce the cutoff frequency and provide broader single mode operation in waveguide components. The synthesis of those structures often involved cross sections involving modal solutions which are not amenable to closed-form analytical expressions. Thus, the use of numerical techniques is a common scenario on that research.

Therefore, the study of the electromagnetic propagation in waveguides with non-analytical cross sections has become a problem of significant interest. Numerical electromagnetics is not among the motivations of this thesis, however, the choice of an adequate numerical tool is essential for the initial steps of this project so a brief introduction is considered here. The different techniques appeared in the literature, mainly back in the eighties, can be split into two groups:

- Methods based on the solutions of integral equations by algorithms, for example the method of moments [9].
- Methods based on finite elements [10] or Transmission Line Modelling [11] like the transverse resonance field matching method applied in this thesis.

The numerical methods employed for the analysis of passive microwave components aim to describe the propagation of electromagnetic waves in closed physical geometries consisting of various materials. Despite the large variety of numerical methods, all of them derive from Maxwell's equations. It is indeed the different mathematical formulations of the Maxwell's equations what lead to different electromagnetic modeling techniques [12], [13]. As mentioned above, the study of numerical electromagnetic techniques is out of the motivations of this project, rather than being the starting tool for the modal analysis of the non-analytical structures for the novel filter structure involved. For that purpose, as it will be justified later, the transverse resonance field matching is the technique employed to solve those structures.

1.2 OBJECTIVES OF THE THESIS

The main objective of the present thesis is to analyze and design novel E-Plane filters configurations with improved performance for microwave applications. This general objective can be split in a more concrete form as follows:

- Full modal analysis of waveguides with ridge coaxial cross-section. For that purpose, a well know technique, the transverse resonance field matching, is the electromagnetic numerical technique of choice.
- Investigation of the mixed electric and magnetic coupling present in parallel coupled ridge waveguides. Identify the nature of the transmission zero emerged from these structures.
- Synthesis of filters with parallel coupled resonators. Through even and odd mode analysis to investigate the possibility to control the mixed coupling present in this structure in order to introduce transmission zeros at desired frequencies. Evaluate other advantages: improved skirt selectivity and miniaturization.
- Report easy design guidelines towards higher order bandpass filters based on parallel coupled resonators. Present realization examples with numerical and experimental results to validate the arguments.
- Apply the analysis of parallel coupled ridge waveguides and resonators to design high order stop-band and dual stop-band filters. Provide numerical and experimental results.
- Investigation of a microwave chemical/biochemical sensing device for the characterization and detection of cells in chemical substances and cells in solution in micro-litre volumes.

1.3 STRUCTURE OF THE THESIS

The thesis is structured in seven chapters. Chapter 2 includes an up-to-date review on E-Plane Filters. Due to the focus of this thesis, special emphasis is made on filters with pseudo-elliptic response, or those E-Plane filters which provide improved performance by introducing additional transmission zeros. Chapter 3 comprises waveguide analysis. In particular, the full modal characterization of a ridged coaxial waveguide by the transverse resonance method is presented. The results computed are demanded for the development of the following chapters. In Chapter 4 a novel coupling scheme for filter design of stringent performance is considered. First of all, a careful investigation of the mixed electric and magnetic coupling present in parallel coupled ridge waveguides is performed. In short the analysis leads to the realization of parallel coupled resonator with transmission zeros at selected locations. General design procedures are derived and the filter concept is demonstrated by means of a realization of examples. In Chapter 5 are discussed some aspects regarding the limits of the technology: suggestions for optimization are reported, including Q factor assessments towards lower insertion loss in the passband and further size reduction. In Chapter 6 three further in-line filter applications arised from the analysis of Chapter 3 and 4 are presented. Section 6.1 describes the realization of higher order stopband and dual stopband filters. The configuration presented preserves the straightforward design procedure providing quasi independently coupled stopbands. Both single and dual stopband configurations are validated with numerical and experimental results. In section 6.2 a microwave chemical/biochemical sensing device for the characterization and detection of cells in chemical substances and cells in solution in micro-litre volumes is presented. Promising preliminary results and status of research are reported. The last application is a waveguide T-Junction diplexer, presented in 6.3. In summary, Chapter 7 compiles the conclusions outlined from the thesis and suggests some directions of future work.

The synopsis of this thesis has been schematically depicted in Fig. 1-1:

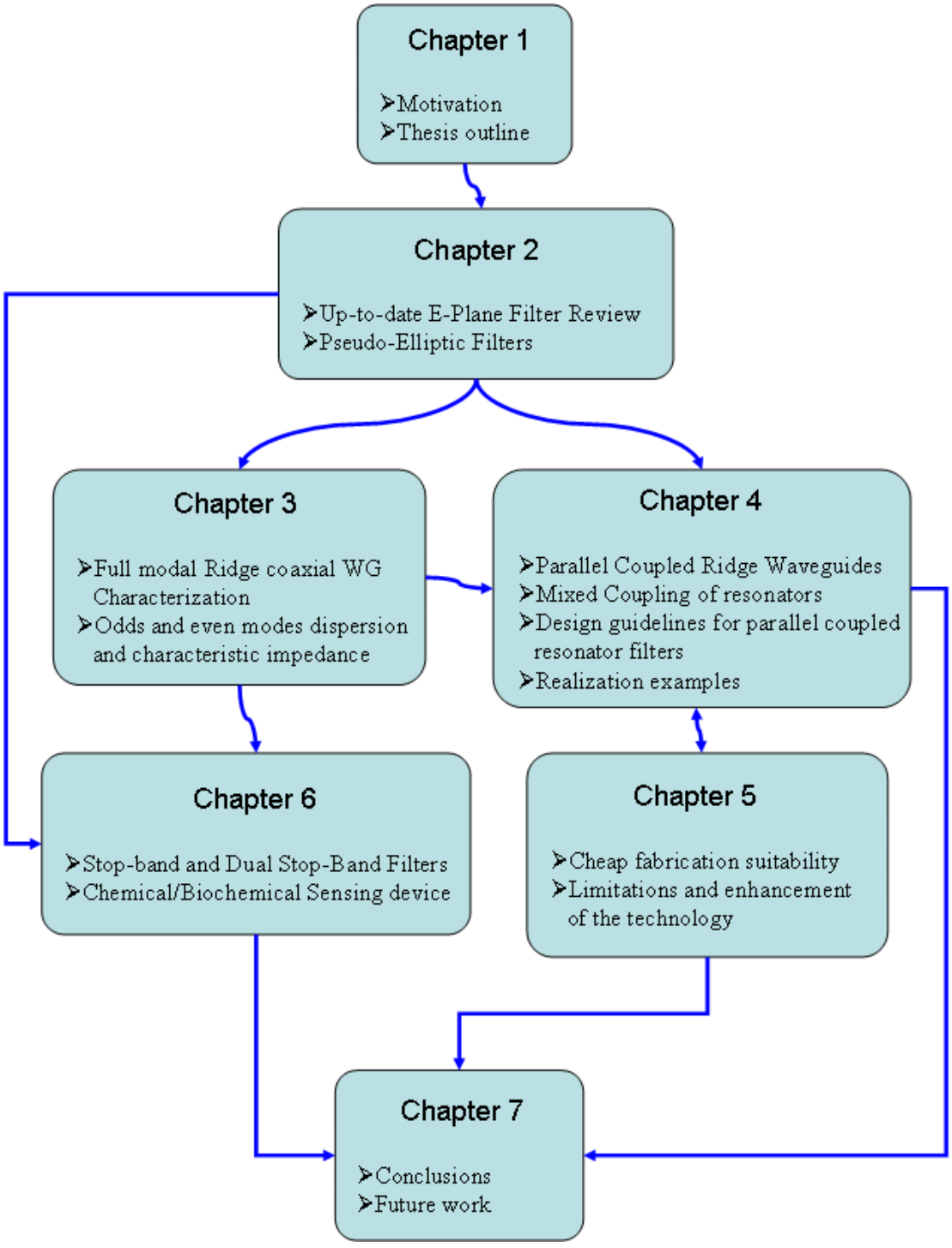

Fig. 1-1. Synopsis of the thesis.

CHAPTER 2

All-Metal-Insert E-Plane Waveguide Filter Configurations

2.1 INTRODUCTION

Quasi-planar filters have received an extensive interest by RF/Microwave community since the first configuration appeared back in 1974 [1]. The term "quasi-planar" was originally used to refer a microstrip or slotline (planar circuit) suspended in the E or H plane of a rectangular waveguide. The concept was extended later on in [28] to structures with all-metal-inserts provided that the metal insert sheet allows the photoetching technique to realize the insert pattern. Therefore there are two classes of filters: those containing dielectric material to support a thin metallization pattern and those with relatively thick metallization (inserts placed in the housing waveguide not requiring supporting substrate). The first class of filters is suitable for large-scale integration on the same substrate material while the second group has been a commonly used solution for high power signals and for stand-alone filter components, benefiting from lower losses because the absence of lossy substrate. Due to the motivations of this thesis and the vast extension on the topic, only the second class of filters (without substrate) and just those E-Plane realizations, are compiled along this summary.

In fact, E-Plane all-metal-inserts configurations alone have been already largely reported in the literature [15-34]. Demonstrated excellence of the technology in order to satisfy stringent filter performance is well known, providing two attractive advantages of E-Plane configurations: ease of the design and compatibility with low-cost fabrication. All-metal-inserts E-plane filters can be fabricated with well-developed processes that yield good tolerances even in large production scale. All that has made all-metal-inserts waveguide E-Plane filters one of the most widely used solution in space and ground communication systems [51]. However the limitations of the technology are also well known: bulky size and fairly poor skirt selectivity for some applications. For example, in multichannel applications for such filters it is desirable to improve their skirt selectivity saving the

number of sections but maintaining the level of losses. Devoted research effort has been directed over the last two decades in order to overcome those disadvantages [15-34].

In this chapter to the most commonly employed all-metal-insert E-Plane filter configurations are compiled from an extensive literature survey. Attending to their applications, a general review of the most commonly employed Low-pass, Bandpass and Bandstop E-Plane Filter configurations are described in section 2.2. In particular due to the relevance and related with the motivation of the thesis special emphasis is put on describing filter configurations with improved skirt selectivity by means of producing controllable transmission zeros. Section 2.3 comprises all-metal-insert E-Plane configuration offering a pseudo-elliptic response.

Finally, a very brief introduction on diplexer realizations employing waveguide E-Plane filter channel is included in section 2.4. A novel diplexer aplication will be presented at the end of Chapter 6.

2.2 E-PLANE FILTERS

E-Plane filters with all-metal inserts were originally proposed in 1974 as low-cost mass producible circuits for microwave frequencies [1], [14], such as bandpass filters. During the early eighties, at the time more advanced computer-based routines based on accurate analysis were developed, publications including general design theory and extending the original concept to millimetre-wave application increasingly began to appear. E-plane Filters, like other Filter devices, have the property of frequency-selective transmission. They are designed to attenuate energy in one or more stopbands while transmitting energy in one or more passbands. Filters can be classified into different categories in many ways. According to their general frequency response they can be devided into three basic types: lowpass, bandpass and finally stopband filters. As this work concentrates mainly in bandpass filters, emphasis on these devices is made in this literature review.

2.2.1 Low-pass filters

Low-pass filters can be designed using any structure with alternating impedance steps. Waveguide low-pass E-Plane filters are only quasi-low-pass; any equivalent circuit will have a dominant-mode cutoff frequency, which yields below that of the housing waveguide without any insert. Three commonly employed configurations are depicted in Fig. 2-1. The structure in Fig. 2.1a shows large impedance steps between alternating sections of overlapping (low impedance) and non overlapping (high impedance) inserts. Fig. 2-1b shows the design employed in [15] using a series of approximately quarter-wavelength coupled notches. An interesting structure published in [16] is depicted in Fig. 2-1c. Here a broadside-coupled microstrip circuit is suspended in the E-Plane of a rectangular waveguide.

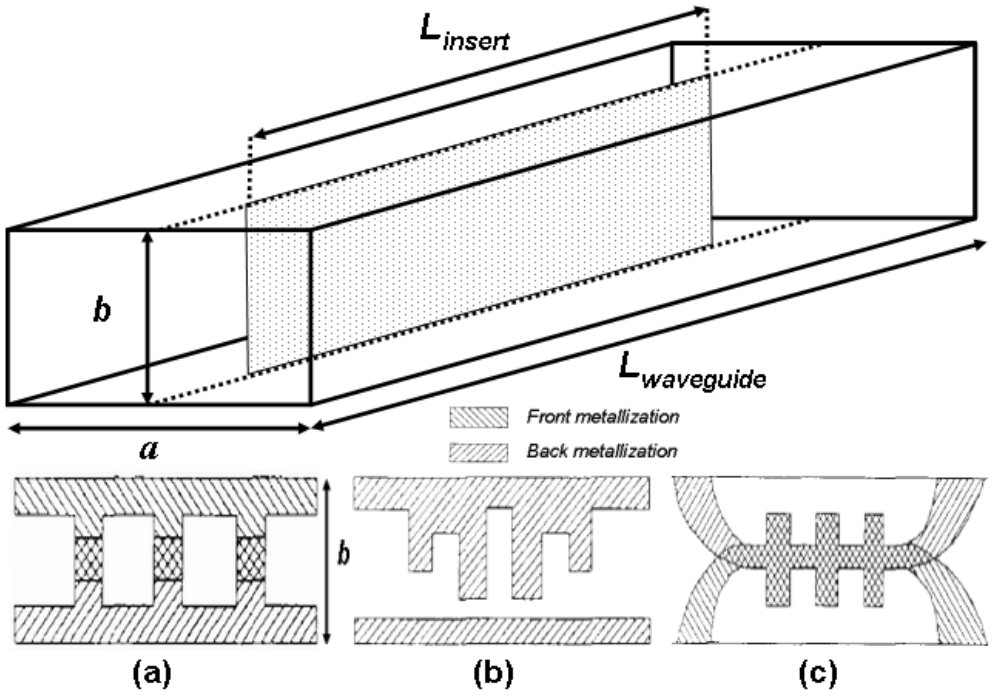

Fig. 2-1. Typical insert structures for low-pass filters mounted on the E-Plane of a rectangular Waveguide [15]

More recently, an accurate description of the structure depicted in Fig. 2.1b based on Electromagnetic Band Gaps has been employed for different applications [17]. EBG structures have a frequency band in which no electromagnetic mode can propagate. Furthermore, at other frequencies, EBG structures have the property of reducing the phase velocity of EM modes, according to the slow wave effect. Typically, the EBG property

emerges by virtue of periodic reactive loading of the guiding structure. In the general case, adopting an equivalent circuit approach, simple loads can be inductive (L), capacitive (C) or resonant (both L and C), in either series or shunt topology [17]. An interesting structure is included in Fig. 2-2a. E-plane split-block housing topology offers a suitable platform for the realization of a waveguide with periodic resonant loads, in the form of thin ridges (Fig. 2-2b).

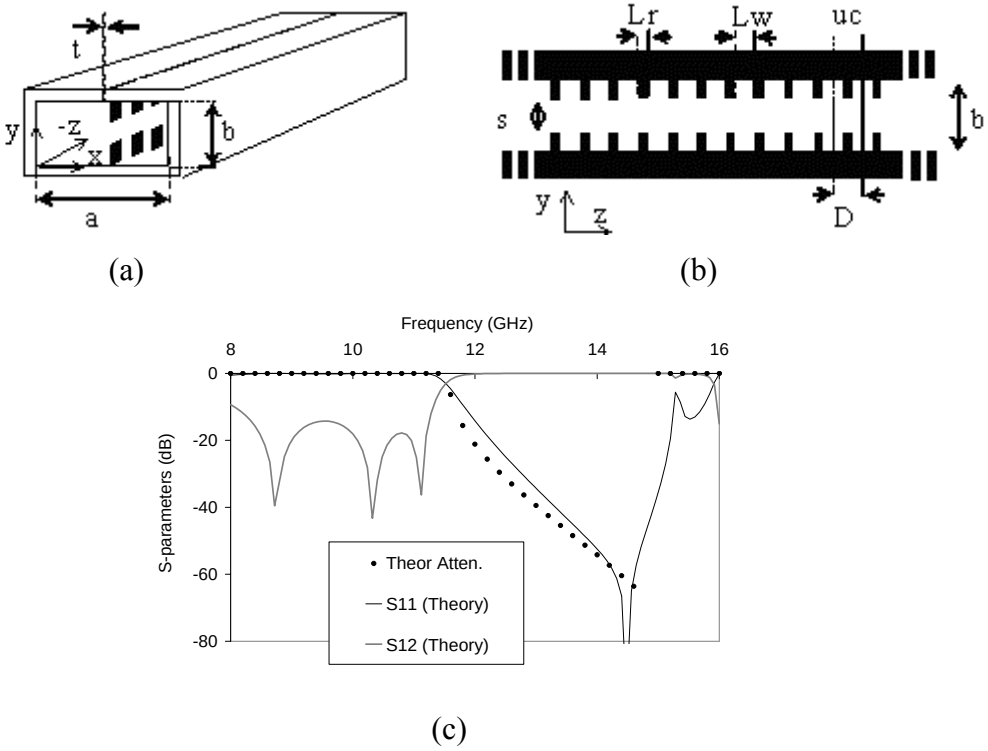

Fig. 2-2. Periodically loaded E-Plane Filter [17]. Layout of the E-plane EBG waveguide (a), cross sectional view (b) and simulated mode matching results for a fifth-order low-pass prototype (c). Dots shows S12 as estimated from the attenuation constant of the infinite structure. Dimensions: Lw=6 mm, Lr=2 mm, s=1 mm. Thickness of metal insert is t=0.1 mm.

The band gap corresponds to the stopband, provided that matching with the input and output is achieved. A simple optimization using a full-wave mode matching model for the finite structure has been performed. The full-wave response is reproduced in Fig. 2-2c, where is demonstrated that a transmission zero is introduced as a result of the periodic loading resonance. This is identified in Fig. 2-2c as the sharp minimum at about 14.2GHz. In the eigenvalue solution, the transmission zero is identified by a sharp peak in the

attenuation coefficient, α, in the band gap. The theoretical attenuation as calculated by $e^{-\alpha z}$ is also compared in Fig. 2-3c. It is interesting to note that the attenuation coefficient derived for the infinite structure predicts to a good extent the response of the finite structure.

2.2.2 Band-pass filters

One of the most challenging problem for designers to overcome is dissipation loss in filter realizations. The unloaded quality factor (Q) of the resonators used in a microwave filter depends on their physical realizations. The insertion loss in the passband is inversily proportional to the filter bandwidth and the resonator Q-factor is proportional to the number of resonators used. Hence, for narrow-band applications, resonators with high Unloaded Q must be used in order to achieve low passband loss [8]. On top of that, the skirt selectivity of a filter can be improved by increasing the number of resonators which makes the filter longer and increases the loss.

The band-pass E-Plane Filter has been one of the most reported filters in the literature. The standard configuration for E-plane filters is to use a split block waveguide housing and place inductive typically all metal septa, in the E-plane of a rectangular waveguide, at spacing close to a half wavelength apart. This configuration is depicted in Fig. 2-3

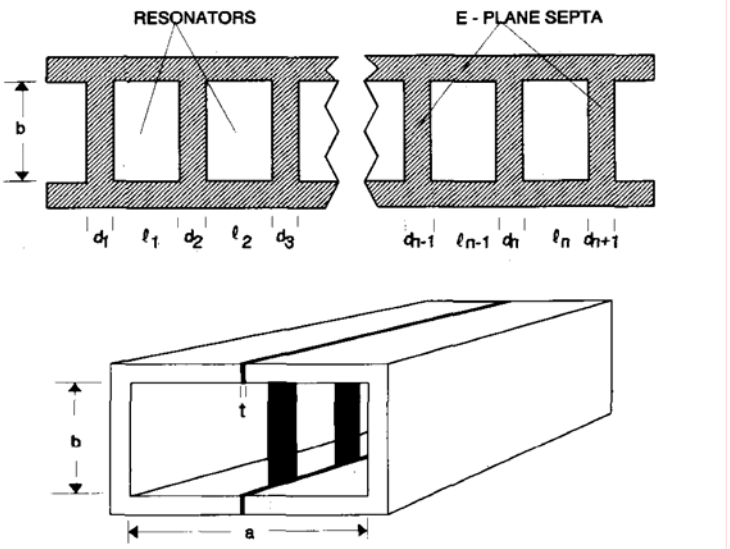

Fig. 2-3. Common E-Plane bandpass filter topology [18].

Because dielectric losses are absent, the structure has a high transmission Q factor and is suitable for narrow-band high-Q applications. Furthermore, these E-plane filters are very easy to build due to the fact that the design is based on printed circuits fabricated with photolithographic process and no need for tuning.

The configuration of Fig. 2-3 is originally suggested back in 1974 [1], about one decade after together with the development of more efficient computer aided design (CAD) tools, a detailed analysis of the bandpass filter in the X-Band including the effect of finite-thickness septa appeared [18]. The study of the effect of the metalization for the conventional E-Plane Filter shows that the increase in septum thickness effectively shortens the equivalent length of the resonators formed between two septa, thus shifting the resonant frequency upward. For a filter prototype of fourth order it was about 150 MHz per 1-mil increase in thickness. In addition to this shift in frequency, the Compuer Aided Design (CAD) tool employed predicted a slight increase in pass-band ripple. Over the following two years, a general study in the W-Band [19] as well as an accurate design description [20] of the filter prototypes were reported. However, despite their favourable characteristics, E-plane filters suffer from bulky size and stop-band performance that may often be too low and too narrow for many applications.

Over the following years different solutions to overcome with this limitation and enhance the performance of the technology were consequently presented. The first variation of the topology presented in [21] suggested locating the ladder-type insert in a waveguide section which is either wider or narrower than the embedding standard waveguide (see Fig 2-4). Both types of filters provide significantly improved stop-band attenuation and a have a better suppression of spurious passbands. In particular for the protype of Fig 2-4b a 7GHz sporiuous resonance shift or approximately a 15% over normalized frequency. Similar elements were argued for finline filters (substrates).

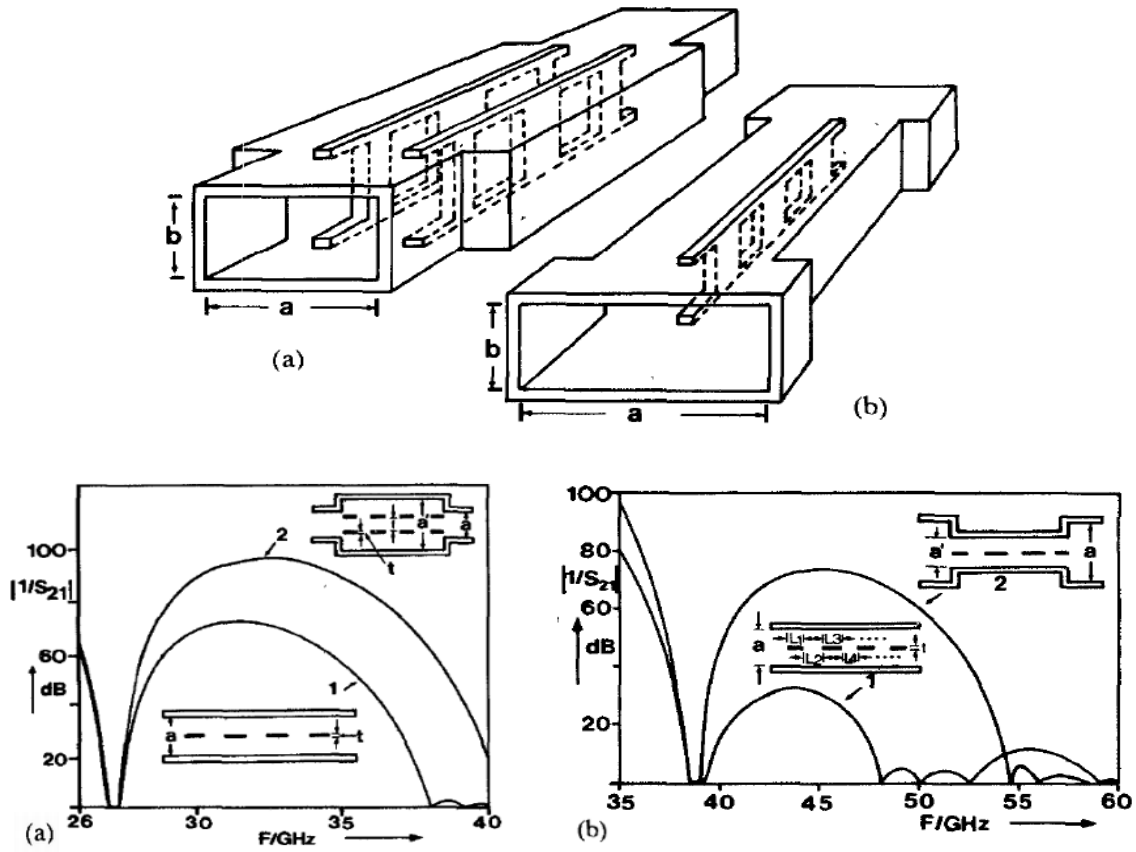

Fig. 2-4. Band-pass configurations for stop-band enhancement based on WG section. (a) Filter with enlarged section and a twin metal insert and (b) a single metal insert filter in a narrower waveguide section. Comparative standard fourth Filter responses shown below [21].

Towards improving the skirt selectivity of standard millimetre-wave E-Plane Filters but simultaneously maintaining the compatibility with the integrated circuit manufacturing process. An interesting optimization-based approach to the design of asymmetrical filter structures (Fig. 2-5) having the maximum number of return- or insertion-loss ripples in the pass-band such a as those based on Chebyshev function prototypes was presented in [22].

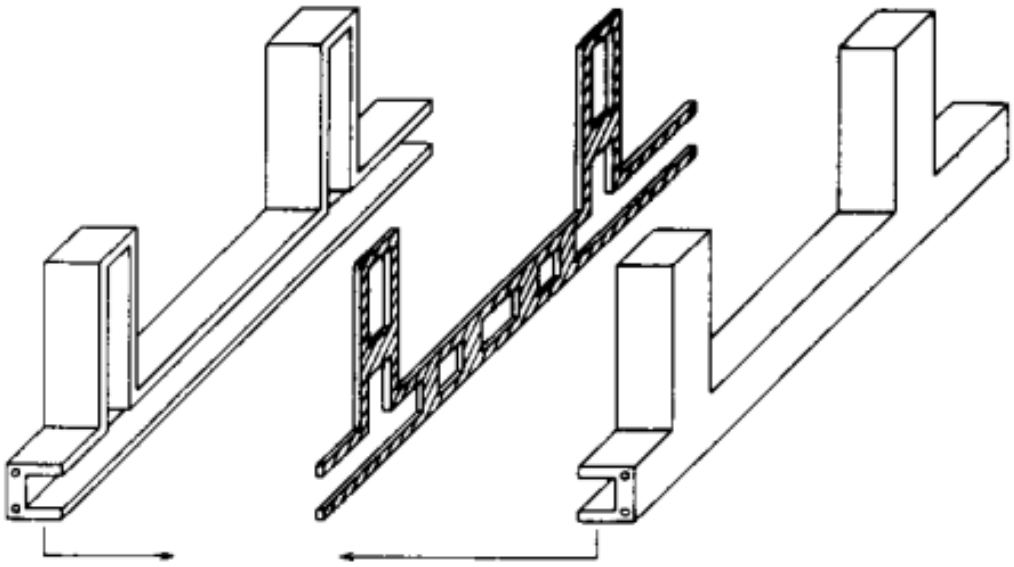

Fig. 2-5. Improved-selectivity asymmetrical E-Plane filter configuration: a three-resonator filter including two stop-band stubs [22].

This design is based on inductively coupled stop-band sections in addition to the conventional component, hence introducing attenuation peaks near the pass-band that improves the selectivity. However the highly unsymmetrical filter structure sacrifices the response in the lower stop-band in benefit of the attenuation poles close to the upper band edge. This feature is getting more critical as those poles are closer to the pass-band.

Maintaining the original configuration, an optimized procedure for the design of asymmetrical (shown in Fig. 2-6) microwave filters was presented in [23]. This method provides a guiding-tool for the design of filters with strict stopband performance.

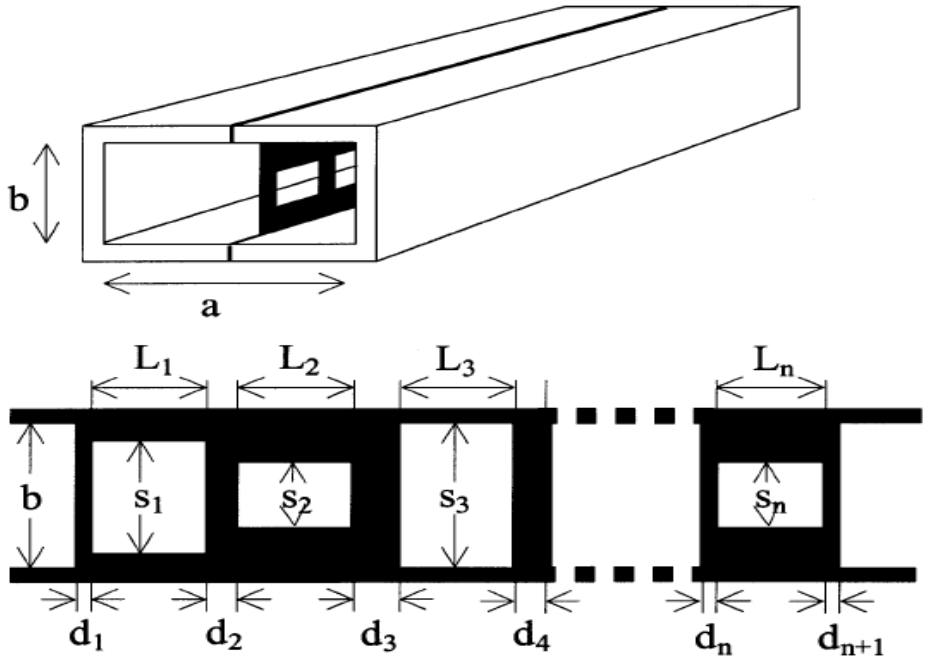

Fig. 2-6. Compact Asymmetrical Ridge Waveguide Filter Configuration [23].

The configuration maintains similar size than the standard prototypes providing suppression of the spurious resonance. Compactness is achieved in the band-pass section taking advantage of the properties of the slow waves in half wave resonators, while spurious behaviour suppression is achieved by means of an integrated low-pass structure [23].

Moreover, combining these elements with those described in the EBG waveguides [24] a low-pass filter has been integrated with an E-plane band-pass filter in order to suppress the spurious harmonic resonance of the latter [5]. The measured response and a photograph of the prototype are shown in Fig 2-7. The stop-band of the E-plane filter, which originally extended up to about 12.5 GHz, now extends to about 15 GHz, without any associated increase in the fabrication complexity.

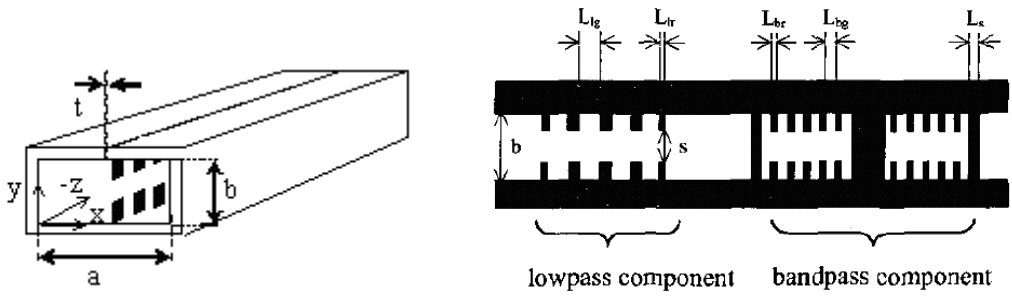

(a)

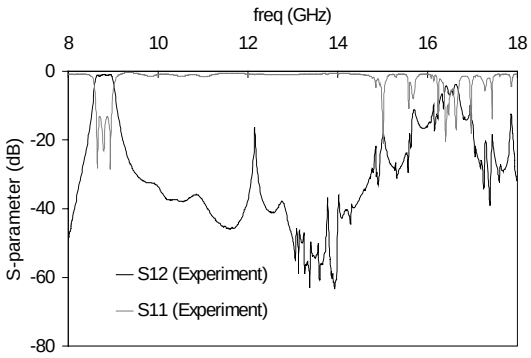

(b)

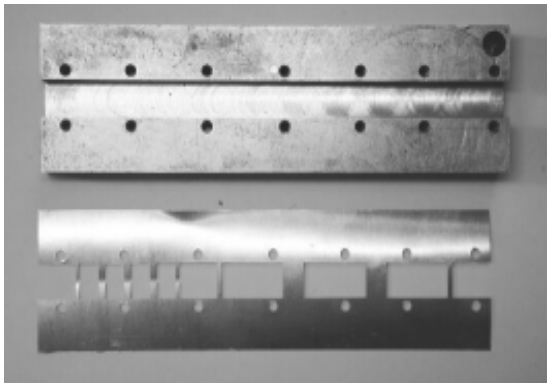

(c)

Fig. 2-7. Compact Ridge Waveguide Integrated E-Plane Filters (a), measured response (b), and photograph (c), of a fabricated 3rd order E-plane filter integrated with the lowpass structure for suppression of spurious passband [5].

More recently, a novel class of E-Plane all-metal-insert filter structure showed the replacement of the conventional section of rectangular waveguide E-Plane filters with the respective S-shaped resonators proposed in [26]. By employing those resonators the cutoff frequency of the conventional resonator is changed and a higher loaded Q can be achieved with shorter resonator lengths [27]. The improvement is due to the slow wave effect; the phase velocity and the guided wavelength of the slow wave are significantly reduced when compared to those of a wave propagating in a comparable homogeneous resonator structure. The schematic of this configuration is depicted in Fig. 2-8.

Significant size reduction is obtained, furthermore the extended upper stop-band was to 17.5 GHz at a rejection level of 15 dB.

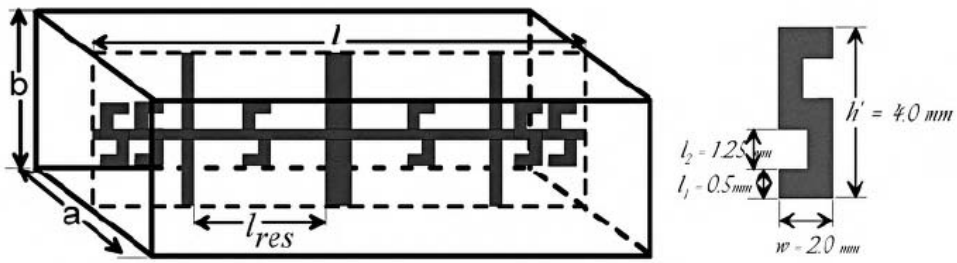

Fig. 2-8. Configuration of an all-metal-insert S-shaped resonator waveguide filter [27].

2.2.3 Bandstop filters

The presence of the bandstop filter configuration in E-plane technology in the literature is fairly limited. As it was reported in [28] this is due to the difficulty in producing equivalent circuit elements to design bandstop filters. Among the proposed ideas, the use of a reaction type resonator was suggested in [29]. Even though the very high flexibility in the design for microwave narrow band applications the bandstop selectivity that can be achieved is fairly poor. In chapter 6 it will be discussed on the possibility to improve this limitation as well as to extend the concept to dual bandstop applications.

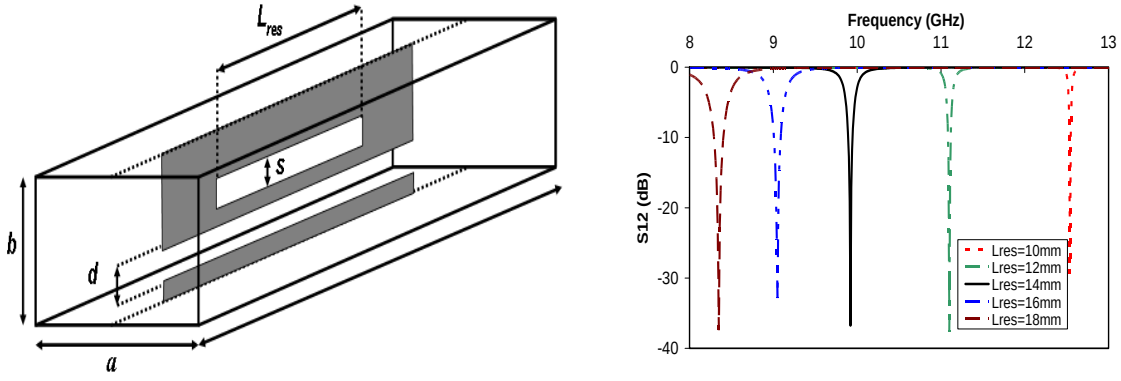

Fig. 2-9. E-Plane Bandstop Filter realization based on reaction type resonators (a) and Transmission response in term of the resonator length [29].

2.3 E-PLANE FILTER REALIZATIONS OF PSEUDO-ELLIPTIC FILTERS

A common disadvantage of E-Plane bandpass filters is that for a given number of resonators they do not provide steep enough attenuation slopes. However this features is required in many broad-band front end circuits, in particular for diplexer aplications with sharp cutoff between the channels to avoid cross-talk. The design of planar band-pass filters with attenuation (Transmission Zeros) poles based on half wavelength resonator has been a recurrent solution. The possibilty to introduce Transmission Zeros at desired frequencies is interesting to implement filters with excellent attenuation characteristics. Even though it is possible indeed to generate finite transmission zeros in direct-coupled resonator filters if the coupling coefficient between the resonator is strongly dispersive [30] many structures with different coupling schemes have been presented over the last decade. According to the nature of the coupling which introduce additional transmission zero, pseudo-elliptic Filters will be clasified in four groups: extracted poles, cross coupling, over-moded cavities and parallel coupling.

2.3.1 Extracted poles

A new class of integrated E-Plane bandpass circuit was introduced to provide high skirt selectivity having an asymmetric transfer function [31]. That was achieved using extracted pole resonators to produce finite transmission zeros which can be placed asymmetrically at the frequencies of interest. The extracted pole resonators are realised by parallel coupled finline tracks as shown in Fig. 2-10. The resultant structure consists entirely of a single circuit board or metal inserts held in a rectangular waveguide as with conventional E-Plane filters. Practical results were presented in the X-Band. The imperfect match of the filter is due to the approximate design procedure not taking into account the interaction between successive discontinuities.

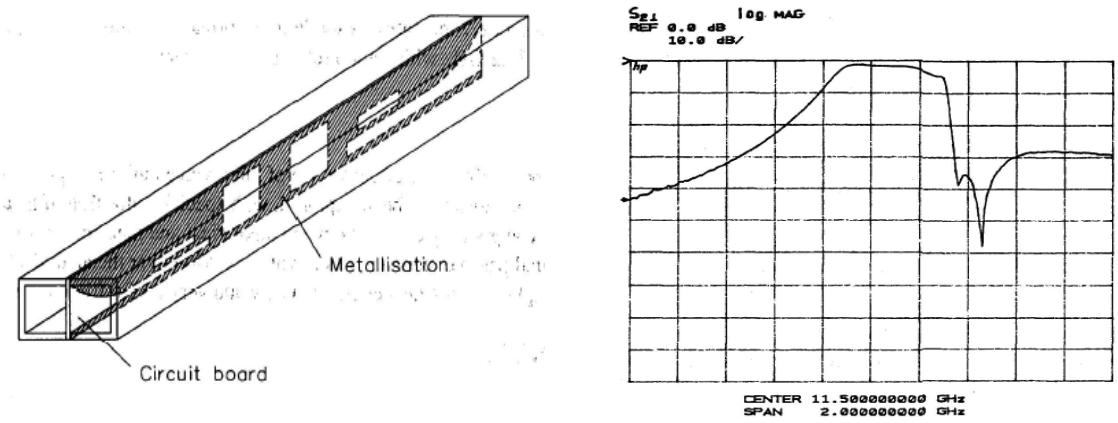

Fig. 2-10. E-plane Filters with extracted poles [31].

2.3.2 Cross coupling

In E-Plane Filters, more extensively, the use of attenuation poles near the passband has been published based on cross-coupled resonators. In [32], [33] different configurations with two transmission zeros of compact E-Plane Ridge Waveguide Filters with pseudo-elliptic response were reported. The skirt selectivity and the stopband performance of the prototypes presented is widely improved compared with the possibilities of the original E-Plane of the same order. However, the complexity in the design and the highly asymmetrical final configuration were a disadvantage (Fig. 2-11)

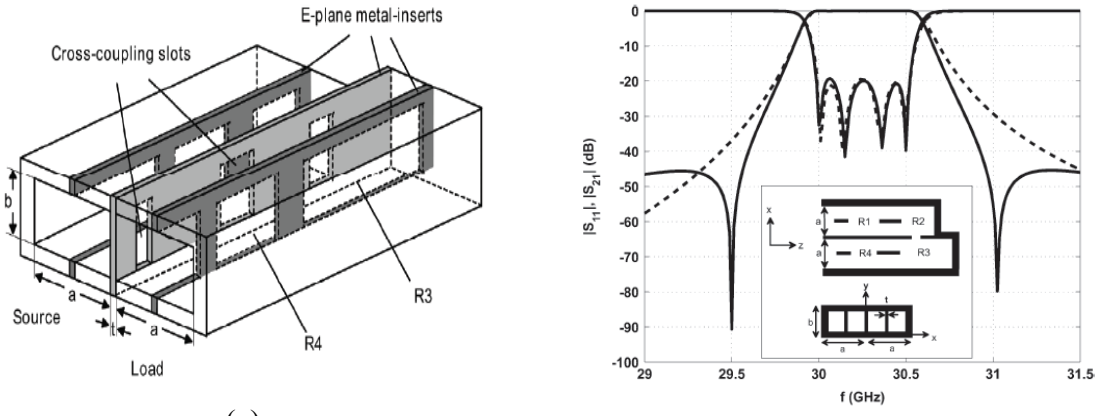

Fig. 2-11. Cross-coupling E-Plane filter configuration (a) and its transmission and reflection response compared with an standard E-Plane single metal-insert filter (b) [33].

2.3.3 Over moded cavities

For some applications where only one transmission zero is required, E-Plane filter realizations can be achieved by using dispersive stubs as suggested in [33]. Here, it is also considered all resonators coupled via metal inserts. The coupling coefficient between resonator 2 and the over-moded cavity is approximately known (Fig. 2-12). The design is made by setting the slot width in the separating wall coupling resonator 2 and 3 to produce the same coupling coefficient. A transmission zero occurs either on the left or right side of the passband when the coupling slot is positioned in the second half of the over-moded cavity.

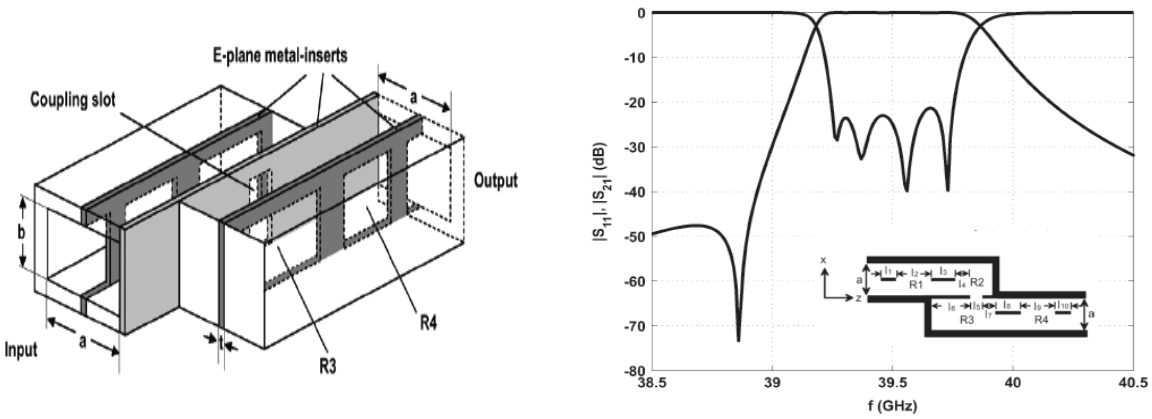

Fig. 2-12. Over-modded cavity Filter with one transmission zero [33].

2.3.4 Parallel coupling

Far from that complexity of those configurations, an alternative design maintains the simplicity of the standard E-Plane prototypes producing selectively located transmission zeros [34]. Suppression of the spurious resonances and hence improvement of the stopband performance it is also achieved by introducing parallel coupling between the resonators of waveguide filters (Fig. 2-13). This also results in a significant reduction of the total size of the filter. This topology allows for cross-coupling between the resonators, thus introducing transmission zeros at finite frequencies.

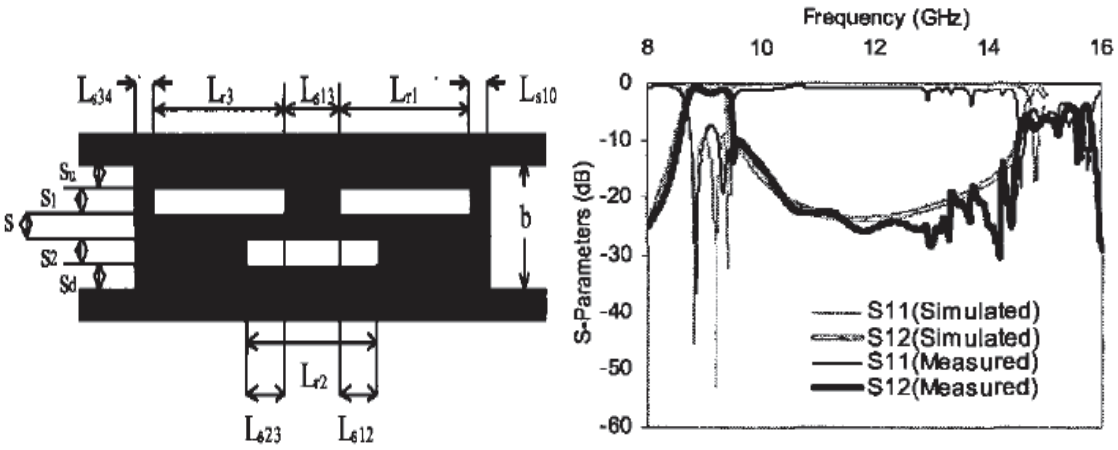

Fig. 2-13. E-plane Filters with Transmission zeros based on parallel coupling [34].

2.4 E-PLANE DIPLEXER

Diplexers are important components in communication systems for splitting a frequency into two sub-bands. Basically a diplexer consists of a power divider and two filter channels. A large variety of geometrical realisations combining diferent structures for the power divider and the filter channels have been reported in the literature [84]. Commonly employed Diplexer configurations with E-Plane filter channels are depicted in Fig. 2-14.

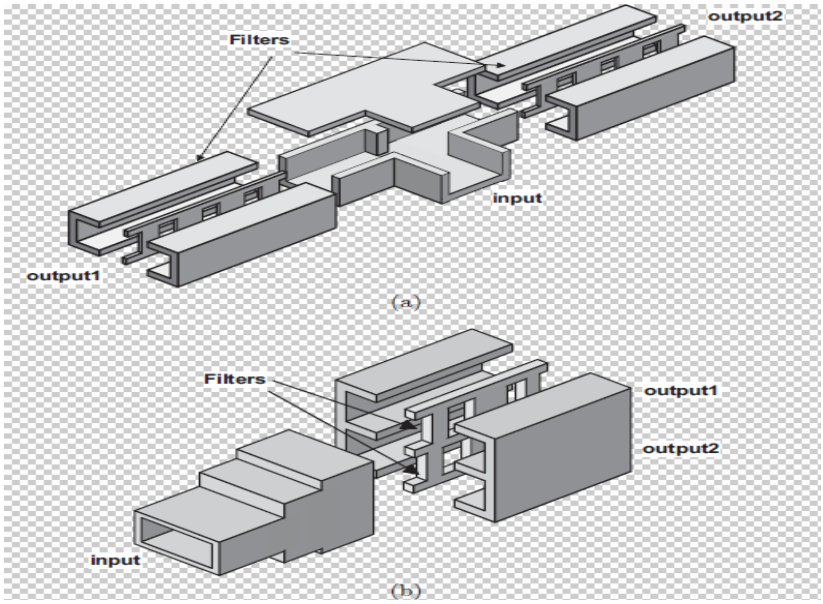

Fig. 2-14. Conventional E-Plane Filter Diplexers with H-Plane Power Divider (a) and with E-Plane Power Bifurcation Divider (b) [106].

2.5 CONCLUSSION

This chapter compiled a revision of the most commonly employed E-Plane filter for microwave and millimeter-wave applications. According to their general frequency response they have been classified into three basic types: lowpass, bandpass and bandstop filters. The emphasis has been directed to those configurations suitable to introduce selectively located transmission zeros. Also, a brief introduction on diplexors based on E-plane filters has been included: these will be mentioned in the Chapter 6 of this thesis. In this context, the prototypes presented so far suffer from bulky size for realizations involving a high numer of resonator, while practical designs can be dificult. For the future, small and simple filtering waveguide structures able to provide stringent passband selectivity are considered of potential interest.

CHAPTER 3

Full Modal Analysis of a Ridge Coaxial Waveguide

3.1 INTRODUCTION

Coaxial waveguides have been largely investigated in the recent past due to their practical different applications. Among them, they can be employed to produce EM fields with predefined characteristics [35],[36] or as TEM cells for study of electromagnetic compatibility and the effect of RF radiation [37],[38]. Moreover, transmission lines operating in the TEM regime are widely used in microwaves circuits. In many cases, TEM and non-TEM devices need to be connected in a cascaded configuration, requiring a transition between the two types of lines. Such a transition would possess some of the geometrical features of the two lines at both ends.

In the recent past, related with the increased interest for the development and synthesis of a large range of E-plane filters it has been shown this technology offers the possibility of realizing low cost, mass producible and low dissipation millimeter-wave filters [42]. In the context of filters with coupled resonators [43] a transition between a coaxial TEM line and a double-ridged waveguide has been devised. However, the electromagnetic analysis of such structure involves a surface discontinuity, an example is a Ridge Coaxial Waveguide (RCWG) which has received little attention in the literature. To overcome this requirement and hence to explore in further work some potential practical filter applications, a full characterization is presented in this chapter. The TEM mode has been rigorously solved using the integral equation formulation and the method of Moments [41]. In this contribution therefore a full wave solution of higher order TE and TM modes as well as the TEM mode for the Ridge Coaxial Waveguide is presented.

In this chapter the full modal characterization of the double ridged coaxial waveguide is described. The analysis of this structure will be useful in further chapters, where the results

obtained are employed in the design of novel E-Plane involving Ridge Coaxial Waveguide (RCWG) cross-sections.

As introduced in Chapter 1, the choice of a particular numerical method depends on different considerations; mainly on the geometry of the structure studied but also the required accuracy, speed, storage requirements and versatility. In closed waveguide structures with axial uniformity, it is common to express the propagating electromagnetic waves in terms of orthogonal modes whose cross-sectional shape and electrical properties do not vary along the axis. Several methods have been employed to determine the cutoff frequency and the field distribution in a waveguide. Some of them are the finite element method, the variational method, the integral eigenvalue method and the transverse resonance field matching technique.

In the finite element method, the region of interest is divided into mesh points. A Cartesian lattice (orthogonal and equidistant vertices) is used. The quantity of interest is expressed in terms of its derivatives, which are calculated as finite differences along the mesh. It is the least analytical method. The mathematical pre-processing is minimal and the method can be applied to a wide range of structures, including those with odd shapes. The major drawback is computational inefficiency, since it requires a large number of mesh points. Another problem of this method is the difficulty of fitting random shaped boundaries (e.g. curved) with a rectangular mesh. But this problem does not appear in the finite element method.

According to the Variational method, an eigenvalue problem is formed and a parameterised function is assumed to be the eigenfunction in this method. Minimising the eigenvalue equation with respect to its parameters, an upper bound of the eigenvalue is obtained. This method however may call for considerable mathematical insight on the part of the user.

The field matching method thus requires thorough description of the field distribution of each mode. As we pointed out before, in hollow rectangular waveguides, the field distribution of the modes is easily derived analytically, but in RCWG because the boundary conditions imposed by the cross-section are more complicated, an analytical solution is not obtainable. A numerical solution is therefore required to solve the propagation in RCWG.

For this purpose, the transverse resonance field matching method is the modelling tool chosen to characterize this structure.

The concept of transverse resonance is a rather old one and is equally well applied in equivalent circuit analysis [39] or rigorous full wave solutions [40]. According to this method, the propagation characteristics for each mode can be analysed at its cutoff frequency, where there is no z-dependence and hence a three dimensional problem is transformed into a two dimensional one. Application of field matching is then from a physical (and mathematical) point of view very similar to the mode matching approach. The cross-section of the waveguide is divided in discrete regions with simple shape. The fields of the standing wave are expressed independently in an orthogonal basis in each region and are matched at common surface.

First of all, section 3.2 presents a literature review to motivate the choice of the Transverse Resonance Field Matching technique to obtain the full modal analysis of the Ridge Coaxial Waveguide. Section 3.2.1 provides a basic theoretical introduction on how to express the electromagnetic wave modes in terms of vector potentials, which is a more convenient formulation of the modes prior to application of the transverse resonance technique. After some symmetrical considerations the Field matching analysis of the discrete regions employed in the analysis is discussed in section 3.2.2. The computational tool developed allows easy characterization of the waveguide for up to 50 modes. Due to the practical filter realizations considered in further chapters (classical waveguide housing of 22.86x10.16 mm) the cutoff frequency of higher order modes is above operating range, that is, the filters basically operate in dual mode, a detailed field distribution of the first TE, TM as well as the TEM is included. In fact those results will be of significant importance later on to exploit the asymmetric parallel coupled ridged waveguides for bandpass filter structures (Chapter 4). Also the results are of relevance for the stopband and dualbandstop realizations investigated in Chapter 5. Section 3.3 include the validation of the numerical results obtained: those are compared with the partial results obtained thorough other techniques like method of moments for the TEM mode of the Ridge Coaxial Waveguide (section 3.3.4) or the particular case of a Coaxial Waveguide (section 3.3.3).

3.2 TRANSVERSE RESONANCE FIELD MATCHING ANALYSIS

The transverse resonant technique uses the fact that for homogeneously filled waveguides, the cross-sectional distribution of the field for each mode is independent of the frequency [49]. This fact is derived as a result of separability of the wave equation for spatial and time coordinates and is fundamental in the mode-approach of waveguide propagation. The knowledge of the cutoff frequency is then sufficient to determine the propagation constant at any frequency (from the vector Helmholtz equation) since for a given mode, the relative field structure will be the same at every cross-section and every frequency. The fields are therefore analysed at cutoff frequency, assuming standing waves along the transverse coordinates and no propagation along the longitudinal axis (transverse resonance, $k_z = 0$). The longitudinal dependence of the field can thus be neglected and the derivative with respect to it taken as zero. Hence the three-dimensional problem is reduced to two dimensions. The latter will give the cross-sectional distribution of the electromagnetic field for TE and TM modes, which will be valid for frequencies other than the cutoff frequency.

The concept of field-matching lies into theoretical division of the cross section under consideration into discrete regions. The fields in each region (or equivalently the vector potentials) are then expressed in an orthonormal basis. The regions should have simple geometrical form (simple boundaries), so that it will be easy to apply the boundary conditions. An interface relation should then be applied, according to which the tangential fields should be continuous at the common surface. Using the orthogonality property of the basis, this relation is reduced to a linear system. Hence we can obtain a basis that describes the field.

3.2.1 Modal field distribution

Before applying the technique it is interesting to make some remarks concerning the geometrical and electromagnetic symmetries of waveguides that can simplify the problem. Such symmetry considerations are derived from physical insight of the problem and can prove to be very useful in reducing the mathematical and computational complexity of the numerical solution.

From circuit theory the analysis of a symmetrical circuit can be expressed as a superposition of even and odd mode solutions [48]. Even mode in this case implies that equal potentials apply at each end of the circuit; so an open circuit along the line of symmetry can be considered. Odd-mode implies opposite potentials at each end of the circuit; in this case a short circuit along the line of symmetry. The transfer matrix of a network can then be given in terms of the even and odd mode admittances.

This idea can be extended to distributed 3D structures such as waveguides. In waveguides a short circuit is represented by a electric wall. This is well understood since the tangential electric field along such a surface is zero and hence the equivalent voltage is zero. Inside a waveguide an electric wall is a surface where the tangential components of the electric fields are zero By analogy, an open circuit is represented by a magnetic wall; for zero tangential magnetic field, the equivalent current is also zero [49]. Hence an even and odd analysis of symmetrical distributed microwave structures can in principle be made assuming magnetic and electric wall along the symmetry plane. The overall problem can be split in four smaller problems: odd TE modes, even TE modes, odd TM modes and even TM modes.

However in this particular case, assuming always the excitation is symmetrical, the even and odd mode are also incident to a discontinuity which preserves the same geometrical symmetry over the E-Plane (x=0 in Fig. 3-1), therefore, from the Helmholtz vector equation the problem can be simplified considering just an equivalent structure of half physical size with a magnetic wall along the symmetry plane for both even and odd TE and TM modes.

Other boundary conditions can be applied considering the physical insight of the discontinuity: as the fundamental mode of rectangular waveguides has component of the electric field only along the E-plane, the field distribution of E_y does not depend on the y spatial coordinate but only on x and z. Hence if an obstacle lies along the E-plane isotropically, and therefore does not introduce new boundary conditions on the field so far as the y-coordinate is concerned, the entire scattered field must also be independent from y. Furthermore it immediately follows that this field must have only a single component of electric field, directed along the y-axis. That can be visualized considering the x and z components of the E-Fields of value more than zero. Then, since the electric field must be

normal to all metallic surfaces, each would have to vanish on the walls of the waveguide at y=-b/2 and y=b/2. However, since the field is independent of y, these boundary conditions can be satisfied only if each of these components is identically zero everywhere [48].

Taking into account of these symmetry considerations as it is shown in Figure 3-1, the RCWG has the symmetric shape in the right and left hand side to y axis at x=a/2, so only one half of the structure needs to be analysed.

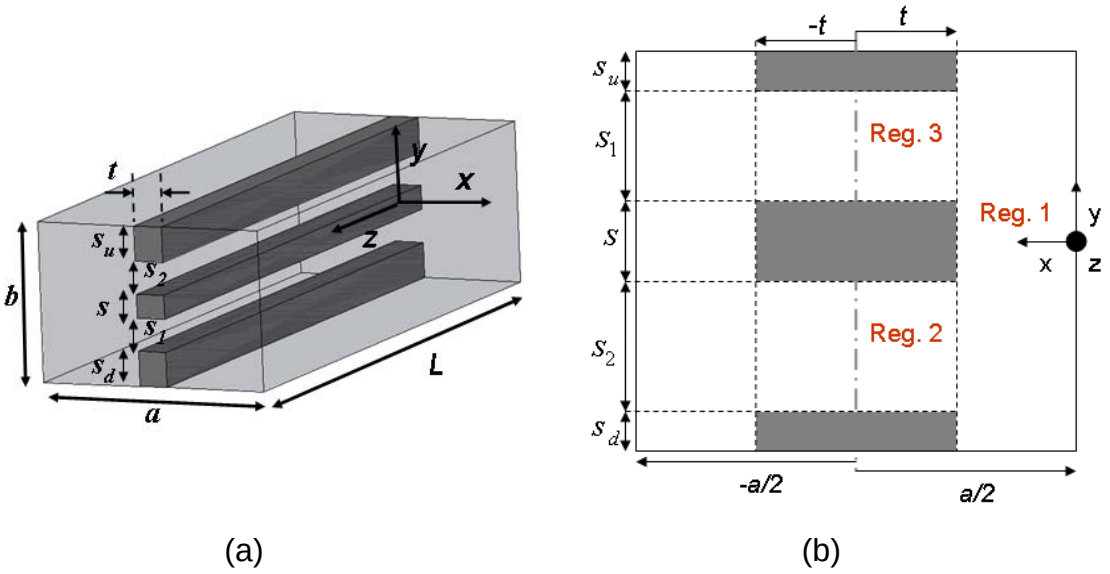

Fig. 3-1. Ridge Coaxial waveguide schematic (a) and its cross section (b)

This will lead to matching unknown fields on two common surfaces and hence to a simplified problem. In order to account for all possible cases, along the symmetry plane we should consider both an electric and a magnetic wall. It can be also considered the use of an electric wall along the y-symmetry, however the general case will be studied in order to allow for asymmetrical geometries.

In ridge coaxial waveguide the boundary conditions imposed by the cross section are complicated, so it is convenient to split up the cross section into three rectangular regions with simple shapes and to match the field at the respective boundaries between each region.

Hence referring to a RCWG (Figure 3-1), the optimal choice of regions is:

- Region 1 will be from x= 0 to x= e (trough region)
- Region 2 will be from x=e to x=a/2 and from y=-b/2+c1 to y=-b/2+c1+s1 (lower gap region).
- Region 3 will be from x=e to x=a/2 and from y=b/2-c1-s1 to y=b/2-c1 (upper gap region).

In this fashion the difficulty of the analysis it is reduced, so the Ridge Coaxial Waveguide can be analyzed step by step, studying the field distribution of the different regions separately and then applying the field matching technique at the common surfaces.

It is interesting to make some remarks concerning the characteristics of waveguides. Such considerations derive from physical insight of the problem and can justify the calculation of the TE and TM modes separately without any coupling between each other. These considerations are, on one hand, that there is no discontinuity along the axis (z) due to the fact that the obstacles lie along this axis isotropically and, on the other hand, that the waveguides under study are homogeneous, there is no dielectric material within the waveguide. Taking into account all the considerations explained above, the procedure will be described in the following sections starting with TE modes.

3.2.1.1 TE modes

The field distribution of each mode (*T(x,y)*) is independent of the frequency (due to the separability of the wave equation). Therefore the fields can be analyzed at cutoff frequency where K_z=0 and no spatial variation along z exists ($\frac{\partial}{\partial z} = 0$), so there is no propagation along z, transverse propagation only.

This condition of the vector potential *A* can be expressed as:

$$\nabla \times \nabla \times A = \overbrace{\frac{\partial^2 A}{\partial x \partial z}}^{0} \hat{x} + \overbrace{\frac{\partial^2 A}{\partial y \partial z}}^{0} \hat{y} + \left(K_c^2 A + \overbrace{\frac{\partial^2 A}{\partial z^2}}^{0} \right) \hat{z} = K_c^2 A \hat{z} \qquad \textbf{(3-1)}$$

At cutoff frequency: $K_0 = K_c$

Hence the expressions for the transverse dependence of the electric and magnetic Hertzian type of potentials in each region can be easily derived. The magnetic type of vector potential (TE modes) for the three regions is derived from the two dimensional Helmholtz equations, under appropriate boundary conditions. The transverse dependence for the vectors potential is derived below. Appendix B provides further explanation of this mathematical derivation.

Region 1:

The magnetic type of vector potential for this region can be expressed as:

$$T_{hq}{}^{1}(x,y) = \sum_{m=0}^{M1} \left[A_{qm}{}^{1} e^{+j \cdot K_{xqm}{}^{1} \cdot x} + B_{qm}{}^{1} e^{-j \cdot K_{xqm}{}^{1} \cdot x} \right] \frac{\cos\left(\frac{m\pi}{b} \left(y + \frac{b}{2} \right) \right)}{\sqrt{1 + \delta_{om}}} \qquad \textbf{(3-2)}$$

Where the boundary condition satisfied in this case is:

$$E_y(x = 0) = 0 \qquad \textbf{(3-3)}$$

Hence, the transverse dependence for the magnetic type of vector potential is determined by:

$$T_{hq}{}^{1}(x,y) = \sum_{m=0}^{M1} A_{qm}{}^{1} \cos\left(K_{xqm}{}^{1} x \right) \frac{\cos\left(\frac{m\pi}{b} \left(y + \frac{b}{2} \right) \right)}{\sqrt{1 + \delta_{om}}} \qquad \textbf{(3-4)}$$

Where the cutoff wavenumber is:

$$\left(K_{xhm}{}^{q1} \right)^2 = \left(K_0 \right)^2 - \left(K_{zqm} \right)^2 - \left(\frac{m\pi}{b} \right)^2$$

In our case $K_{zqm} = 0$ so $K^2{}_{cutoff} = K^2{}_x + K^2{}_y$

Region 2:

The magnetic type of vector potential for this region is:

$$T_{hq}{}^{2}(x,y)=\sum_{m=0}^{M2}\left[A_{qm}{}^{2}e^{+j\cdot K_{xqm}{}^{2}\cdot x}+B_{qm}{}^{2}e^{-j\cdot K_{xqm}{}^{2}\cdot x}\right]\frac{\cos\left(\frac{m\pi}{s_1}\left(y+\frac{b}{2}-c_1\right)\right)}{\sqrt{1+\delta_{om}}} \qquad \textbf{(3-5)}$$

The boundary condition to be satisfied in this case is:

$$H_z\left(x=\frac{a}{2}\right)=H_y\left(x=\frac{a}{2}\right)=0 \qquad \textbf{(3-6)}$$

By applying **(3-6)** yields:

$$T_{hq}{}^{2}=\sum_{m=0}^{M2}A_{qm}{}^{2}\frac{1}{K_{xqm}{}^{2}}\sin\left(K_{xqm}{}^{2}\cdot(x-\frac{a}{2})\right)\cdot\frac{\cos\left(\frac{m\pi}{s_1}\left(y+\frac{b}{2}-c_1\right)\right)}{\sqrt{1+\delta_{om}}} \qquad \textbf{(3-7)}$$

Where the cutoff wavenumber is:

$$\left(K_{xhm}{}^{q2}\right)^2=\left(K_0\right)^2-\left(K_{zqm}\right)^2-\left(\frac{m\pi}{s_1}\right)^2 \qquad \textbf{(3-8)}$$

Region 3:

Region 3 has the same shape and the same boundary condition than region 2 so we only show the final result:

$$T_{hq}{}^{3}=\sum_{m=0}^{M3}A_{qm}{}^{3}\frac{1}{K_{xqm}{}^{3}}\sin\left(K_{xqm}{}^{3}\cdot(x-\frac{a}{2})\right)\cdot\frac{\cos\left(\frac{m\pi}{s_2}\left(y-\frac{b}{2}+c_2+s_2\right)\right)}{\sqrt{1+\delta_{om}}} \qquad \textbf{(3-9)}$$

Where the cutoff wavenumber is:

$$\left(K_{xhm}{}^{q3}\right)^2=\left(K_0\right)^2-\left(K_{zqm}\right)^2-\left(\frac{m\pi}{s_2}\right)^2 \qquad \textbf{(3-10)}$$

3.2.1.2 TM modes

Similarly the transverse dependence for the electric type of vector potential (TM modes) is determined in a similar way to the magnetic case (TE modes). The electric type of vector potential for each region is shown bellow:

Region 1:

$$T_{ep}{}^{1}(x,y)=\sum_{l=1}^{M1}B_{pl}{}^{1}\frac{1}{K_{xel}^{p1}}\sin\left(K_{xel}{}^{p1}x\right)\sin\left(\frac{l\cdot\pi}{b}\left(y+\frac{b}{2}\right)\right) \quad \textbf{(3-11)}$$

Region 2:

$$T_{ep}{}^{2}=\sum_{l=1}^{M2}B_{pl}{}^{2}\cos\left(K_{xel}{}^{p2}\cdot(x-\frac{a}{2})\right)\cdot\sin\left(\frac{l\cdot\pi}{s1}\left(y+\frac{b}{2}-c1\right)\right) \quad \textbf{(3-12)}$$

Region 3:

$$T_{ep}{}^{3}=\sum_{l=1}^{M3}B_{pl}{}^{3}\cos\left(K_{xel}{}^{p3}\cdot(x-\frac{a}{2})\right)\cdot\sin\left(\frac{l\pi}{s2}\left(y-\frac{b}{2}+c2+s2\right)\right) \quad \textbf{(3-13)}$$

Where the cutoff wavenumber are defined as:

Region 1: $$\left(K_{xel}{}^{p1}\right)^2=\left(K_0\right)^2-\left(K_{zpl}\right)^2-\left(\frac{l\cdot\pi}{b}\right)^2$$

Region 2: $$\left(K_{xel}{}^{p2}\right)^2=\left(K_0\right)^2-\left(K_{zpl}\right)^2-\left(\frac{l\cdot\pi}{s1}\right)^2$$

Region 3: $$\left(K_{xel}{}^{p3}\right)^2=\left(K_0\right)^2-\left(K_{zpl}\right)^2-\left(\frac{l\cdot\pi}{s2}\right)^2$$

In this case $K_{zpl}=0$, hence $K^2{}_{cutoff}=K^2{}_x+K^2{}_y$

3.2.1.3 TEM mode

In the TEM mode, due to both electric and magnetic fields are perpendicular to the direction of propagation, the electromagnetic fields can be derived from a scalar function and satisfies the Laplace equation:

$$\nabla^2\phi=0 \quad \textbf{(3-14)}$$

The electromagnetic potential solution of the Laplace equation can be expressed as:

$$\phi=\phi(x,y)=(Ax+B)\cdot(Cy+D)+\mathrm{X}(x)\cdot\mathrm{Y}(y) \quad \textbf{(3-15)}$$

Where:

$$\mathrm{X}(x)=A\cdot\cos(kx)+B\cdot\sin(kx) \quad \textbf{(3-16)}$$

$$\mathrm{Y}(y)=A\cos(ky)+B\sin(ky) \quad \textbf{(3-17)}$$

The boundary conditions required are:

1. $\phi(y=0)=\phi(y=b)=0$ **(3-18)**
2. $\phi(x=a/2)=\phi(x=-a/2)=0$ **(3-19)**
3. $\phi(x,y)=\phi(-x,y)$ **(3-20)**

After a little algebra:

Region 1:

$$\phi(x,y)=\sum_{m=1}^{Ma} F_m{}^a\left[\exp(\frac{m\pi}{b}(x-\frac{a}{2}))+\exp(-\frac{m\pi}{b}(x+\frac{a}{2}))\right]\cdot\sin\left(\frac{m\cdot\pi}{b}(y+\frac{b}{2})\right) \quad \textbf{(3-21)}$$

Region 2:

$$\phi=\frac{V}{s_1}(y+\frac{b}{2}-c_1)+2\sum_{m=1}^{Mb} F_m{}^b\left[\cosh(\frac{m\pi}{s_1}(-x+\frac{a}{2}))\right]\cdot\sin\left(\frac{m\cdot\pi}{s_1}(y+\frac{b}{2}-c_1)\right) \quad \textbf{(3-22)}$$

Region 3:

$$\phi=V-\frac{V}{s_2}(y+\frac{b}{2}-h)+2\sum_{m=1}^{Mc} F_m{}^c\left[\cosh(\frac{m\pi}{s_2}(-x+\frac{a}{2}))\right]\cdot\sin\left(\frac{m\cdot\pi}{s_2}(y+\frac{b}{2}-h)\right) \quad \textbf{(3-23)}$$

3.2.2 Field matching

The next step is to match the tangential components (y- and z- components) of the electric and magnetic fields at the common surface for every mode. According to the assumptions stated above, we annihilate the z-propagation of the fields. However, since the cross section field distribution of each mode is the same for propagating waves, and since each mode propagates with a distinctive constant, k_z, this condition has to be satisfied for every single mode separately.

Hence the boundary conditions at this discontinuity for the electric (3-24) and magnetic (3-25) fields are:

$$E_1(e)=\begin{cases} E_2(e)\Rightarrow -\left(\frac{b}{2}-c1\right)<y<-\left(\frac{b}{2}-c1-s1\right) \\ E_3(e)\Rightarrow \left(\frac{b}{2}-c2-s2\right)<y<\left(\frac{b}{2}-c2\right) \\ 0\Rightarrow other\_case \end{cases} \quad \textbf{(3-24)}$$

$$H_1(e)=\begin{cases} H_2(e)\Rightarrow -\left(\frac{b}{2}-c1\right)<y<-\left(\frac{b}{2}-c1-s1\right) \\ H_3(e)\Rightarrow \left(\frac{b}{2}-c2-s2\right)<y<\left(\frac{b}{2}-c2\right) \end{cases} \quad \textbf{(3-25)}$$

So on, the field matching condition leads to an equivalent matching of both types the vector potentials and their derivatives with respect to x.

3.2.2.1 TE modes

For TE modes we see that the magnetic field matching is equivalent to vector potential matching and the electrical field matching is equivalent to the matching of the derivative of the magnetic potential with respect to x. Hence:

$$A:\left.\frac{\partial T_{hq}{}^{1}}{\partial x}\right|_{x=e}=\begin{cases} \left.\frac{\partial T_{hq}{}^{2}}{\partial x}\right|_{x=e}\Rightarrow -\left(\frac{b}{2}-c1\right)<y<-\left(\frac{b}{2}-c1-s1\right) \\ \left.\frac{\partial T_{hq}{}^{3}}{\partial x}\right|_{x=e}\Rightarrow \left(\frac{b}{2}-c2-s2\right)<y<\left(\frac{b}{2}-c2\right) \\ 0\Rightarrow other\_case \end{cases} \quad \textbf{(3-26)}$$

$$B:T_{hq}{}^{1}(x=e)=\begin{cases} T_{hq}{}^{2}(x=e)\Rightarrow -\left(\frac{b}{2}-c1\right)<y<-\left(\frac{b}{2}-c1-s1\right) \\ T_{hq}{}^{3}(x=e)\Rightarrow \left(\frac{b}{2}-c2-s2\right)<y<\left(\frac{b}{2}-c2\right) \end{cases} \quad \textbf{(3-27)}$$

This way, the electric and magnetic field matching is imposed at the common surface among the three regions.

In summary, field matching leads the the following expressions:

$$\left[A^{q1}\right]=-\frac{2}{b}\cdot D_e^{q1}\cdot\left[\left[J_2\right]^T\cdot D_e^{q2}\cdot\left[A^{q2}\right]+\left[J_3\right]^T\cdot D_e^{q3}\cdot\left[A^{q3}\right]\right] \quad \textbf{(3-28)}$$

$$\left[A^{q2}\right] = -\frac{2}{s1} \cdot D_h^{q2} \cdot \left[J_2\right] \cdot D_h^{q1} \cdot \left[A^{q1}\right] \quad \textbf{(3-29)}$$

$$\left[A^{q3}\right] = -\frac{2}{s2} \cdot D_h^{q3} \cdot \left[J_3\right] \cdot D_h^{q1} \cdot \left[A^{q1}\right] \quad \textbf{(3-30)}$$

Substituting into the previous equations the characteristic equation for the magnetic type of vector potential (for the case of the magnetic wall symmetry) is:

$$\left[A^{q1}\right] = \frac{4}{b} \cdot D_e^{q1} \cdot \left[\frac{1}{s1} \cdot \left[J_2\right]^T \cdot D_e^{q2} \cdot D_h^{q2} \cdot \left[J_2\right] + \frac{1}{s2} \cdot \left[J_3\right]^T \cdot D_e^{q3} \cdot D_h^{q3} \cdot \left[J_3\right] \right] \cdot D_h^{q1} \cdot \left[A^{q1}\right] \quad \textbf{(3-31)}$$

(3-31) can be rearranged in a more convenient form as:

$$\underbrace{\left\{ \left[D_e^{q1}\right]^{-1} - \frac{4}{b} \cdot \left[\frac{1}{s1} \cdot \left[J_2\right]^T \cdot D_e^{q2} \cdot D_h^{q2} \cdot \left[J_2\right] + \frac{1}{s2} \cdot \left[J_3\right]^T \cdot D_e^{q3} \cdot D_h^{q3} \cdot \left[J_3\right] \right] \cdot D_h^{q1} \right\}}_{Matrix} \cdot \left[A^{q1}\right] = 0 \quad \textbf{(3-32)}$$

The equation above is a homogeneous linear indeterminate system which can be computationally solved setting the convenient parameters. Nontrivial solutions for this system exist as long as the determinant of the expression in brackets is zero. By varying frequency, we may solve the characteristic determinant for its eigenvalues k_c. After having found the cutoff wavenumbers k_c, the coefficients A^{q1} can be determined solving equation (3-32), which is the eigenvector of the problem.

The numerical analysis has been implemented in Fortran, mainly implementing the matrix equation (3-32) for a defined by user number of expansion terms. From that, the coefficients A^{q2} and A^{q3} respectively are easily determined in the same program from the relations to the cofficients A^{q1} expressed in equations (3-28) and (3-29). Details can be followed in the main subroutine of the TEM mode (similar eigenvalue problem) included in Appendix E.

So on the TE modal characterization of a Ridge Coaxial Waveguide is completed. Below is shown the E-Field distribution of the first mode, which is the TE mode supported by waveguide X-band filter configuration investigated in next chapters. Fig. 3-2 has been obtained using a matlab routine which extracts the data produced (modal field distribution) in the previously mentioned fortran code.

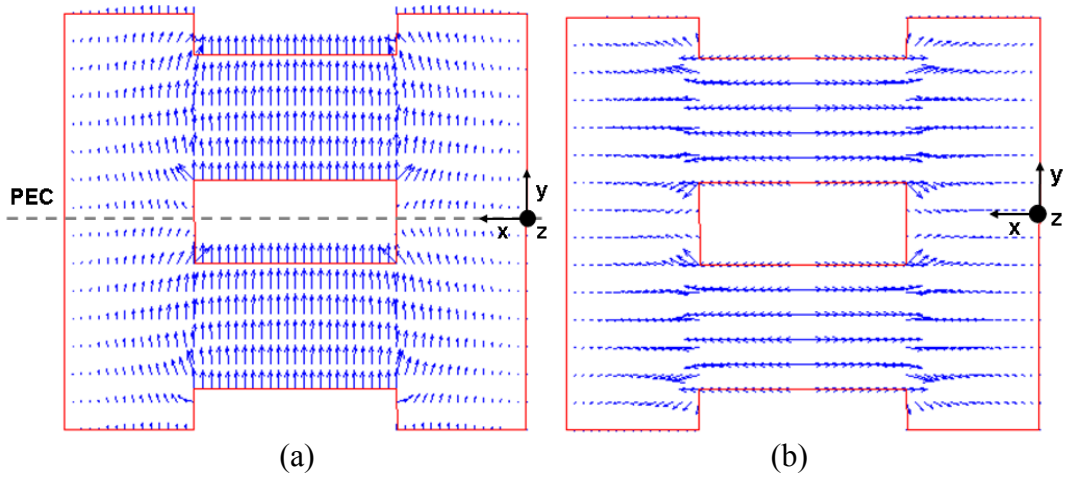

(a) (b)

Fig. 3-2. Modal E-Field (a) and H-Field (b) distribution of the first TE mode. The dimensions in mm are: a=22.86, b=20.16, s=4, s_1=s_2=6.08, s_u=s_d=2, t=5.

3.2.2.2 TM modes

Similar is the procedure followed to solve the TM modes. In this case the solution will be found after imposing electric field matching. From the field expression we see that the magnetic field matching is equivalent to the matching of the derivative of the magnetic potential with respect to x and the electrical field matching is equivalent to vector potential matching.

$$A: T_{ep}^{\ 1}(x=e) = \begin{cases} T_{ep}^{\ 2}(x=e) \Rightarrow -\left(\frac{b}{2}-c1\right) < y < -\left(\frac{b}{2}-c1-s1\right) \\ T_{ep}^{\ 3}(x=e) \Rightarrow \left(\frac{b}{2}-c2-s2\right) < y < \left(\frac{b}{2}-c2\right) \\ 0 \Rightarrow other\_case \end{cases} \quad \textbf{(3-33)}$$

$$B: \left.\frac{\partial T_{pl}^{\ 1}}{\partial x}\right|_{x=e} = \begin{cases} \left.\frac{\partial T_{pl}^{\ 2}}{\partial x}\right|_{x=e} \Rightarrow -\left(\frac{b}{2}-c1\right) < y < -\left(\frac{b}{2}-c1-s1\right) \\ \left.\frac{\partial T_{pl}^{\ 3}}{\partial x}\right|_{x=e} \Rightarrow \left(\frac{b}{2}-c2-s2\right) < y < \left(\frac{b}{2}-c2\right) \end{cases} \quad \textbf{(3-34)}$$

The algebra for the TM modes is also included in Appendix. Final expressions are shown below:

$$\left[B^{p1}\right]=\frac{2}{b}\cdot D_e^{p1}\cdot\left[\left[J_2\right]^T\cdot D_e^{p2}\cdot\left[B^{p2}\right]+\left[J_3\right]^T\cdot D_e^{p3}\cdot\left[B^{p3}\right]\right] \quad \textbf{(3-35)}$$

$$\left[B^{p2}\right]=\frac{2}{s1}\cdot D_h^{p2}\cdot\left[J_2\right]\cdot D_h^{p1}\cdot\left[B^{p1}\right] \quad \textbf{(3-36)}$$

$$\left[B^{p3}\right]=\frac{2}{s2}\cdot D_h^{p3}\cdot\left[J_3\right]\cdot D_h^{p1}\cdot\left[B^{p1}\right] \quad \textbf{(3-37)}$$

Substituting the equations(3-36) and (3-37) in (3-35) we can derive the characteristic equation for the electric type of vector potential (for the case of the magnetic wall symmetry):

$$\left[B^{p1}\right]=\frac{4}{b}\cdot D_e^{p1}\cdot\left[\frac{1}{s1}\cdot\left[J_2\right]^T\cdot D_e^{p2}\cdot D_h^{p2}\cdot\left[J_2\right]+\frac{1}{s2}\cdot\left[J_3\right]^T\cdot D_e^{p3}\cdot D_h^{p3}\cdot\left[J_3\right]\right]\cdot D_h^{p1}\cdot\left[B^{p1}\right]$$

Which rearranged can be expressed as:

$$\underbrace{\left\{\left[D_e^{p1}\right]^{-1}-\frac{4}{b}\cdot\left[\frac{1}{s1}\cdot\left[J_2\right]^T\cdot D_e^{p2}\cdot D_h^{p2}\cdot\left[J_2\right]+\frac{1}{s2}\cdot\left[J_3\right]^T\cdot D_e^{p3}\cdot D_h^{p3}\cdot\left[J_3\right]\right]\cdot D_h^{p1}\right\}}_{Matrix}\cdot\left[B^{p1}\right]=0 \quad \textbf{(3-38)}$$

As well as for the TE modes, the final matrix equation for the TM modes is a homogeneous linear NxN system. After calculating the cutoff wavenumbers, kc, a set of amplitude coefficients, B^p, can be produced for each region using the equations of (3-35), (3-36) and (3-37). As before the field distribution plot corresponding the first TM mode is shown in Fig. 3-3. This mode however is not relevant in this work; for the dimensions of the filter realizations considered the cutoff frequency of the first TM mode is above the X-Band.

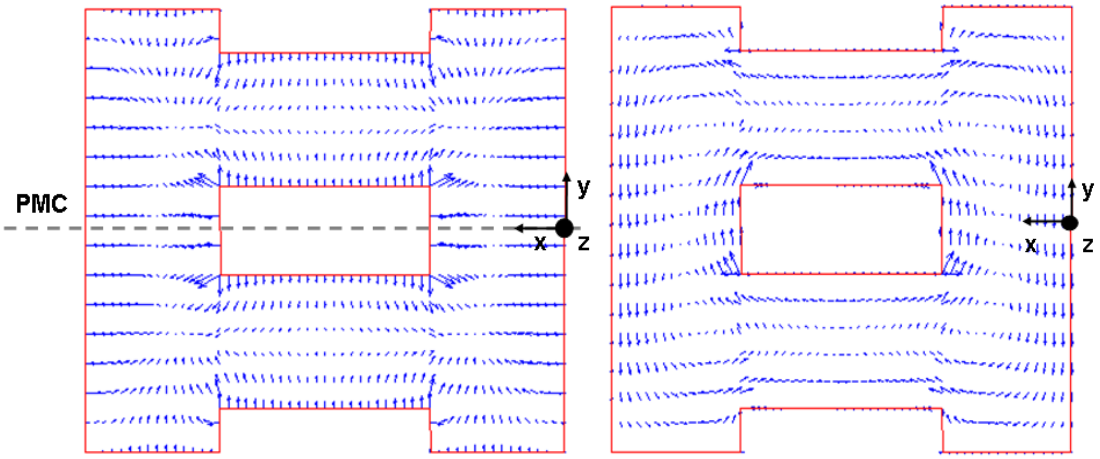

(a) (b)

Fig. 3-3. Modal E-Field (a) and H-Field (b) distribution of the first TM mode. The dimensions in mm are: a=22.86, b=20.16, s=4, s_1=s_2=6.08, s_u=s_d=2, t=5.

3.2.2.3 TEM mode

In the case of the TEM mode the matching of the fields at the discontinuities yield the following equations:

$$A:\left.\frac{\partial\phi^1}{\partial y}\right|_{x=e}=\begin{cases}\left.\dfrac{\partial\phi^2}{\partial y}\right|_{x=e}\Rightarrow -\left(\dfrac{b}{2}-c1\right)<y<-\left(\dfrac{b}{2}-c1-s1\right)\\ \left.\dfrac{\partial\phi^3}{\partial y}\right|_{x=e}\Rightarrow \left(\dfrac{b}{2}-c2-s2\right)<y<\left(\dfrac{b}{2}-c2\right)\\ 0\Rightarrow other\_case\end{cases} \tag{3-39}$$

$$B:\left.\frac{\partial\phi^1}{\partial x}\right|_{x=e}=\begin{cases}\left.\dfrac{\partial\phi^2}{\partial x}\right|_{x=e}\Rightarrow -\left(\dfrac{b}{2}-c1\right)<y<-\left(\dfrac{b}{2}-c1-s1\right)\\ \left.\dfrac{\partial\phi^3}{\partial x}\right|_{x=e}\Rightarrow \left(\dfrac{b}{2}-c2-s2\right)<y<\left(\dfrac{b}{2}-c2\right)\end{cases} \tag{3-40}$$

The mathematical analysis leads the following condition for field matching:

$$\underbrace{\left\{\left[D_e^{p1}\right]^{-1}-\left[\left[J_{E2}\right]^T\cdot D_e^{p2}\cdot D_h^{p2}\cdot\left[J_{M2}\right]^T+\left[J_{E3}\right]^T\cdot D_e^{p3}\cdot D_h^{p3}\cdot\left[J_{M3}\right]\right]\cdot D_h^{p1}\right\}}_{Matrix}\left[C^{p1}\right]=E_k \qquad \textbf{(3-41)}$$

Besides the TE and TM modes the final system of linear equations is a non homogeneus linear system. That is a consequence of the form of the electromagnetic potentials derived from Laplace equation (3-14). They include a scalar term E_k which is determined through next section by imposing power normalization. That is independent of the field distribution pattern, which is shown in Fig. 3-4.

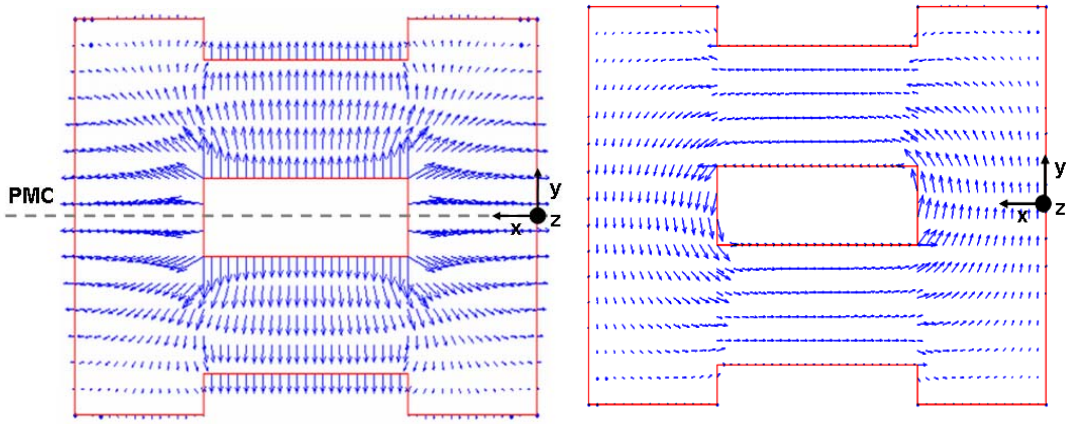

(a) (b)

Fig. 3-4. Modal E-Field (a) and H-Field (b) distribution of the TEM mode. The dimensions in mm are: a=22.86, b=20.16, s=4, s_1=s_2=6.08, s_u=s_d=2, t=5.

The main subroutine to produce the coefficients and the Fields of the TEM mode is included in Appendix E.

3.2.3 Power normalization of the ridge coaxial waveguides

Power normalisation is not required to obtain the field distribution of the TE, TM modes and TEM mode presented in the previous section. To calculate the characteristic impedance of the TEM line, is imposed beforehand that the power transferred by the TEM mode between two arbitrary ports of the Ridge Coaxial Waveguide is independent of the cross-sectional shape. Also, for the benefit of future analysis involving transitions of surface discontinuities, the coefficients A^p, B^p and C^p of equations (3-32), (3-38) and (3-41) must be normalized to ensure the power transferred by each mode of a unity amplitude at both sides of the discontinuity are independent of the cross-sectional shape.

Therefore, assuming each mode power amplitude equal to unity, and referring to equations (3-32) and (3-38), then the total power transferred by a mode of forward propagating coefficient F= 1 and backward propagating coefficient B= 0 (same as F= 0 and B= 1 for backwards propagating mode), must be equal to 1W. This condition will ensure that the S-parameters of the scattering matrix are normalised between 0 to 1. Also the coefficients D_k from equation (3-41) will be normalized so before calculating the characteristic impedance of the TEM mode.

As outlined in section 3.2, for the Ridge Coaxial Waveguide, the transverse dependence of Hertzian potential distribution for a single TE_q or TM_p mode is expressed in an orthogonal basis as truncated series. One series gives the distribution of the vector potential in the trough region and the others in the gap regions. The field matching at the common surface derivation is what gives as a result a relation between the coefficients of the three series.

For the i^{th} propagating TE mode, the power normalization condition is:

$$\iint_s \left(\nabla \cdot T_h^i\right)^2 ds = 1 \tag{3-42}$$

It can be expanded in this case as following:

$$\iint_{s1} \left(\nabla \cdot T_h^{1q}\right)^2 ds + \iint_{s2} \left(\nabla \cdot T_h^{2q}\right)^2 ds + \iint_{s3} \left(\nabla \cdot T_h^{3q}\right)^2 ds = 1 \tag{3-43}$$

Where,

$$\iint_{s1}\left[\left(\frac{\partial T_h^{1q}}{\partial x}\right)^2 + \left(\frac{\partial T_h^{1q}}{\partial x}\right)^2\right] xdy + \iint_{s2}\left[\left(\frac{\partial T_h^{2q}}{\partial x}\right)^2 + \left(\frac{\partial T_h^{2q}}{\partial x}\right)^2\right] xdy + \iint_{s3}\left[\left(\frac{\partial T_h^{3q}}{\partial x}\right)^2 + \left(\frac{\partial T_h^{3q}}{\partial x}\right)^2\right] xdy = 1 \tag{3-44}$$

Upon analytical integration of these integrals in the case of magnetic type of Hertzian potential, we obtain the following expressions:

$$\int_{-\frac{b}{2}}^{\frac{b}{2}}\int_0^e \left(\frac{\partial T_h^{1q}}{\partial x}\right)^2 dxdy = \sum_{m=1}^{M1}\left(A_m^{1q} \cdot K_{xhm}^{1q}\right)^2 \cdot \left(\frac{b}{4}\right)\left(e - \frac{\sin\left(2 \cdot K_{xhm}^{1q} \cdot e\right)}{2 \cdot K_{xhm}^{1q}}\right) \tag{3-45}$$

$$\int_{-\frac{b}{2}}^{\frac{b}{2}}\int_0^e \left(\frac{\partial T_h^{1q}}{\partial y}\right)^2 dxdy = \sum_{m=0}^{M1}\left(A_m^{1q} . \frac{m \cdot \pi}{b}\right)^2 \cdot \left(\frac{b}{4(1+\delta_{om})}\right)\left(e + \frac{\sin\left(2 \cdot K_{xhm}^{1q} \cdot e\right)}{2 \cdot K_{xhm}^{1q}}\right) \tag{3-46}$$

$$\int_{-(\frac{b}{2}-c1)}^{-(\frac{b}{2}-c1-s1)}\int_{e}^{a/2}\left(\frac{\partial T_h^{2q}}{\partial x}\right)^2 dxdy=\sum_{m=1}^{M2}\left(A_m^{2q}\right)^2\cdot\left(\frac{s1}{8}\right)\left(t+\frac{\sin\left(K_{xhm}^{2q}\cdot t\right)}{K_{xhm}^{2q}}\right) \quad \textbf{(3-47)}$$

$$\int_{-(\frac{b}{2}-c1)}^{-(\frac{b}{2}-c1-s1)}\int_{e}^{a/2}\left(\frac{\partial T_h^{2q}}{\partial y}\right)^2 dxdy=\sum_{m=0}^{M2}\left(A_m^{2q}\cdot\frac{m\cdot\pi}{s1\cdot K_{xhm}^{2q}}\right)^2\cdot\left(\frac{s1}{8(1+\delta_{om})}\right)\left(t-\frac{\sin\left(K_{xhm}^{2q}\cdot t\right)}{K_{xhm}^{2q}}\right) \quad \textbf{(3-48)}$$

$$\int_{(\frac{b}{2}-c2-s2)}^{(\frac{b}{2}-c2)}\int_{e}^{a/2}\left(\frac{\partial T_h^{3q}}{\partial x}\right)^2 dxdy=\sum_{m=1}^{M3}\left(A_m^{3q}\right)^2\cdot\left(\frac{s2}{8}\right)\left(t+\frac{\sin\left(K_{xhm}^{3q}\cdot t\right)}{K_{xhm}^{3q}}\right) \quad \textbf{(3-49)}$$

$$\int_{(\frac{b}{2}-c2-s2)}^{(\frac{b}{2}-c2)}\int_{e}^{a/2}\left(\frac{\partial T_h^{3q}}{\partial y}\right)^2 dxdy=\sum_{m=0}^{M3}\left(A_m^{3q}\cdot\frac{m\cdot\pi}{s2\cdot K_{xhm}^{3q}}\right)^2\cdot\left(\frac{s2}{8(1+\delta_{om})}\right)\left(t-\frac{\sin\left(K_{xhm}^{3q}\cdot t\right)}{K_{xhm}^{3q}}\right) \quad \textbf{(3-50)}$$

In a similar way, for TM modes the power normalisation condition is:

$$\iint_{s}\left(\nabla\cdot T_e^i\right)^2 ds=1 \quad \textbf{(3-51)}$$

Which can be expanded as:

$$\iint_{s1}\left(\nabla\cdot T_e^{1p}\right)^2 ds+\iint_{s2}\left(\nabla\cdot T_e^{2p}\right)^2 ds+\iint_{s3}\left(\nabla\cdot T_e^{3p}\right)^2 ds=1 \quad \textbf{(3-52)}$$

In a more concrete form:

$$\iint_{s1}\left[\left(\frac{\partial T_e^{1p}}{\partial x}\right)^2+\left(\frac{\partial T_e^{1p}}{\partial x}\right)^2\right]xdy+\iint_{s2}\left[\left(\frac{\partial T_e^{2p}}{\partial x}\right)^2+\left(\frac{\partial T_e^{2p}}{\partial x}\right)^2\right]xdy+\iint_{s3}\left[\left(\frac{\partial T_e^{3p}}{\partial x}\right)^2+\left(\frac{\partial T_e^{3p}}{\partial x}\right)^2\right]xdy=1$$

(3-53)

The corresponding integrals of the electric type of Hertzian potentials have the following analytical solution:

$$\int_{-\frac{b}{2}}^{\frac{b}{2}}\int_{0}^{e}\left(\frac{\partial T_e^{1p}}{\partial x}\right)^2 dxdy=\sum_{l=1}^{M1}\left(B_l^{1p}\right)^2\cdot\left(\frac{b}{4}\right)\left(e+\frac{\sin\left(2\cdot K_{xel}^{1p}\cdot e\right)}{2\cdot K_{xel}^{1p}}\right) \quad \textbf{(3-54)}$$

$$\int_{-\frac{b}{2}}^{\frac{b}{2}}\int_{0}^{e}\left(\frac{\partial T_e^{1p}}{\partial y}\right)^2 dxdy=\sum_{l=1}^{M1}\left(B_l^{1p}\cdot\frac{l\cdot\pi}{b\cdot K_{xel}^{1p}}\right)^2\cdot\left(\frac{b}{4}\right)\left(e-\frac{\sin\left(2\cdot K_{xel}^{1p}\cdot e\right)}{2\cdot K_{xel}^{1p}}\right) \quad \textbf{(3-55)}$$

$$\int_{-(\frac{b}{2}-c1-s1)}^{-(\frac{b}{2}-c1)} \int_{e}^{a/2} \left(\frac{\partial T_e^{2p}}{\partial x} \right)^2 dxdy = \sum_{l=1}^{M2} \left(B_l^{2p} K_{xel}^{2p} \right)^2 \cdot \left(\frac{s1}{8} \right) \left(t - \frac{\sin\left(K_{xel}^{2p} \cdot t \right)}{K_{xel}^{2p}} \right) \quad \textbf{(3-56)}$$

$$\int_{-(\frac{b}{2}-c1-s1)}^{-(\frac{b}{2}-c1)} \int_{e}^{a/2} \left(\frac{\partial T_e^{2p}}{\partial y} \right)^2 dxdy = \sum_{l=1}^{M2} \left(B_l^{2p} \cdot \frac{l \cdot \pi}{s1} \right)^2 \cdot \left(\frac{s1}{8} \right) \left(t + \frac{\sin\left(K_{xel}^{2p} \cdot t \right)}{K_{xel}^{2p}} \right) \quad \textbf{(3-57)}$$

$$\int_{(\frac{b}{2}-c2-s2)}^{(\frac{b}{2}-c2)} \int_{e}^{a/2} \left(\frac{\partial T_e^{3p}}{\partial x} \right)^2 dxdy = \sum_{l=1}^{M3} \left(B_l^{3p} K_{xel}^{3p} \right)^2 \cdot \left(\frac{s2}{8} \right) \left(t - \frac{\sin\left(K_{xel}^{3p} \cdot t \right)}{K_{xel}^{3p}} \right) \quad \textbf{(3-58)}$$

$$\int_{(\frac{b}{2}-c2-s2)}^{(\frac{b}{2}-c2)} \int_{e}^{a/2} \left(\frac{\partial T_e^{3p}}{\partial y} \right)^2 dxdy = \sum_{l=1}^{M3} \left(B_l^{3p} \cdot \frac{l \cdot \pi}{s2} \right)^2 \cdot \left(\frac{s2}{8} \right) \left(t + \frac{\sin\left(K_{xel}^{3p} \cdot t \right)}{K_{xel}^{3p}} \right) \quad \textbf{(3-59)}$$

The power normalization condition for the TEM mode can be expressed as:

$$\iint_{s} \left(\nabla \cdot \phi^i \right)^2 ds = 1 \quad \textbf{(3-60)}$$

Expanded over the three defined regions yields:

$$\iint_{s1} \left(\nabla \cdot \phi^1 \right)^2 ds + \iint_{s2} \left(\nabla \cdot \phi^2 \right)^2 ds + \iint_{s3} \left(\nabla \cdot \phi^3 \right)^2 ds = 1 \quad \textbf{(3-61)}$$

Therefore:

$$\iint_{s1} \left[\left(\frac{\partial \phi^1}{\partial x} \right)^2 + \left(\frac{\partial \phi^1}{\partial y} \right)^2 \right] dS + \iint_{s2} \left[\left(\frac{\partial T \phi^2}{\partial x} \right)^2 + \left(\frac{\partial T \phi^2}{\partial y} \right)^2 \right] dS + \iint_{s3} \left[\left(\frac{\partial T \phi^3}{\partial x} \right)^2 + \left(\frac{\partial T \phi^3}{\partial y} \right)^2 \right] dS = 1 \quad \textbf{(3-62)}$$

As for the TE and TM modes that leads to the calculation of 6 surface integrals, from the equation (3-62):

$$\iint_{s1} \left(\nabla \cdot \phi^1 \right)^2 ds = -\frac{2 \cdot \pi}{b} \cdot \left(\frac{a}{2} - t \right) \sum_{n=1}^{M1} \left(A_n^1 \right)^2 \cdot n^2 \cdot \exp\left(-\frac{n \cdot \pi \cdot a}{b} \right) \quad \textbf{(3-63)}$$

$$\iint_{s2}\left(\nabla\cdot\phi^{2}\right)^{2}ds=\frac{2\cdot t\cdot V^{2}}{s_{1}}+\pi\sum_{n=1}^{M2}\left(A_{n}^{2}\right)^{2}\cdot n\cdot\left[\exp\left(\frac{2\cdot n\cdot\pi\cdot t}{s_{1}}\right)-\exp\left(-\frac{2\cdot n\cdot\pi\cdot t}{s_{1}}\right)\right] \quad \textbf{(3-64)}$$

$$\iint_{s3}\left(\nabla\cdot\phi^{3}\right)^{2}ds=\frac{2\cdot t\cdot V^{2}}{s_{2}}+\pi\sum_{n=1}^{M3}\left(A_{n}^{3}\right)^{2}\cdot n\cdot\left[\exp\left(\frac{2\cdot n\cdot\pi\cdot t}{s_{2}}\right)-\exp\left(-\frac{2\cdot n\cdot\pi\cdot t}{s_{2}}\right)\right] \quad \textbf{(3-65)}$$

Rearranging in equation **(3-62)** the power normalization for the TEM mode results:

$$2\sqrt{\frac{\varepsilon}{\mu}}\left[\begin{array}{l}\dfrac{t\cdot V^{2}}{s_{1}}+\dfrac{t\cdot V^{2}}{s_{2}}-\dfrac{\pi^{2}}{b}\left(\dfrac{a}{2}-t\right)\displaystyle\sum_{n=1}^{M1}\left(A_{n}^{1}\right)^{2}\cdot n^{2}.\exp\left(-\frac{n\cdot\pi\cdot a}{b}\right)+\\ \pi\displaystyle\sum_{n=1}^{M2}\left(A_{n}^{2}\right)^{2}\cdot n\cdot\sinh\left(\frac{2\cdot n\cdot\pi\cdot t}{s_{1}}\right)+\pi\sum_{n=1}^{M3}\left(A_{n}^{3}\right)^{2}\cdot n\cdot\sinh\left(\frac{2\cdot n\cdot\pi\cdot t}{s_{2}}\right)\end{array}\right]=1 \quad \textbf{(3-66)}$$

3.3 VALIDATION OF THE METHOD

As mentioned in the introduction, a full modal characterisation of the Ridge Coaxial Waveguide has yet to be appeared in the literature. However, the results obtained can be validated with those previously published for the Coaxial Waveguide and the Ridge Waveguide structures. The comparison is presented in section 3.3.3 and 3.3.4 respectively.

3.3.1 Characteristic impedance of the TEM lines

The characteristic impedance values will be of relevance for the filter design content in further chapters. Once the electric and magnetic fields have been solved, from the Poynting vector expression over the cross-section of the waveguide, the total power transferred by the waveguide structure can be produced.

$$\iint_{S}P\cdot ds=\mathrm{Re}\iint_{S}E_{t}\times H_{t}^{*}\cdot ds \quad \textbf{(3-67)}$$

Now the characteristic impedance of the TEM line can be calculated [48]. From the voltage-power expression:

$$Z_0 = \frac{V^2}{P} \tag{3-68}$$

The Fortran code implemented can be also useful to produce parametric plots for the ridge coaxial waveguide operating at a fixed impedance. In Fig. 3-5 a waveguide of different coaxial and ridge thickness operating at the vacuum impedance (50 Ω) is presented.

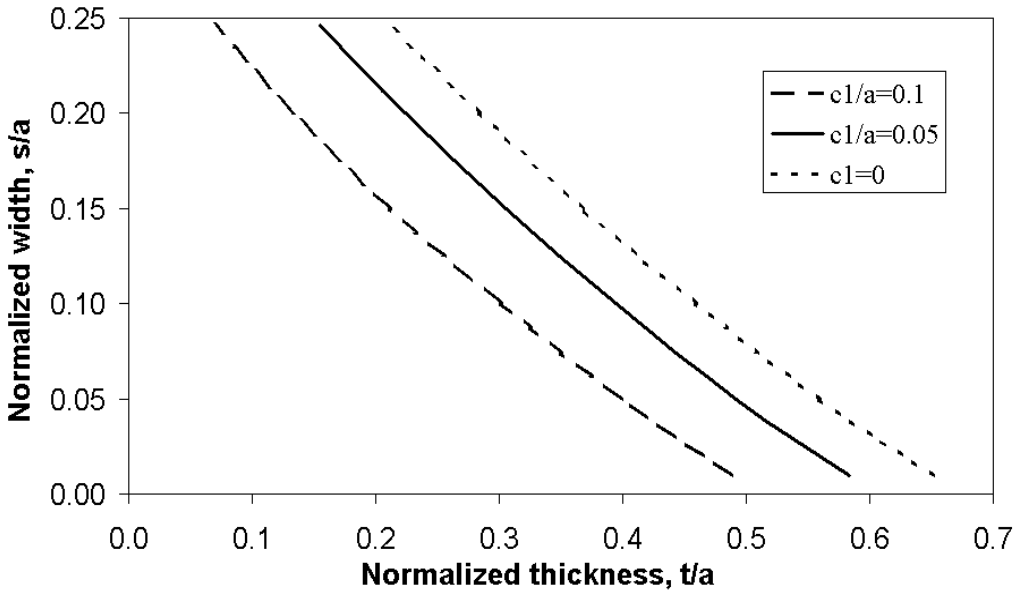

Fig. 3-5. Parametric curves of a rectangular single ridged coaxial transmission line at 50 Ω, b/a=0.8, s_1/b=0.3, c_1=var, c_2=0.

3.3.2 Convergence of the transverse resonance method

The results computed in this way are presented in Table 1 in order to validate the literature results [39]. They illustrate the convergence characteristics of the impedance Z_0 of the square coaxial line (a=b, t=g, c1=c2=0) as the number of series expansion terms (see eq. 3-41) considered for each region, M=M1=M2=M3 is increased up to a finite value of M=20. Also, in the last line of Table 1 the values produced with commercial software Ansoft

HFSS are listed. Agreement between calculated impedances and the values simulated with a finite element method show the convergence of the method

M	t=0.05	t=0.15	t=0.25	t=0.35	t=0.45
1	192.06	70.3	37.56	18.84	5.495
2	195.38	70.41	37.67	18.64	5.482
3	147.7	69.11	37.7	18.51	5.385
4	148.42	68.53	37.61	18.42	5.356
5	137.62	68.01	37.14	18.33	5.247
6	137.92	67.93	37.12	18.26	5.189
7	134.64	67.65	37.1	18.15	5.146
8	134.79	67.44	37.1	18.14	5.119
9	133.77	67.32	36.99	18.12	5.103
10	133.85	67.27	36.98	18.12	5.098
11	133.6	67.21	36.98	18.11	5.094
12	133.64	67.15	36.98	18.1	5.093
13	133.63	67.13	36.93	18.08	5.093
14	133.66	67.11	36.93	18.08	5.093
15	133.76	67.1	36.93	18.07	5.093
16	133.73	67.1	36.93	18.07	5.093
17	133.69	67.08	36.9	18.07	5.093
18	133.67	67.08	36.9	18.07	5.093
19	133.61	67.07	36.9	18.07	5.093
20	133.59	67.07	36.9	18.07	5.093
HFSS	**133.6**	**67.15**	**37**	**18.12**	**5.11**

Table 3-1. Characteristic impedance, Z_0, convergence of a rectangular square coaxial line and comparison with the numerical value obtained from commercial software based on finite element method, HFSS.

3.3.3 Coaxial waveguide validation

The normalized wavelengths of the first modes of a Coaxial Waveguide can be validated with these values published by Gruner [40] . They are compared in Fig. 3-6a, while the results for a ridge coaxial waveguide can be validated with a full wave commercial software HFSS (Fig. 3-6b).

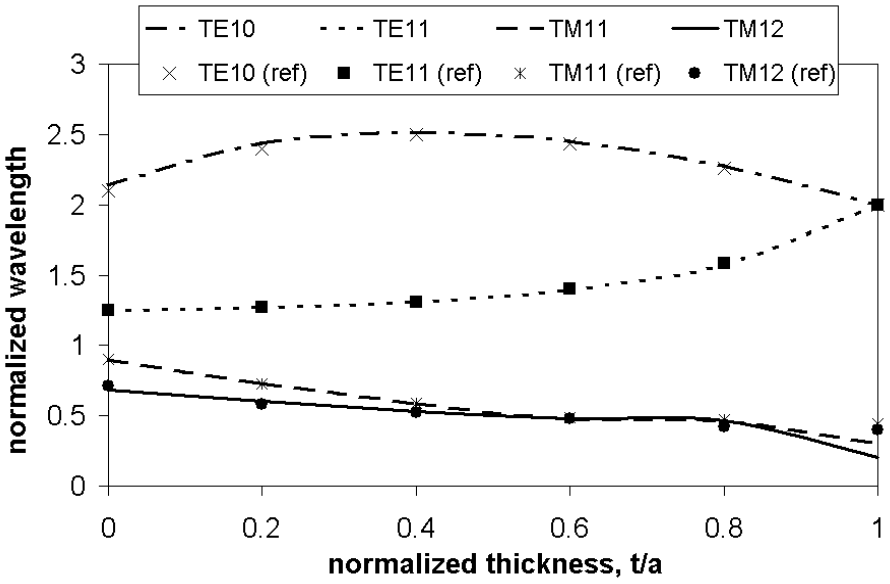

(a)

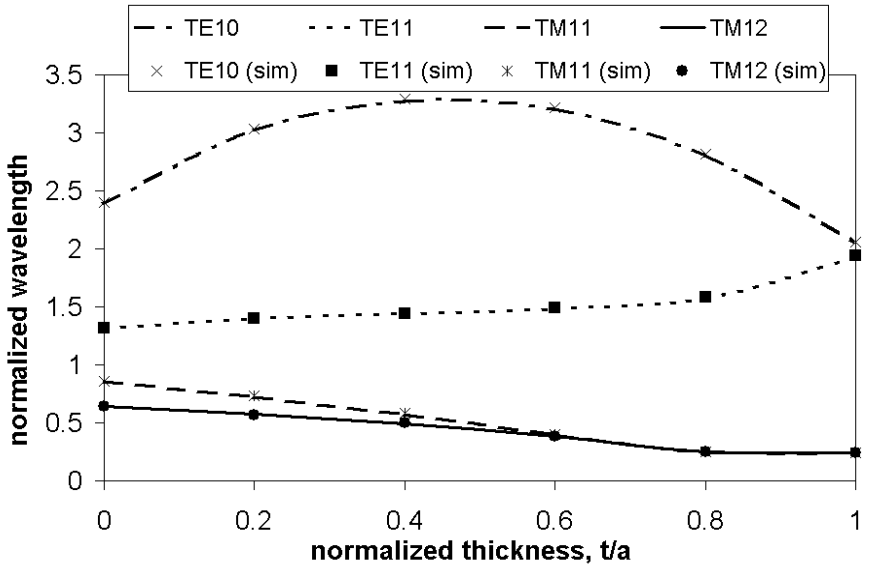

(b)

Fig. 3-6. Typical mode characteristic for a rectangular coaxial waveguide and comparison with reference [40] Dimensions: b/a=0.8, s1/b=0.3, c1=0, c2=0 (a) and for a square coaxial ridged waveguide, comparison with commercial software based on finit element method (b) Dimensions: b/a=0.8, s1/b=0.3, c1/b=0.1, c2=0

3.3.4 Single ridge waveguide validation

Further validation can be made by comparing the Characteristic Impedance obtained by Kobe and Garb [41] employing the method of moments for the analysis of a single Ridge Waveguide. A comparison is presented in Fig. 3-7.

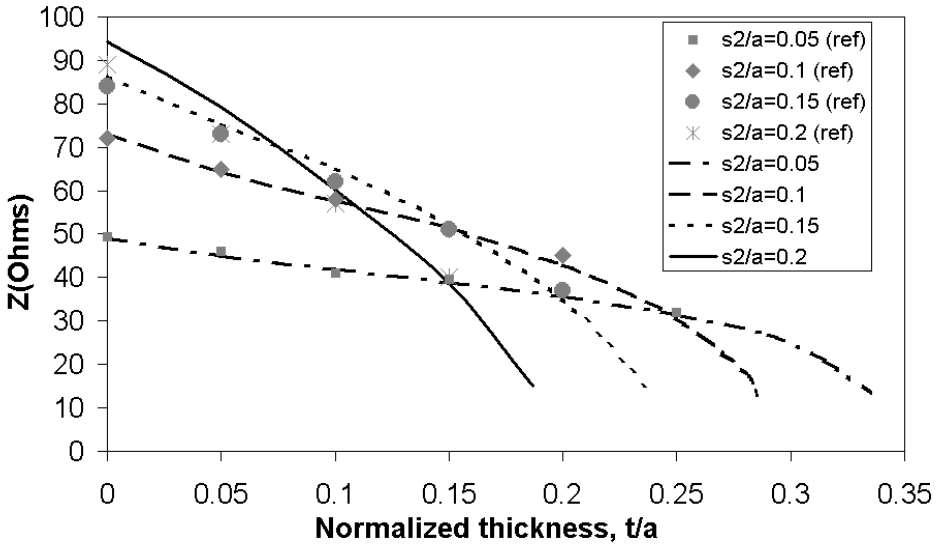

Fig. 3-7. Characteristic impedance of a rectangular ridged TEM line versus inner [41]. Dimensions: b/a=0.5, c1=0, s2/a=0.1.

There is well agreement between the impedance values obtained from both methods for values of thickness, t, greater than zero. However discrepancy seems to appear in the limit where t and s2 are close to zero, that is, in the limit of a rectangular waveguide. That can be due to the fact the number of expansion terms employed in that particular case is not sufficient to obtain an accurate value.

3.4 EVEN AND ODD MODES OF A RIDGE COAXIAL WAVEGUIDE

A practical application for the waveguide filter design is depicted in this section and will be used in the next chapter. Within the frequency band of interest for microwave filter realizations, the ridge coaxial waveguide (dimensions below Fig. 3-8) supports two propagating modes. The lowest cutoff frequency corresponds to the fundamental TE mode, TE_1. For a ridge coaxial waveguide symmetrical with respect to the y= 0 plane (Fig. 3-1b),

this mode corresponds to the fundamental mode of the ridge waveguides that emerge assuming a perfect electric conductor at the *xz*-plane. This mode therefore corresponds to the odd mode of the structure [44]. Moreover the ridge coaxial waveguide supports a TEM mode with zero cutoff frequency. Assuming the same geometrical symmetry, this mode preserves an open circuit (magnetic wall) symmetry along the *xz*-plane and therefore corresponds to the even mode of the structure. The TE_1 of this waveguide has been already presented in reference [45]. Interestingly, the former is characterised by a hollow waveguide mode dispersion, while the latter a linear dispersion (i.e. non-dispersive mode).

A working example of a ridge coaxial waveguide in an X-band housing with outer dimensions a= 22.86 mm and b= 10.16 mm is employed to demonstrate the dispersion and impedances of the odd and even modes. The thickness of the metal insert is t= 0.10 mm (Fig. 3-1b). For simplicity, the ridge coaxial waveguide is symmetric with respect to the *xz*-plane. Referring to Fig. 4-2, s_1= 2.1 mm and s= 1.5 mm. The dispersion curves for the TE_1 and TEM modes for this example are shown in Fig. 3-8a.

For comparison, Fig. 3.8a also shows the dispersion of the asymmetric ridge waveguide that emerges at the limit when s_1= 0. This is the only mode supported in the asymmetric ridge waveguide, which corresponds to the input and output ports. The corresponding characteristic impedances are shown in Fig. 3-8b. The impedance of the (conservative) TEM mode is uniquely defined and is constant for all frequencies. Regarding the TE modes, that is obtained selecting the power-current definition of the impedance [48], which exhibits a pole at the cutoff frequency and reduces with increasing frequency.

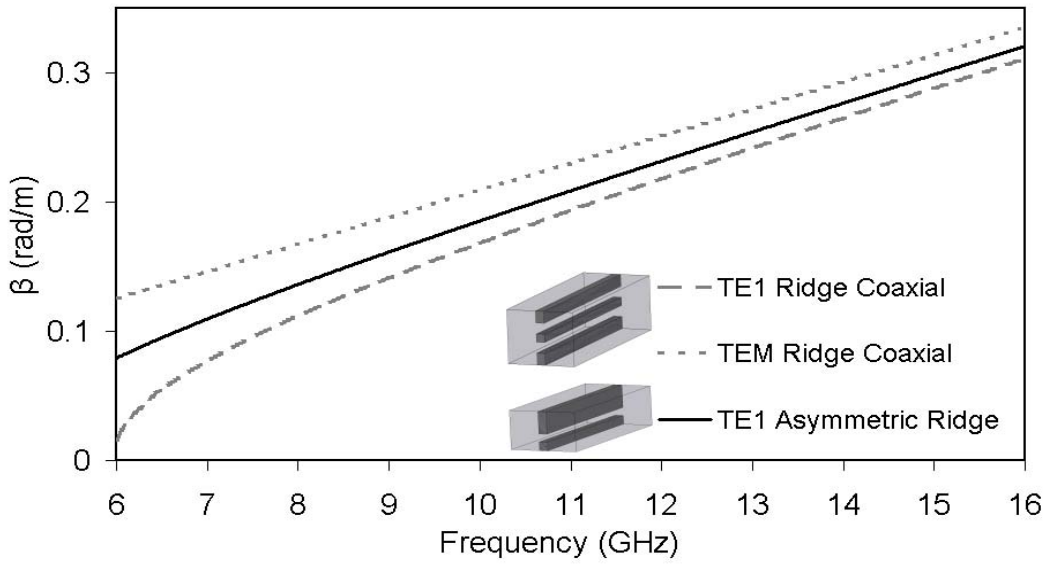

(a)

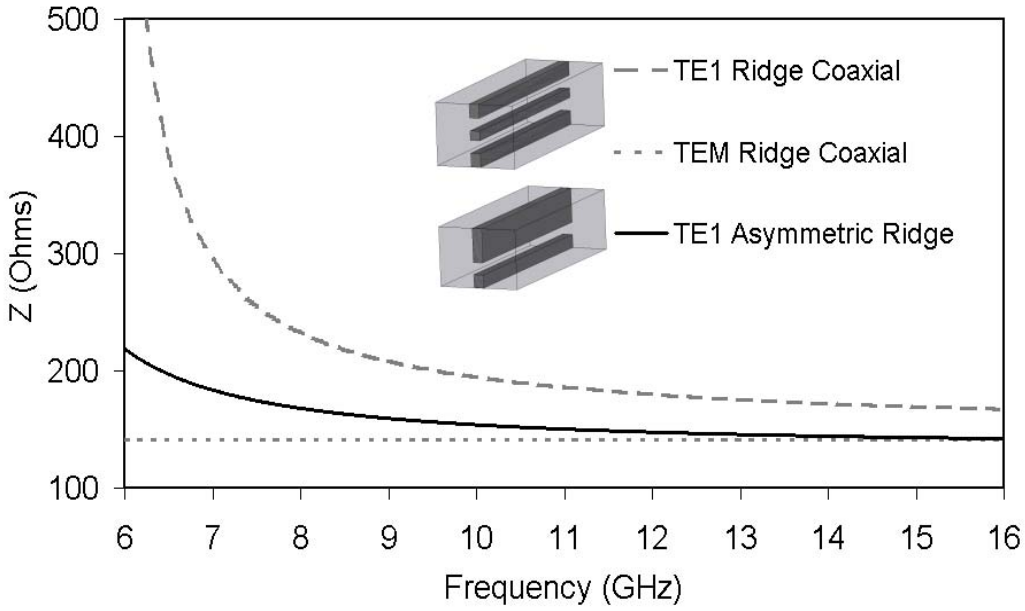

(b)

Fig. 3-8. (a) Dispersion and (b) characteristic impedance of the TEM and TE10 mode of a ridge coaxial waveguide with dimensions (in mm) a=22.86, b=10.16, s=1.5, s_1=s_2=2.1, s_u=s_d=2.23, t=0.1. The dispersion and characteristic impedance of the single ridge coaxial and asymmetric waveguide that emerges in the limit of s_2=0 is also superimposed.

3.5 SUMMARY

A full modal characterisation of the double ridged coaxial waveguide has been derived thorough this chapter. Due to the cross-section shape of this structure, the solution is not analytical. A numerical solution has been derived applying the Transverse Resonance Field Matching method.

The analysis of this structure will be useful in further chapters, where the results obtained are employed in the design of novel E-Plane involving Ridge Coaxial Waveguide (RCWG) cross-sections. The computational tool developed is capable of calculating the field distribution of the waveguide for up to 50 modes. In the practical filter realizations considered in further chapters (X-Band) the cutoff frequency of higher order modes is above operating range, that is, the filters basically operate in dual mode. For that reason a detailed field distribution of the first TE and TM modes, as well as the TEM mode is presented.

From the analysis performed, power normalisation of the TE/TM modes and TEM mode has been included. In fact these results will be of significant importance later on to exploit the asymmetric parallel coupled ridged waveguides for the bandpass filtering structures described (Chapter 4). Also the results are of relevance for the stopband and dual bandstop realizations investigated in Chapter 5. Numerical results haven been validated by comparing them with the partial results obtained thorough other techniques like method of moments for the TEM mode of the Single Ridge Coaxial Waveguide (section 3.3.4) or the particular case of a Coaxial Waveguide (section 3.3.3). Also the propagation characteristics of the first modes within a double ridged coaxial waveguide have been validated using a full wave simulation tool (HFSS). The results from this chapter are a solid basis for the filter modelling work of next chapters.

CHAPTER 4

Parallel Coupled Resonators for Bandpass Filter Applications

4.1 INTRODUCTION

Microwave filter configurations capable of providing selectively located transmission zeros are of interest as the improved stopband performance which those configurations can offer is a suitable solution to meet the increasing requirements for spectrum efficiency in modern communication systems [51]. In this context, cross-coupling of resonators, like the E-Plane filters described in section 2.3.2, is a widely employed technique to introduce additional transmission zeros in bandpass filters [53-58], including extra couplings from the original E-Plane configurations, like source-load coupling [57],[58]. However, the complexity in the physical implementation of cross-coupled filters typically increases with the order of the filter, introducing higher manufacturing costs. Inline configurations are often preferred solutions for the simplicity of the physical realisation.

As depicted in chapter 2, an extensively investigated low-cost solution for the realisation of microwave filters is the thin all-metal insert split-block housing E-plane filter [19-23], [60-67]. In order to overcome the poor stopband performance characteristic of E-Plane configurations increasing the filter order is not always a favourable solution, as this is associated with larger physical dimensions. It should be remarked the attractiveness of bandpass filters with selectively located transmission zeros, is that not only they can provide better skirt selectivity, but also improve stopband performance.

Among the large effort carried out over the last years in that direction, evanescent mode filters, based on ridge waveguide resonators housed in waveguide of reduced cross-section were proposed as means to extend the out of band rejection [62-63]. Before that, transmission zeros by extraction were introduced in [31] using resonators printed on the same metal insert and within a uniform waveguide housing but this was at a cost of larger total length. Inductively coupled stopband stubs have also been proposed to improve the

attenuation slope by extracting attenuation poles [64]. However these solutions involve non-uniform waveguide housing. A different solution involved multiple metal-inserts as means to improve the stopband performance in [4], at the cost of fabrication complexity and/or dielectric losses.

Introducing ridges in the resonators of E-plane filters slightly improved the stop-band performance within the same waveguide housing [65], however enhancement may not satisfy some applications. Based on that concept it was suggested a filter structure where the uniform waveguide resonators were periodically loaded with ridges [66], although improving the stop-band and reducing the size, does not selectively introduce transmission zeros. Similar disadvantages are associated with the integration of a low-pass with a pass-band filter in an all-metal insert [17]. Recently, [67] a folded configuration has been proposed that allows cross-coupling between the resonators in order to produce a pseudo-elliptic response [67], at the cost of fabrication complexity.

In [43] a 3rd order E-plane filter compatible with the standard E-plane topology was demonstrated to produce sharp higher frequency roll-off implementing a transmission zero close to the passband. The topology in [43] involved asymmetric ridge waveguide resonators (Fig. 4-1a) coupled in series (e.g., as in [23]) as well as in parallel (Fig. 4-2b), hence significantly reducing the overall size. However this topology is not easily extended to higher order filters. More recently, second order filters with parallel coupled asymmetrical ridge waveguide resonators were demonstrated to produce selectively located transmission zeros [68].

This chapter comprises further analysis of the configuration presented in [68] and investigate the extension of the concept to realizations with a higher number of resonators. We propose an equivalent circuit for this geometry based on an even-odd mode analysis [69-71], we demonstrate that the parallel coupling introduces transmission zeros due to the simultaneous propagation of the TEM and TE mode in the coupling section. For narrowband filters, this allows to control the coupling coefficient in the passband and also introduce transmission zeros out of band, similar to recent work in alternative topologies that involve mixed electric and magnetic coupling [72-73]. Following a theoretical analysis of this coupling, we proceed to outline a design procedure for filters of higher order.

Numerical and experimental results with a fourth order prototype will be provided for validation.

4.2 PARALLEL COUPLED RIDGED WAVEGUIDES

The proposed topology involves two parallel coupled asymmetric ridge waveguides. As it can be followed in Fig. 4-1a section of ridge coaxial waveguide emerges when two asymmetric ridge waveguides are coupled in parallel (Fig. 4-1b). The schematic of this geometry is shown in Fig. 4-1c. In this section we analyse that structure by means of an equivalent circuit and demonstrate that it can produce one transmission zero. The study on the nature of the transmission zero since, it will be revealed the frequency of the transmission zero is strongly dependent on the length of the coupling section between asymmetric ridge waveguide, is the key element to show how a careful choice of L allows to selectively position the transmission zero.

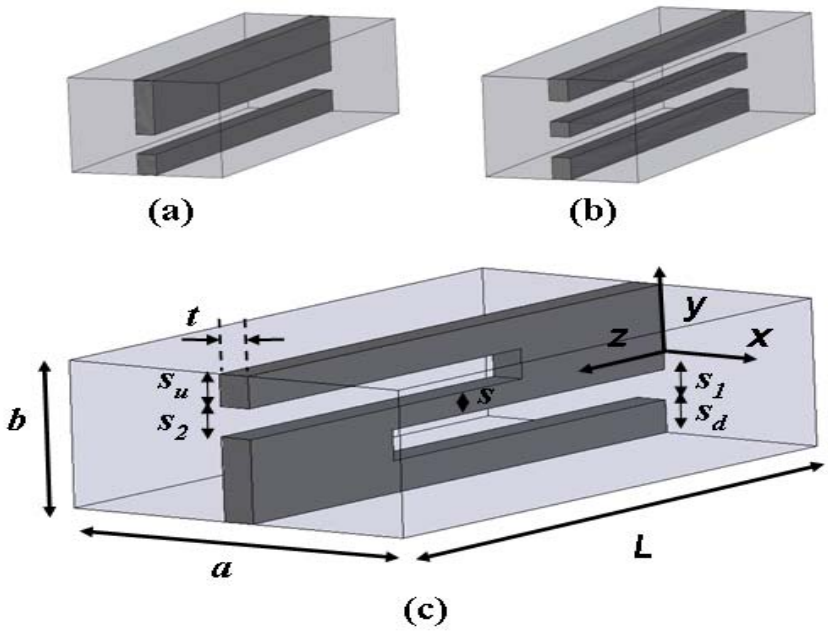

Fig. 4-1. (a) Asymmetric ridge waveguide, (b) Parallel coupling of asymmetric ridge waveguides, and (c) Ridge coaxial waveguide.

From the dispersion analysis of the proposed structure in terms of supported odd and even mode the guidelines of filter design are derived. The results obtained in section 4.2 are successfully employed in the design of bandpass filter configurations with selectively located transmission zeros. Numerical and experimental results are presented in section 4.3 and 4.4.

4.2.1 Equivalent electrical circuit

The equivalent circuit of the structure depicted in Fig. 4-2a is shown in Fig. 4-2b. The ports represent the asymmetric ridge waveguides (Fig. 4-1a) at the two ends. The coupling section is modelled by a pair of parallel coupled transmission lines, corresponding to a four port network (which in [69] is termed general four-port chain) with two ports terminated to Z_L.

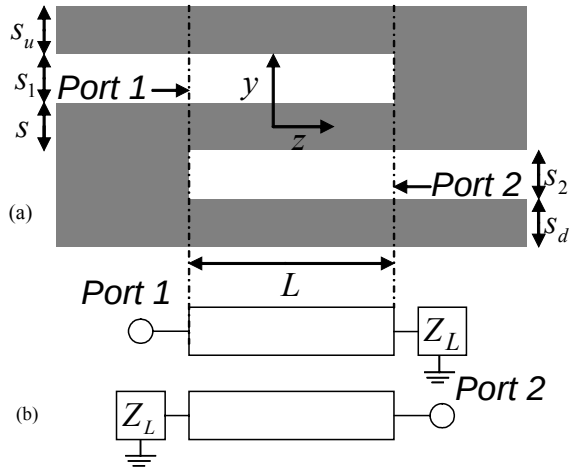

Fig. 4-2. Side view schematic (a). Equivalent electrical circuit of two parallel coupled asymmetric ridge waveguides (b).

The reactive loads, Z_L, represent the terminations experienced at the two ends of the ridge coaxial waveguide section. From HFSS simulations is estimated an initial value of 300 Ω. The reflection and transmission coefficient of this 2-port circuit can be obtained through an even/odd mode analysis [69]. In [69] a general even-odd analysis of the four-port network was presented and the impedance matrices were derived. Moreover the interdigital and combline cases with short- and open-circuited ends were studied [69]. In [70] the case where the two ports on the same side of the four-port chain are terminated with reactive

load (combline topology) was studied and the transmission zero conditions were derived. In [71] transmission zero conditions for the parallel (interdigital) and antiparallel (combline) coupled line circuits were obtained.

In the following we present the general impedance matrix for the interdigital parallel coupled line topology (Fig. 4-2b) and demonstrate that this structure can produce one selectively located transmission zero. We commence from the general impedance matrix Z^{4port} of the four-port chain derived in [69]. Applying the impedance termination at the two diagonal ports and after some algebra, we obtain the following impedance matrix for the circuit of Fig. 4-2b:

$$\begin{bmatrix} V_1 \\ V_2 \end{bmatrix} = \begin{bmatrix} Z_{11} & Z_{12} \\ Z_{21} & Z_{22} \end{bmatrix} \begin{bmatrix} I_1 \\ I_2 \end{bmatrix} \tag{4-1}$$

The impedance parameters of this matrix are given by

$$Z_{11} = Z_{22} = Z_{11}^{4port} + Z_{12}^{4port} \cdot A + Z_{14}^{4port} \cdot B \tag{4-2}$$

$$Z_{12} = Z_{21} = Z_{13}^{4port} + Z_{12}^{4port} \cdot B + Z_{14}^{4port} \cdot A \tag{4-3}$$

where $Z_{11}^{4port}, Z_{12}^{4port}, Z_{13}^{4port}, Z_{14}^{4port}$ refer to the impedance parameters found in the first row of the general four-port network impedance matrix and have been derived in [69]. They are reproduced here for completeness.

$$Z_{11/12}^{4port} = -j\frac{1}{2}\left[Z_{0e}cot\theta_e \pm Z_{0o}cot\theta_o\right] \tag{4-4}$$

$$Z_{13/14}^{4port} = -j\frac{1}{2}\left[Z_{0e}csc\theta_e \mp Z_{0o}csc\theta_o\right] \tag{4-5}$$

The electrical lengths of the odd, θ_o, and even, θ_e, mode are:

$$\theta_o = \beta_o L \qquad \theta_e = \beta_e L$$

The parameters A and B are obtained as:

$$A = \frac{\left(Z_L - Z_{11}^{4port}\right)\cdot Z_{12}^{4port} + Z_{13}^{4port}\cdot Z_{14}^{4port}}{(Z_L - Z_{11}^{4port})^2 - Z_{13}^{4port\,2}} \quad \textbf{(4-6)}$$

$$B = \frac{\left(Z_L - Z_{11}^{4port}\right)\cdot Z_{14}^{4port} + Z_{13}^{4port}\cdot Z_{14}^{4port}}{\left(Z_L - Z_{11}^{4port}\right)^2 - Z_{13}^{4port\,2}} \quad \textbf{(4-7)}$$

Together with the characteristic impedances of the input and output port, these expressions predict the transmission and reflection characteristics of two parallel coupled transmission lines shown in Fig. 4-2b. As will be shown, this is a good model for the parallel coupled asymmetric ridge waveguides (Fig. 4-2a). In order to employ these expressions for the structure of Fig. 4-2a, the characteristic impedances and propagation constants of the structures involved (namely the ridge coaxial waveguide and the asymmetric ridge waveguide) are required.

4.2.2 Parallel coupling of asymmetric ridge waveguides

In order to demonstrate the performance of the ridge coaxial waveguide as a coupling section between two asymmetric ridge waveguides the equations derived in the previous section are implemented in matlab. Fig. 4-3 includes the position of the Transmission zeros predicted by the circuit model for the structure depicted in Fig. 4-2.

The comparison between the results obtained from an implemented software based on the odd and even mode circuit analysis and a full wave commercial software [50] yields a good approximation when the termination impedance is set to be a fixed value of Z_L=i300 within the X-Band. All the calculations have been derived from the power-current definition of the impedance.

.

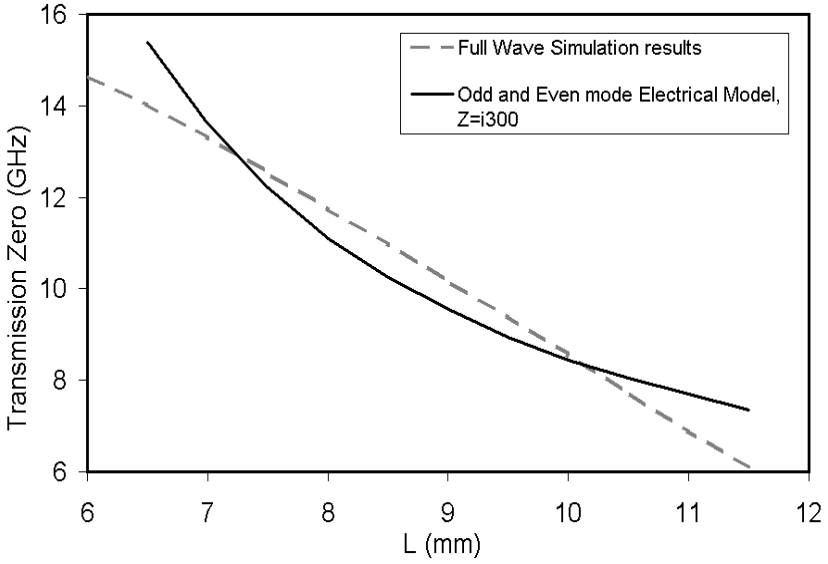

Fig. 4-3. Transmission Zeros location for the structure depicted in Fig. 2 obtained for a fixed value of the Impedance Load, Z=i300, and comparison with full wave commercial software. Dimensions in mm: s_u=s_d=2.23, s_1=s_2=2.1, s=1.5.

However the termination impedance, Z_L, is considered in general dispersive. Taking that into account a more accurate model can be implemented. Fig. 4-4a shows the transmission coefficient (magnitude and phase) extracted from the structure depicted in Fig. 4-2 for four different values of the coupling length, *L*. All other dimensions are as in Fig. 4-3. For comparison, Fig. 4-4b shows the transmission coefficient as obtained from the circuit of Fig. 4-2 and equations (4-2) and (4-3) for the same values of the coupling lengths, *L* using the impedances and propagation constants of Fig. 4-3. For that model the Power-current definition has been employed to estimate the values of the termination impedance, Z_L. The agreement between the two plots validates the equivalent circuit as a good qualitative model of the structure in Fig. 4-2a. Some discrepancies are attributed to the fact that the termination impedance, Z_L, is in general dispersive.

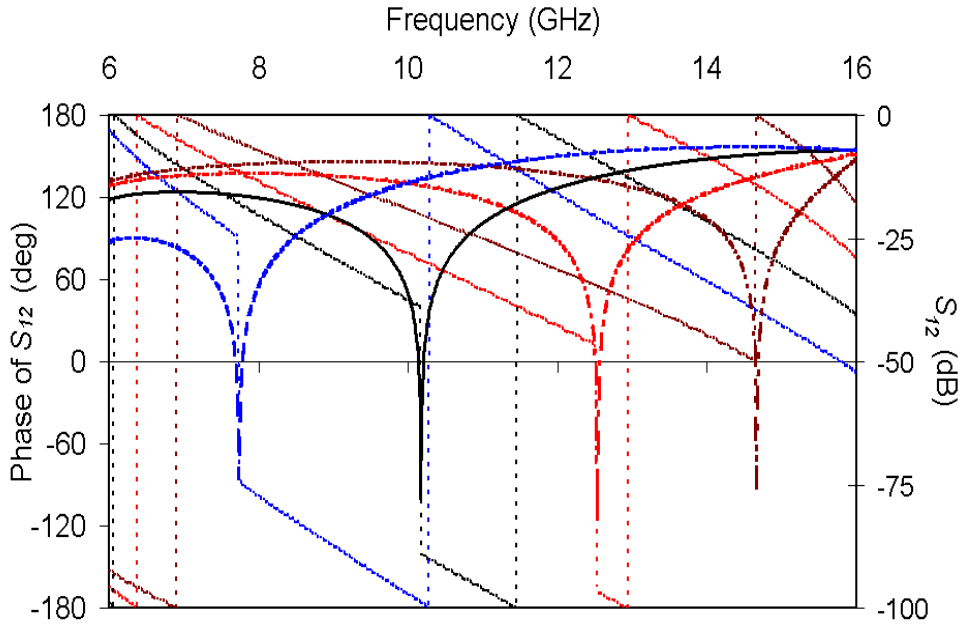

(a)

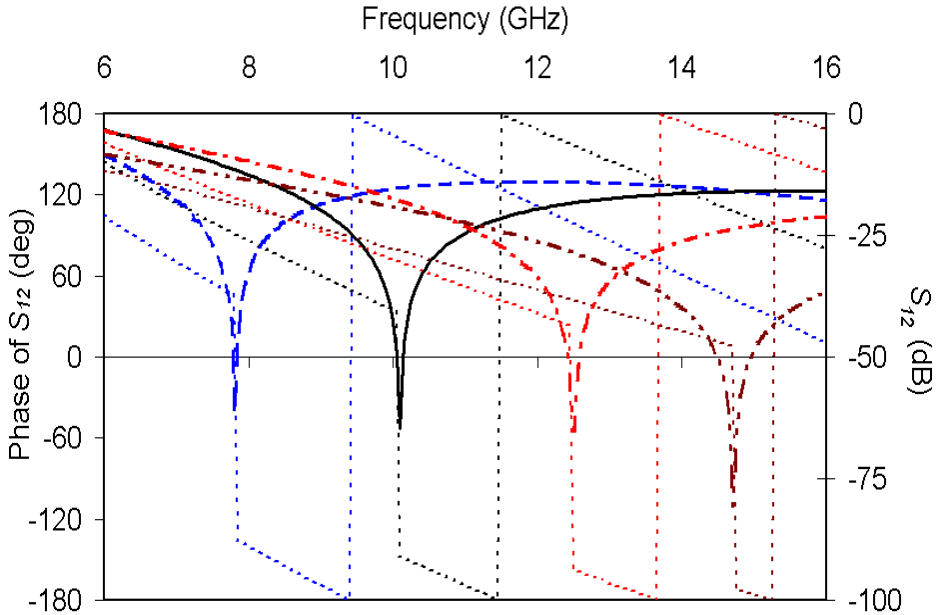

(b)

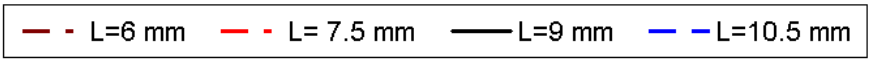

Fig. 4-4. Magnitude and Phase of S_{12} for the structures of Fig 2. (a) full wave simulation and (b) circuit model for different values of the coupling length, *L*. Dimensions as in Fig. 3.

Due to the different dispersion relations of modes in the ridge coaxial waveguide (Fig. 3-8), the coupling between the two asymmetrical ridge waveguides is strongly dispersive. The positive sign of the transmission coefficient phase at lower frequencies suggests a predominantly inductive coupling, which is associated with the TEM mode. At frequencies higher than the transmission zero, the negative phase of the transmission coefficient reveals that the coupling is predominantly capacitive, and is associated with the TE1 mode. This is depicted in Fig. 4-5 where the electric field distribution for the structure with L= 9mm is depicted at 7 GHz (inductive coupling) and at 12 GHz (capacitive coupling).

The modal distributions of the TEM and TE_1 mode can be respectively identified as dominant in either case respectively. At a certain frequency point the two contributions exactly cancel out, giving rise to a transmission zero. Significantly, the frequency of the transmission zero is strongly dependent on the length of the coupling section L, as the simulation results of Fig. 4-4 show in good agreement between them. Hence a careful choice of the coupling length, L, allows controlling the frequency of the transmission zero.

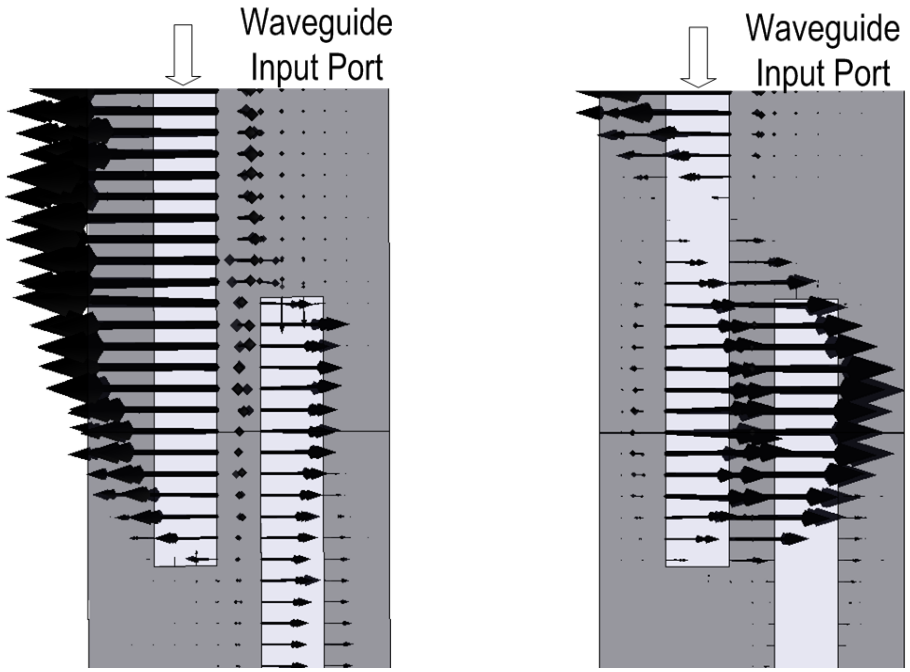

Fig. 4-5. Electric field distribution corresponding to the trace L=9 mm in Fig. 4-2 (a) at 7 GHz and (b) at 12 GHz, showing predominant coupling through the TEM and TE_{10} modes respectively.

4.3 FILTERS WITH SELECTIVELY LOCATED TRANSMISSION ZEROS

In this section we employ parallel coupling of asymmetric ridge waveguide resonators and demonstrate that by varying the geometry it is possible to independently control the coupling coefficient within a narrow passband and the location of an out-of-band transmission zero. Initially we demonstrate that by varying the geometrical characteristics it is possible to achieve predominantly electric or magnetic coupling of a fixed magnitude. This is an indication of a mixed coupling mechanism [72-73], which is known to allow selectively located transmission zeros. Subsequently we proceed to produce design guidelines for inline E-plane filters with selectively located transmission zeros. Numerical and experimental results are presented for validation.

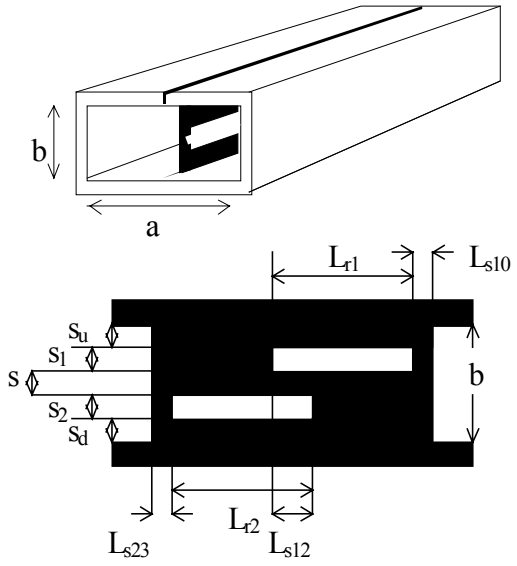

Fig. 4-6. Schematic of the two parallel coupled resonators concept

4.3.1 Electric and magnetic coupling of resonators

In order to demonstrate the mixed coupling mechanism, here we employ an example involving two pairs of parallel coupled asymmetrical ridge waveguide resonators. The two designs here are selected so that they yield the similar value of coupling coefficient but with opposite sign. Both designs are housed in X-band rectangular waveguide of cross-section 22.86x10.16mm, and the metal insert thickness is t=0.1 mm. The resonator lengths

are 16 mm and in both cases they are symmetric with respect to the *xz*-plane. Referring to Fig. 4-2, in design 1, *s*=1.5 mm and the coupling length, *L*=12 mm. For design 2, *s*=2.25 mm and the coupling length, *L*=5.25 mm. The transmission coefficient for the two designs upon weak external excitation, achieved by using input and output coupling septa equal to 8 mm, is shown in Fig. 4-7.

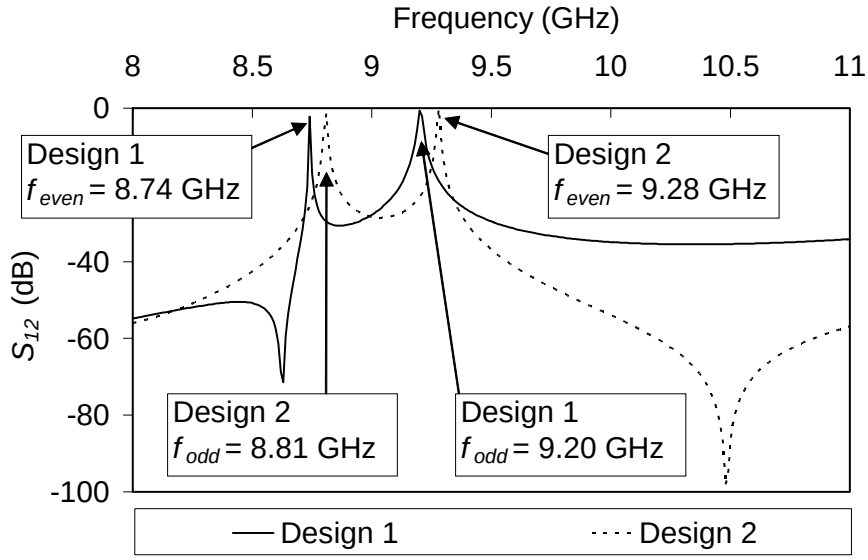

Fig. 4-7. Transmission coefficient for two weakly excited asymmetrical ridge waveguide resonator designs coupled in parallel configuration exhibiting similar levels of electric and magnetic coupling with transmission zeros at frequencies higher and lower than the resonances respectively.

The coupling between a pair of synchronously tuned resonators can be estimated from the split of the even and odd mode resonances upon weak external excitation [44] and is approximately 0.052 for both designs. The field distribution at the two resonant peaks for design 1 and 2 is shown in Fig. 4-8 and Fig. 4-9 respectively. As shown, the even resonance (which respects a magnetic symmetry) for design 1 occurs at lower frequencies than the odd resonance (which respects an electric symmetry). This reveals a predominantly magnetic coupling. On the contrary, the odd resonance for design 2 occurs at lower frequencies than the even resonance, revealing a predominantly electric coupling. The even and odd resonant frequencies are also marked in Fig. 4-7 for convenience. As is common in the case with mixed coupled resonators [72-73], the transmission zero swaps either side of the passband when the coupling mechanism changes.

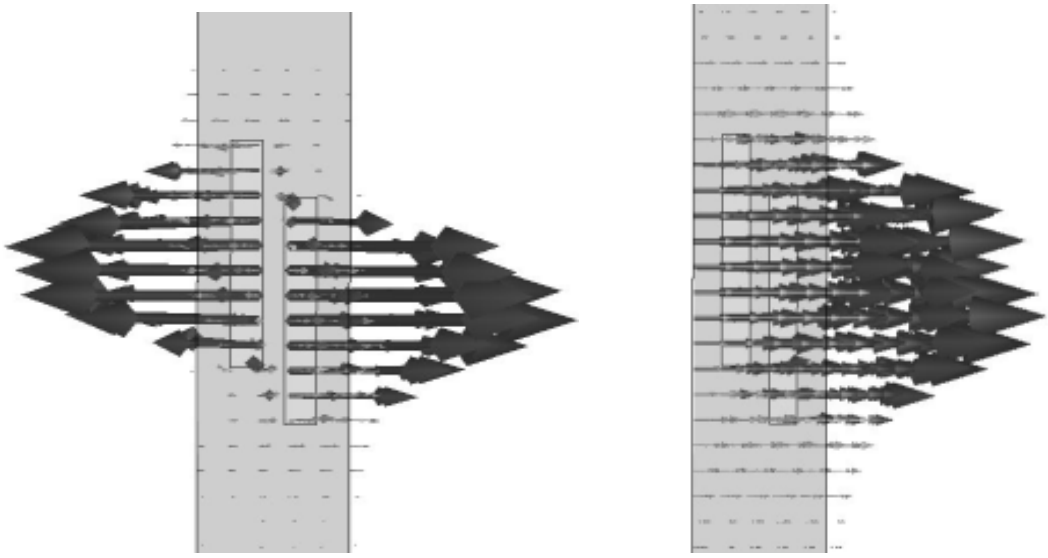

(a) (b)

Fig. 4-8. Lower zero prototype with weak external coupling (a) E-field at the first resonance 8.74 GHz and (b) at the second resonance 9.2 GHz. Dimensions (in mm):L_r=16; s=1.5, Ls_{12}=12, a=22.86, b=10.16, s_1= s_2= 2.1, s_u= s_d= 2.23. The thickness of the insert is 100 μm

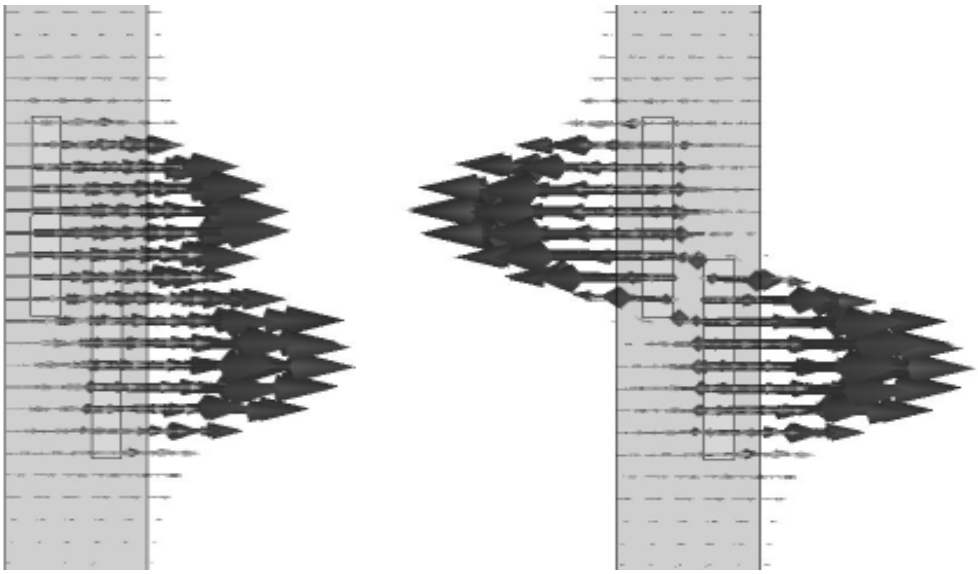

(a) (b)

Fig. 4-9. Upper zero prototype with weak external coupling (a) E-field at the first resonance 8.81 GHz and (b) at the second resonance 9.28 GHz .Dimensions (in mm): L_r= 16, s= 2.25, L_{s12}= 4.5, a=22.86, b=10.16, s_1= s_2= 2.1, s_u= s_d= 2.23. The thickness of the insert is 100 μm.

A rigorous study of the coupling coefficient and the frequency of the transmission zero based on the geometrical characteristics of the coupling structure has been undertaken employing pairs of synchronously tuned resonators of length 16 mm, such as those depicted in Fig. 4-8 and Fig. 4-9. Symmetric structures with respect to the *xz*-plane have been considered with reference to Fig. 2, we report the outcome for three different values of the parameter *s* and varying coupling length, *L*, and vice versa. The location of the transmission zero and the derived coupling coefficient are reported in Fig. 4-10 and Fig. 4-11 respectively. For the sign of the coupling coefficient we have employed the usual convention, where positive coupling corresponds to predominantly electric coupling [56].

$$k = \frac{f_{odd}^2 - f_{even}^2}{f_{odd}^2 + f_{even}^2} \qquad \textbf{(4-8)}$$

Careful investigation along a curve with a minimum reveals that the even and odd resonance swap in frequency close to the minimum, which corresponds to change in sign of the coupling coefficient into a negative value. Significantly, this study reveals that the parallel coupling of asymmetrical ridge waveguide resonators allows to independently control the value of the coupling coefficient and the location of the transmission zero, as also experimentally corroborated in [68]. Moreover, the parametric curves of Fig. 4-10 and Fig. 4-11 can be employed for the initial design of the dimensions of filters with selectively located transmission zeros.

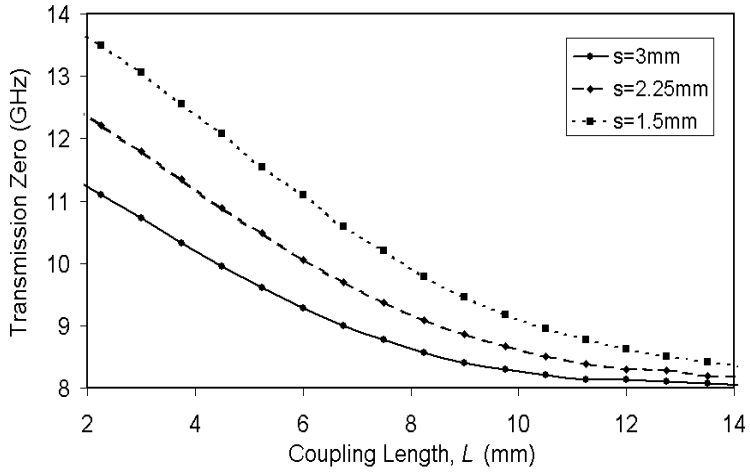

Fig. 4-10. Selectively positioning of the Transmission zeros produced by a synchronously coupled asymmetrical ridge waveguide resonators of length 16 mm with varying separation.

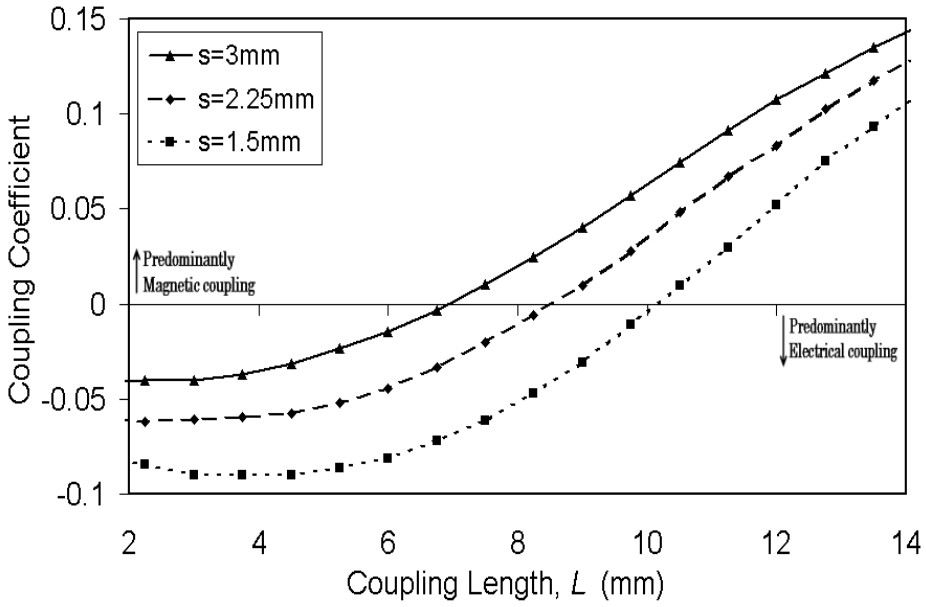

(a)

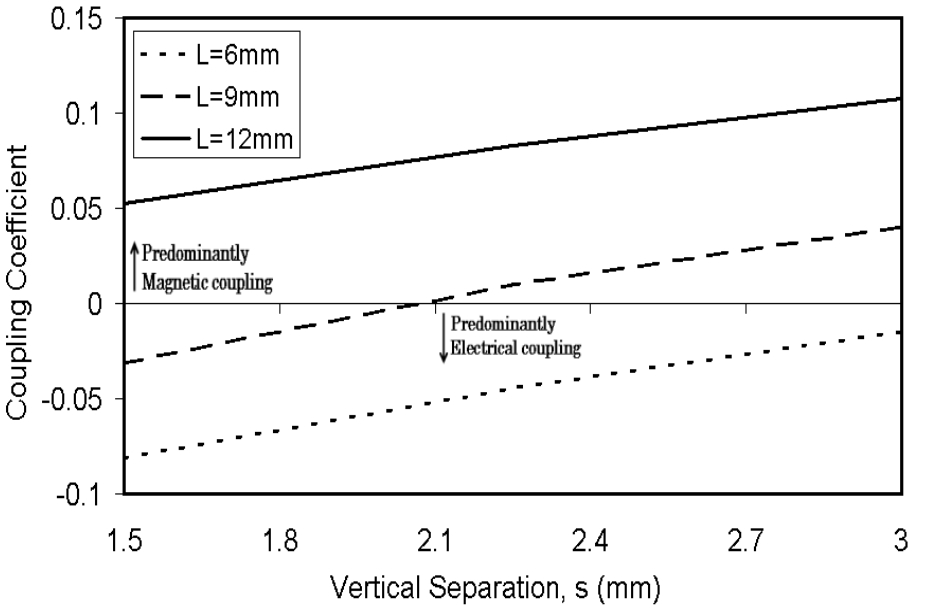

(b)

Fig. 4-11. Coupling coefficient control of a synchronously coupled asymmetrical ridge waveguide resonators varying separation, L (a) and s (b) Other dimensions as in Fig. 9.

In Fig. 4-11 is revealed an increasing coupling towards predominately magnetic (electric) coupling as larger (shorter) the coupling length or the vertical separation between the resonator is. From equation (4-8) can be seen that is due on how the split resonance shift for diferent coupling mechanism. At the point where k=0 the two resonances swap from lower to upper frequencies and vice versa, is then when also the transmission zero shifts from lower to upper/ upper to lower stopband.

4.3.2 Second order bandpass filter design

In order to demonstrate the practical application of the elements described in the previous section, Fig. 4-12 presents a series of approximate second order filter designs obtained using full wave simulation software Ansoft HFSS. Passbands are centered at 8.9 GHz and and transmission zeros are located at diferent positions. In particular, Fig. 4-12a shows a parametric study varying the overlap length L_{s12} for an arrangement with L_{r1}=L_{r2}=16 mm, s_1=s_2=2.1 mm, s=1.7 mm, which produces a transmission zero in the upper stopband. As shown, increasing L_{s12} results in narrower passbands, due to the reduced coupling coefficient between the two resonators (see Fig. 4-11a). Moreover, in accordance to Fig. 4-10, for increasing L_{s12}, the transmission zero emerges at increasingly lower frequencies approaching the upper cutoff. A similar graph is shown in Fig. 4-12b for transmission zeros located in the lower stopband. To illustrate the possibility to selectively position the transmission zero in this case, several parameters of the filter had to be adjusted. Nevertheless, as shown in Fig. 4-12, the arrangement of Fig. 4-6 allows for selective location of the transmission zeros on either side of the passband.

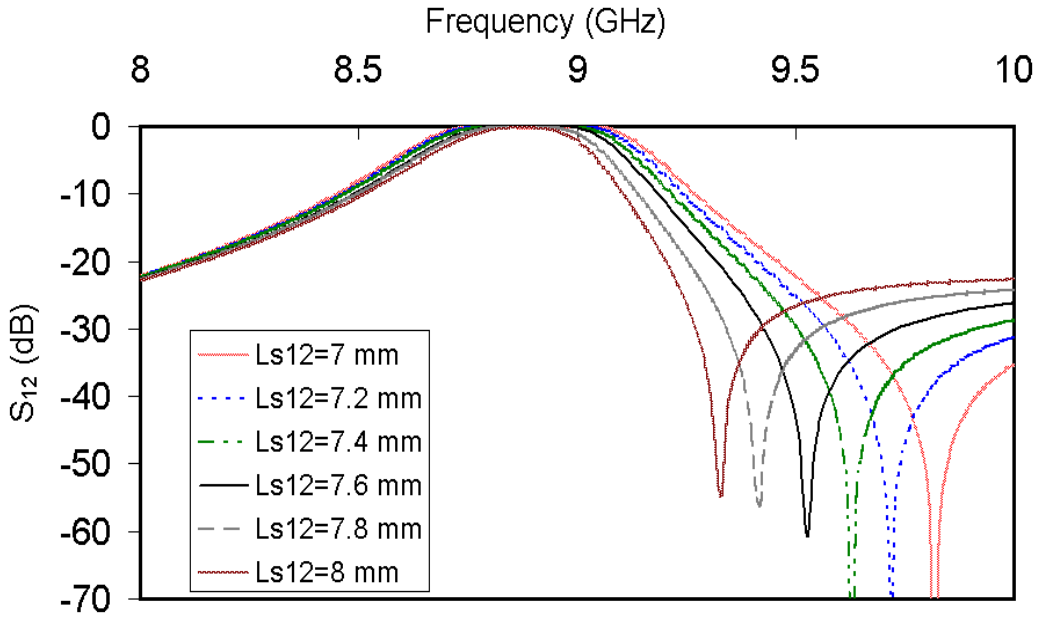

(a)

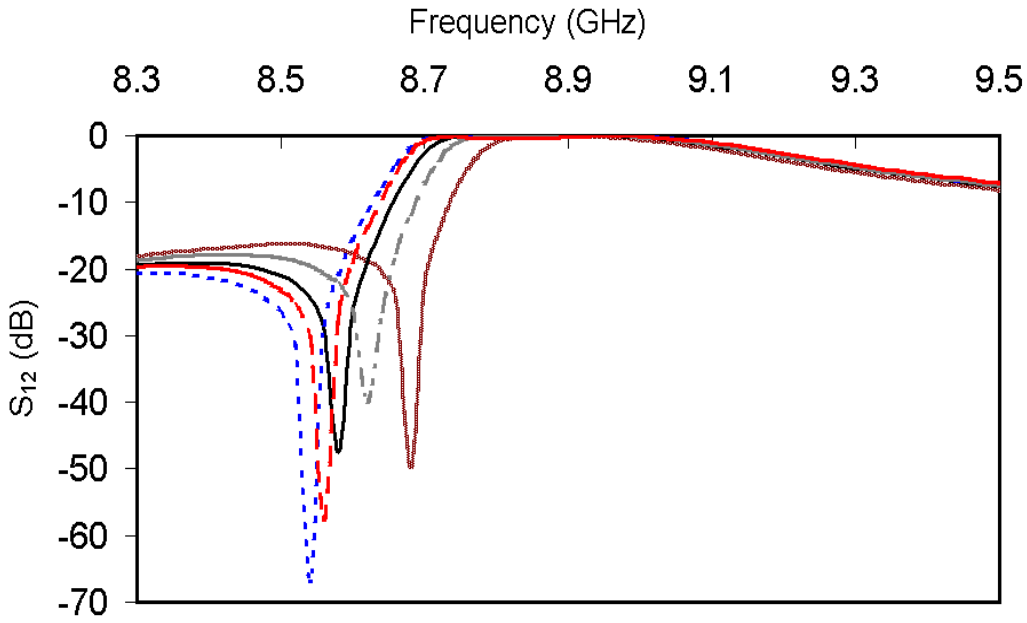

(b)

Fig. 4-12. Second order filters with passband centred approximately at 8.9GHz and transmission zeros located in the (a) upper and (b) lower stopband. Dimensions (in mm) (a) L_{r1}= L_{r2}= 16, s_1= s_2= 2.1, s= 1.7 and (b) varying dimensions.

4.3.2.1 Numerical and experimental results

To demonstrate the above, two second order filter X-band prototypes have been designed to produce approximately the same passband characteristics but a sharp roll-off on either the lower or higher frequency cutoff. In the following these will be referred to as the Lower and Upper Transmission Zero (TZ) prototype respectively. The dimensions (in mm) for the Lower TZ prototype are L_{r1}= L_{r2}= 16, s_1= s_2= 2.1, s= 1.5 L_{s12}= 11.4 while for the Upper TZ prototype they are L_{r1}= L_{r2}= 16, s_1= s_2= 2.1, s= 1.7, L_{s12}= 8.4.

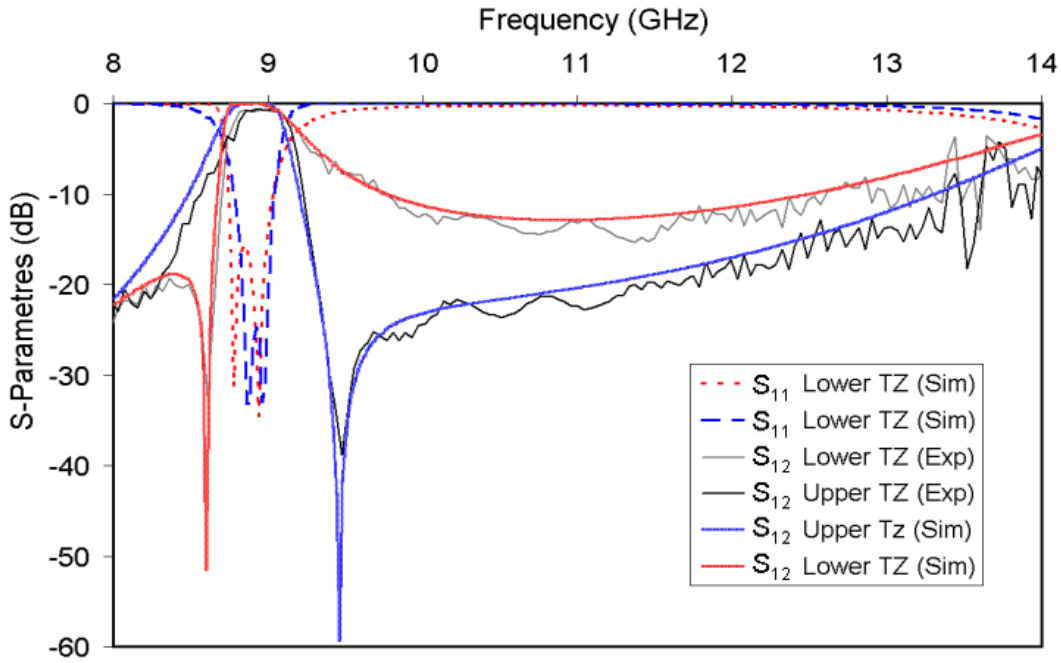

Fig. 4-13. Simulated and measured transmission coefficient for the Lower TZ and Upper TZ designed filter prototypes (a). Dimensions depicted in Table 4-1 (in mm).

Prototype	L_{r1}	L_{r2}	s_1	s_2	s	L_{s12}	L_{s10}	L_{s23}
Lower TZ	16	16	2.1	2.1	1.5	11.4	1	1
Upper TZ	16	16	2.1	2.1	1.7	8.4	1	1

Table 4-1. Dimensions (in mm) of the Lower and Upper TZ prototypes designed (see Fig. 4-6).

The simulated transmission coefficient for the two prototypes is shown in Fig. 4-13 (dashed lines). The simulated reflection coefficient is shown in Fig. 4-14a and Fig. 4-14b for the Lower and Upper TZ prototype respectively.

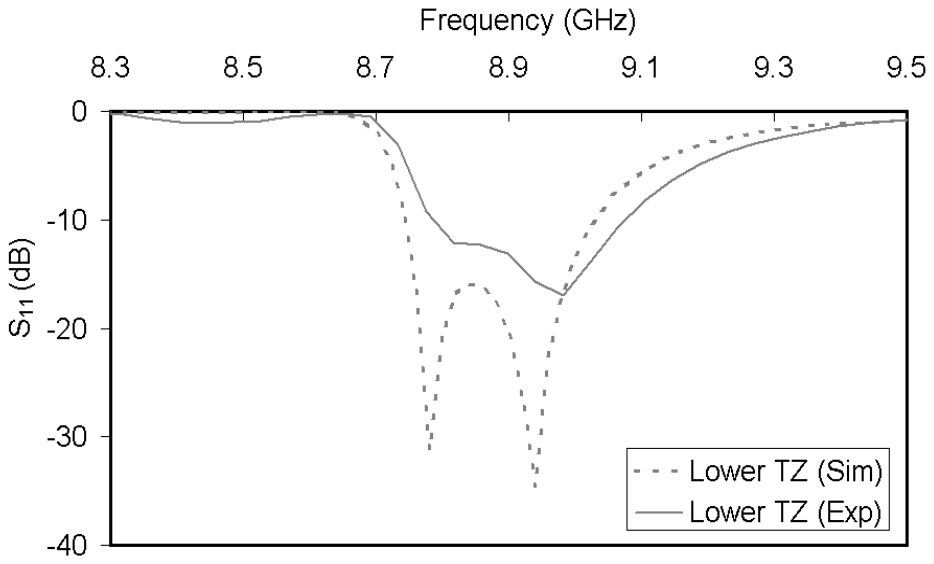

(a)

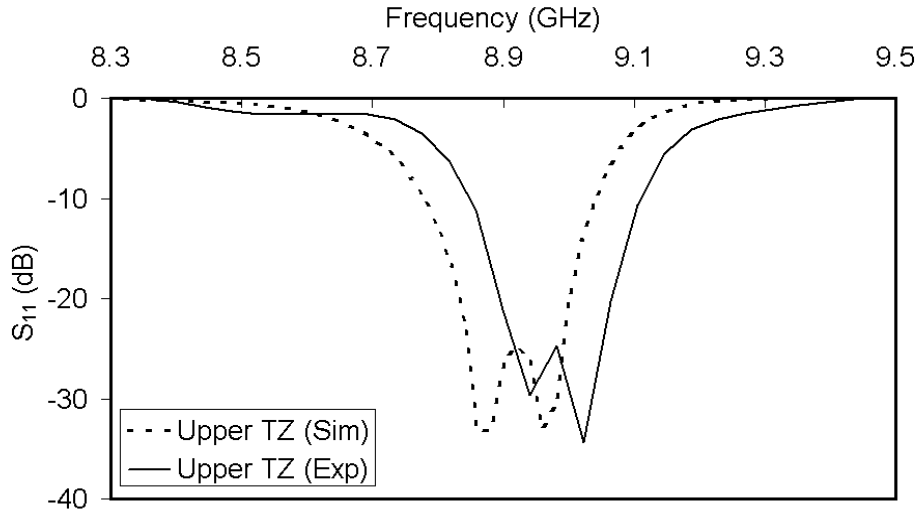

(b)

Fig. 4-14 Simulated and measured reflection coefficient for the Lower TZ (a) and Upper TZ (b) designed filter prototype. Dimensions in mm depicted in Table 4-1.

The passband for both filters is to a good approximation between 8.75GHz and 9.10GHz. Although there is a difference of about 10dB in the maximum value of the reflection coefficient, both maintain reflection levels below -15dB, hence demonstrating the selective positioning of the transmission zero. The transmission zeros are located at 8.6GHz and 9.45

GHz for the Lower TZ and Upper TZ prototype respectively. This produces a sharp roll-off rate at the lower and upper cutoff frequency respectively. The spurious harmonic resonance is above 14 GHz for both prototypes. This is more than 1 GHz improvement compared to the conventional E-plane filters, e.g. [58]. Moreover, the total lengths are 22.4 mm and 25.4 mm for the Lower TZ and Upper TZ respectively. This compares to about 46 mm required for a conventional second order E-plane filter of reference [58], corresponding to about 50% size reduction. Shifting of the measured reflection compared to the simulated is atributed to the fabrication tolerances: the milling procedure employed got estimated a sensitivity of about $\pm 50\ \mu m$, which in terms of the physical length of the resonator means a shif in frequency as that shown in Fig. 4-14b.

In order to validate the simulations, the two prototypes have been fabricated. A 100μm copper foil has been routed to etch the filter circuit, which was mounted in a machined brass waveguide housing. A photograph of the two prototypes is shown in Fig. 4-15. The prototypes were measured in an HP8510 vector network analyser, using commercial X-band flanges. The calibration was made to the level of the coaxial cable. The comparison of the simulated results with the measured results shown in Fig. 4-13, reveal a good agreement, validating the possibility to selectively locate the transmission zero. Fig. 4-14a and 4-14b reveal a frequency shift between 50 and 100MHz. This is attributed to the fabrication process tolerances.

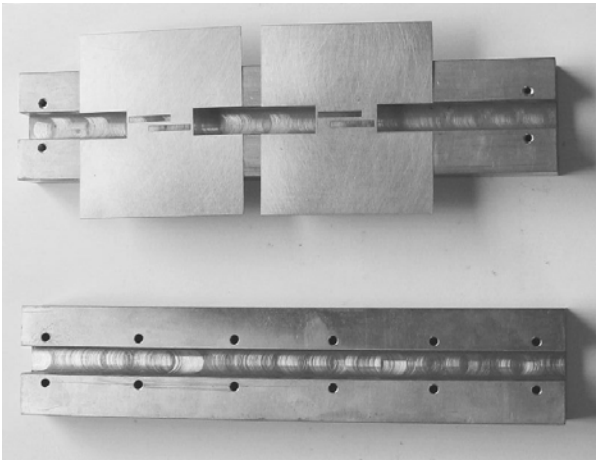

Fig. 4-15. Photograph of the fabricated second order filter prototypes. Total lengths are 25.4 mm and 22.4 mm for the Upper TZ (left) and Lower TZ (right) respectively.

4.3.2.2 Tolerances analysis

A fabrication tolerance analysis for the filter configurations of Fig. 4-6 is reported in this section. A parametric study is presented to evaluate the effect of fabrication tolerances in the filter performance. From the filter realizations of Fig. 4-13, with dimension specified in Table 4-1, small dimension variations up to the fabrication accuracy are considered to validate the fabrication technique employed.

This section contains some parametric studies in order to demonstrate one of the main advantages of the filter realizations presented:, namely low-cost fabrication reliability. In order to prove the validity of the photo-etching technique for the fabrication of filters involving parallel coupled resonators, here a set of parametric studies for each one of the prototypes designed, fabricated and tested in the previous chapters is presented. Numerical results are presented commencing from the original dimensions of the prototypes described in Chapter 4, and the filter performance considering random dimensional variations of ±50 μm are assessed. The target here is to assess the fabrication tolerances in terms of the final response of the filter.

The parametric analysis is first made for the second order prototypes. The most sensitive dimension parameters with the coupling are: the vertical separation and coupling lengths respectively, S_1 and S_2 and L (see Fig. 4-6). The study has covered the tolerance range of the photo-etching technique employed for the fabrication of the prototypes, which is estimated to be no more than ±20 μm. However extending that sensitivity range, the parametric studies shown are based on ±50 μm variations of s and L (see Fig. 4-6) from the ideal prototypes design values.

The starting dimensions for this tolerance study are those reported in Table 4-1 for both the lower and upper zero prototypes designed. Fig. 5-1 includes a study for the basic second order prototypes with Upper Transmission Zero (a) and Lower Transmission Zero (b) respectively.

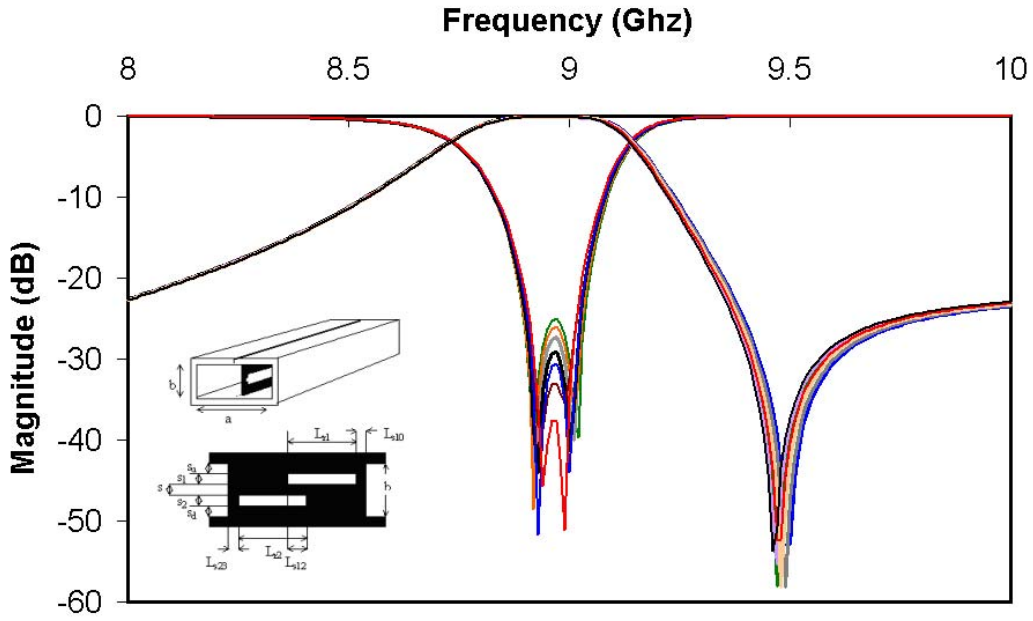

(a)

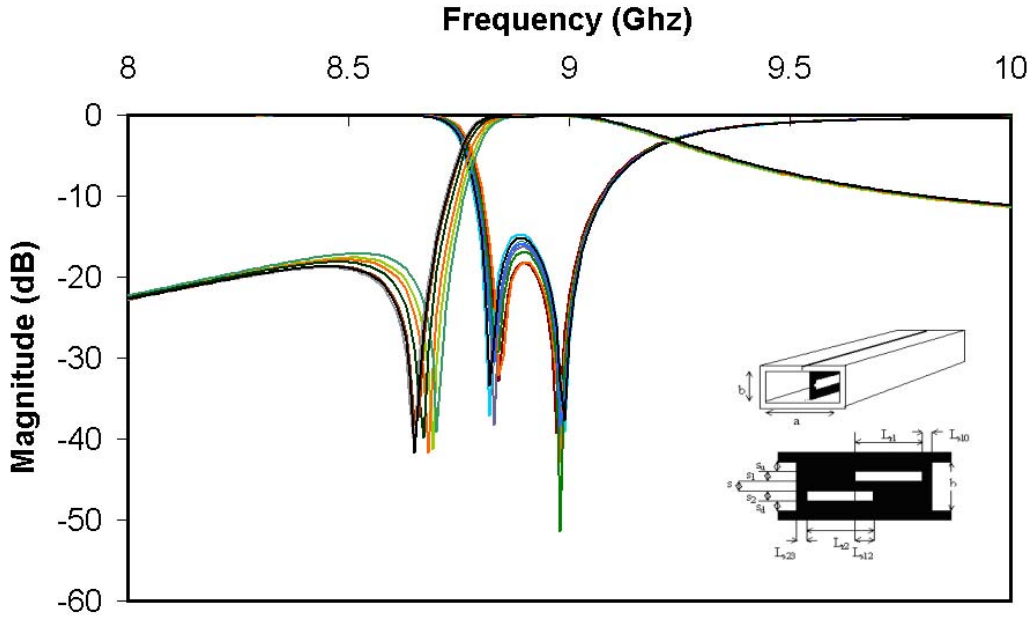

(b)

Fig. 4-16. Fabrication tolerance of the second order bandpass filter prototype with Upper (a) Lower Transmission Zeros (b).

4.4 SYNTHESIS OF HIGHER ORDER FILTERS

This section contains all the elements required for higher order realization of bandpass filters with parallel coupled resonators. In section 4.4.1 it is reported by means of a realization example using the general design guidelines towards higher order filters with parallel coupled resonator configurations. These general design guidelines are derived from a technique suggested in reference [74]. As described in 4.4.1, the technique is based on the matching of the group delay of the reflection coefficient. The adapted synthesis procedure is proved very efficient to design fourth order bandpass prototypes with two transmission zeros located at desired frequencies. The first step is to design a classical direct-coupled filter of the same order opperating at the frequency and with bandwidth as desired for the novel filter. Then, the phase of the group delay values for the designed classical filter is extracted. Finally, the novel filter (with parallel coupled resonators) is modelled step by step as described in section 4.4.1 in order to match those group delay values of the classical filter.

Although the implemented technique employed in this realization example is considered suitable for any other topologies, an alternative approach is also included in Appendix C. That procedure is based on the well known method of mode matching at surface discontinuities, Appendix C contains the derivation of the scattering matrix for such particular surface discontinuity, which can be also of interest for the integration within a numerical tool involving the analysis of other waveguide discontinuities. However the Ness procedure is considered sufficient and much easier to be implemented, so on is the one to follow thorough below. A prototype has been fabricated and experimentally tested following those derived guidelines.

4.4.1 Phase of group delay matching technique

Higher order filters can be realised employing a cascade of series and parallel coupled resonators, implementing an in-line prototype. Each pair of parallel coupled resonators can in general introduce one selectively located transmission zero. The schematic of a 4^{th} order filter (cross-section) which can produce up to 2 transmission zeros is shown in Fig. 4-16. Here we employ this topology as an example to demonstrate a practical X-band filter

centred at about 8.8 GHz. The synthesis of a narrowband filter commences by extracting the coupling matrix for the in-line prototype that satisfies the passband requirements. These coupling coefficients are obtained from a code implemented for classical direct-coupled filters.

The in-band coupling matrix of the prototype for this example is selected:

$$k = 1x10^{-02} \cdot \begin{bmatrix} 0 & 2.271 & 0 & 0 \\ 2.271 & 0 & -1.781 & 0 \\ 0 & -1.781 & 0 & -2.271 \\ 0 & 0 & -2.271 & 0 \end{bmatrix} \quad \textbf{(4-9)}$$

That yields a reflection coefficient in the passband is at the -20 dB level. The filter is designed at X-band with 3 dB passband between 8.5 GHz and 8.75 GHz. For the purposes of this example we have selected the transmission zeros at frequencies adjacent to the passband (8.3 GHz and 9 GHz respectively) in order to improve the skirt selectivity.

The initial height of the resonators, s_r, is selected between one quarter and one fifth of the waveguide housing. In this example we chose this value to be 2.1 mm. The starting value for the resonator's lengths is selected using dispersion diagrams, such as those in Fig. 4-3, so that the resonators are about half of the guided wavelength. Here we commence with L_r= 16 mm.

The starting dimensions for the geometrical features of the parallel couplings ($L_{1,2}$ and $s_{1,2}$) are obtained with the assistance of parametric curves such as those in Fig. 4-10 and Fig. 4-11. In particular from Fig. 4-10 we select the possible combinations of parallel coupling lengths, L, and distance, s, that yield the transmission zeros at the required frequencies. Subsequently, among the possible pairs of L and s for each pair, we select the one that produces the required coupling coefficient using Fig. 4-11. The series coupling and external quality factors are implemented in the usual way for E-plane filters [1],[19-20],[53-65]. This procedure yields a good starting value for the filter dimensions.

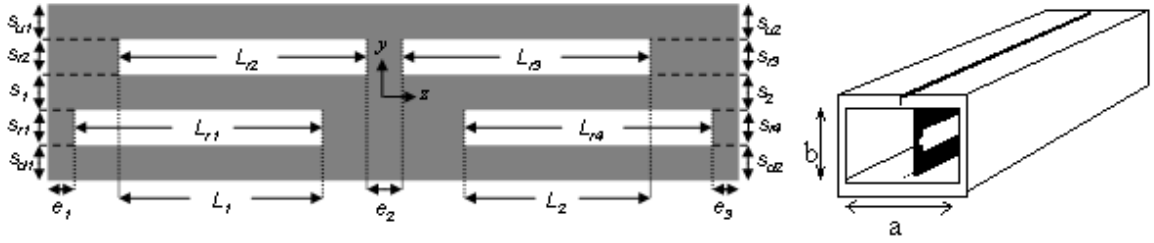

Fig. 4-17. Schematic of the fourth order filter including two parallel-coupled pairs of resonators.

In order to further improve the initial estimation, and therefore reduce the computational effort required for the optimisation, the procedure outlined in [74] can be employed. The resonators can be detuned by introducing a shorting septum halfway along their length. By shorting all the resonators but the first, the group delay of the reflection coefficient is numerically estimated and selected to match one of the prototype.

The procedure is repeated in stages by removing the next shorting septum and matching the group delay of the reflection coefficient. In Fig. 4-17a it is shown the matching level achieved after the first stage. For a filter of the 4th order, this procedure involves three steps, which are schematically depicted above the legend of Fig. 4-17b. Identically it is proceed for the remaining stages.

A final optimization step involves setting the septa length, e_3, and a small correction of the dimensions in order to achieve the performance of the filter described. The group delays numerically obtained for each stage are shown in Fig. 4.17b and match to a good approximation to those predicted for an in-line Chebyshev filter of the 4th order. The final dimensions of the filter as obtained from this procedure are: s_{r1}= s_{r2}= s_{r3}= s_{r4}= 2.1 mm, L_{r1}= 16.94 mm, L_{r2}= 17.32 mm, L_{r3}= 17.54 mm, L_{r4}= 17.00 mm, L_1= 10.62 mm, L_2= 9.47 mm, s_1= 2.18 mm, s_{u1}= 2.11 mm, s_{d1}= 2.11 mm, s_2= 1.92 mm, s_{u2}= 2.21 mm, s_{d2}= 2.27 mm, s_2= 1.48 mm, e_1= 0.83 mm, e_2= 7.28 mm, e_3= 0.85 mm.

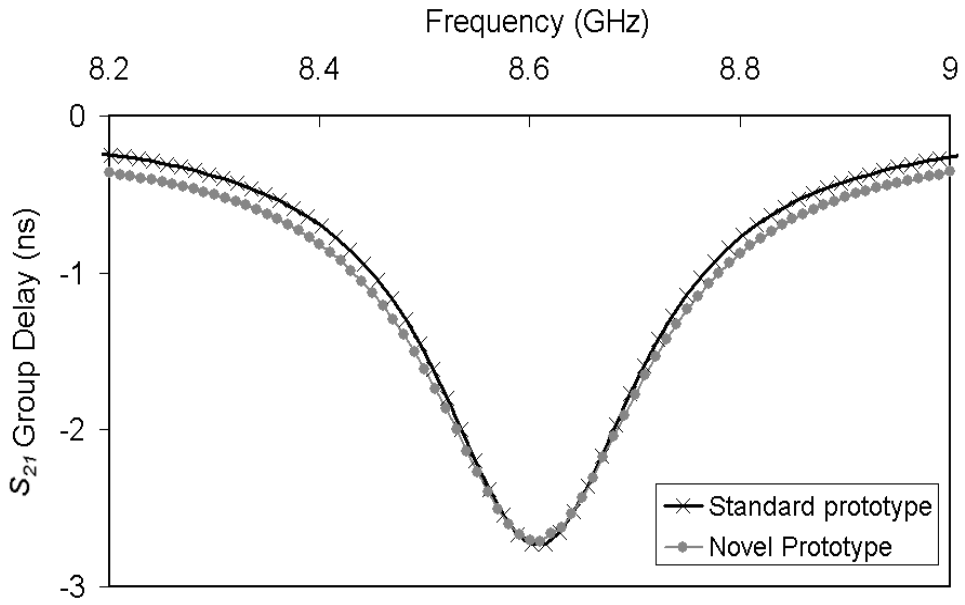

(a)

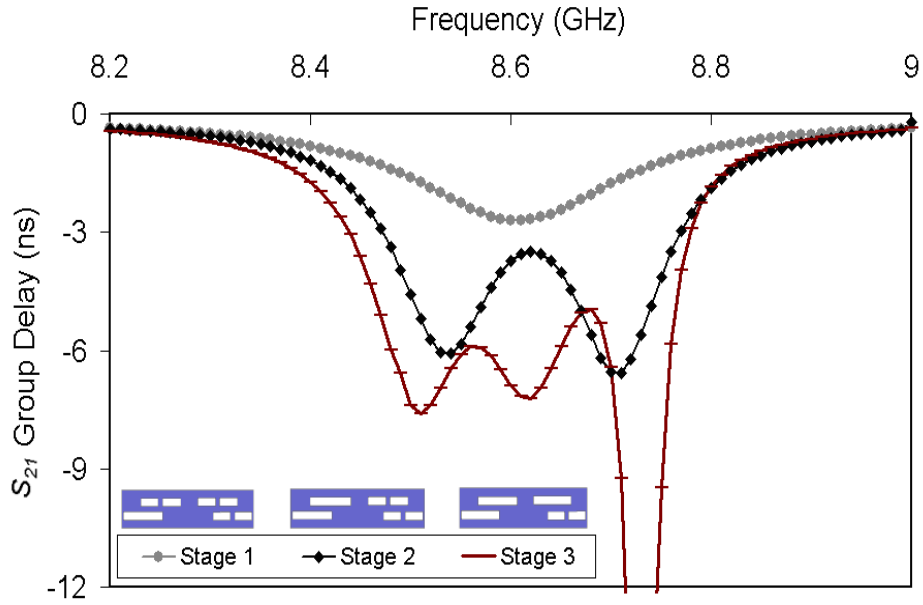

(b)

Fig. 4-18. Matching of the Group the delay of the transmission coefficient at stage 1 (a), here three of the resonators are shorted. Group delay of the reflection coefficient after optimisation for the three stages (b) of tuning the dimensions of the 4th order filter of Fig. 4.16 according to the procedure outlined in [74]. The layout of the E-plane insert for each stage is schematically depicted above the legend.

4.4.2 Numerical and experimental results

The simulated in-band and out-of-band response of the designed filter is shown in Fig. 4-18a. The reflection coefficient in the passband is below -20 dB. For comparison, the out-of-band response of a conventional E-plane filter that implements the same coupling matrix is also shown in Fig. 4-18a. The rejection at 8.3 GHz and 9 GHz is improved by about 30 dB as a result of the transmission zeros. Moreover the overall lengths for the proposed and the conventional filters are 57.64 and 108.41 mm respectively (see Fig. 4-19), meaning a 53% reduction for the proposed filter. In addition, the emergence of the spurious resonances is extended for about 1.5 GHz as a result of the asymmetric ridge waveguide dispersion. This value represents a 13% shift, which is similar to the normalized value of the prototype with wider WG section presented in Fig. 2-4. On the other hand, the narrow gap of the resonators results in increased ohmic losses. The predicted insertion loss in the passband for the proposed filter with a copper E-plane insert in aluminium waveguide housing as obtained with HFSS is of the order of -0.4 dB. For the conventional filter this reduces to -0.25 dB. However the latter would increase for a filter of higher order, which would be required to achieve skirt selectivity comparable to that of the proposed filter.

In order to validate the above, the designed filter has been fabricated and experimentally tested. A routing procedure was employed for the etching of a copper foil of thickness 100 μm. A photograph of the insert is shown in the inset of Fig. 4-18a. An aluminium split-block waveguide housing fabricated using traditional milling procedures was employed. The filter was tested and the simulated results are superimposed on Fig. 4-18b. Good agreement between the measured and simulated results is obtained. The measured losses in agree well with the simulations. The slightly higher measured losses are attributed to the roughness introduced during etching of the insert. Improved experimental performance can be achieved by photoetching and silver plating the metal insert.

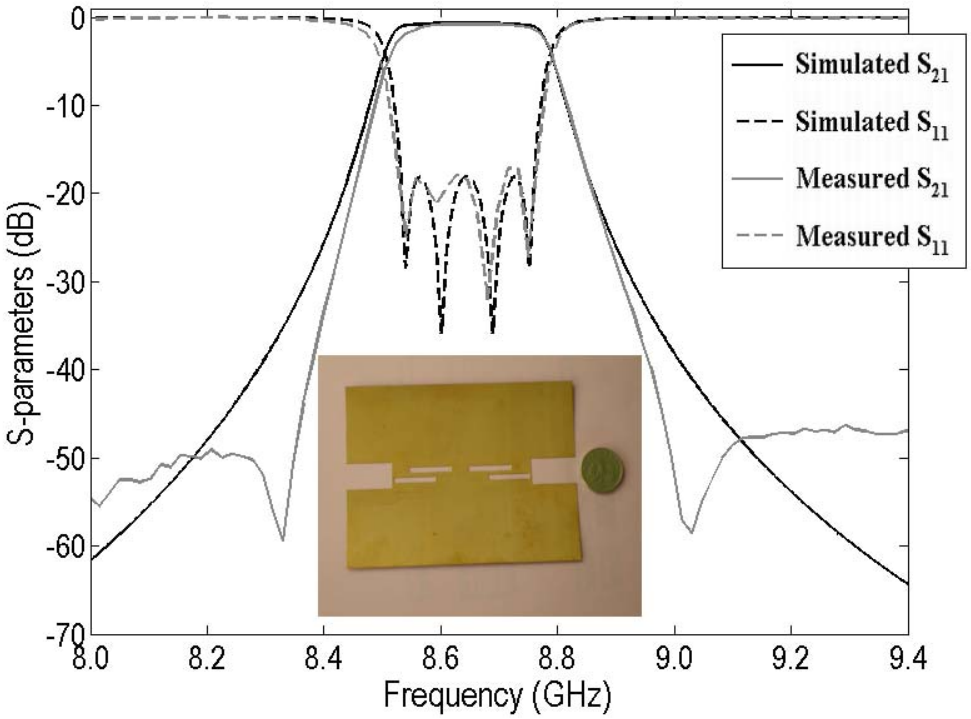

(a)

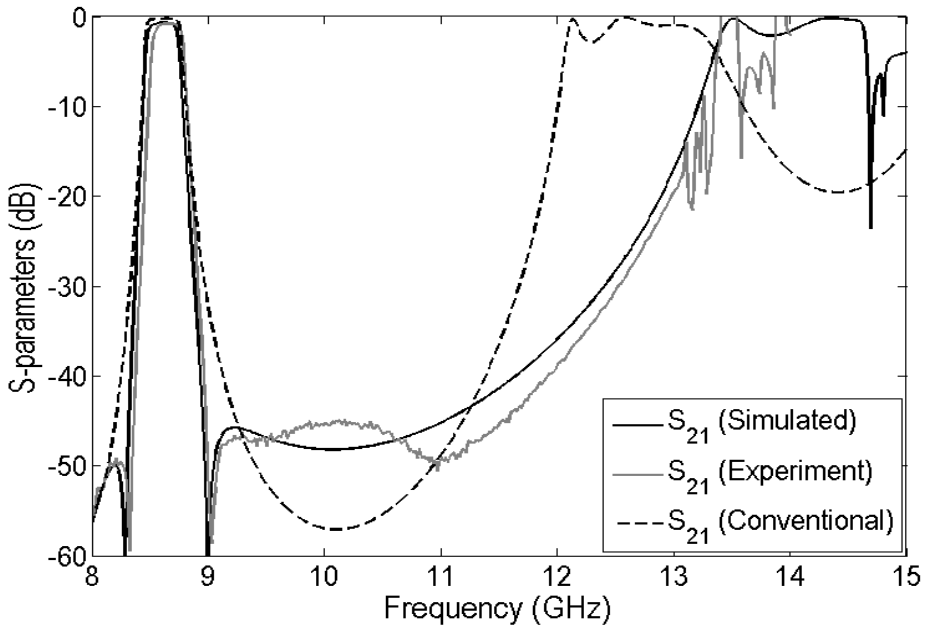

(b)

Fig. 4-19. Simulated and measured response in the passband (a). Simulated and measured out of band response as well as response of conventional E-plane filter implementing the same coupling matrix implementing the same bandwidth (b). The dimensions in mm are included in Table 4-2.

L_{r1}	L_{r2}	L_{r3}	L_{r4}	L_1	L_2	e_1	e_2	e_3	t
16.94	17.32	17.54	17	10.62	9.47	0.83	7.28	0.85	0.1
S_{r1}	S_{r2}	S_{r3}	S_{r4}	S_1	S_2	S_{u1}	S_{d1}	S_{u2}	S_{d2}
2.1	2.1	2.1	2.1	1.74	1.48	2.11	2.11	2.21	2.27

Table 4-2. Dimensions (in mm) of the designed 4th order filter (Fig. 4-16).

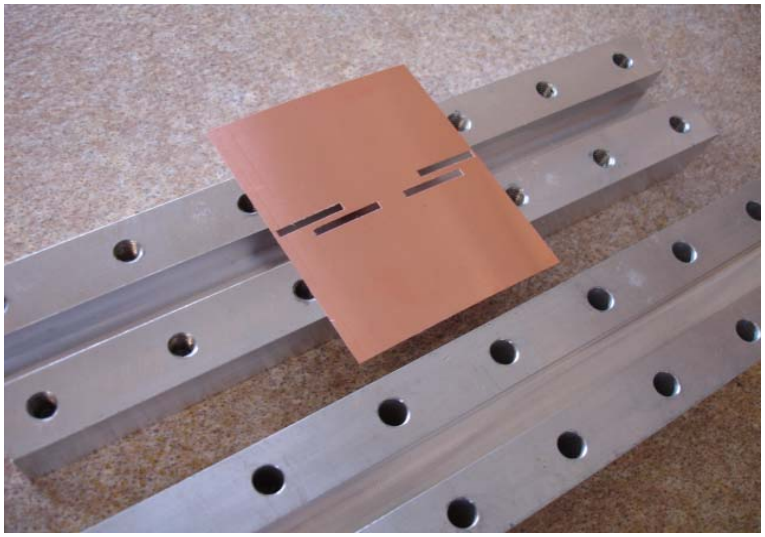

(a)

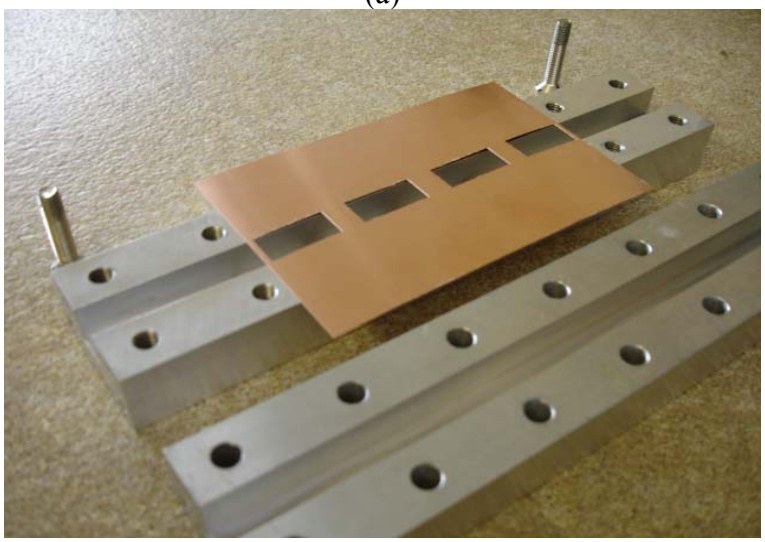

(b)

Fig. 4-20. Photograph of prototype fabricated prototypes. Dimensions as in Table 4-2. The total length of the bandpass filter with selectively located Transmission Zeros (a) is 57.64 mm, while the conventional prototype (b) used for comparison is 108.41 mm.

4.4.3 Tolerances analysis

In similar manner a study for the fourth order bandpass filter configuration presented in Fig 4-16 is shown in Fig 5-2. For the tolerance range study of the fourth order prototype the most sensitive parameters affecting the coupling are the vertical separation between resonators, the coupling lengths and the distance between the second and third resonator, $S_{1,2}$ and $L_{1,2}$ and e_2, respectively. Once again, random variations of ±50 μm for those parameters are considered.

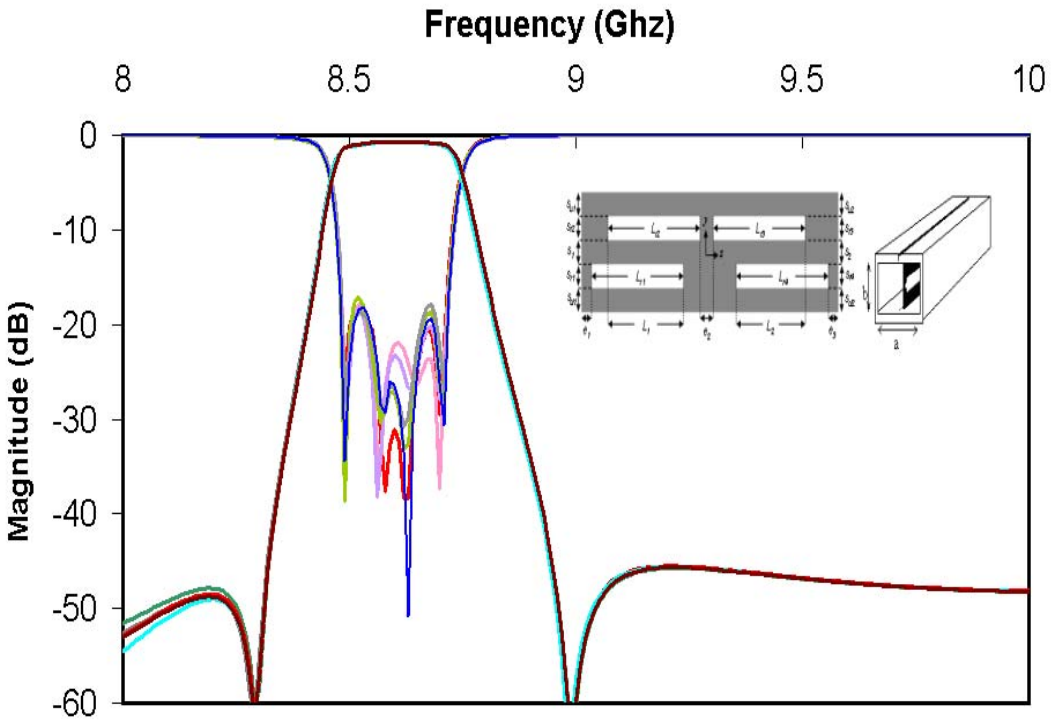

Fig. 4-21. Fabrication tolerance study of the fourth order bandpass filter prototype under random ±50 μm perturbation of coupling sensitive dimensions $S_{1,2}$ and $L_{1,2}$ and e_2 (other dimensions as reported in Fig. 4-18).

In essence the results show up to a good extend that at the opperating frequencies of the filter, fabrication tolerances of the milling procedure employed are within are within a reasonable range of sensitivity.

4.5 SUMMARY

In this chapter a new topology of E-plane filters compatible with the traditional low-cost single metal insert in a split-block housing topology has been proposed. The proposed filters consist of asymmetric ridge waveguide resonators coupled in series and in parallel. By means of equivalent circuits as well as full-wave simulations it was demonstrated in first place that the parallel coupling of the resonators can introduce a selectively located transmission zero provided a realisation of a predetermined coupling coefficient. An efficient synthesis procedure method has been outlined and the concept has been demostrated by means of examples. Second and fourth order prototypes have been fabricated and tested. In summary it has been shown that improved out-of-band rejection can be achieved by virtue of the transmission zeros, significantly reducing the total size, in a trade-off involving small increment of the insertion loss in the passband.

CHAPTER 5

Quality Factor Assessment of an Uniform Resonator and of a Periodically Loaded Resonator

5.1 INTRODUCTION

E-Plane filters have been preferred solutions due to their manufacturing simplicity. A favourable feature is the performance reliability in conjunction with the compatibility with low-cost fabrication techniques (e.g. photolithographic processes). This chapter examines several realisation considerations for the proposed E-plane filter topologies. The following sections include studies intended to clarify the limitations of the technology, but also highlight some directions towards the performance optimisation of future filter realisations. In particular, the following aspects are being investigated:

- Q factor assessment- Passband insertion loss improvement and its limits.
- Miniaturization- Further size reduction by periodically loaded resonators.

Analysis of the limitations as well as suggestions for the enhancement of the technology is addressed in section 5.3. The Quality factor assessment of the E-plane ridge waveguide resonator is obtained for different heights of the ridges. The objective of that study is to evaluate the limitations in the performance of future filter realizations in terms of passband losses. Studies on the finite conductivity of the printed circuit and mounted waveguide as well as finite thickness of the insert are presented.

Section 5.4 is devoted to discuss the final size of the filter. Athough the parallel coupled resonators topology has already demonstrated a size reduction of over 50% when compared with those standard filter of similar requirements, some elements to achieve even further final size reduction are presented in section 5.4. The idea is defended presenting in similar manner as in section 5.3, the Q factor assessment of a periodically loaded resonator. Numerical and experimental results are included to quantify those improvements can be achieved.

5.2 QUALITY FACTOR OF A WAVEGUIDE RESONATOR ANALYSIS

The quality factor of a resonant system is in general defined as the average energy stored per period of oscillation over the energy loss per second [85]. For a resonator in isolation, energy loss comes solely through thermal dissipation and this case corresponds to the unloaded quality factor definition, Q_U [85]. A resonator that is excited externally is invariably coupled to other circuitry. As a result some power exchange with the external circuitry occurs and the overall quality factor, or loaded Q, Q_L, is in practice reduced compared to Q_U. For reasonably narrowband resonators it can be shown that the loaded and unloaded quality factors, Q_L and Q_U, are given by:

$$Q_L = \frac{\omega_0}{\Delta\omega_{3dB}} \quad \textbf{(5-1)}$$

$$Q_U = \frac{Q_L}{1 - 10^{-\frac{S_{21}(dB)}{20}}} \quad \textbf{(5-2)}$$

Where ω_0 and $\Delta\omega_{3dB}$ are the resonant frequency and the 3dB bandwidth of the resonator respectively. $S_{21}(dB)$ is the insertion loss at ω_0.

The following analysis provides a characterisation of the Quality factor of the proposed filter resonators, and evaluates routes to design filter prototypes which resonators carry higher Q and hence are optimal to design filters with improved performance like suitable for higher fractional bandwidths and/or with reduced insertion loss in the bandwidth.

The heigth of a waveguide resonator was reported in [20] to be directly related with its quality factor. In particular the following study quantifies how much is the ratio of the Loaded and Unloaded Q when varying s.

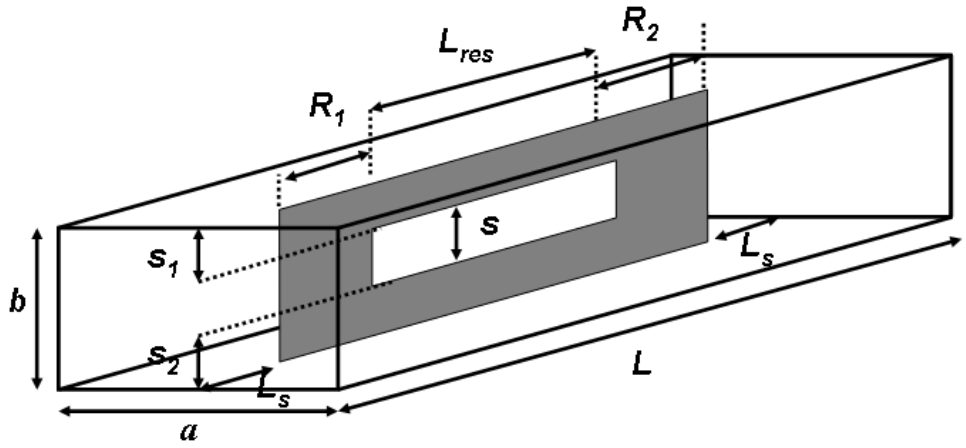

Fig. 5-1. Schematic of the one resonator configuration employed to extract the quality factor.

The study commences by modeling the resonator filter scheme of Fig. 5-3, using a full-wave commercial simulation software. Varying the height of the resonator from s=1.2 mm to s=10.16mm (no ridges) the resonant frequencies for a set of resonator height s, are produced, those are superimposed and depicted in Fig. 5-4. It should be noted that the study includes the value of s=2.1mm, which is the height corresponding the resonators involved in the passband filter prototypes designed in the previous chapter.

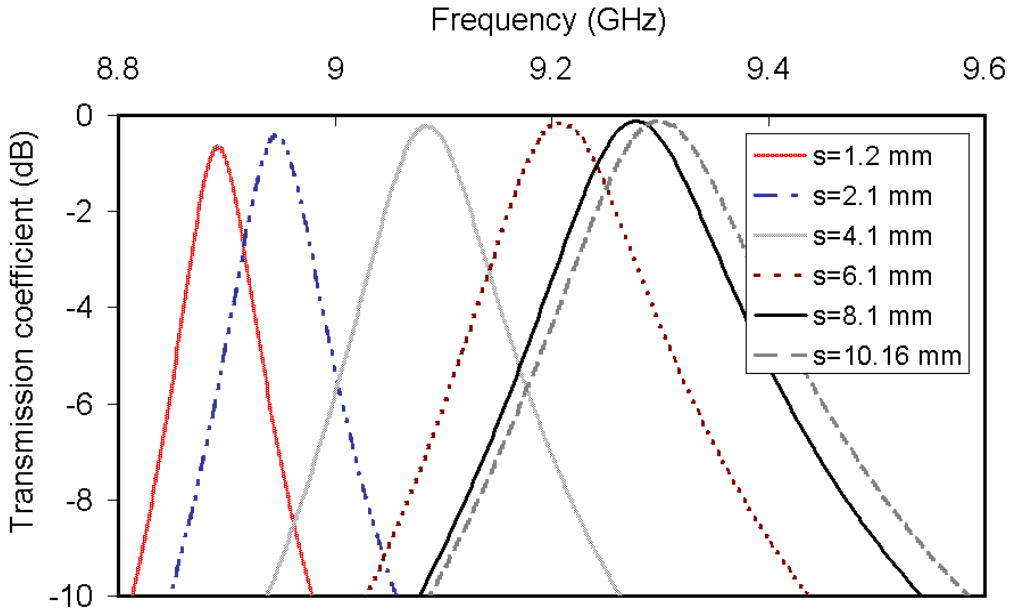

Fig. 5-2. Resonant frequencies obtained for varying the resonator height. Dimensions (in mm): a=22.86, b=10.16, L_{res}=16, L_s=10; s=var, s_1= s_2= var. The thickness of the insert is 100 μm.

From the results obtained, therefore the loaded and unloaded Q can be easily extracted applying the corresponding values on equations (5-1) and (5-2). The Q factor assessment is shown in Fig. 5-5, where it can be seen how much the Unloaded Quality factor increases in terms of the resonator height. The passband filter prototypes designed in chapter 4 were initially designed from resonators of 2.1 mm height for which the unloaded Q is about 2500. Fig. 4-11 and Fig. 4-12 demonstrate similar filter requirements can be satisfied starting from resonators of longer heights, that is, identical operating frequency, level of coupling and location of Transmission Zeros. For a resonator of height equal 4 mm, the associated Unloaded Q can be increased up to 3200, which represent a 30% increment. As the insertion loss is inversely proportional to the resonator unloaded Q that would effectively lead to improve the passband limitations and hence further realizations can be suitable for higher performance requirements.

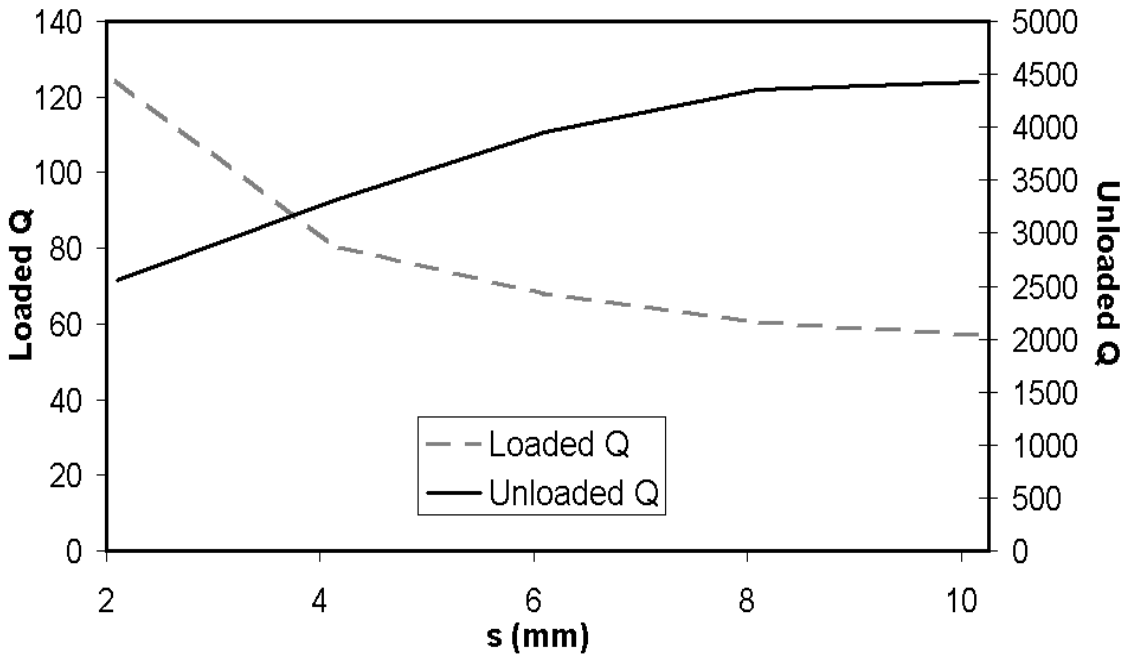

Fig. 5-3. Loaded and Unloaded Q in terms of the physical height of the resonator. Dimensions as in Fig. 5-4.

5.2.1 Asymmetrically positioned resonator

The previous study is based on a resonator of identical size to those from the prototypes design (varying s) symmetrically located in the waveguide housing; however in the parallel coupling scheme the resonators are not etched in the centre. The purpose of the following study is to demonstrate that shifting slightly from the centre a resonator (maintaining other dimensions identical) the associated Unloaded Quality factor of the resonator is not substantially affected.

Fig. 5-6 shows that the Unloaded Q of a resonator centred (d=0) is approximately equal (2500) to a resonator of identical dimensions shifted 2mm from the centre (d=2mm corresponding to the position of the prototypes optimized in Chapter). Suggesting the Quality factor analysis from section 5-3, and further conclusions, are essentially valid for the particular case of those resonators etched slighly shifted from the centre.

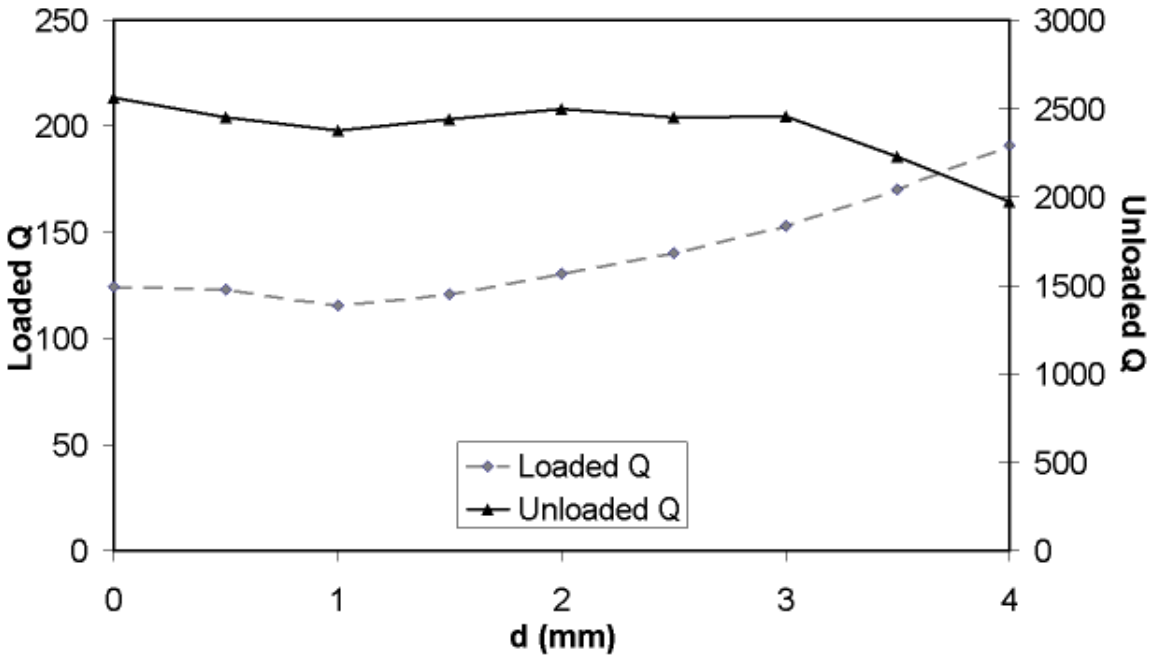

Fig. 5-4. Loaded and unloaded Q considering a resonator asymetrically etched. Dimensions: a=22.86, b=10.16, L_{res}=16, L_s=10; s=2.1, s_1= b-s-s_2-d. Prototypes about 2 mm shifted from the centre. Other dimensions as in Fig. 5-2.

5.2.2 Variation with the conductivity of the metal insert

The insertion loss in the passband of the filters can be improved by using inserts made of metals with higher finite conductivity. Fig. 5-9 shows the comparison of the Unloaded Q for a copper insert (the one it was employed for the fabrication) and silver. The Unloaded Q is increased from 2500 to 2600 for a resonator of the dimensions employed in the filter prototypes (s=2.1mm). However the increment is bigger in the scenario where resonators are of larger physical height. A resonator of 6mm etched in silver has an unloaded Q of 4200 compared to less than 4000 of the one etched in copper, since the conductivity of silver is better than the one of copper by a factor of about 1.057.

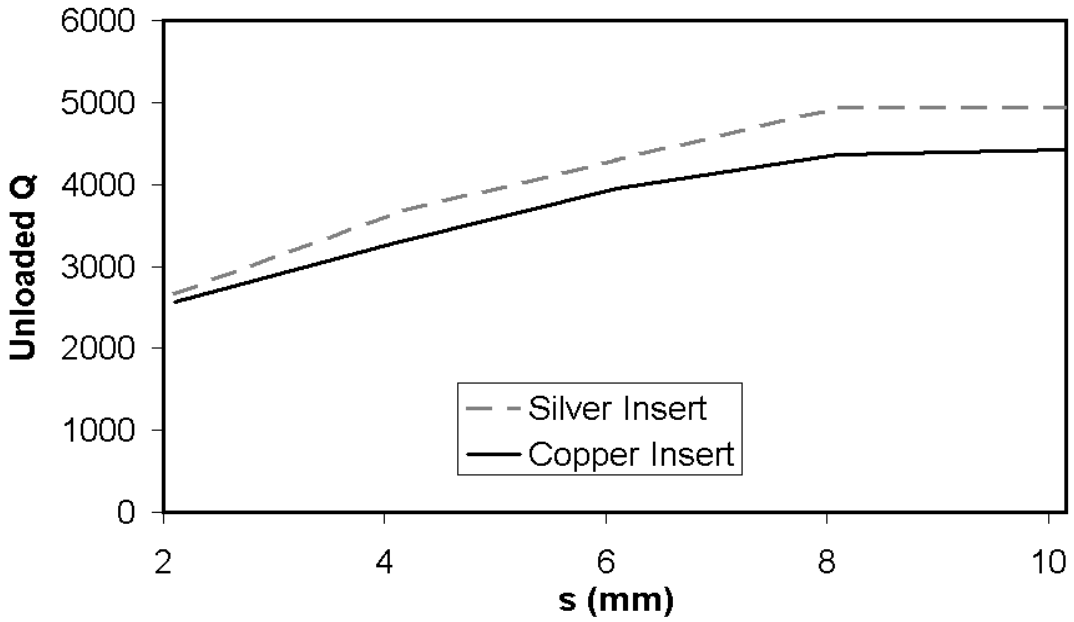

Fig. 5-5. Comparison of the Unloaded Q for two different metal insert: copper (employed in the fabrication of the prototypes) and silver. Dimensions as in Fig. 5-4.

5.2.3 Variation with the thickness of the insert

In similar manner it is interesting to see the effect of the thickness on the Unloaded Q. By increasing the thickness of the fabricated prototypes from 100 μm up to 4 mm the Unloaded Q is significantly decreased. This can be due to the fact in the thin metallic

septum the electromagnetic fields penetrate into the coupling region left and right from the septum and hence increases the electrical length significantly rather than for wider thicknesses. Hence it is justified the original thickness as optimal.

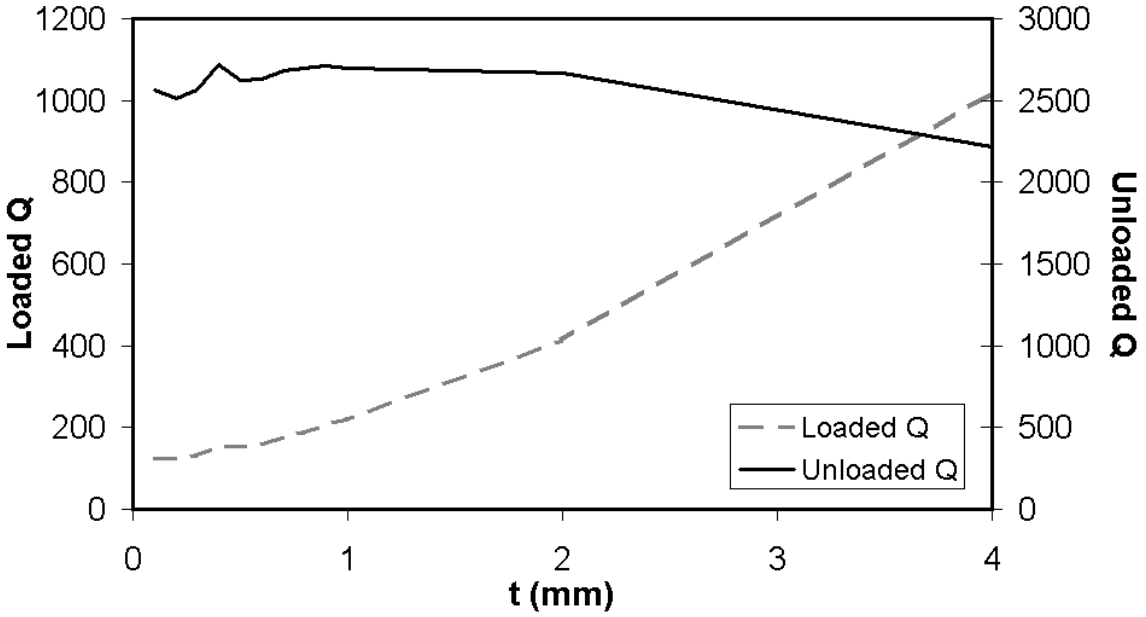

Fig. 5-6. Loaded and unloaded Q varying t. Dimensions: a=22.86, b=10.16, L_{res}=16, L_s=10; s=2.1, , s_1= s_2= 4.03. Thickness variable. Other dimensions as in Fig. 5-4.

5.3 SIZE REDUCTION FOR THE PERIODICALLY LOADED RESONATOR

The idea to achieve further reduction of the waveguide resonator length and hence the final filter size is based on the elements reported in [17]. Here the quality factor of microwave resonators miniaturized by virtue of periodic loading is assessed. A total of five X-band resonators in E-plane design with different miniaturization factors have been designed to resonate at approximately the same frequency.

The loaded quality factor is extracted from the fractional bandwidth and subsequently employed to estimate the unloaded quality factor. The study reveals that the unloaded quality factor drops approximately linearly with the miniaturization. Those results can be

useful to asses further size reduction in the filter configurations previously reported. Full wave simulated and experimental results are presented to validate the study.

5.3.1 Periodically loaded waveguides

Periodically loaded E-plane waveguides have in the past been employed for the realisation of bandpass filters with miniaturized resonators [17, 77] and integrated lowpass-bandpass filters with improved stopband performance [24]. Miniaturization of resonators is achieved by virtue of the slow-wave effect, according to which the phase velocity and the guided wavelength of the slow wave are significantly reduced relative to those of a wave propagating in a comparable homogeneous line.

The miniaturization factor of a periodically loaded transmission line typically depends on the periodicity as well as the internal geometry of each unit cell, that was demonstrated for periodically loaded E-plane waveguides in [17]. Slow-wave regions in periodic transmission lines are typically separated by electromagnetic band gaps, which are exploited to produce the lowpass response in the case of E-plane filters [17, 77]. In [17] it was demonstrated that transmission zeros emerge in the bandgap due to the resonant nature of the periodic loading.

Despite such favorable characteristics, propagation in periodic structures is associated with increased thermal losses. This deteriorates the quality factor of miniaturized periodically loaded resonators, which reflects in higher insertion loss and poorer selectivity in filters of higher order. The trade-off between miniaturization and quality factor is general in microwave resonators beyond periodically loaded ones (e.g. dielectric filling, step impedance resonators etc.). This in turn poses the requirement for a quantitative assessment between the miniaturization and the quality factors. For the case of periodically loaded E-plane resonators, such an assessment has yet to appear.

A thorough investigation of the quality factor for periodically loaded resonators with different miniaturization factors is presented. Those elements are considered of practical interest for the design of filter applications involving demanding Quality factor and physical size considerations. Using numerical and experimental results, we draw design curves that quantify the trade-off between miniaturization and unloaded quality factor.

5.3.2 Unloaded Q assessment

In order to compare the quality factors for periodically loaded resonators, we have designed a series of four periodically loaded E-plane resonators and one uniform E-plane resonator all resonant at the same frequency. The realization is based on the all metal insert split-block housing E-plane topology [18], which is compatible with traditional printing techniques. A schematic layout of the resonator geometry is shown in Fig. 5-12. The ridge waveguide loads behave as series LC loads [17]. The operation of the periodic E-plane resonator is typically below the resonant frequency of the LC loads. By reducing the gap, s, the guided wavelength shrinks so that if all other dimensions remain constant, the resonant frequency would drop.

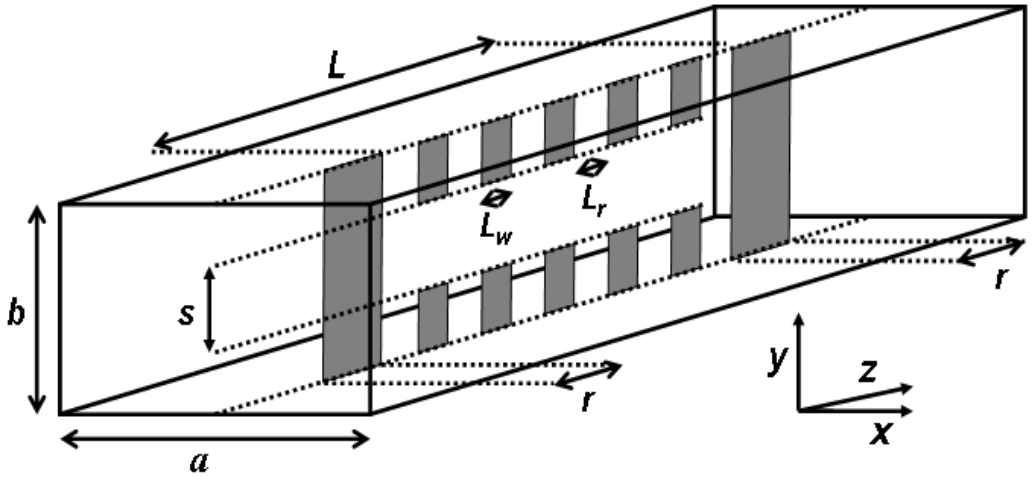

Fig. 5-7. Layout of the periodically loaded waveguide housing resonator

5.3.2.1 Numerical and experimental results

In order to maintain the resonant frequency at a fixed value, for every lower value of the gap, s, we also reduce the separation L_2. The commercial FEM software tool is used for the numerical optimization of the pairs (G, L_2) in order to produce 5 resonators all at the same central frequency. Loaded and Unloaded Q are extracted from equations (5-1) and (5-2). A homogeneous resonator (where s= b) was designed also using HFSS. In all cases the input and output coupling septa were fixed at r=5mm. The thickness of the metal insert is

assumed to be 100μm for all resonators. The transverse dimensions of all six resonators are given in Table 5-1.

	s= 1 mm	**s= 3 mm**	**s= 5 mm**	**s= 7 mm**	**s=b= 10.16 mm**
L_w (mm)	1	1	1	1	n/a
L_r (mm)	0.5	1.31	1.9	2.25	n/a
L (mm)	8	12.86	16.4	18.5	19.52
Miniaturisation (L/19.52 %)	41%	66%	84%	95%	100%
Q_U (exp)	632	1537	2553	3001	3465

Table 5-1. Dimensions of periodic waveguide resonators structures depicted in Fig. 5-9. All resonant at the same frequency of 8.82 GHz.

The simulated transmission coefficient for all resonators of Table 5-1 is shown in Fig. 5.10. The resonant frequency is approximately 8.82 GHz in all cases. In the simulation, the metal insert is assumed to be made of copper and the waveguide housing of aluminium. As shown, the 3dB fractional bandwidth and the minimum insertion loss increases for more miniaturized designs. In order to quantify the increase of the fractional bandwidth, Fig. 5.11a shows the loaded quality factor, Q_L, as calculated from the responses of Fig. 5-10 and using equation (5-1). Fig. 5.11b shows the estimated unloaded quality factor as calculated from equation (5-2). In both graphs the quality factors are plotted against the length of the resonator, L, normalized to the length of the homogeneous resonator with s= b.

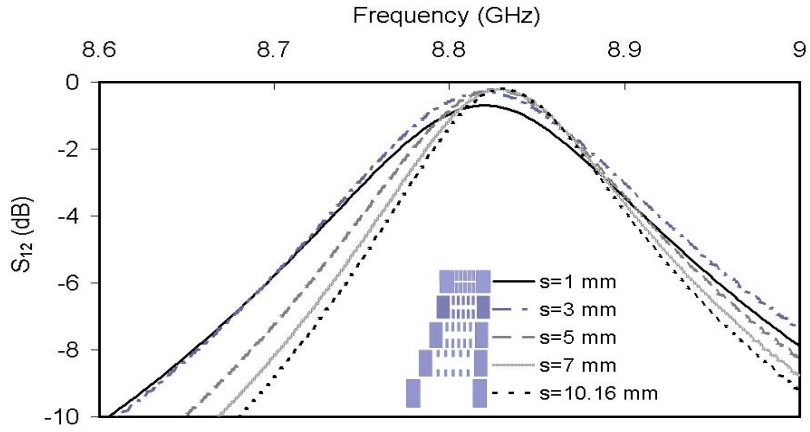

Fig. 5-8. Simulated insertion loss of the 5 prototypes with dimensions as in table 5-1.

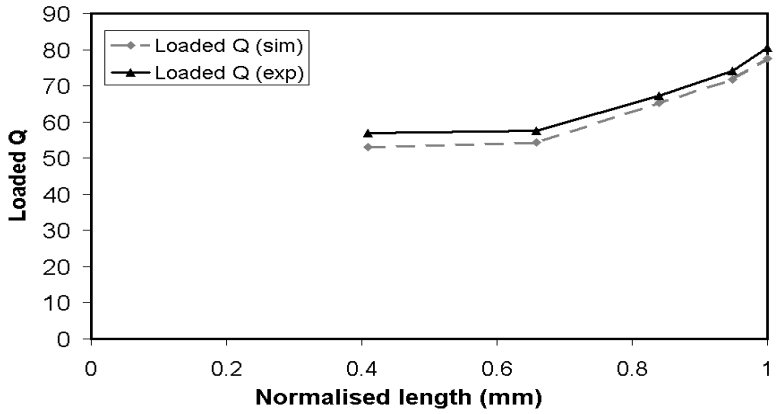

(a)

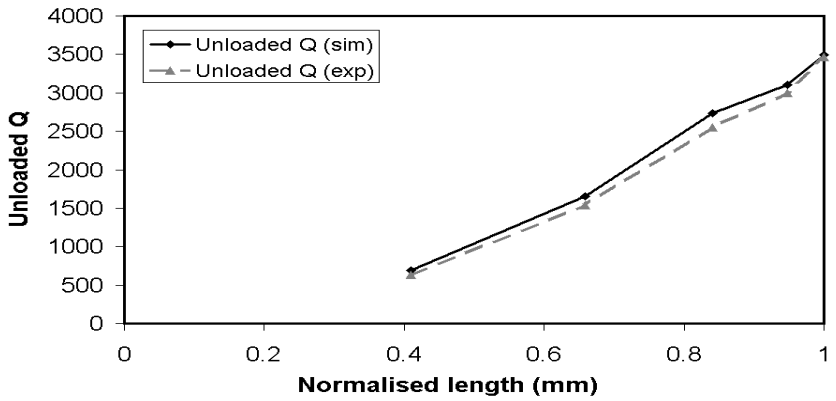

(b)

Fig. 5-9. Simulated and measured (a) Loaded and (b) Unloaded Quality factors for the resonators of Table 5-1.

As shown in Fig. 5-11b, the unloaded quality factor reduces approximately linearly with the normalized resonator length. The loaded quality factor, Q_L, depicted in Fig. 5-11a is about one order of magnitude reduced compared to the unloaded quality factor, Q_U. This is attributed to the power exchange between the resonator and the input and output port, which is determined by the reflectivity of the coupling discontinuity. Longer coupling septa, *r*, produce more weakly coupled resonators that correspond to higher loaded quality factors.

In order to validate the above, the designed resonators have been fabricated and experimentally tested. A routing procedure was employed for the etching of a copper foil of thickness 100 μm. A split-block waveguide housing milled in aluminium was employed. A photograph of the prototypes is shown in Fig. 5-13. The resonators were experimentally measured and the experimentally determined loaded and unloaded quality factors are superimposed in Fig. 5-11. Good agreement is observed between the simulated and measured results. This suggests that the despite the rough edges on the copper insert as a result of the routing procedure, the quality factor is not significantly deteriorated. Fig. 5-11b provides a useful guide for the designer, in order to predict the insertion loss of a higher order filter based on the degree of miniaturisation.

Fig. 5-10. Photograph of the HP8510 vector network analyser employed.

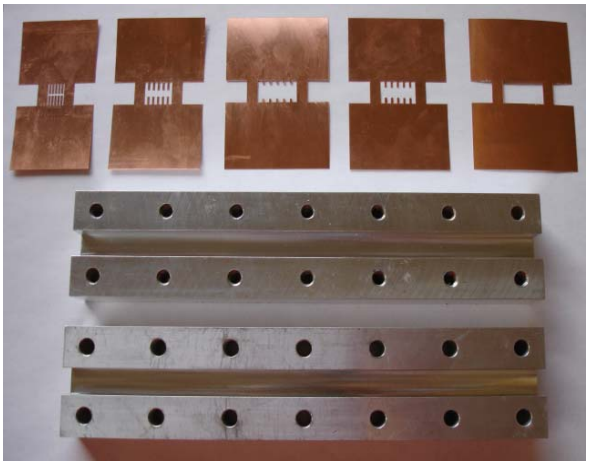

Fig. 5-11. Photograph of the periodically loaded resonators fabricated by etching.

5.4 SUMMARY

In conclusion, reliability of low cost fabrication has been demonstrated and two new ideas in order to improve the performance of further realizations have been outlined. The first one intended to achieve reduction of insertion losses in the passband by introducing resonators with higher Unloaded Q: that is demonstrated for resonators of higher heights, also considering metal inserts of higher finite conductivity than the copper one employed. The second idea proposed outlined how to achieve filters with even further size reduction: numerical and experimental results demonstrate the assessment of miniaturization of the resonator by introducing loads not deteriorating significantly the Unloaded Q of the resonator. In summary those elements offer potential solutions for narrowband filter realizations keeping the advantages of those designs presented in Chapter 4 but making them suitable for more strict requirements.

CHAPTER 6

Further In-Line Filter Applications

6.1 INTRODUCTION

The main motivation which entailed to the full characterization of the Ridge Coaxial waveguide (RCWG) stemed from the potential passband filter applications devised in filters with coupled resonators [87-92]. The property of strongly dispersive coupling which introduces a transmission zero exhibited in parallel-coupled asymmetric ridge waveguides has been demonstrated useful for bandpass filter applications. However, the extent of the electromagnetic analysis performed on that structure can be of benefit to investigate other devices beyond the bandpass filters originally intended.

The present chapter is devoted to describe a couple of novel applications derived from the reported properties of parallel-coupled asymmetric ridge waveguides. The first one comprises the realization of bandstop and dual bandstop filters. The concept is based on similar elements (strongly dispersive parallel-coupled asymmetric ridge waveguides introducing transmission zeros), however the configuration does not involve pairs of resonators coupled in parallel but a resonator and a slot line, which effectively means a reaction type resonators producing coupled full reflexion points. The configuration presented allows to design two sets of reaction type resonators quasi independently coupled. This property is exploited to design a novel type of dual bandstop filters. Practical realizations with numerical and experimental results are presented for validation.

In a second part of the Chapter, the possibility to apply that strongly dispersive coupling property of parallel-coupled asymmetric ridge waveguides is investigated for a novel label-free chemical/biochemical sensing device. In particular, efforts are directed towards a microwave chemical/biochemical sensing device for the characterization and detection of cells in chemical substances and cells in solution in micro-litre volumes. Design guidelines

of the prototype, fabrication of the microfluidic network and microwave resonator are described throughout section 6.3. Initial testing of the prototype at X-band is examined with promising results. In the last stage, 6.3.4, is proposed a Low Temperature Co-fired Ceramic (LTCC) integration scheme for the miniaturization of the device to be used in the THz regime.

6.2 BANDSTOP FILTERS

Over the last years high performance single and dual-band bandstop filters have aroused the dedication of researchers [2],[87-92]. That is due to these structures can meet the requirements application main reason of that increased interest is due to the important role to play of those filters in the design of telecommunication and broadcast system mainly to prevent interference with unwanted bands.

The recently proposed configurations include a variety of realizations involving waveguide cavities [86], Low-temperature-cofired ceramic (LTCC) [87], and microstrip filters [88-92]. However realizations of dual-band stopband Filters in E-Plane technology have not been reported in the literature. As it was introduced in Chapter 2.2.3 it is possible to use a resonant slot parallel to the input line to create a reaction type resonator. In this case the network of this filter involves series connection of an inductive and capacitive element in shunt with the transmission line and produces a selectively located transmission zero.

From the realization presented in [29] the possibility to extend the filter concept to higher orders is investigated. Those configurations would be based on increasing the number of coupled resonant slots parallel to the input line. In this manner single and dual stopband filters can be produced. In chapter 6.2 is described the design guidelines for higher order stopband filters.

Practical realization will be demonstrated with numerical and experimental results by means of a third order prototype. Chapter 6.3 includes a novel configuration towards dual stopband filters where rejection bands can be designed quasi independently. Also a practical example will validate the practical realization. As pointed out in [28] the difficulty

to find out equivalent electrical circuit realization for E-Plane stopband Filters is the reason why their presence in the literature being limited. The configuration presented in reference [29] may not be satisfactory for applications where the skirt selectivity of stopband is stringent. Over the next sections the design of higher order prototypes will be described.

First in section 6.2.1 the electrical equivalent circuit is described. In section 6.2.2 is shown how the resonances produced by the pair of resonators can be easily controlled to design higher order filter. The last step is to choose a convenient transition structure in order to optimize the transmission in the passband of the filter. That together with the numerical and experimental results of a third order bandstop prototype is included in section 6.2.3 to validate the configuration

6.2.1 Single stopband realizations

Among the few number of bandstop filter realizations reported in section 2.2.3 is a matter of attention in this section the configuration depicted in Fig 6-1 and presented in [29]. This configuration creates a reaction-type resonator by placing a resonant slot parallel to the input finline.

Schematic of this configuration is shown in Fig. 6-1 together with the transmission response obtained when varying the length of the resonator. The synthesis of the bandstop filter is based on those waveguide sections employed to implement the bandpass filters of chapter 4. As described in section 4.2.2, a ridge coaxial waveguide with outer dimensions a= 22.86 mm and b= 10.16 mm, supports two modes within the frequency of interest, X-band. Those modes are the fundamental TE_1, which corresponds with lowest cutoff frequency and the TEM mode with zero cutoff frequency.

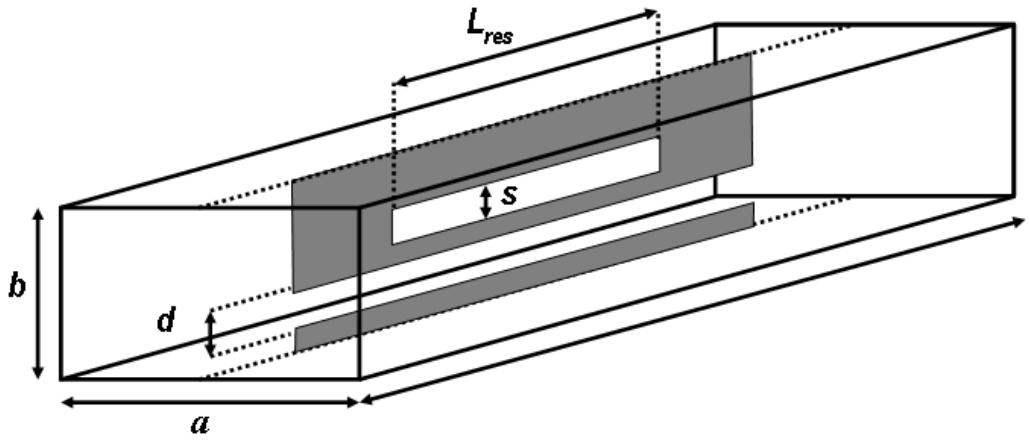

(a)

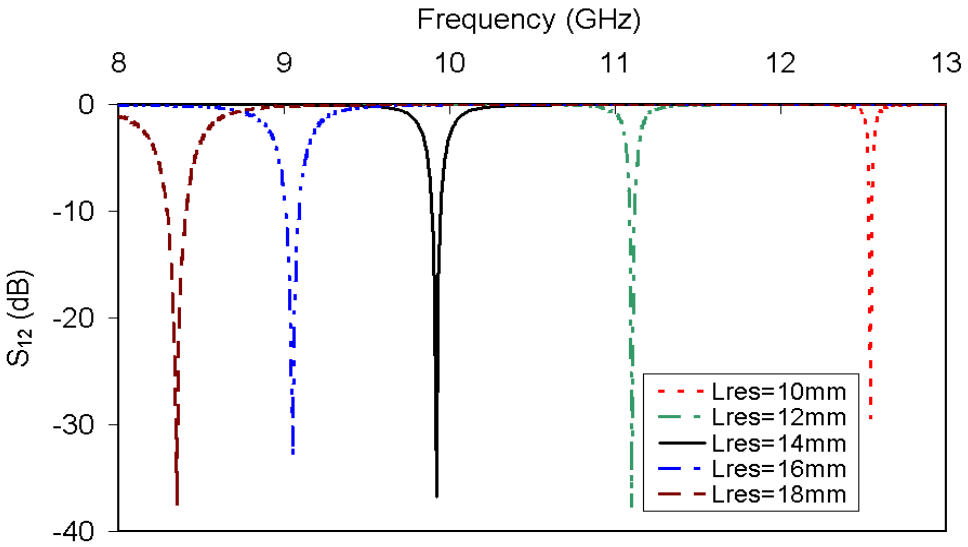

(b)

Fig. 6-1. Reaction type resonator schematic (a) and transmission response modifying the physical length of the resonator (b).

The filter realization involves a Ridge coaxial waveguide with a single ridge. The effect of that ridge on the dispersion and Impedance is show in Fig. 6-2.

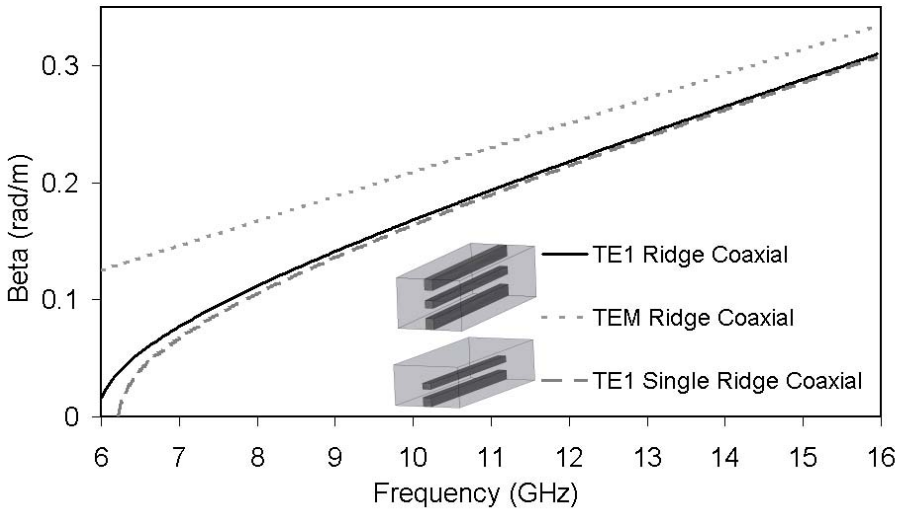

Fig. 6-2. Dispersion the TE1 mode of the single ridge coaxial waveguide with dimensions (in mm) a=22.86, b=10.16, s_1=2.1, s_u=2.23, t=0.1. The dispersion and characteristic impedance of the doble ridge coaxial waveguide that emerges with s_2=2.1 is also superimposed

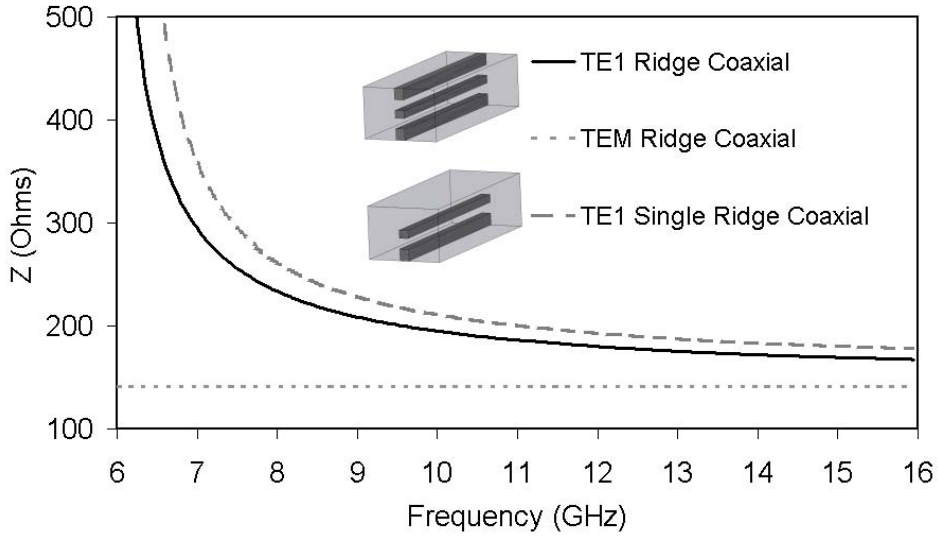

Fig. 6-3. Characteristic Impedance of the TE1 mode of the single ridge coaxial waveguide with dimensions (in mm) a=22.86, b=10.16, s_1=2.1, s_u=2.23, t=0.1. The dispersion and characteristic impedance of the doble ridge coaxial waveguide that emerges with s_2=2.1 is also superimposed

6.2.1.1 Modeling of coupled resonances

In order to show how easily the coupled resonances of higher order filters can be modeled to design stopband filters a structure involving two coupled resonators is considered (Fig. 6-4). The pair of electrically coupled resonators parallel to the input line produce a pair of coupled resonances. The separation of the split resonances depends on the strength of the coupling between the resonators. This is demonstrated in Fig. 6-5 for an example with h=4 mm; d= 6.16 mm; e= 10 mm; L_{res}= 14 mm; while Ls is varied.

As shown, by increasing (decreasing) the separation, Ls, the stopband becomes more narrow (wide). This is attributed to the lower (higher) coupling between the resonators. For a finite number of synchronously tuned resonators, a higher number of coupled resonances appear.

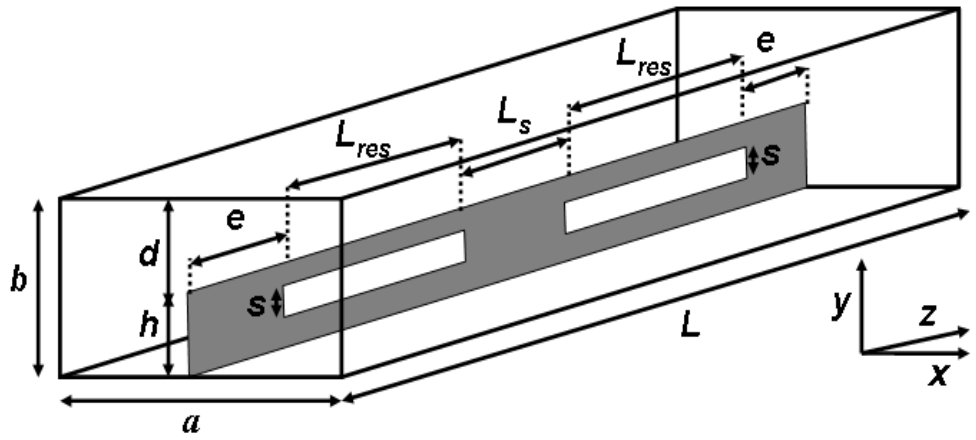

Fig. 6-4. Schematic of the bandstop filter.

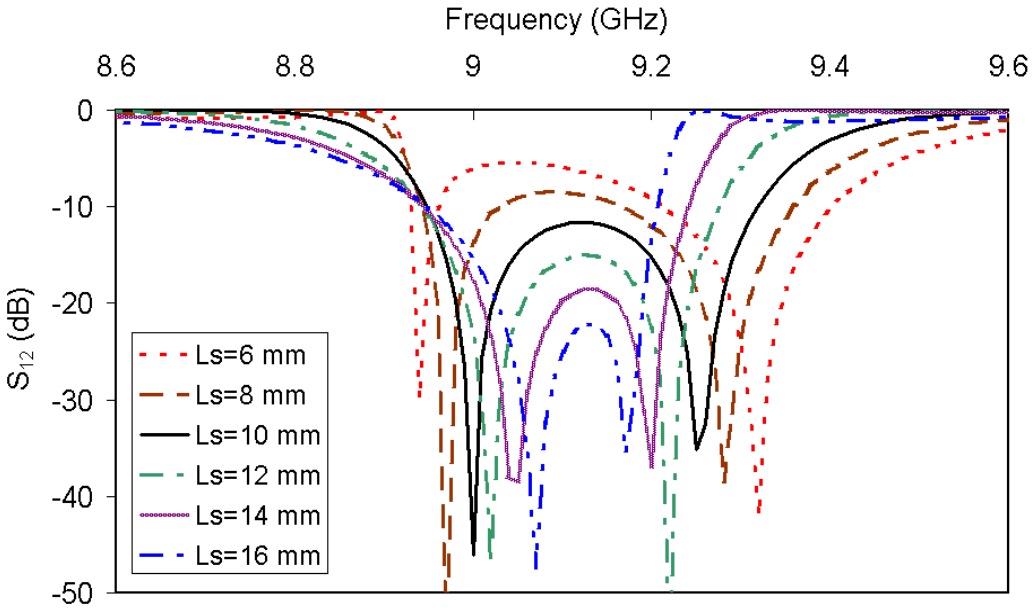

(a)

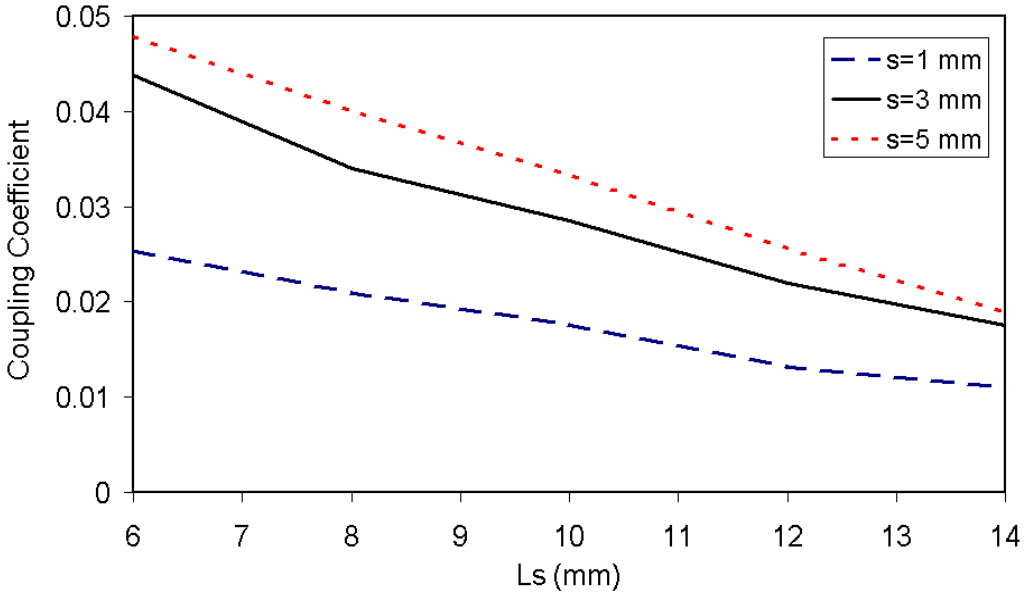

Fig. 6-5. Transmission coefficient for the two coupled reaction type resonators depicted in Fig. 6.4 obtained varying Ls (a) and coupling coefficient for three different values of s. Dimensions (in mm) h=4; d=6.16; varying L_s=10; L_{res}=16; All resonators height is s=2mm (a) and variable (b) and they are etched centered in the inset over y.

6.2.1.2 Single Bandstop filters

In this section first we demonstrate an example involving the design of a single bandstop filter based on three coupled resonators parallel to the input line. From the empirical elements described in the previous section different transitions to optimized the final response of the pursued filter (higher transmission as possible in the passband) have been considered. A shape of the form of a semi-ellipsoid offered better results. So on, in order to taper the asymmetric ridge waveguide (input and output port in Fig. 6-4) to the input and output rectangular waveguide ports, we employ a section of an ellipse.

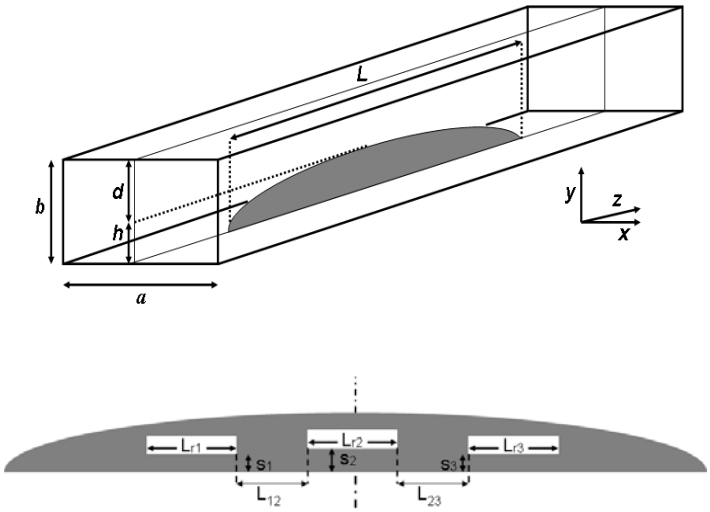

Fig. 6-6. Schematic layout of the bandstop filter.

Simulation results based for the structure shown in Fig. 6-6 (top) on full wave commercial software yield an insertion loss (S_{12}) in the X-band lower than 0.05 dB. The major radius of the semi-ellipsoid is 2.5mm, while ratio is 21; L=150 mm. For the single band design, three resonators are etched in this inset, as shown in Fig. 3 (bottom). The dimensions (in mm) are given in Table 6-1..

The simulated stopband of the prototype is of about 150 MHz and is centred approximately at 11GHz. This is shown in Fig. 6-7. About 20 dB rejection in the stopband is obtained. The

transmission levels outside the stopband and between 8 and 14 GHz are always less than 0.1 dB. The resonant frequency can be controlled by adjusting the lengths of the resonators.

In order to validate the above, the designed filter has been fabricated and experimentally tested. A routing procedure was employed for the etching of a copper foil of thickness 100 μm. The prototype was tested with an HP8510 vector network analyser, using commercial X-band flanges. A photograph of the inset mounted in a machined aluminium waveguide housing is shown in Fig. 6-8 together with the aluminium split-block waveguide housing fabricated using traditional milling procedures.

The measured results are shown in Fig. 6-7, where the simulation is also shown for convenience. Good agreement between the measured and simulated results is obtained. A distortion in the in-band reflection coefficient (the simulated bandwidth of the prototype is 150 MHz while the measured is about 200 MHz) is attributed to the fabrication tolerances.

.

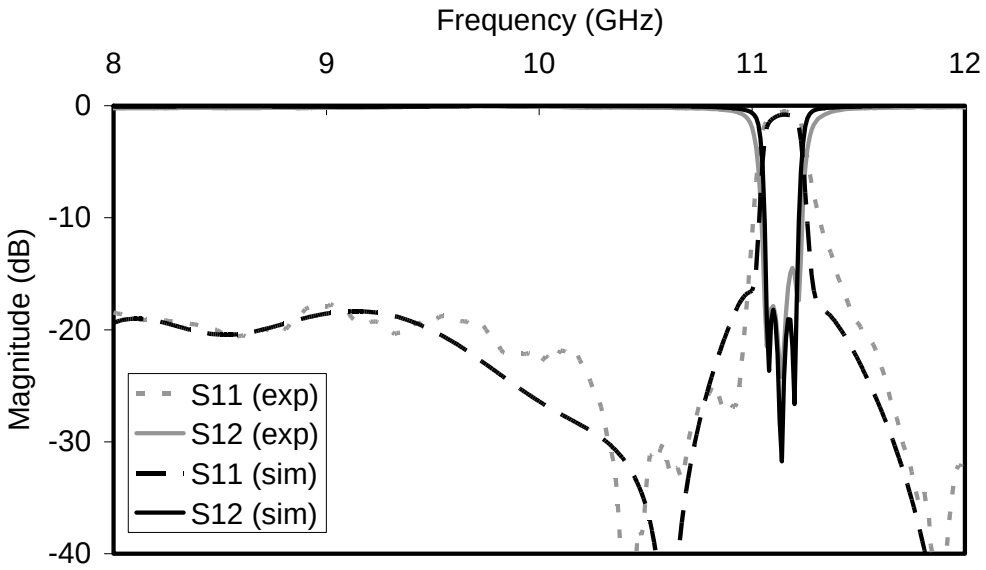

Fig. 6-7. Simulated (a) and tested response near the stop-band comparison (b) of the proposed third order prototype. Dimensions (in mm) depicted in Table 6-1. All three resonators height is 1.2.

L_{r1}	L_{r2}	L_{r3}	L_{12}	L_{23}	s_1	s_2	s_3	h	L
12	12.9	12.1	12.5	12.5	0.5	0.7	0.5	2.5	150

Table 6-1. Dimensions (in mm) of the bandstop filter

Fig. 6-8. Photograph of the fabricated bandstop prototype.

6.2.2 Dualband bandstop filter design

The suggested design of the dual band bandstop filter is based on the elements described for the single stopband filter. As it will be shown the limitations of the novel configuration is that each single bandstop can be modeled almost independently from the other as the resonators etched on each inset are very weakly coupled with those from the second inset. Therefore, a dualband bandstop filter can be easily designed from two single stopband prototypes. It is only required a small optimization to fine tune the poles in order to satisfy the goal requirements.

6.2.2.1 Numerical and experimental results

For a dualband bandstop filter, the structure depicted in Fig. 6-9 is proposed. The dimensions of each semi-ellipsoid employed for the dual-band filter are the same as shown in Fig. 6-6: the major radius of the semi-ellipsoid is 2.5mm, while ratio is 21; L=150 mm. The dimensions of the filter are shown in Fig. 6-9.

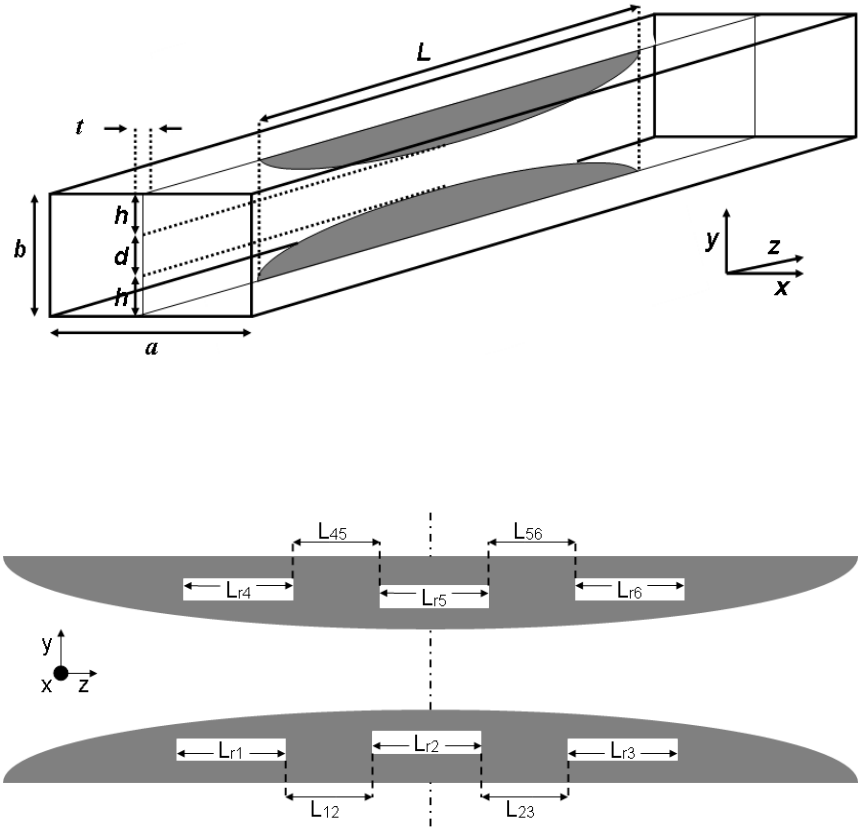

Fig. 6-9. Schematic layout of the Dual-band Bandpass Filter.

It is interesting to note that the lower inset is almost identical to the one of the previous section. A small correction in L_{12}=L_{23} (from 12.5 to 13mm) is made to maintain good performance. Otherwise, this suggests that the two bands can be initially designed independently.

The simulated results are displayed in Fig. 6.10. The small variation in the single stopband when it is integrated in a dual-ban stopband filter, is due to the fact the two sets of three coupled resonators are not totally independently coupled each other. The insertion loss outside the stopbands is now of the order of 0.1dB. The lower stopband is approximately centred at 10 GHz, while the upper stopband is centered about 11 GHz, with about 150 and 160 MHz of bandwidth respectively. In order to validate the above, the designed filter has been fabricated and experimentally tested. A routing procedure was employed for the etching of a copper foil of thickness 100 μm.

A photograph of the fabricated prototype is shown in Fig. 6-11. The measured results are compared in Fig. 6-10. Good agreement between the measured and simulated results is obtained. The measured bandwidths are increased from about 150-160 MHz of the bandstops of the simulated prototype to up to 230 MHz. These discrepancies are attributed to the fabrication sensitivity.

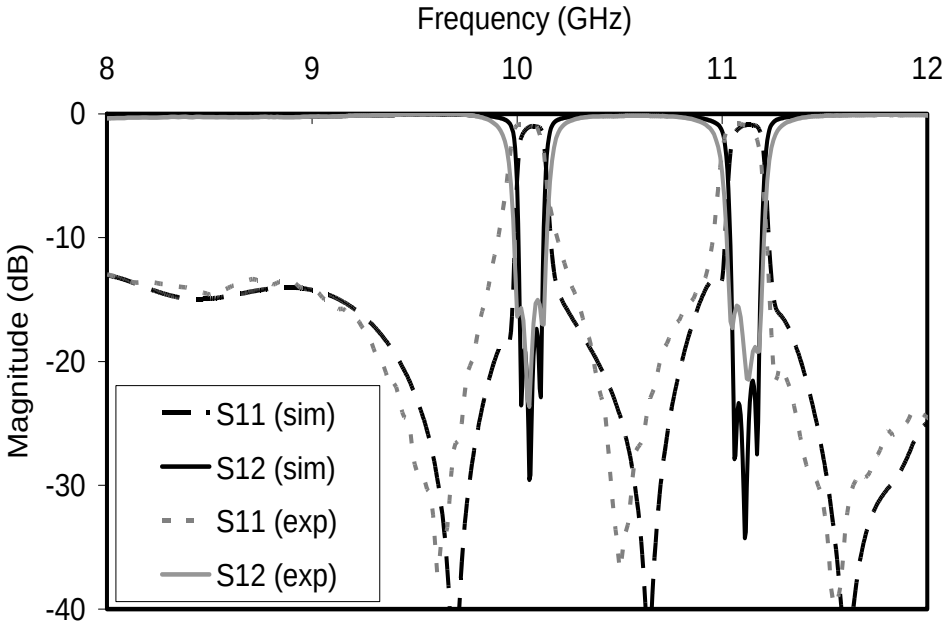

Fig. 6-10. Simulated (a) and measured response superimposed with simulated response near the stopband (b) of the proposed dual-band bandstop prototype. Dimensions (in mm) expressed in Table 6-2. All resonators heigth 1.2 mm.

L_{r1}	L_{r2}	L_{r3}	L_{12}	L_{23}	s_1	s_2	s_3	h	L
12	12.9	12.1	13	13	0.5	0.7	0.5	2.5	150
L_{r4}	L_{r5}	L_{r6}	L_{45}	L_{56}	s_4	s_5	s_6	h	L
13.5	13.4	13.6	13	13	0.5	0.7	0.5	2.5	150

Table 6-2. Dimensions (in mm) of the dualband bandstop filter shown in Fig. 6-9.

Fig. 6-11. Photograph of the fabricated dual bandstop prototype

6.3 A LABEL-FREE CHEMICAL/BIOCHEMICAL SENSING DEVICE

Another application of the strongly dispersive coupling producing a transmission zero characteristic of parallel coupled ridged waveguides is presented here. In this section a novel application of the paralel coupled asymmetric ridge coaxial waveguide is investigated for a label-free chemical/biochemical sensing device. A micromachinned copper filter has been integrated with a microfluidic channel prototype. The aim is to investigate a microwave chemical/biochemical sensing device for the characterization and detection of cells in chemical substances and cells in solution in micro-litre volumes. The design of the prototype as well as the fabrication of the microfluidic network and microwave resonator are described throughout this chapter. Initial testing of the prototype at X-band is examined with promising results. In the last stage it is propose a Low Temperature Co-fired Ceramic (LTCC) integration scheme for the miniaturization of the device for use in the THz regime.

6.3.1 Brief state of the art

Microfluidics is the use of micro-scale devices to perform laboratory processes in micro-nano-, and even pico-litre volumes. Such devices are manufactured using microfabrication technology to produce channels, pumps, and valves to manipulate, mix and analyze solutions [94-96]. A particular application which has flourished with the development in microfluidics are biosensors. These systems use chemical, electrical or optical detection techniques for rapid sensitive analysis of samples. One commercially available biosensor is the glucose monitor [97], which takes a tiny sample of blood and outputs the amount of glucose in that sample. Such biosensors require attachment of chemical and/or optical labels, which not only alters the sample completely making it unsuitable for further analysis but also may alter the biological function of the sample itself.

The use of electromagnetic (EM) waves to characterize and study the dielectric properties of biological substances such as tissues and cell suspensions is well established through the work of Schwan [98]. In his work, three distinct regions were indentified in which the electrical properties of tissues and cell suspension change with frequency. They are termed the α-, β-, and γ- dispersions pertaining from low frequencies (<100Hz), intermediate RF frequencies (around 100Hz to 10MHz) and frequencies above 1GHz.

The use of EM waves offers a number of advantages including a non-invasive, contactless label-free solution with the ability to achieve fast measurements and precise characterization. Moreover, with today's fabrication techniques and advances in microfluidics the development of lab-on-a-chip (LOC) devices has become available.

In this context, the integration of a microfluidic channel within a waveguide-based resonator with localized increased near-fields and sharp resonant features for label-free chemical/biochemical sensing is proposed.

6.3.2 Prototpe sensing concept

The concept is closely related to the one employed for the bandpass filters of chapter 4. Also here the modelling of a pair of parallel coupled resonators is the starting scenario. Commencing from two identical resonators of dimensions exactly as those specified for the Lower Transmission zero prototype specified in Table 4-1 but here with $Ls_{12}=L_{r1}=L_{r2}$ (instead of 11.4 mm). The response is shown in Fig. 6-12a. This prototype consist of three cascated waveguide sections: a rectangular waveguide, a reduced waveguide, and a ridge coaxial waveguide (RCWG).

By reducing the physical length of one resonator, in Fig 6-12b from 16 to 15 mm, an assymmetric ridge waveguide is then another cascated waveguide section in the filter. Therefore, the effect of perturbing one of the resonators by adjusting its physical length arises in the excitation of the TE_{10} assymetric ridge waveguide mode and the introduction of an extra narrow resonance with a Transmission Zero (TZ) in the X-band. The assymmetric ridge waveguide section for the example of Fig 6-12b is of 0.5 mm length. This produces a TE_{10} mode transmission located at 8.32 GHz and also a slight shift to upper frequencies of the coupled TEM mode resonance.

The goal here is to investigate the possibility to effectively control the TE10 resonance and locate the Transmission Zero produced by the parallel coupling as closer as possible to that resonance. Indeed, let be the two resonators identical then the two resonances will become degenerate and not distinguishable. So on, by setting slightly different lengths we can make the two resonances distinguishable. In addition to that and because the tow resonances are coupled, at a certain frequency they exactly cancel out producing a transmission zero. These elements are shown in Fig. 6-12.

In conclusion, the combined effect leads to a sharp feature which can be potentially exploited in sensing. The arising resonance appear at 8.32 GHz corresponds with the odd mode. While the resonance present at both structures corresponds with the excitation of the even mode, 9.55 GHz. At the even resonance the apertures electromagnetically coupled apertures are excited in equal amplitude and equal phase (both positive), the normal component of the Electric Field is zero. These elements are shown in Fig. 6-13b. Highly

stronger the fields are present at the odd resonance: over one order strengths compare with the fields at the even resonance (Fig. 6-13a).

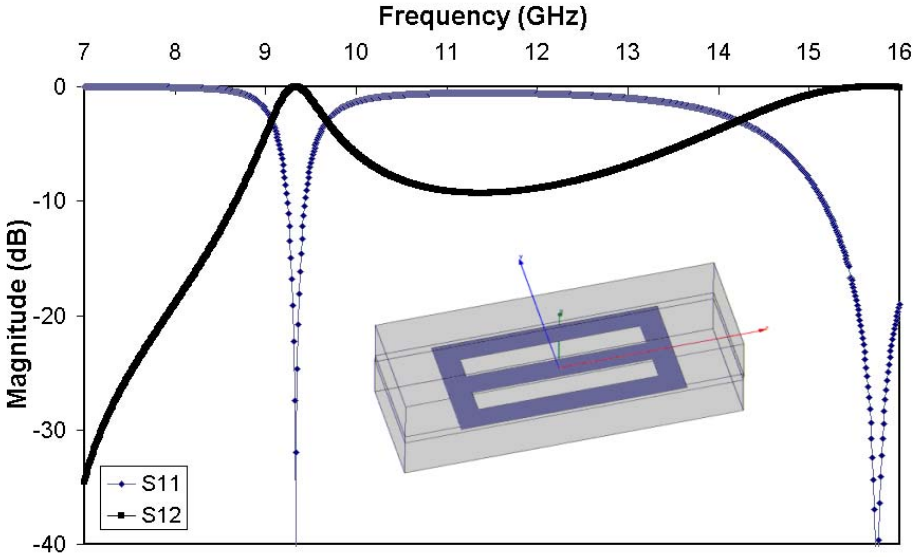

(a)

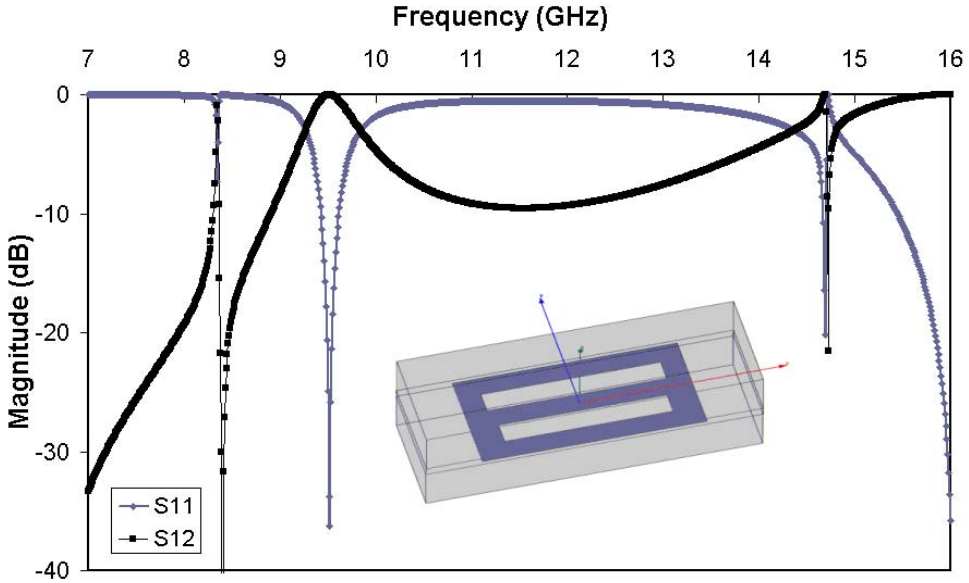

(b)

Fig. 6-12. Designed non-perturbed (a) and perturbed prototype (b) S-Parametres.

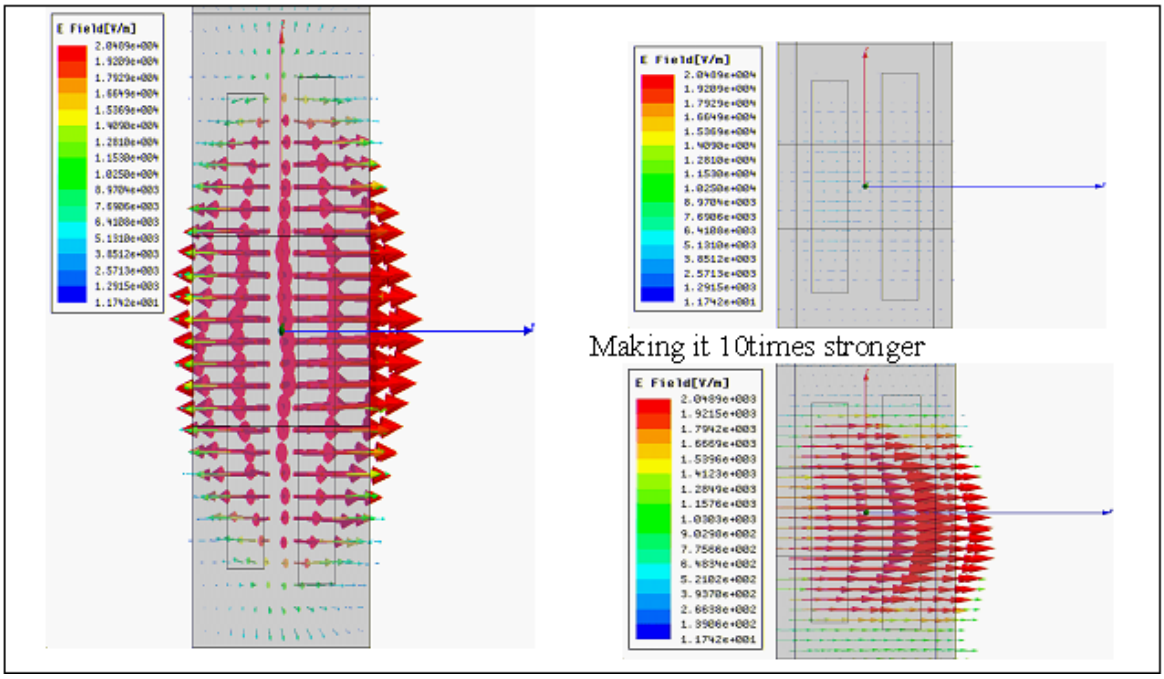

Fig. 6-13. Electric field distribution in the metal plane at the odd (a) and even (b) resonance frequencies.

To demonstrate the validity of the preliminary sensing concept, the filter prototype has been designed, fabricated and tested. The filter has a TE_{10} mode transmission at about 8.32 GHz and a transmission zero at about 8.36 GHz.

The prototype has been measured in an HP8510 vector network analyser, using commercial X-band flanges. The calibration was made to the level of the coaxial cable. The comparison of the simulated results with the measured results is shown in Fig. 6-14. It shows a frequency shift of about 50 MHz. This is attributed to relative convergence of our simulations, experimental tolerances as well as the fact that the simulations did not account for the finite thickness of the copper insert. Photography of the fabricated inset is shown in Fig. 6-15.

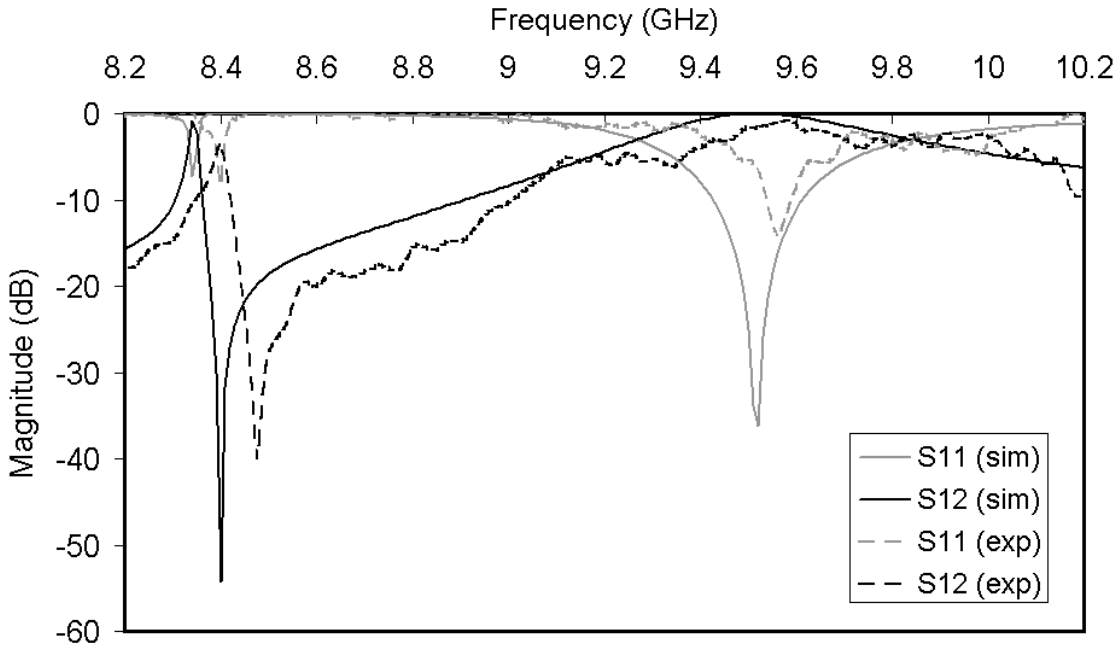

Fig. 6-14. Simulated and measured insertion loss response.

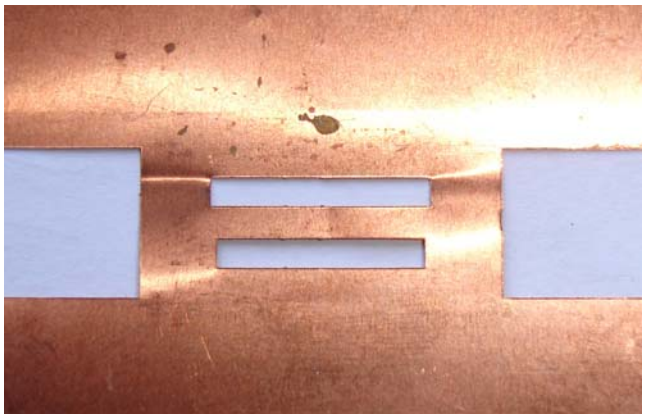

Fig. 6-15. A micromachined copper filter

The next step is to show how effectively it is possible to shift the resonances and the transmission zero to satisfy specific requirements. In Fig. 6-16, a method to control the gap length between this first narrow resonance and the TZ by varying the length of the smaller resonator is illustrated. The dimensions employed in the prototype modeling are as follows. The height of both resonators is 2.1 mm. The vertical separation is 2 mm while the length of the longer resonator is 16 mm. The length of the shorter resonator in this study varies from 7mm to 15mm. The filter with Lres2=15mm will be considered further on as the first

prototype. The design of the perturbed aperture filter (shown in Fig. 6-12) was obtained using a commercially available Finite Element Method (FEM) software Ansoft HFSS.

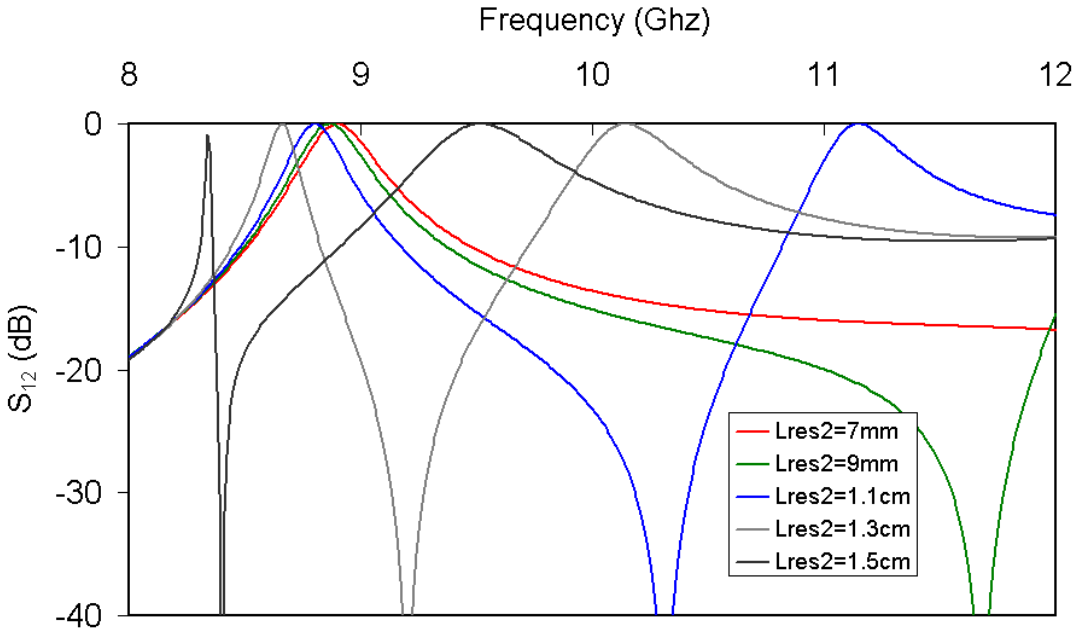

Fig. 6-16. Modeling of the two split resonances by just adjusting the physical length of one resonator.

The sensor works on the principle of shift in the TE_{10} mode resonance with respect to frequency for a minute change in dielectric constant and for liquids of micro-litre volumes. The E-plane filter has a transmission bandwidth of 10 MHz and a sharp upper atenuation slope by means of a Transmission Zero located about 6 MHz from the center of the TE_{10} mode resonance. Further proximity can be achieved by modelling the physical dimensions of the resonators to make them similar. The microfluidic channel filled with different biological and chemical substances would be initially characterised at around 8.4 GHz band.

The proposed device has been initially modeled with inside a normal rectangular waveguide cavity and with a capillary tube (microfluidic channel) of inner diameter 100 µm. The capillary tube is filled with a liquid of loss tangent 0.02 and dielectric constant 81

for Fluid A and 75 for Fluid B. As seen in Fig. 6-17 there is a shift of about 40 MHz in the band gap between the odd mode transmission resonance (8.32 GHz to 8.36 GHz) and the transmission zero (8.38 GHz to 8.42 GHz). The lower transmission zero coupled with the smaller band gap provides an excellent package for fabricating high sensitive sensors for particle or cell detection. The proposed sensor could be modelled extensively with different sizes and shapes of microfluidic/capillary tubes along with different chemical and biological materials inside them.

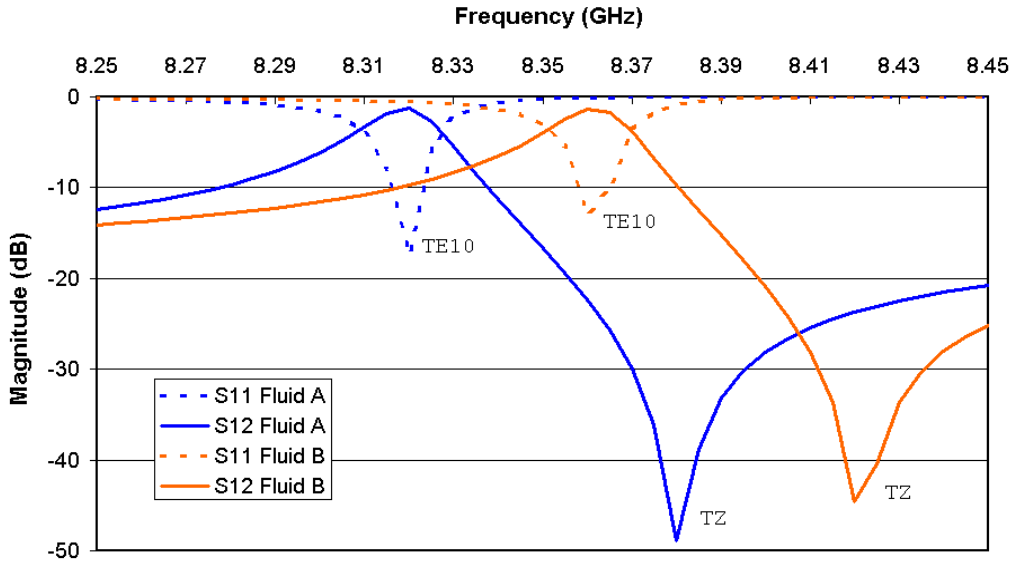

Fig. 6-17. Simulated results showing high sensitivity narrow band gap from the microfluidic capillary channel. Dielectric constants: Fluid A=81, Fluid B=75

To optimise the sharp response and bandwidth we performed a study on the relative lengths of the resonators with the top resonator measuring 13mm and the bottom resonator varying from 12 mm to 13 mm in 0.25 mm increments. The results of this study are shown in Fig. 6-18.

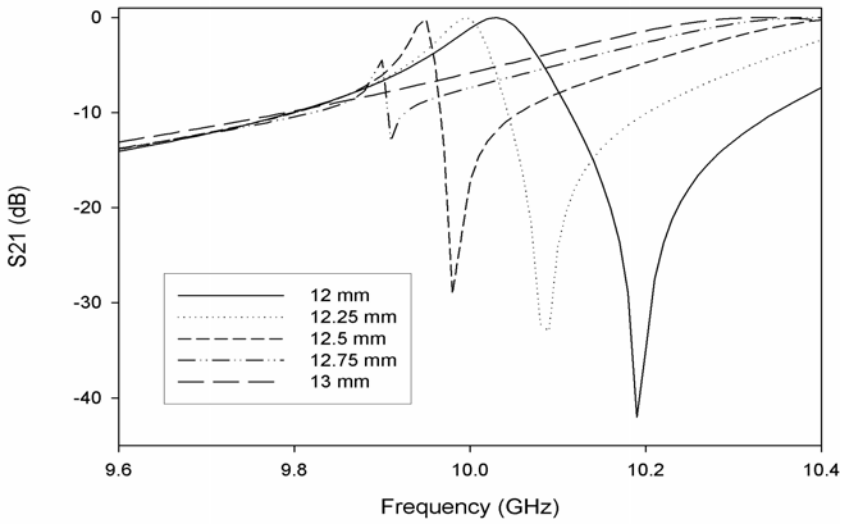

Fig. 6-18. Simulated transmission for different bottom resonators lengths

An optimum length of 12.25 mm for the bottom resonator was chosen as a trade-off between the sharpness of the transmission response and the absorption losses. The resulting transmission pole is at approximately 9.99 GHz with -0.091dB and the transmission bandwidth is 90 MHz with a sharp roll-off. The narrow bandwidth allows for a higher sensitivity in sensing. Layout is shown in Fig. 6-19

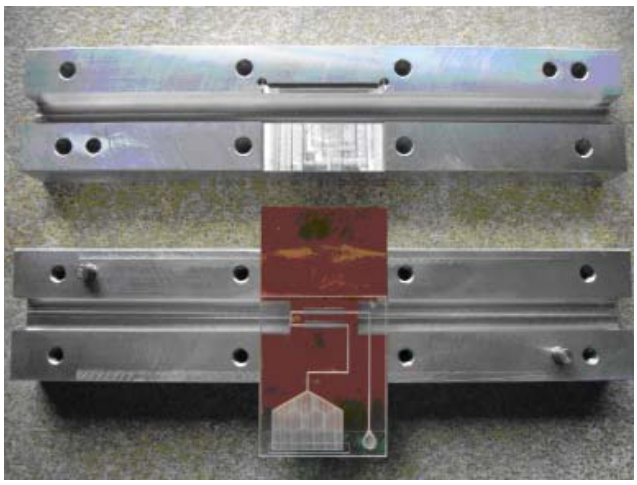

Fig. 6-19. Classical 22.86x10.16 mm waveguide halved along the E-Plane with insert for filter and microfluidic channel.

The microfluidic channels were fabricated from Polymethylmethacrylate (PMMA), which is sold under various trade names such as Plexiglas®. Using an Epilog Legend Elite Series CO_2 laser system [19] we engraved 350 μm deep channels. The channel structure is shown in Fig. 6-20; it consists of an inlet port, two parallel channels which align with the resonators and a microfluidic pump at the outlet. This microfluidic pump works on natural capillary forces which draws the fluid from the inlet to the vent (outlet) [100]. The channel was then bonded to another sheet of PMMA with access holes for the inlet and outlet.

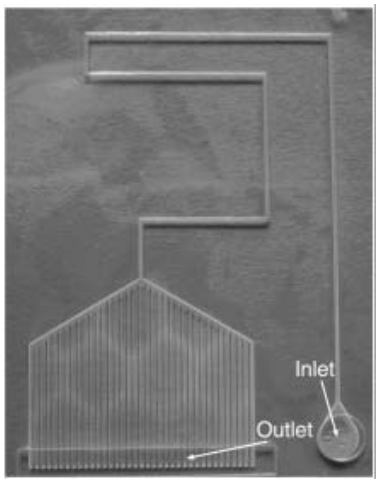

Fig. 6-20. Laser machined PMMA microfluidic channel.

6.3.3 Preliminary results

The waveguide was connected to the connectors of a HP 8510 Vector Network Analyser (VNA) as shown in Fig. 6-21.

Fig. 6-21. Waveguide showing connections to VNA and insert of the filter and microfluidic channel.

The forward transmission coefficient, S_{21}, was measured for an empty channel and a channel filled with Phosphate Buffer Saline (PBS) of dielectric constant equal to 175. PBS is a salt solution used in biology to dilute blood while maintaining cell integrity and in solution as a Ph balancer. The results are depicted in Fig. 6-22.

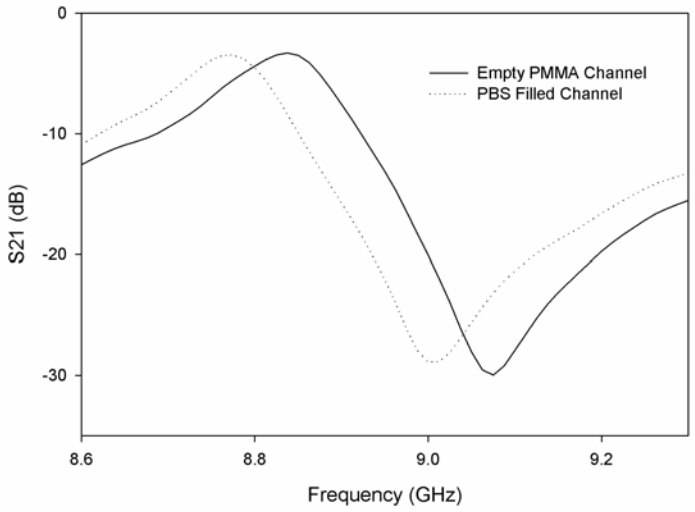

Fig. 6-22. S_{21} Transmission coefficient for PBS and air filled empty channel.

A significant difference between the empty channel and when it is filled with PBS can be appreciated in Fig. 6-22. The resonant frequency of the empty channel is 9.8375 GHz whereas when filled with PBS it becomes 9.775 GHz. The difference is 62.5 MHz, which is more than sufficient in order to distinguish between the two media.

6.3.4 Future work: LTCC Integration

Low Temperature Co-fired Ceramic (LTCC) is a multilayer manufacturing platform that exhibits good electromagnetic immunity, which is therefore used primarily in microwave electronics. The process uses a material, when unfired, is called green tape, where individual sheets are processed in parallel then aligned and stacked prior to firing at a temperature below 1000 °C. This temperature allows the integration of highly conductive

metals such as gold and silver that cannot be realised at higher temperatures. As the sheets are all fired together this reduces the overall manufacturing cost, saving time. Due to the dielectric constant of the material the dimensions of the resulting circuits can also be reduced. Another advantage of this technology is the parallelism in which every layer can be inspected before firing ensuring that one does not have to manufacture an entirely new device.

LTCC exhibits very good electrical and mechanical properties, high reliability and stability with the capability of manufacturing three-dimensional (3-D) structures. It has made its way into many applications, one such area of interest is Biological MicroElectroMechanical Systems (BioMEMS). This area uses the concepts of MEMS and applies them to biology to create examples such as microfluidics [101], PCR systems [102], biosensors [103], and bioreactors [104]. The proposed prototype is a substrate integrated waveguide of the pillars in air design. The integration of our filter and microfluidic channel is shown in Fig. 6-23.

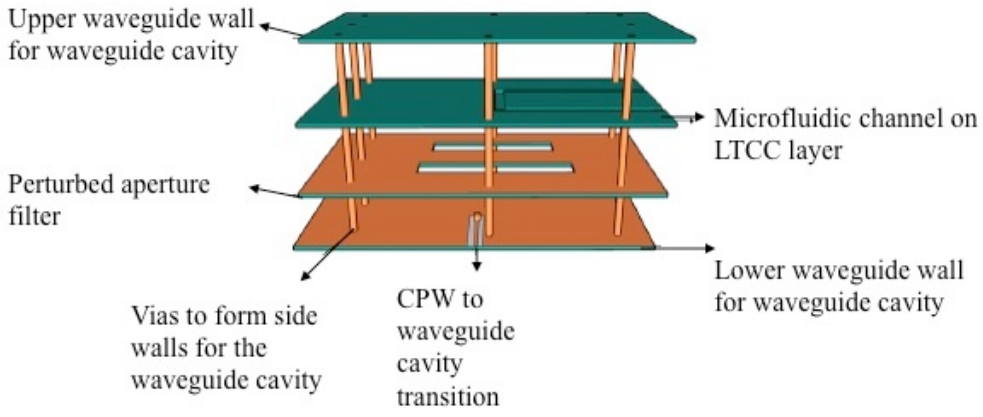

Fig. 6-23. Proposed LTCC post wall waveguide design with integrated filter and microchannel

The sidewalls of the cavity are realised in closely spaced pillars with tape layers for the top and bottom. The microfluidic channel and filter can be realised in layers of ceramic material and embedded within the cavity. The waveguide is fed with a Coplanar Waveguide (CPW) to waveguide cavity transition as shown in the diagram.

6.4 COMPACT T-JUNCTION DIPLEXER DESIGN

In this section is presented a compact version of the structure depicted in Fig. 2-14 (a). Essentially the T-power divider element is combined here with those filter prototypes designed in Fig. 4-13. Before addresing the design procedure for the novel diplexer realization, are introduce some notes on the distributed parametres analysis of the filter channel: the one presented in Fig. 4-6.

6.4.1 Distributed parametres analysis of the filter concept

An alternative electrical circuit model based on the distributed parametres analysis of the filters depicted in Fig. 4-6 is here proposed.

The electrical circuit model of Fig. 6-24 is composed of two ports, two resonant elements, and five admitance inverters to characterize the each one of the couplings involved in the filter.

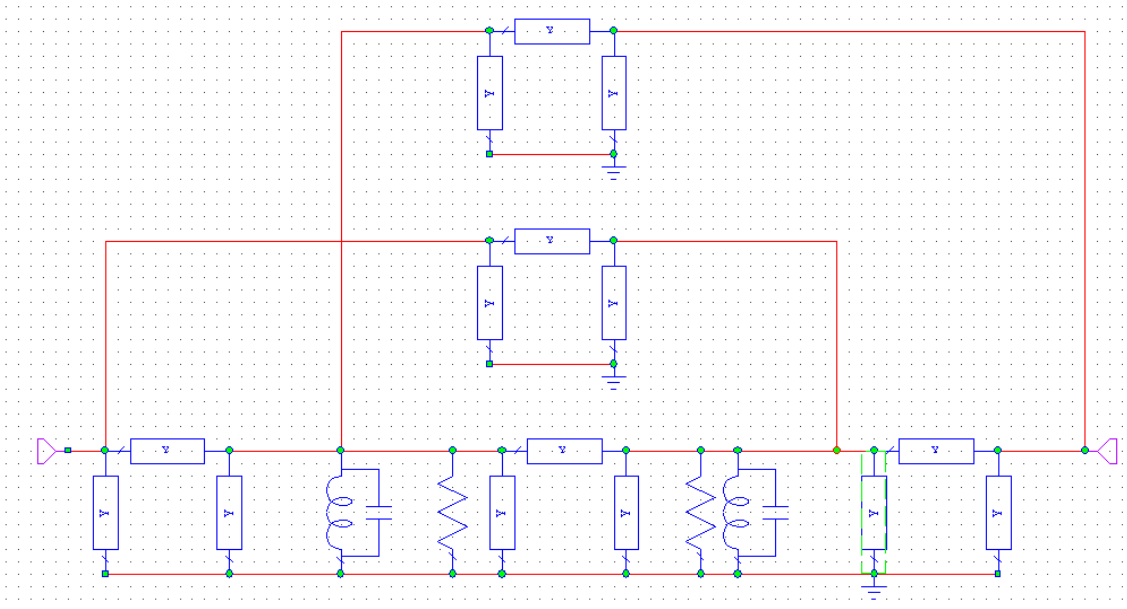

Fig. 6-24. AWR Circuit modeling of parallel coupled resonators (Fig. 4-6)

The synthesis process commence by obtaining the admittance inverter and LC parametres producing the desired characteristics of the implemented filter design. Then, the normalized matrix coupling elements of such circuit model can be calculated. The optimization process consists on matching the normalized copling matrix elements from those corresponding to the preliminary prototype; the filtering structures of Fig. 4-1 with dimensions depicted in

Table 4-2, with those obtained previously for the ideal circuit model of Fig. 6-24. After a few numerical iterations the matching of the ideal filter prototype sought can be achieve to a good extent. The comparison of circuit model (AWR) and full wave simulated results (CST) for the upper and lower Transmission Zeros corresponding the structures of Fig. 4-6 are shown in Fig. 6-25a and Fig. 6-25b respectively:

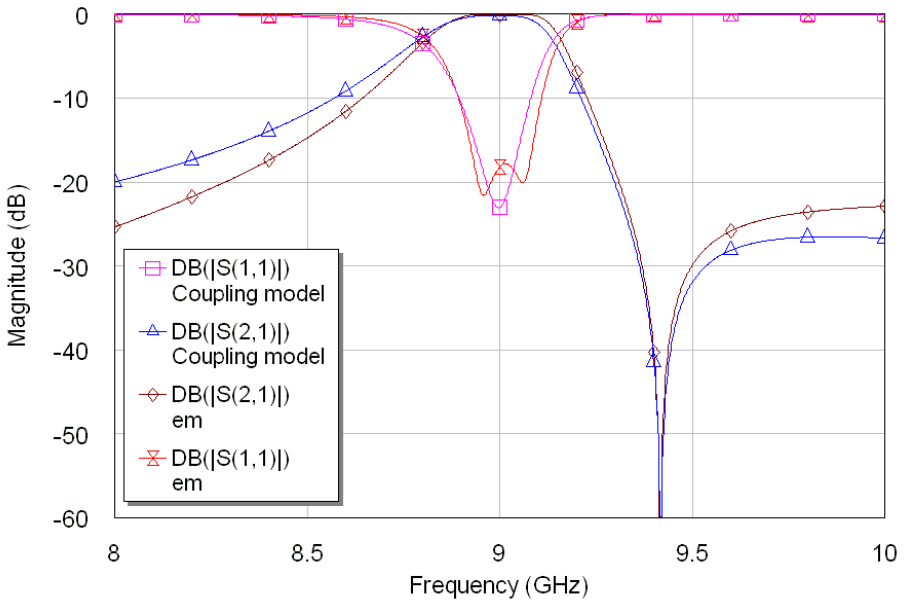

(a)

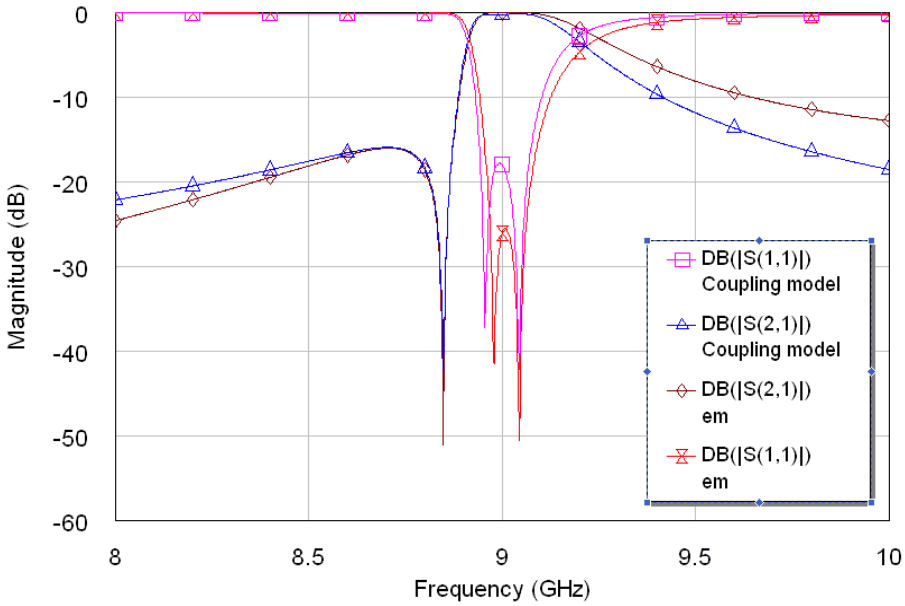

(b)

Fig. 6-25. Superimposed circuit modeling and em full wave simulations for the parallel coupled resonators inline E-Plane Filters with upper TZ (a) and lower TZ (b) of Fig. 4-6.

The values obtained of both, circuit model distributed parametres and physical dimensions of the filtering structures, will be the initial values considered to start the same iteration process, in order to go through the design of a novel diplexer structure along the next section.

6.4.2 Compact T-junction diplexer

A T-Junction Diplexer with compact (by means of parallel coupled resonators) E-Plane Filter channels is shown in Fig. 6-26. By comparison with the classical T-Junction E-Plane Diplexers introduced in Fig. 2-14, the filter channels of these Diplexor are expected to be almost 50% more compact for a similar narrow band application operating about 9 GHz (dimensions of housing waveguides: 22.86x10.16 mm)

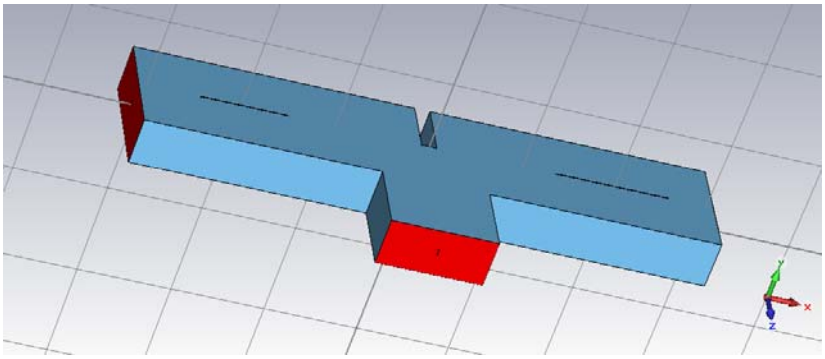

(a)

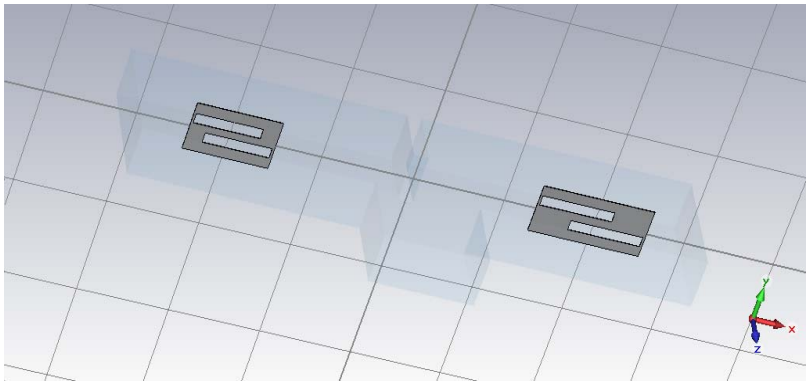

(b)

Fig. 6-26. Schematic of the proposed diplexer with H-Plane T-Junction Power divider and two filter channels (a). Inside of the E-Plane Filter channels.

For this diplexer, the proposed distributed parametres circuit model is shown in Fig. 6-27.

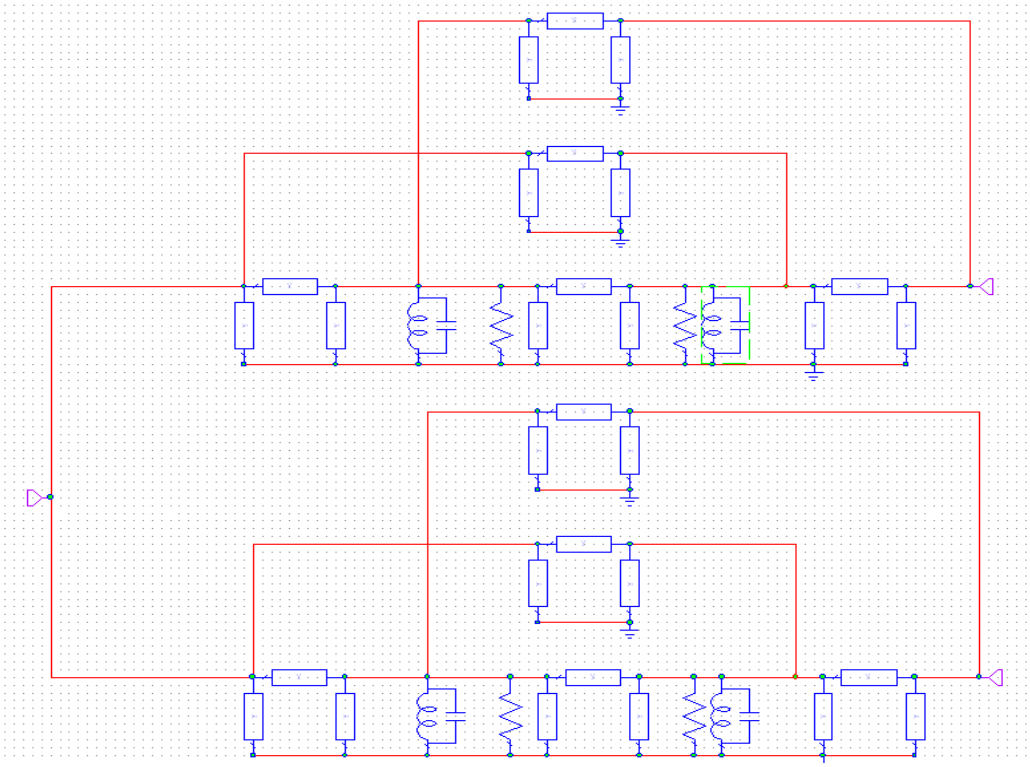

Fig. 6-27. Distributed parameters circuit model of the T-Junction Diplexor depicted in Fig. 6-26.

The circuit model consists of three ports and a pair of schemes as the one Fig 6-24, each one aim to model a channel filter.

A realization example is considered. The operating centre frequency passbands of the filter channels 1 and 2 are selected at 9.1 GHz and 9.5 GHz respectively. Taking as starting values those admitance inverter, LC parametres, and the physical dimensions of the two filter prototypes detailed in Table 4-2. Again as in section 6.4.1, a few numerical iterations lead to a good extent matching between the normalized coupling elements of the circuit model and the full wave simulation of the diplexer structure. Superimposed transmission and reflection coefficients for the optimized diplexor and its ideal circuit model are depicted in Fig. 6-28.

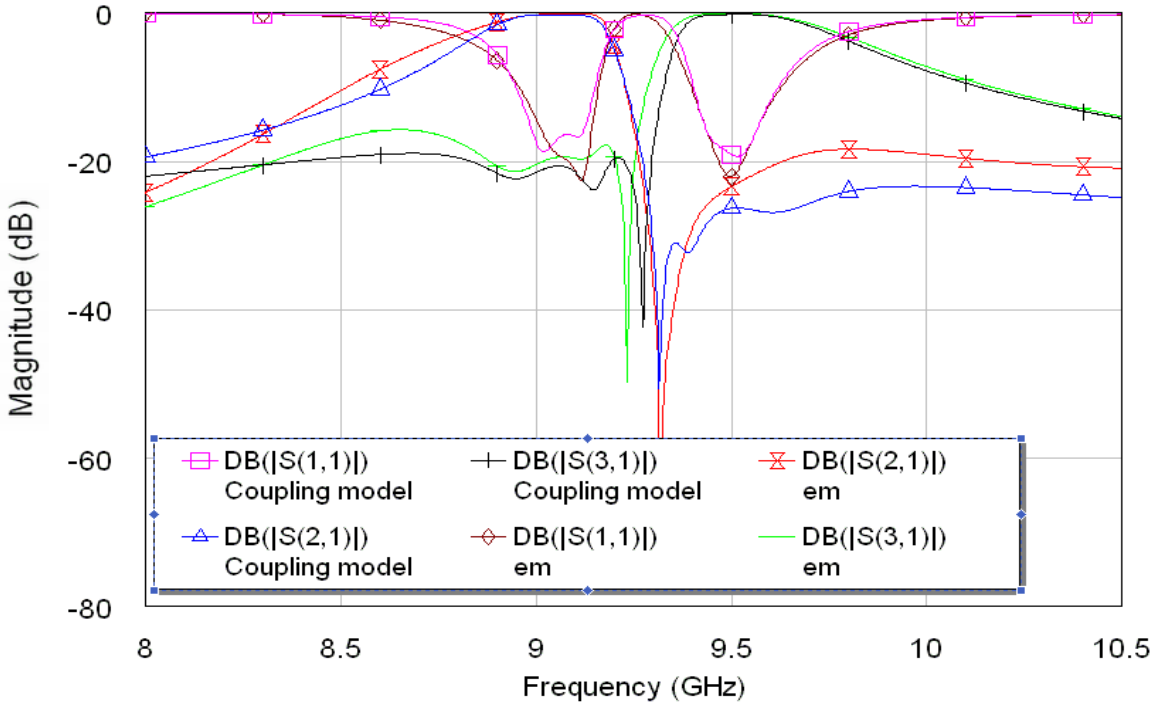

Fig. 6-28. Compact Diplexor comparison of full wave simulated response and circuit modelling.

6.5 SUMMARY

In this chapter the analysis elements reported in chapter 3 and chapter 4 have been employed to investigate two different filter applications.

The first filter application comprises the analysis and design of a novel class of dual-band stop filters. The concept is based on similar elements (strongly dispersive parallel-coupled asymmetric ridge waveguides introducing transmission zeros) however the configuration does not involves a coupled of resonators coupled in parallel but a resonator and a slot line, which effectively means a reaction type resonators producing coupled full reflection points. The analysis commenced by demonstrating those elements for practical realizations of a single reaction type resonator. Later on, the concept was successfully extended to dual band-stop filters. The configuration presented allows to design two sets of reaction type resonators quasi independently coupled. Practical filter design guidelines have been derived. The proposed designs maintain low-cost and are suitable for mass manufacturing. Practical prototypes have been fabricated and experimentally tested to validate the concept.

The second application proposed is a microwave biochemical sensor. A prototype waveguide cavity with integrated microfluidic sensor has been discussed. Preliminary numerical and experimental results have been presented demonstrating the suitability of the device for the characterization and detection of cells and chemical substances within the channel. Also a packaging technique has been proposed for application at higher frequencies, which can be expected to enhance the sensing device making it capable of outperforming the low throughput of counting cells associated with optical techniques offering higher sensitivy when compared to lower frequencies and DC devices.

Regarding the Diplexer application of section 6.4, the synthesis procedure followed here has been proved valid for a diplexer composed of a T-Junction power divider and two compact E-Plane Filter with parallel coupled resonators. Hence, extending the advantages of the novel filter concept to diplexer applications. The present procedure can be of interest to design diplexers of higher order filter channels, also combined with other Power divider elements.

CHAPTER 7

Conclusions and Future Work

7.1 CONCLUSION

The thesis began with a brief introduction on passive microwave components and the numerical methods have been employed in the past. In particular, those methods employed to synthesize some structures that have attracted special attention due to the range of practical applications for which they can be of interest: rectangular or circular waveguides with ridges.

Chapter 2 is an up-to-date review on the most commonly employed E-Plane Filters, in particular and due to the interest of this project special emphasis is made on filters with pseudo-elliptic response, or those E-Plane filters which provide improved performance by introducing additional transmission zeros. Advantanges and Handicaps of the diferent realizations have been remarked, motivating the investigation of the novel filter concept.

Chapter 3 presents the full modal analysis of a ridged coaxial waveguide. By applying the transverse resonance field-matching method a double ridge waveguide is fully characterized. These elements are implemented in a program based in Fortran and matlab. This numerical tool produces the fields of the modes present in the RCWG calculating the series of expnasion terms defined by user. Results derived thorough this chapter are used for the filter analysis of the following chapter. Also, the understanding of the electromagnetic nature of this structure led to other directions of research reported in the following chapters.

Chapter 4 describes in detail the parallel coupling of waveguide resonators. The mixed electric and magnetic coupling present in this structure introduces transmissions zeros at desired frequencies. The property is used to design filters with improved skirt selectivity and miniaturization when compared with the classical direct-coupled E-Plane Filters.

Numerical and experimental values are presented, validating the mentioned advantages at the cost of deteriorating slighly the insertion loss in the passband.

Chapter 5 compiles a Q factor assessment of the waveguide uniform resonator employed in the filter realisations of Chapter 4. The anlysis demostrates that a reduction of the insertion losses in the passband of those filter prototypes can be achieved by introducing resonators with higher Unloaded Q, that means resonators of larger higth (like from 2.1 mm up to 4 mm).
In the second part of the Chapter, a similar Q factor assessment is addressed to resonators with periodical loads, demonstrating even further miniaturization can be achieved. The size reduction can be implemented at the cost of deterioring slighly the Unloaded Q of the resonator. Numerical and experimental values are reported to validate the study.
In summary, future narrowband filter designs as those described in Chapter 4 can benefit of a more stringent performance, that is, lower losses and reduced size by considering the elements described through this chapter.

Chapter 6 introduces three further applications arised from the analysis, modelling and design of previous chapters. The first one presents a novel type of Finline Dual-Band Stopband Filters. Filter design is show easy, as the present topology benefits from sets of resonators quasi independently coupled, which means each stopband can be modelled indepentely. Design procedures are validated with numerical and experimental results for different filter prototypes. In the second part a a label-free chemical/biochemical sensing device was proposed. The concept is intended for the characterization and detection of cells in chemical substances and cells in solution in micro-litre volumes. Preliminary steps of the investigation were outlined. Finally a compact diplexer consisting of a T-Junction and two filter channels as those from section 4-3 has been presented.

In conclussion the contribution of this thesis can be summarized as follows:

- Due to potential filter application, a Double Ridge Coaxial Waveguide has been fully characterized applying Transverse Resonance field matching technique.

- Inline E-plane filters with selectively located transmission zeros are presented. It is demonstrated that parallel-coupled asymmetric ridge waveguides produce strongly dispersive coupling which introduces a transmission zero. This property has been exploited to investigate a novel class of In-Line E-Plane Bandpass Filters with improved performance: higher skirt selectivity and size reduction . General design guidelines have been derived. Also, numerical and experimental results are presented as validation of the novel filter scheme.

- A novel dual-band bandstop E-plane filter topology is proposed and experimentally tested. This novel topology involves a finite number of coupled resonators to realise single and dual-bandstop response. Practical filter design guidelines are presented. The proposed designs maintain low-cost and are suitable for mass manufacturing. The fabricated and tested prototypes validate the proposed dual-band stopband filter configuration.

- A prototype microwave waveguide cavity with integrated microfluidics has been proposed. The device is intended for the characterisation and detection of cells and various chemical substances from within a variety of micro-litre test samples. Design guidelines and fabrication description of the integrated microfluidic network and microwave resonator were outlined. Initial testing of the prototype at X-band is examined with promising results. At a final stage, a Low Temperature Co-fired Ceramic (LTCC) integration scheme for the miniaturization of the device for use in the THz regime was proposed.

7.2 FUTURE WORK

Further work can be addressed to implement a tool based on mode matching technique to solve the surface discontinuity between a Ridge Waveguide and a Ridge Coaxial Waveguide. The theoretical derivation as well as all the corresponding numerical elements, are contained in the appendix of this thesis.

For the porpoise of this project, the design procedure derived based on the Ness technique was demonstrated easy, practical and efficient. However, such numerical tool can be useful

to devise new directions of research. Also, the possibilities when integrated as part of a modular numerical tool involving the analysis of other surface discontinuities are yet to be explored.

Regarding the Dualband Bandstop Filters presented in section 6.2, those can benefit from similar optimization analysis as presented in chapter 5. Careful investigation on the limitations regarding the stop bandwidth and operating range capability would be beneficial to evaluate the potential of the configuration.

Miniaturizated resonators by virtue of inserted loads demonstrate size reduction can be achieved without deteriorating significantly the Unloaded Q of the resonator. However not filter realizations were proposed considering those elements. Following the design guidelines of chapter 4, it can be of interest to implement a filter realization targeting the same goals based on a resonator with periodic loads. Comparison with the prototype presented in Chapter 4 would be of interest.

Appendix

APPENDIX A. SURFACE SYMMETRIC BOUNDARY CONDITIONS: ELECTRIC AND MAGNETIC WALL.

Boundary conditions at electric and magnetic surfaces can be derived by the appropriate behaviour of the tangential fields.

Electric wall

An electric wall is a surface where the tangential components of the electric fields are zero. Ideal metallic surfaces (infinite conductivity) are electric surfaces.

The boundary conditions for the magnetic and electric potential vectors for the TE and TM modes respectively are obtained as follows:

$$E \times \hat{n} = 0 \Rightarrow (\nabla \times A_h) \times \hat{n} = 0 \Rightarrow \left(\frac{\partial A_h}{\partial y} \hat{x} - \frac{\partial A_h}{\partial x} \hat{y} \right) \times \hat{n} = 0 \qquad \textbf{(A-1)}$$

$$E \times \hat{n} = 0 \Rightarrow (\nabla \times \nabla \times A_e) \times \hat{n} = 0 \Rightarrow \left[\frac{\partial^2 A_e}{\partial x \partial z} \hat{x} + \frac{\partial^2 A_e}{\partial y \partial z} \hat{y} + \left(K_0^2 A_e + \frac{\partial^2 A_e}{\partial z^2} \right) \hat{z} \right] \times \hat{n} = 0 \qquad \textbf{(A-2)}$$

where $\hat{n}$ is the unity vector perpendicular to the surface.

Magnetic wall

A magnetic wall is a surface on which the tangential fields of the magnetic field are zero. A material with such a property does not exist, but this concept is useful in order to analyse odd modes.

The boundary conditions for the magnetic and electric potential vectors for the TE and TM modes respectively are obtained as follows:

$$H \times \hat{n} = 0 \Rightarrow (\nabla \times \nabla \times A_h) \times \hat{n} = 0 \Rightarrow \left[\frac{\partial^2 A_h}{\partial x \partial z} \hat{x} + \frac{\partial^2 A_h}{\partial y \partial z} \hat{y} + \left(K_0^2 A_h + \frac{\partial^2 A_h}{\partial z^2} \right) \hat{z} \right] \times \hat{n} = 0 \qquad \textbf{(A-3)}$$

$$H \times \hat{n} = 0 \Rightarrow (\nabla \times A_e) \times \hat{n} = 0 \Rightarrow \left(\frac{\partial A_e}{\partial y} \hat{x} - \frac{\partial A_e}{\partial x} \hat{y} \right) \times \hat{n} = 0 \qquad \textbf{(A-4)}$$

APPENDIX B. WAVES PROPAGATING IN A RECTANGULAR COORDINATE FRAME

TE,TM waves

The electric and magnetic field for the TE and TM modes can be derived from the following vector potential expressions:

$$E = \nabla \times A_h + \frac{1}{j\omega\varepsilon}\nabla \times \nabla \times A_e \quad \textbf{(B-1)}$$

$$H = \nabla \times A_e - \frac{1}{j\omega\mu}\nabla \times \nabla \times A_h \quad \textbf{(B-2)}$$

Supposing z-propagation for electromagnetic wave and separable solution for the vector potentials, the magnetic and electric type of vector potential can be expanded as sum of modes:

$$A_h = \sum_{q=1}^{\infty} \sqrt{Z_{hq}} \cdot T_{hq}(x,y) \cdot \left[F_{hq} e^{-j \cdot K_{zhq} \cdot z} + B_{hq} e^{+j \cdot K_{zhq} \cdot z} \right] \hat{z} \quad \textbf{(B-3)}$$

$$A_e = \sum_{p=1}^{\infty} \sqrt{Y_{ep}} \cdot T_{ep}(x,y) \cdot \left[F_{ep} e^{-j \cdot K_{zep} \cdot z} - B_{ep} e^{+j \cdot K_{zep} \cdot z} \right] \hat{z} \quad \textbf{(B-4)}$$

where Z and Y are the waveguide impedance and admittance of the TE and TM modes respectively and are given by the expressions:

$$Z_{hq} = \frac{\omega\mu}{K_{hq}} = \frac{1}{Y_{hq}} \qquad Y_{ep} = \frac{\omega\mu}{K_{ep}} = \frac{1}{Z_{ep}}$$

Then, assuming the discontinuity plane at z=0, with no loss of generality, the fields can be expanded as series by:

$$E_t^{TE} = \sum_{q=1}^{\infty} \sqrt{Z_{hq}} \left(\nabla T_{hq} \times \hat{z} \right) \cdot \left(F_{hq} + B_{hq} \right) \quad \textbf{(B-5)}$$

$$E_t^{TM} = \sum_{p=1}^{\infty} \sqrt{Y_{ep}} \left(\nabla T_{ep} \right) \cdot \left(F_{ep} + B_{ep} \right) \quad \textbf{(B-6)}$$

$$H_t^{TE} = \sum_{p=1}^{\infty} \sqrt{Y_{hq}} \left(\nabla T_{hq} \right) \cdot \left(F_{hq} - B_{hq} \right) \quad \textbf{(B-7)}$$

$$H_t^{TM} = \sum_{p=1}^{\infty} \sqrt{Y_{ep}} \left(\nabla T_{ep} \times \hat{z} \right) \cdot \left(F_{ep} - B_{ep} \right) \quad \textbf{(B-8)}$$

TEM waves

The Electric and Magnetic Field have only transverse components $e_z = h_z = 0$, so then $\nabla \times E_t = 0$, that permits E_t to be expressed as the gradient of the scalar potential:

$$E_t = -\nabla_t \phi(x, y) e^{\mp j\beta z} \quad \textbf{(B-9)}$$

And from Maxwell' s curl equations:

$$\nabla \times E_t = -j\omega\mu H_t \quad \textbf{(B-10)}$$

$$\nabla \times H_t = -j\omega\varepsilon E_t \quad \textbf{(B-11)}$$

The Fields can be expressed, assuming again z=0, by the following expressions:

$$E_t = -\nabla_t \phi(x, y) \cdot (F_{TEM} + B_{TEM}) \quad \textbf{(B-12)}$$

$$H_t = Y_0 \hat{z} \times (-\nabla_t \phi(x, y)) \cdot (F_{TEM} - B_{TEM}) \quad \textbf{(B-13)}$$

APPENDIX C. RCWG TO RIDGE WG MODE MATCHING OF SURFACES DISCONTINUITIES ANALYSIS

In this appendix is described the Mode Matching analysis of a surface discontinuity between a RCWG and a Ridge Waveguide. The derived scattering matrix and coupling integrals for such discontinuity can be of interest for the synthesis of future filter configurations involving both waveguide structures.

A generalized layout of an E-plane filter metal insert involving different waveguide sections can be decomposed into the cascade connection of such elements, the like of rectangular waveguide, reduce waveguide, ridge waveguide or ridge coaxial waveguide. A concrete case showing the cross-section of these structures is depicted in Fig. C-1 (b).

The waveguide section between two subsequent metal septa form a resonator and subsequent resonators are coupled through the couplers realized by the metal septa. The metal septa is basically a reduced waveguide section. Incorporating asymmetric ridge waveguide and ridge coaxial waveguide in the all-metal E-plane split-block-housing

technology as resonators, in its variation with thin ridges and the inner conductor printed on an all-metal E-plane insert with no further fabrication complexity allows altered propagation characteristics along the same waveguide housing.

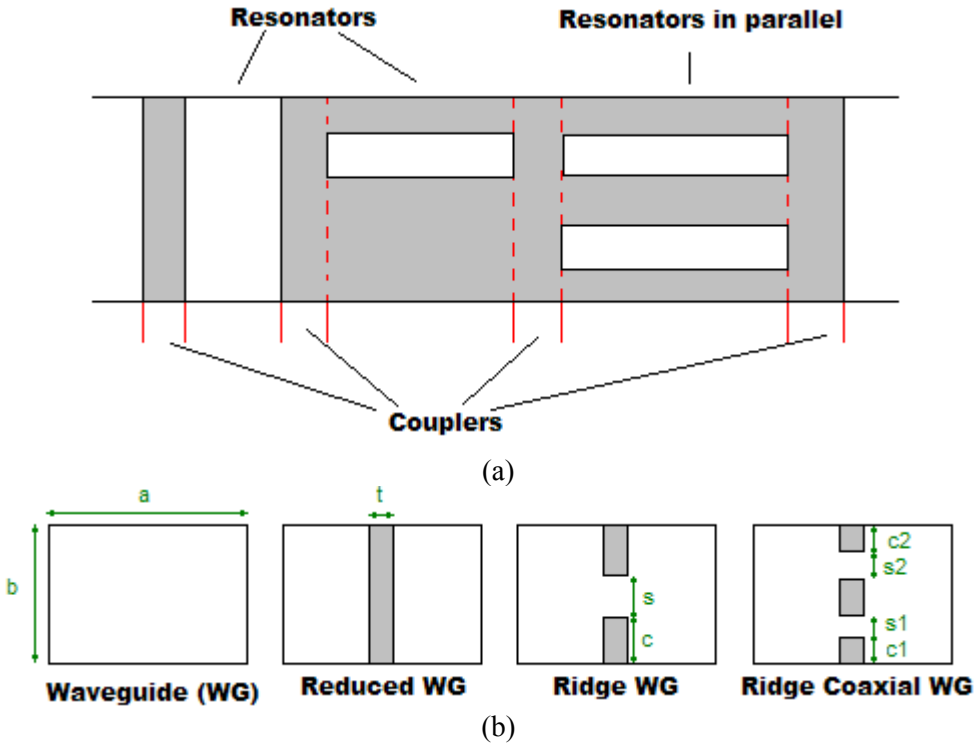

Fig. C-1. All-metal insert indicating the possible parts of a E-Plane filter (a), and cross section of different waveguides (b).

The second problem consists of using the solution from the first problem to apply the mode matching method, including higher order modes, in order to obtain the electromagnetic performance of an E-plane filter. To achieve this, the modelling of the discontinuities formed between the different sections is required. In particular the analysis of the discontinuity formed between the Ridge Coaxial Waveguide (RCWG) and ridge waveguide is described in the next section.

C.1 Scattering matrix

Let be refered the regions at both sides of the discontinuity as I and II, forward propagating waves ($F_{hq}e^{-j\cdot K_{zhq}\cdot z}$) and backward propagating waves ($B_{hq}e^{j\cdot K_{zhq}\cdot z}$) appear. At this point we should mention that for simplicity, the common surface is the complete cross section of the smaller region. With no further loss of generality we assume this region to be region II.

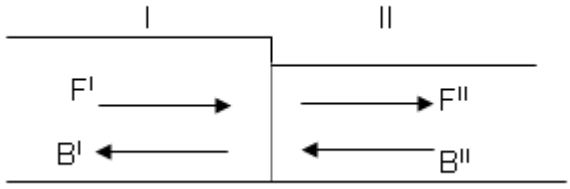

Fig. C-2. Forward and Backward propagating waves both sides of a ridge waveguide to RCWG discontinuity.

The generalized scattering matrix aims to solve for the scattered waves at the discontinuity when the incident waves are known:

$$\begin{bmatrix} B^{I} \\ F^{II} \end{bmatrix} = \begin{bmatrix} S_{11} & S_{12} \\ S_{21} & S_{22} \end{bmatrix} \cdot \begin{bmatrix} F^{I} \\ B^{II} \end{bmatrix} \qquad \textbf{(C-1)}$$

In order for the S-parameters of the generalized scattering matrix to have amplitude between 0 and 1, being able therefore to use them globally and without further analysis, the power carried by each mode with constant amplitude at any side of the discontinuity should have constant value. For simplicity we set the power of any a forward/backward propagating mode with amplitude F/B equal to $1\sqrt{W}$ to be 1W. For convenience the cross section of the RCWG and ridge waveguide structure subject of the study are divided into three and two regions respectively. This is depicted in Fig. C-3.

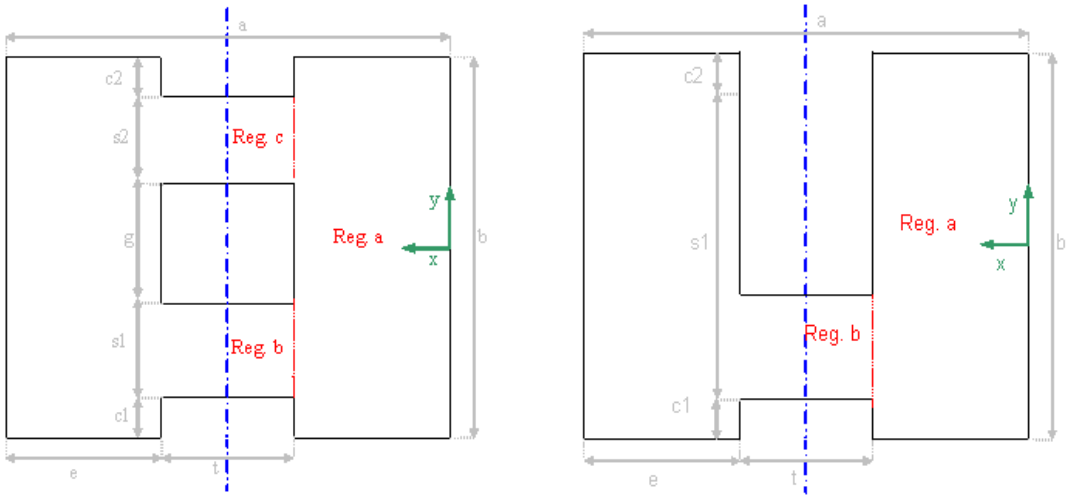

Fig. C-3. Ridge coaxial waveguide and ridge waveguide mode matching.

The expressions for the Helmholtz vector potential relative to TE and TM modes and for the scalar Laplace potential relative to the TEM mode for each structures are:

RCWG (Region I)

- **TE**

Reg a:
$$T_{hq}^{Ia}(x,y) = \sum_{m=0}^{Ma} A_{qm}^{a} \cos\left(K_{xqm}^{a} x\right) \frac{\cos\left(\frac{m\pi}{b}\left(y+\frac{b}{2}\right)\right)}{\sqrt{1+\delta_{om}}} \qquad \textbf{(C-2)}$$

Reg b:
$$T_{hq}^{Ib} = \sum_{m=0}^{Mb} A_{qm}^{b} \frac{1}{K_{xqm}^{b}} \sin\left(K_{xqm}^{b}\cdot\left(x-\frac{a}{2}\right)\right) \cdot \frac{\cos\left(\frac{m\pi}{s1}\left(y+\frac{b}{2}-c1\right)\right)}{\sqrt{1+\delta_{om}}} \qquad \textbf{(C-3)}$$

Reg c:
$$T_{hq}^{Ic} = \sum_{m=0}^{Mc} A_{qm}^{c} \frac{1}{K_{xqm}^{c}} \sin\left(K_{xqm}^{c}\cdot\left(x-\frac{a}{2}\right)\right) \cdot \frac{\cos\left(\frac{m\pi}{s2}\left(y-\frac{b}{2}+c2+s2\right)\right)}{\sqrt{1+\delta_{om}}} \qquad \textbf{(C-4)}$$

- **TM**

Reg a: $$T_{er}^{\ Ia}(x,y)=\sum_{m=1}^{Ma} D_{rm}^{\ a}\,\frac{1}{K_{xrm}^{a}}\sin\left(K_{xrm}^{a}x\right)\sin\left(\frac{m\cdot\pi}{b}\left(y+\frac{b}{2}\right)\right) \qquad \textbf{(C-5)}$$

Reg b: $$T_{er}^{\ Ib}=\sum_{m=1}^{Mb} D_{rm}^{\ b}\cos\left(K_{xrm}^{b}\cdot(x-\frac{a}{2})\right)\cdot\sin\left(\frac{m\cdot\pi}{s1}\left(y+\frac{b}{2}-c1\right)\right) \qquad \textbf{(C-6)}$$

Reg c: $$T_{er}^{\ Ic}=\sum_{m=1}^{Mc} D_{rm}^{\ c}\cos\left(K_{xrm}^{c}\cdot(x-\frac{a}{2})\right)\cdot\sin\left(\frac{m\pi}{s2}\left(y-\frac{b}{2}+c2+s2\right)\right) \qquad \textbf{(C-7)}$$

- **TEM**

Reg a: $$\phi(x,y)=2\sum_{m=1}^{Ma} F_{m}^{\ a}\cdot\exp\left(-\frac{m\cdot\pi\cdot a}{2\cdot b}\right)\cdot\sinh\left(\frac{m\cdot\pi}{b}\cdot x\right)\cdot\sin\left(\frac{m\cdot\pi}{b}(y+\frac{b}{2})\right) \qquad \textbf{(C-8)}$$

Reg b: $$\phi=\frac{V}{s_1}(y+\frac{b}{2}-c_1)+2\sum_{m=1}^{Mb} F_{m}^{\ b}\left[\cosh(\frac{m\pi}{s_1}(x-\frac{a}{2}))\right]\cdot\sin\left(\frac{m\cdot\pi}{s_1}(y+\frac{b}{2}-c_1)\right) \qquad \textbf{(C-9)}$$

Reg c: $$\phi=V-\frac{V}{s_2}(y+\frac{b}{2}-h)+2\sum_{m=1}^{Mc} F_{m}^{\ c}\left[\cosh(\frac{m\pi}{s_2}(x-\frac{a}{2}))\right]\cdot\sin\left(\frac{m\cdot\pi}{s_2}(y+\frac{b}{2}-h)\right)$$

(C-10)

RWG (Region II)

- **TE**

Region a:
$$T_{hs}^{IIa}(x,y) = \sum_{m=0}^{Ma} A_{sm}{}^{a} \cos\left(K_{xsm}^{a} x\right) \cdot \frac{\cos\left(\frac{m\pi}{b}\left(y+\frac{b}{2}\right)\right)}{\sqrt{1+\delta_{om}}} \quad \textbf{(C-11)}$$

Region b:
$$T_{hs}^{IIb} = \sum_{m=0}^{Mb} A_{sm}{}^{b} \frac{1}{K_{xsm}^{b}} \sin\left(K_{xsm}^{b} \cdot (x-\frac{a}{2})\right) \cdot \frac{\cos\left(\frac{m\pi}{s1}\left(y+\frac{b}{2}-c1\right)\right)}{\sqrt{1+\delta_{om}}} \quad \textbf{(C-12)}$$

- **TM**

Region a:
$$T_{et}^{IIa}(x,y) = \sum_{m=1}^{Ma} D_{tm}{}^{a} \frac{1}{K_{xtm}^{a}} \sin\left(K_{xtm}^{a} x\right) \sin\left(\frac{m\cdot\pi}{b}\left(y+\frac{b}{2}\right)\right) \quad \textbf{(C-14)}$$

Region b:
$$T_{et}^{IIb} = \sum_{m=1}^{Mb} D_{tm}{}^{b} \cos\left(K_{xtm}^{b} \cdot (x-\frac{a}{2})\right) \cdot \sin\left(\frac{m\cdot\pi}{s1}\left(y+\frac{b}{2}-c1\right)\right) \quad \textbf{(C-15)}$$

The continuity property of electric fields can now take the following formulation.

$$E_t^{TEM} + E_t^{TE,I} + E_t^{TM,I} = E_t^{TE,II} + E_t^{TM,II} \Rightarrow$$
$$-\nabla_t \phi(F_{TEM} + B_{TEM}) + \sum_{q=1}^{\infty} \sqrt{Z_{hq}^{I}} \left(\nabla T_{hq}^{I} \times \hat{z}\right) \cdot \left(F_{hq}^{I} + B_{hq}^{I}\right) - \sum_{r=1}^{\infty} \sqrt{Z_{er}^{I}} \nabla T_{er}^{I} \cdot \left(F_{er}^{I} + B_{er}^{I}\right) =$$
$$\sum_{s=1}^{\infty} \sqrt{Z_{hs}^{II}} \left(\nabla T_{hs}^{II} \times \hat{z}\right) \cdot \left(F_{hs}^{II} + B_{hs}^{II}\right) - \sum_{t=1}^{\infty} \sqrt{Z_{et}^{II}} \nabla T_{et}^{II} \cdot \left(F_{et}^{II} + B_{et}^{II}\right)$$

(C-16)

Similarly, the continuity of the tangential magnetic field H_t yields to (C-17).

$$H_t^{TEM} + H_t^{TE,I} + H_t^{TM,I} = H_t^{TE,II} + H_t^{TM,II} \Rightarrow$$
$$Y_0 \hat{z} \times (-\nabla_t \phi)(F_{TEM} - B_{TEM}) + \sum_{q=1}^{\infty} \sqrt{Y_{hq}^I} \nabla T_{hq}^I \cdot \left(F_{hq}^I - B_{hq}^I\right) + \sum_{r=1}^{\infty} \sqrt{Y_{er}^I} \left(\nabla T_{er}^I \times \hat{z}\right) \cdot \left(F_{er}^I - B_{er}^I\right) =$$
$$\sum_{s=1}^{\infty} \sqrt{Y_{hs}^{II}} \nabla T_{hs}^{II} \cdot \left(F_{hs}^{II} - B_{hs}^{II}\right) + \sum_{t=1}^{\infty} \sqrt{Y_{et}^{II}} \left(\nabla T_{et}^{II} \times \hat{z}\right) \cdot \left(F_{et}^{II} + B_{et}^{II}\right)$$

(C-17)

In order to solve for the F and B parameters, the x- and t- dependence implied in the cross section functions T shall be canceled. As proceed through the field matching procedure applied to obtain the solution of the ridge waveguide propagation, we must ensure that the tangential electric field of the larger region is zero at metallic boundaries. We therefore successively multiply (C-16) with each of the TEM, TE and TM modal distributions, $-\nabla_t \phi$, $\nabla T_{hq}^I \times \hat{z}$ and $-\nabla T_{er}^I$, then integrate over the cross-section surface of region I to enforce the continuity even in this part o f the cross-section of the RCWG that is shot-circuited.

We use the relation of (C-18) and (C-19)

$$\iint_S \left(\nabla T_{h,ei}^I \times \hat{z}\right) \cdot \left(\nabla T_{h,ej}^I \times \hat{z}\right) \cdot dS = \iint_S \nabla T_{h,ei}^I \cdot \nabla T_{h,ej}^I \cdot dS = \delta_{ij} \qquad \textbf{(C-18)}$$

$$\iint_S \left(\nabla T_{er}^I \times \hat{z}\right) \cdot \nabla T_{hq}^I \cdot dS = \iint_S \nabla T_{er}^I \cdot \left(\nabla T_{hq}^I \times \hat{z}\right) \cdot dS = 0 \qquad \textbf{(C-19)}$$

(C-18) is the mathematical expression of the fact that both the sets of TE and TM modes are orthogonal (C-19) is the mathematical expression of the fact that TE and TM modes in a hollow waveguide are uncoupled. These identities are easily verified upon substitution of the transverse dependence functions.

Upon rearrangement of the expressions in matrix form, is obtained:

$$\left(F_{TEM}^{I}+B_{TEM}^{I}\right)=J_{TEMh}\cdot diag\left\{\sqrt{Z_{hs}^{II}}\right\}\cdot\left(F_{h}^{II}+B_{h}^{II}\right)+J_{TEMe}\cdot diag\left\{\sqrt{Z_{et}^{II}}\right\}\cdot\left(F_{e}^{II}+B_{e}^{II}\right) \quad \textbf{(C-20)}$$

$$diag\left\{\sqrt{Z_{hq}^{I}}\right\}\cdot\left(F_{h}^{I}+B_{h}^{I}\right)=J_{hh}\cdot diag\left\{\sqrt{Z_{hs}^{II}}\right\}\cdot\left(F_{h}^{II}+B_{h}^{II}\right)+J_{he}\cdot diag\left\{\sqrt{Z_{et}^{II}}\right\}\cdot\left(F_{e}^{II}+B_{e}^{II}\right) \quad \textbf{(C-21)}$$

$$diag\left\{\sqrt{Z_{er}^{I}}\right\}\cdot\left(F_{e}^{I}+B_{e}^{I}\right)=J_{eh}\cdot diag\left\{\sqrt{Z_{hs}^{II}}\right\}\cdot\left(F_{h}^{II}+B_{h}^{II}\right)+J_{ee}\cdot diag\left\{\sqrt{Z_{et}^{II}}\right\}\cdot\left(F_{e}^{II}+B_{e}^{II}\right) \quad \textbf{(C-22)}$$

Similar procedure we follow in order to eliminate the x- and y- dependence from H_t. However now, since we are dealing with magnetic fields, there is no zero condition for tangential components at metallic boundaries. Hence now we successively multiply (C-17) with ∇T_{hs}^{II} and $\nabla T_{et}^{II}\times\hat{z}$ and then integrate over the smaller cross-section (region II). Upon rearrangement in a matrix form, we finally obtain:

$$J_{hh}^{T}\cdot diag\left\{\sqrt{Y_{hq}^{I}}\right\}\cdot\left(F_{h}^{I}-B_{h}^{I}\right)+J_{eh}^{T}\cdot diag\left\{\sqrt{Y_{er}^{I}}\right\}\cdot\left(F_{e}^{I}-B_{e}^{I}\right)=diag\left\{\sqrt{Y_{hs}^{II}}\right\}\cdot\left(F_{h}^{II}-B_{h}^{II}\right) \quad \textbf{(C-23)}$$

$$J_{he}^{T}\cdot diag\left\{\sqrt{Y_{hq}^{I}}\right\}\cdot\left(F_{h}^{I}-B_{h}^{I}\right)+J_{ee}^{T}\cdot diag\left\{\sqrt{Y_{er}^{I}}\right\}\cdot\left(F_{e}^{I}-B_{e}^{I}\right)=diag\left\{\sqrt{Y_{et}^{II}}\right\}\cdot\left(F_{e}^{II}-B_{e}^{II}\right) \quad \textbf{(C-24)}$$

The matrices J are given at the following expressions:

$$\left(J_{hTEM}\right)_{q}=\iint_{SII}(\nabla T_{hq}^{II}\times\hat{z})\cdot(-\nabla_{t}\Phi)dS \quad \textbf{(C-25)}$$

$$\left(J_{eTEM}\right)_{p}=\iint_{SII}(\nabla T_{ep}^{II})\cdot(-\nabla_{t}\Phi)dS \quad \textbf{(C-26)}$$

$$\left(J_{hh}\right)_{qs}=\iint_{SII}(\nabla T_{hq}^{I}\times\hat{z})\cdot(\nabla T_{hs}^{II}\times\hat{z})dS \quad \textbf{(C-27)}$$

$$\left(J_{eh}\right)_{rs}=\iint_{SII}(-\nabla T_{er}^{I})\cdot(\nabla T_{hs}^{II}\times\hat{z})dS \quad \textbf{(C-28)}$$

$$\left(J_{he}\right)_{qt}=\iint_{SII}(\nabla T_{hq}^{I}\times\hat{z})\cdot(-\nabla T_{et}^{II})dS \quad \textbf{(C-29)}$$

$$\left(J_{ee}\right)_{rt}=\iint_{SII}(-\nabla T_{er}^{I})\cdot(-\nabla T_{et}^{II})dS \quad \textbf{(C-30)}$$

$$\left(J_{TEMh}\right)_{s}=\iint_{SII}(-\nabla_{t}\Phi)\cdot(\nabla T_{hs}^{II})dS \quad \textbf{(C-31)}$$

$$\left(J_{TEMe}\right)_t = \iint_{SII} (-\nabla_t \Phi)\cdot(\nabla T_{et}^{II} \times \hat{z}) dS \qquad \textbf{(C-32)}$$

The integral of equation (C-29) is identically zero, thus suggesting that TE modes of region I are not couple with TM modes of region II. Also, eq. (C-25) and (C-26) are identical to 16 and 17, so only the latter are calculated The five J matrices (C-27), (C-29), (C-30), (C-31), (C-32) are analytically solved in Appendix C.2.

Upon multiplication (C-21),(C-22),(C-23**)** and (C-24) with, $diag\left\{\sqrt{Y_{hq}^I}\right\}$, $diag\left\{\sqrt{Y_{er}^I}\right\}$, $diag\left\{\sqrt{Y_{hs}^{II}}\right\}$, $diag\left\{\sqrt{Y_{ey}^{II}}\right\}$ respectively, we can write in a matrix form:

$$\begin{bmatrix} F_{TEM}^I + B_{TEM}^I \\ F_h^I + B_h^I \\ F_e^I + B_e^I \end{bmatrix} = M \cdot \begin{bmatrix} F_h^{II} + B_h^{II} \\ F_e^{II} + B_e^{II} \end{bmatrix} \qquad \begin{bmatrix} F_h^{II} - B_h^{II} \\ F_e^{II} - B_e^{II} \end{bmatrix} = M^T \cdot \begin{bmatrix} F_{TEM}^I - B_{TEM}^I \\ F_h^I - B_h^I \\ F_e^I - B_e^I \end{bmatrix} \qquad \textbf{(C-33)}$$

where:

$$M = \begin{bmatrix} J_{TEMt} \cdot diag\left\{\sqrt{Z_{hd}^{II}}\right\} & J_{TEMe} \cdot diag\left\{\sqrt{Z_{er}^{II}}\right\} \\ diag\left\{\sqrt{Y_{hq}^I}\right\} \cdot J_{hh} \cdot diag\left\{\sqrt{Z_{hs}^{II}}\right\} & diag\left\{\sqrt{Y_{hq}^I}\right\} \cdot J_{he} \cdot diag\left\{\sqrt{Z_{et}^{II}}\right\} \\ diag\left\{\sqrt{Y_{er}^I}\right\} \cdot J_{eh} \cdot diag\left\{\sqrt{Z_{hs}^{II}}\right\} & diag\left\{\sqrt{Y_{er}^I}\right\} \cdot J_{ee} \cdot diag\left\{\sqrt{Z_{et}^{II}}\right\} \end{bmatrix} \qquad \textbf{(C-34)}$$

Rearranging forward and backward waves in equations (C-33), we can derive the scattering matrix:

$$\begin{bmatrix} \begin{bmatrix} B_{TEM}^I \\ B_h^I \\ B_e^I \end{bmatrix} \\ \begin{bmatrix} F_h^{II} \\ F_e^{II} \end{bmatrix} \end{bmatrix} = \begin{bmatrix} S_{11} & S_{12} \\ S_{21} & S_{22} \end{bmatrix} \cdot \begin{bmatrix} \begin{bmatrix} F_{TEM}^I \\ F_h^I \\ F_e^I \end{bmatrix} \\ \begin{bmatrix} B_h^{II} \\ B_e^{II} \end{bmatrix} \end{bmatrix} \qquad \textbf{(C-35)}$$

where:

$$
\begin{aligned}
S_{11} &= -W \cdot \left(U - M \cdot M^T\right) \\
S_{12} &= 2 \cdot W \cdot M \\
S_{21} &= M^T \cdot \left[U + W \cdot \left(U - M \cdot M^T\right)\right] \\
S_{22} &= U - 2 \cdot M^T \cdot W \cdot M
\end{aligned}
\qquad \textbf{(C-36)}
$$

and:

$$W = \left(U + M \cdot M^T\right)^{-1}$$

Hence we have obtained the scattering matrix for a surface discontinuity. This procedure is applicable to all discontinuities that we will discuss further on. We should also mention here that when the Hertzian potentials are expressed as double sums (sum over two indices), we should transform these to single sum (sum over a single index). This is achieved by sorting the modes according to increasing cutoff frequency, and sum over the number of modes.

C.2 Analytical form of the mode-matching coupling integrals

J_{hTEM} SOLUTION (C-25)

After that, we can study each region '*a*' and *'b'* independently.

$$\left(J_{hTEM}\right)_q = \underbrace{\int_0^e \int_{-\frac{b}{2}}^{\frac{b}{2}} (\nabla T_{hq}^{IIa} \times \hat{z}) \cdot (-\nabla_t \phi^{Ia}) dxdy}_{J_{hTEM}^a} + \underbrace{\int_e^{\frac{a}{2}} \int_{-\frac{b}{2}+c1}^{-\frac{b}{2}+c1+s1} (\nabla T_{hq}^{IIb} \times \hat{z}) \cdot (-\nabla_t \phi^{IIb}) dxdy}_{J_{hTEM}^b}$$

Furthermore we can separate $J_{hTEM}{}^a$ and $J_{hTEM}{}^b$ in two parts:

$$J_{hTEM}^a = \underbrace{-\int_0^e \int_{-\frac{b}{2}}^{\frac{b}{2}} \left(\frac{\partial T_{hq}^{IIa}}{\partial y} \cdot \frac{\partial \phi^{Ia}}{\partial x}\right) dxdy}_{J_{hTEM}^{a1}} + \underbrace{\int_0^e \int_{-\frac{b}{2}}^{\frac{b}{2}} \left(\frac{\partial T_{hq}^{IIa}}{\partial x} \cdot \frac{\partial \phi^{Ia}}{\partial y}\right) dxdy}_{J_{hTEM}^{a2}}$$

$$J_{hTEM}^b = \underbrace{\int_e^{\frac{a}{2}} \int_{-\frac{b}{2}+c1}^{-\frac{b}{2}+c1+s1} \left(\frac{\partial T_{hq}^{Ib}}{\partial y} \cdot \frac{\partial \phi^{Ib}}{\partial x}\right) dxdy}_{J_{hTEM}^{b1}} + \underbrace{\int_e^{\frac{a}{2}} \int_{-\frac{b}{2}+c1}^{-\frac{b}{2}+c1+s1} \left(\frac{\partial T_{hq}^{Ib}}{\partial x} \cdot \frac{\partial \phi^{Ib}}{\partial y}\right) dxdy}_{J_{hTEM}^{b2}}$$

This integral can be expanded as:

$$J_{hTEM}^{a1}=-\sum_{m=1}^{Ma}A_{sm}^{a}\cdot F_{m}^{a}\cdot\frac{\pi^2\cdot m^2}{2\cdot b}\cdot\left[\frac{\exp\left(-\frac{m\cdot\pi\cdot a}{b\cdot 2}\right)}{\left(\frac{m\cdot\pi}{b}\right)^2+\left(k_{xsm}^{a}\right)^2}\cdot\left[\begin{array}{l}\exp\left(\frac{m\cdot\pi\cdot e}{b}\right)\cdot\left[\frac{m\cdot\pi}{b}\cdot\cos\left(k_{xsm}^{a}\cdot e\right)+k_{xsm}^{a}\cdot\sin\left(k_{xsm}^{a}\cdot e\right)\right]\\+\exp\left(-\frac{m\cdot\pi\cdot e}{b}\right)\left[-\frac{m\cdot\pi}{b}\cdot\cos\left(k_{xsm}^{a}\cdot e\right)+k_{xsm}^{a}\cdot\sin\left(k_{xsm}^{a}\cdot e\right)\right]\end{array}\right]\right]$$

$$J_{hTEM}^{a2}=\sum_{m=1}^{Ma}A_{sm}^{a}\cdot F_{m}^{a}\cdot k_{xsm}^{a}\cdot\frac{\pi\cdot m}{2}\cdot\left[\frac{\exp\left(-\frac{m\cdot\pi\cdot a}{b\cdot 2}\right)}{\left(\frac{m\cdot\pi}{b}\right)^2+\left(k_{xsm}^{a}\right)^2}\cdot\left[\begin{array}{l}\exp\left(\frac{m\cdot\pi\cdot e}{b}\right)\cdot\left[\frac{m\cdot\pi}{b}\cdot\sin\left(k_{xsm}^{a}\cdot e\right)-k_{xsm}^{a}\cdot\cos\left(k_{xsm}^{a}\cdot e\right)\right]\\+\exp\left(-\frac{m\cdot\pi\cdot e}{b}\right)\left[\frac{m\cdot\pi}{b}\cdot\sin\left(k_{xsm}^{a}\cdot e\right)+k_{xsm}^{a}\cdot\cos\left(k_{xsm}^{a}\cdot e\right)\right]\end{array}\right]\right]$$

$$J_{hTEM}^{b1}=-\sum_{m=1}^{Mb}A_{sm}^{b}\cdot F_{m}^{b}\cdot\frac{\pi^2\cdot m^2}{2\cdot s_1\cdot k_{xsm}^{b}}\cdot\left[\frac{1}{\left(\frac{m\cdot\pi}{b}\right)^2+\left(k_{xsm}^{b}\right)^2}\cdot\left[\begin{array}{l}-\exp\left(\frac{m\cdot\pi\cdot t}{2\cdot s_1}\right)\cdot\left[-\frac{m\cdot\pi}{s_1}\cdot\cos\left(-k_{xsm}^{b}\cdot\frac{t}{2}\right)+k_{xsm}^{b}\cdot\sin\left(-k_{xsm}^{b}\cdot\frac{t}{2}\right)\right]\\+\exp\left(-\frac{m\cdot\pi\cdot t}{2\cdot s_1}\right)\left[\frac{m\cdot\pi}{s_1}\cdot\cos\left(-k_{xsm}^{b}\cdot\frac{t}{2}\right)+k_{xsm}^{b}\cdot\sin\left(-k_{xsm}^{b}\cdot\frac{t}{2}\right)\right]\\\frac{-2\cdot m\cdot\pi}{s_1}\end{array}\right]\right]$$

$$J_{hTEM}^{b2}=\sum_{m=1}^{Mb}A_{sm}^{b}\cdot F_{m}^{b}\cdot\pi\cdot m\cdot\left[\frac{\sinh\left(\frac{m\cdot t}{2\cdot s_1}\right)}{\left(\frac{m\cdot\pi}{s_1}\right)^2+\left(k_{xsm}^{b}\right)^2}\cdot\left[\frac{m\cdot\pi}{s_1}\cdot\cos\left(-k_{xsm}^{b}\cdot\frac{t}{2}\right)+k_{xsm}^{b}\cdot\sin\left(-k_{xsm}^{b}\cdot\frac{t}{2}\right)\right]\right]$$

J_{eTEM} SOLUTION **(C-26)**

After that, we can study each region '*a'* and *'b'* independently.

$$\left(J_{eTEM}\right)_r=\underbrace{\int_0^e\int_{-\frac{b}{2}}^{\frac{b}{2}}(\nabla T_{er}^{IIa})\cdot(-\nabla_t\phi^{Ia})dxdy}_{J_{eTEM}^{a}}+\underbrace{\int_e^{\frac{a}{2}}\int_{-\frac{b}{2}+c1+s1}^{-\frac{b}{2}+c1}(\nabla T_{er}^{IIb})\cdot(-\nabla_t\phi^{IIb})dxdy}_{J_{eTEM}^{b}}$$

Furthermore we can separate $J_{hTEM}{}^{a}$ and $J_{hTEM}{}^{b}$ in two parts:

$$J_{eTEM}^{a}=\underbrace{-\int_0^e\int_{-\frac{b}{2}}^{\frac{b}{2}}(\frac{\partial T_{er}^{IIa}}{\partial x}\cdot\frac{\partial\phi^{Ia}}{\partial x})dxdy}_{J_{eTEM}^{a1}}\underbrace{-\int_0^e\int_{-\frac{b}{2}}^{\frac{b}{2}}(\frac{\partial T_{er}^{IIa}}{\partial y}\cdot\frac{\partial\phi^{Ia}}{\partial y})dxdy}_{J_{eTEM}^{a2}}$$

$$J_{eTEM}^{b}=\underbrace{-\int_e^{\frac{a}{2}}\int_{-\frac{b}{2}+c1}^{-\frac{b}{2}+c1+s1}(\frac{\partial T_{er}^{IIb}}{\partial x}\cdot\frac{\partial\phi^{Ib}}{\partial x})dxdy}_{J_{eTEM}^{b1}}\underbrace{-\int_e^{\frac{a}{2}}\int_{-\frac{b}{2}+c1}^{-\frac{b}{2}+c1+s1}(\frac{\partial T_{er}^{IIb}}{\partial y}\cdot\frac{\partial\phi^{Ib}}{\partial y})dxdy}_{J_{hTEM}^{b2}}$$

This integral can be expanded as a summation of the following terms:

$$J_{eTEM}^{a1}=-\sum_{m=1}^{Ma}D_{sm}^{a}\cdot F_{m}^{a}\cdot\frac{\pi\cdot m}{2}\cdot\left[\frac{\exp\left(-\frac{m\cdot\pi\cdot a}{b\cdot 2}\right)}{\left(\frac{m\cdot\pi}{b}\right)^{2}+\left(k_{xsm}^{a}\right)^{2}}\cdot\left[\begin{array}{l}\exp\left(\frac{m\cdot\pi\cdot e}{b}\right)\cdot\left[\frac{m\cdot\pi}{b}\cdot\cos\left(k_{xsm}^{a}\cdot e\right)+k_{xsm}^{a}\cdot\sin\left(k_{xsm}^{a}\cdot e\right)\right]\\+\exp\left(-\frac{m\cdot\pi\cdot e}{b}\right)\left[-\frac{m\cdot\pi}{b}\cdot\cos\left(k_{xsm}^{a}\cdot e\right)+k_{xsm}^{a}\cdot\sin\left(k_{xsm}^{a}\cdot e\right)\right]\end{array}\right]\right]$$

$$J_{eTEM}^{a2}=\sum_{m=1}^{Ma}D_{sm}^{a}\cdot F_{m}^{a}\cdot\frac{\pi^{2}\cdot m^{2}}{2\cdot b}\cdot\left[\frac{\exp\left(-\frac{m\cdot\pi\cdot a}{b\cdot 2}\right)}{\left(\frac{m\cdot\pi}{b}\right)^{2}+\left(k_{xsm}^{a}\right)^{2}}\cdot\left[\begin{array}{l}\exp\left(\frac{m\cdot\pi\cdot e}{b}\right)\cdot\left[\frac{m\cdot\pi}{b}\cdot\sin\left(k_{xsm}^{a}\cdot e\right)-k_{xsm}^{a}\cdot\cos\left(k_{xsm}^{a}\cdot e\right)\right]\\+\exp\left(-\frac{m\cdot\pi\cdot e}{b}\right)\left[\frac{m\cdot\pi}{b}\cdot\sin\left(k_{xsm}^{a}\cdot e\right)+k_{xsm}^{a}\cdot\cos\left(k_{xsm}^{a}\cdot e\right)\right]\end{array}\right]\right]$$

$$J_{eTEM}^{b1}=-\sum_{m=1}^{Mb}D_{sm}^{b}\cdot F_{m}^{b}\cdot\frac{\pi\cdot m}{2}\cdot\left[\frac{1}{\left(\frac{m\cdot\pi}{b}\right)^{2}+\left(k_{xsm}^{b}\right)^{2}}\cdot\left[\begin{array}{l}-\exp\left(\frac{m\cdot\pi\cdot t}{2\cdot s_{1}}\right)\cdot\left[-\frac{m\cdot\pi}{s_{1}}\cdot\cos\left(-k_{xsm}^{b}\cdot\frac{t}{2}\right)+k_{xsm}^{b}\cdot\sin\left(-k_{xsm}^{b}\cdot\frac{t}{2}\right)\right]\\+\exp\left(-\frac{m\cdot\pi\cdot t}{2\cdot s_{1}}\right)\left[\frac{m\cdot\pi}{s_{1}}\cdot\cos\left(-k_{xsm}^{b}\cdot\frac{t}{2}\right)+k_{xsm}^{b}\cdot\sin\left(-k_{xsm}^{b}\cdot\frac{t}{2}\right)\right]\\\frac{-2\cdot m\cdot\pi}{s_{1}}\end{array}\right]\right]$$

$$J_{eTEM}^{b2}=\sum_{m=1}^{Mb}D_{sm}^{b}\cdot F_{m}^{b}\cdot\frac{\pi^{2}\cdot m^{2}}{s_{1}}\cdot\left[\frac{\sinh\left(\frac{m\cdot t}{2\cdot s_{1}}\right)}{\left(\frac{m\cdot\pi}{s_{1}}\right)^{2}+\left(k_{xsm}^{b}\right)^{2}}\cdot\left[\frac{m\cdot\pi}{s_{1}}\cdot\cos\left(-k_{xsm}^{b}\cdot\frac{t}{2}\right)+k_{xsm}^{b}\cdot\sin\left(-k_{xsm}^{b}\cdot\frac{t}{2}\right)\right]\right]$$

J_{hh} SOLUTION (C-27)

After that, we can study each region '*a*' and *'b'* independently.

$$\left(J_{hh}\right)_{qs}=\underbrace{\int_{0}^{e}\int_{-\frac{b}{2}}^{\frac{b}{2}}(\nabla T_{hq}^{Ia}\times\hat{z})\cdot(\nabla T_{hs}^{IIa}\times\hat{z})dxdy}_{J_{hh}^{a}}+\underbrace{\int_{e}^{\frac{a}{2}}\int_{-\frac{b}{2}+c1}^{-\frac{b}{2}+c1+s1}(\nabla T_{hq}^{Ib}\times\hat{z})\cdot(\nabla T_{hs}^{IIb}\times\hat{z})dxdy}_{J_{hh}^{b}}$$

Furthermore we can separate $J_{hh}{}^{a}$ and $J_{hh}{}^{b}$ in two parts:

$$J_{hh}^{a}=\underbrace{\int_{0}^{e}\int_{-\frac{b}{2}}^{\frac{b}{2}}(\frac{\partial T_{hq}^{Ia}}{\partial y}\cdot\frac{\partial T_{hs}^{IIa}}{\partial y})dxdy}_{J_{hh}^{a1}}+\underbrace{\int_{0}^{e}\int_{-\frac{b}{2}}^{\frac{b}{2}}(\frac{\partial T_{hq}^{Ia}}{\partial x}\cdot\frac{\partial T_{hs}^{IIa}}{\partial x})dxdy}_{J_{hh}^{a2}}$$

$$J_{hh}^{b}=\underbrace{\int_{e}^{\frac{a}{2}}\int_{-\frac{b}{2}+c1}^{-\frac{b}{2}+c1+s1}(\frac{\partial T_{hq}^{Ib}}{\partial y}\cdot\frac{\partial T_{hs}^{IIb}}{\partial y})dxdy}_{J_{hh}^{b1}}+\underbrace{\int_{e}^{\frac{a}{2}}\int_{-\frac{b}{2}+c1}^{-\frac{b}{2}+c1+s1}(\frac{\partial T_{hq}^{Ib}}{\partial x}\cdot\frac{\partial T_{hs}^{IIb}}{\partial x})dxdy}_{J_{hh}^{b2}}$$

If we solve this integrals we obtain the following solutions:

$$J_{hh}^{a1}=\sum_{m=1}^{Ma}A_{qm}^{a}\cdot A_{sm}^{a}\cdot\frac{m^2\pi^2}{4\cdot b}\cdot\left[\frac{\sin\left(\left(k_{xqm}^{a}-k_{xsm}^{a}\right)e\right)}{\left(k_{xqm}^{a}-k_{xsm}^{a}\right)}+\frac{\sin\left(\left(k_{xqm}^{a}+k_{xsm}^{a}\right)e\right)}{\left(k_{xqm}^{a}+k_{xsm}^{a}\right)}\right]$$

$$J_{hh}^{a2}=\sum_{m=0}^{Ma}A_{qm}^{a}\cdot A_{sm}^{a}\cdot k_{xqm}^{a}\cdot k_{xsm}^{a}\,\frac{b}{4}\cdot\left[\frac{\sin\left(\left(k_{xqm}^{a}-k_{xsm}^{a}\right)e\right)}{\left(k_{xqm}^{a}-k_{xsm}^{a}\right)}-\frac{\sin\left(\left(k_{xqm}^{a}+k_{xsm}^{a}\right)e\right)}{\left(k_{xqm}^{a}+k_{xsm}^{a}\right)}\right]$$

$$J_{hh}^{b1}=\sum_{m=1}^{Mb}A_{qm}^{b}\cdot A_{sm}^{b}\cdot\frac{1}{k_{xqm}^{b}\cdot k_{xsm}^{b}}\,\frac{m^2\pi^2}{4\cdot s1}\cdot\left[\frac{\sin\left(\left(k_{xqm}^{b}-k_{xsm}^{b}\right)\frac{t}{2}\right)}{\left(k_{xqm}^{b}-k_{xsm}^{b}\right)}-\frac{\sin\left(\left(k_{xqm}^{b}+k_{xsm}^{b}\right)\frac{t}{2}\right)}{\left(k_{xqm}^{b}+k_{xsm}^{b}\right)}\right]$$

$$J_{hh}^{b2}=\sum_{m=0}^{Mb}A_{qm}^{b}\cdot A_{sm}^{b}\cdot\frac{s1}{4}\cdot\left[\frac{\sin\left(\left(k_{xqm}^{b}-k_{xsm}^{b}\right)\frac{t}{2}\right)}{\left(k_{xqm}^{b}-k_{xsm}^{b}\right)}+\frac{\sin\left(\left(k_{xqm}^{b}+k_{xsm}^{b}\right)\frac{t}{2}\right)}{\left(k_{xqm}^{b}+k_{xsm}^{b}\right)}\right]$$

J_{eh} SOLUTION **(C-28)**

We solve that integral as we solved J_{hh}.

First of all, we can study each region '*a'* and *'b'* independently.

$$\left(J_{eh}\right)_{rs}=\underbrace{\int_{0}^{e}\int_{-\frac{b}{2}}^{\frac{b}{2}}(-\nabla T_{er}^{Ia})\cdot(\nabla T_{hs}^{IIa}\times\hat{z})dxdy}_{J_{eh}^{a}}+\underbrace{\int_{e}^{\frac{a}{2}}\int_{-\frac{b}{2}+c1}^{-\frac{b}{2}+c1+s1}(-\nabla T_{er}^{Ib})\cdot(\nabla T_{hs}^{IIb}\times\hat{z})dxdy}_{J_{eh}^{b}}$$

Furthermore we can separate $J_{eh}{}^{a}$ and $J_{eh}{}^{b}$ in two parts:

$$J_{eh}^{a}=\underbrace{-\int_{0}^{e}\int_{-\frac{b}{2}}^{\frac{b}{2}}(\frac{\partial T_{er}^{Ia}}{\partial x}\cdot\frac{\partial T_{hs}^{IIa}}{\partial y})dxdy}_{J_{eh}^{a1}}+\underbrace{\int_{0}^{e}\int_{-\frac{b}{2}}^{\frac{b}{2}}(\frac{\partial T_{er}^{Ia}}{\partial y}\cdot\frac{\partial T_{hs}^{IIa}}{\partial x})dxdy}_{J_{eh}^{a2}}$$

$$J_{eh}^{b}=\underbrace{-\int_{e}^{\frac{a}{2}}\int_{-\frac{b}{2}+c1}^{-\frac{b}{2}+c1+s1}(\frac{\partial T_{er}^{Ib}}{\partial x}\cdot\frac{\partial T_{hs}^{IIb}}{\partial y})dxdy}_{J_{eh}^{b1}}+\underbrace{\int_{e}^{\frac{a}{2}}\int_{-\frac{b}{2}+c1}^{-\frac{b}{2}+c1+s1}(\frac{\partial T_{er}^{Ib}}{\partial y}\cdot\frac{\partial T_{hs}^{IIb}}{\partial x})dxdy}_{J_{eh}^{b2}}$$

If we solve this integrals we obtain the following solutions:

$$J_{eh}^{a1}=\sum_{m=1}^{Ma}D_{rm}^{a}\cdot A_{sm}^{a}\cdot\frac{m\pi}{4}\cdot\left[\frac{\sin\left(\left(k_{xrm}^{a}-k_{xsm}^{a}\right)e\right)}{\left(k_{xrm}^{a}-k_{xsm}^{a}\right)}+\frac{\sin\left(\left(k_{xrm}^{a}+k_{xsm}^{a}\right)e\right)}{\left(k_{xrm}^{a}+k_{xsm}^{a}\right)}\right]$$

$$J_{eh}^{a2}=-\sum_{m=1}^{Ma}D_{rm}^{a}\cdot A_{sm}^{a}\cdot\frac{k_{xsm}^{a}}{k_{xrm}^{a}}\cdot\frac{m\pi}{4}\cdot\left[\frac{\sin\left(\left(k_{xrm}^{a}-k_{xsm}^{a}\right)e\right)}{\left(k_{xrm}^{a}-k_{xsm}^{a}\right)}-\frac{\sin\left(\left(k_{xrm}^{a}+k_{xsm}^{a}\right)e\right)}{\left(k_{xrm}^{a}+k_{xsm}^{a}\right)}\right]$$

$$J_{eh}^{b1}=-\sum_{m=1}^{Mb}D_{rm}^{b}\cdot A_{sm}^{b}\cdot\frac{k_{xrm}^{b}}{k_{xsm}^{b}}\cdot\frac{m\pi}{4}\cdot\left[\frac{\sin\left(\left(k_{xrm}^{b}-k_{xsm}^{b}\right)\frac{t}{2}\right)}{\left(k_{xrm}^{b}-k_{xsm}^{b}\right)}-\frac{\sin\left(\left(k_{xrm}^{b}+k_{xsm}^{b}\right)\frac{t}{2}\right)}{\left(k_{xrm}^{b}+k_{xsm}^{b}\right)}\right]$$

$$J_{eh}^{b2}=\sum_{m=1}^{Mb}D_{rm}^{b}\cdot A_{sm}^{b}\cdot\frac{m\pi}{4}\cdot\left[\frac{\sin\left(\left(k_{xrm}^{b}-k_{xsm}^{b}\right)\frac{t}{2}\right)}{\left(k_{xrm}^{b}-k_{xsm}^{b}\right)}+\frac{\sin\left(\left(k_{xrm}^{b}+k_{xsm}^{b}\right)\frac{t}{2}\right)}{\left(k_{xrm}^{b}+k_{xsm}^{b}\right)}\right]$$

J_{ee} SOLUTION **(C-30)**

As the previous cases we obtain $J_{ee.}$ Initially, we can study each region '*a'* and *'b'* independently.

$$\left(J_{ee}\right)_{rt}=\underbrace{\int_{0}^{e}\int_{-\frac{b}{2}}^{\frac{b}{2}}(\nabla T_{er}^{Ia})\cdot(\nabla T_{et}^{IIa})dxdy}_{J_{ee}^{a}}+\underbrace{\int_{e}^{\frac{a}{2}}\int_{-\frac{b}{2}+c1}^{\frac{b}{2}+c1+s1}(\nabla T_{er}^{Ib})\cdot(\nabla T_{et}^{IIb})dxdy}_{J_{ee}^{b}}$$

Furthermore we can separate $J_{ee}{}^{a}$ and $J_{ee}{}^{b}$ in two parts:

$$J_{ee}^{a}=\underbrace{\int_{0}^{e}\int_{-\frac{b}{2}}^{\frac{b}{2}}(\frac{\partial T_{er}^{Ia}}{\partial x}\cdot\frac{\partial T_{et}^{IIa}}{\partial x})dxdy}_{J_{ee}^{a1}}+\underbrace{\int_{0}^{e}\int_{-\frac{b}{2}}^{\frac{b}{2}}(\frac{\partial T_{er}^{Ia}}{\partial y}\cdot\frac{\partial T_{et}^{IIa}}{\partial y})dxdy}_{J_{ee}^{a2}}$$

$$J_{ee}^{b}=\underbrace{\int_{e}^{\frac{a}{2}}\int_{-\frac{b}{2}+c1}^{\frac{b}{2}+c1+s1}(\frac{\partial T_{er}^{Ib}}{\partial x}\cdot\frac{\partial T_{et}^{IIb}}{\partial x})dxdy}_{J_{ee}^{b1}}+\underbrace{\int_{e}^{\frac{a}{2}}\int_{-\frac{b}{2}+c1}^{\frac{b}{2}+c1+s1}(\frac{\partial T_{er}^{Ib}}{\partial y}\cdot\frac{\partial T_{et}^{IIb}}{\partial y})dxdy}_{J_{ee}^{b2}}$$

If we solve this integrals we obtain the following solutions:

$$J_{ee}^{a1}=\sum_{m=1}^{Ma}D_{rm}^{a}\cdot D_{tm}^{a}\cdot\frac{b}{4}\cdot\left[\frac{\sin\left(\left(k_{xrm}^{a}-k_{xtm}^{a}\right)e\right)}{\left(k_{xrm}^{a}-k_{xtm}^{a}\right)}+\frac{\sin\left(\left(k_{xrm}^{a}+k_{xtm}^{a}\right)e\right)}{\left(k_{xrm}^{a}+k_{xtm}^{a}\right)}\right]$$

$$J_{ee}^{a2} = \sum_{m=1}^{Ma} D_{rm}^{a} \cdot D_{tm}^{a} \cdot \frac{1}{k_{xrm}^{a} \cdot k_{xtm}^{a}} \frac{m^2 \pi^2}{4 \cdot b} \cdot \left[\frac{\sin\left(\left(k_{xrm}^{a} - k_{xtm}^{a}\right) e\right)}{\left(k_{xrm}^{a} - k_{xtm}^{a}\right)} - \frac{\sin\left(\left(k_{xrm}^{a} + k_{xtm}^{a}\right) e\right)}{\left(k_{xrm}^{a} + k_{xtm}^{a}\right)} \right]$$

$$J_{ee}^{b1} = \sum_{m=1}^{Mb} D_{rm}^{b} \cdot D_{tm}^{b} \cdot k_{xrm}^{b} \cdot k_{xtm}^{b} \cdot \frac{s1}{4} \cdot \left[\frac{\sin\left(\left(k_{xrm}^{b} - k_{xtm}^{b}\right) \frac{t}{2}\right)}{\left(k_{xrm}^{b} - k_{xtm}^{b}\right)} - \frac{\sin\left(\left(k_{xrm}^{b} + k_{xtm}^{b}\right) \frac{t}{2}\right)}{\left(k_{xrm}^{b} + k_{xtm}^{b}\right)} \right]$$

$$J_{ee}^{b2} = \sum_{m=1}^{Mb} D_{rm}^{b} \cdot D_{tm}^{b} \cdot \frac{m^2 \pi^2}{4 \cdot s1} \cdot \left[\frac{\sin\left(\left(k_{xrm}^{b} - k_{xtm}^{b}\right) \frac{t}{2}\right)}{\left(k_{xrm}^{b} - k_{xtm}^{b}\right)} + \frac{\sin\left(\left(k_{xrm}^{b} + k_{xtm}^{b}\right) \frac{t}{2}\right)}{\left(k_{xrm}^{b} + k_{xtm}^{b}\right)} \right]$$

APPENDIX D. EQUIVALENT K-INVERTER OF THE PARALLEL COUPLED RIDGED WAVEGUIDES STRUCTURE. LIMITS POSITIONING POLES NEAR THE PASSBAND.

The object of this study is to obtain an estimation on the limits positioning Transmission Zeros near the passband for those filter prototypes described during this thesis.

We commence by considering the structure depicted in Fig. 4-1b, the so called parallel coupling of asymmetric ridge waveguides. The theory described in reference [105] is applied. Essentially the goal is to relate the structure responsible for the TZ to produce in the filter scheme (parallel coupled asymmetric ridges waveguides) with characteristics of the RCWG section (cutoff, dispersion and Z of the TE mode) and final characteristics of the filter (bandwidth and operating central frequency).

We commence by extracting the reflection coefficient for three structures of dimensions as depicted in Fig. 4.b but selecting the lengths Ls_{12}= 7.2, 7.4 and 8. Other dimensions are s=1.7 (vertical separation between slots), s_1=s_2=2.1 (height of the slots).

Hence, three filters with transmission zeros in the upper stopband are considered (Ls_{12}=7.2, 7.4, 8 in mm), the response for those structures can be followed in Fig. D-1.

From a mathematical analysis of the reactance slope function is considered convenient to start from 3 filters of identical RCWG section (idem s), such the cutoff, dispersion and impedance of the TE mode are the same on that section. Therefore the reactance slope is the same function of frequency for all 3 filters (cutoff, dispersion and Z of the TE mode is

the same). Only the reflection coefficient of the structure from Fig. 4-1b, and hence the equivalent K-value would be different.

So on the reactance slope parameter is obtained in the following manner:

From the theory referred as [105] in, the reactance slope parameter of the resonators shall be defined as:

$$x = -Z \frac{\pi \cdot f_0}{\lambda_g^2} L_{res} \frac{d\lambda_g}{df} \Big/ _{f=f_0} \qquad \textbf{(D-1)}$$

While the impedance inverter, K:

$$K = \frac{k}{x} \qquad \textbf{(D-2)}$$

Substituting eq (D-2) into (D-1)**,** can be expressed in the form:

$$K = \frac{k \cdot c \cdot \sqrt{f_0^2 - f_c^2}}{Z \cdot \pi \cdot L_{res} \cdot \sqrt{\varepsilon_r} \cdot f_0^2} \qquad \textbf{(D-3)}$$

Where the terms expressed in (D-3) are:

k : equivalent K-inverter of a discontinuity embedded between two transmission lines of the same characteristic impedance (parallel coupled ridged waveguides here).

f_0 : average of the even and odd mode resonant frequencies for the filter prototype of consideration under weakly external coupling (approx 9.10 GHz).

f_c : cutoff frequency of the TE1 mode at port 1 of the parallel coupled ridge waveguide, see Fig. 4-1b (cutoff extracted 4.75 GHz).

L_{res} : Resonator filter length, or length of each slot in the asymmetric parallel coupled RCWG (0.016m).

All the terms in equation (D-3) are constants but Z and k, which are both frequency dependent. In the considered example of three filter prototypes of identical RCWG cross-

section (see Fig. 4-12), then all those constant terms are identical (actually f_0 differ a little; in this case f_0 range from 9.075 to 9.1 GHz.

Below are enclosed some preliminary results. They have been obtained assuming the previous considerations: the only frequency dependent element is the impedance of the TE mode (D-1), other elements are constant, which are the same due to the fact the RCWG section is the same for all three prototypes chosen. The Impedance term of equation (D-3) has been calculated using the power-current expression, Zpi.

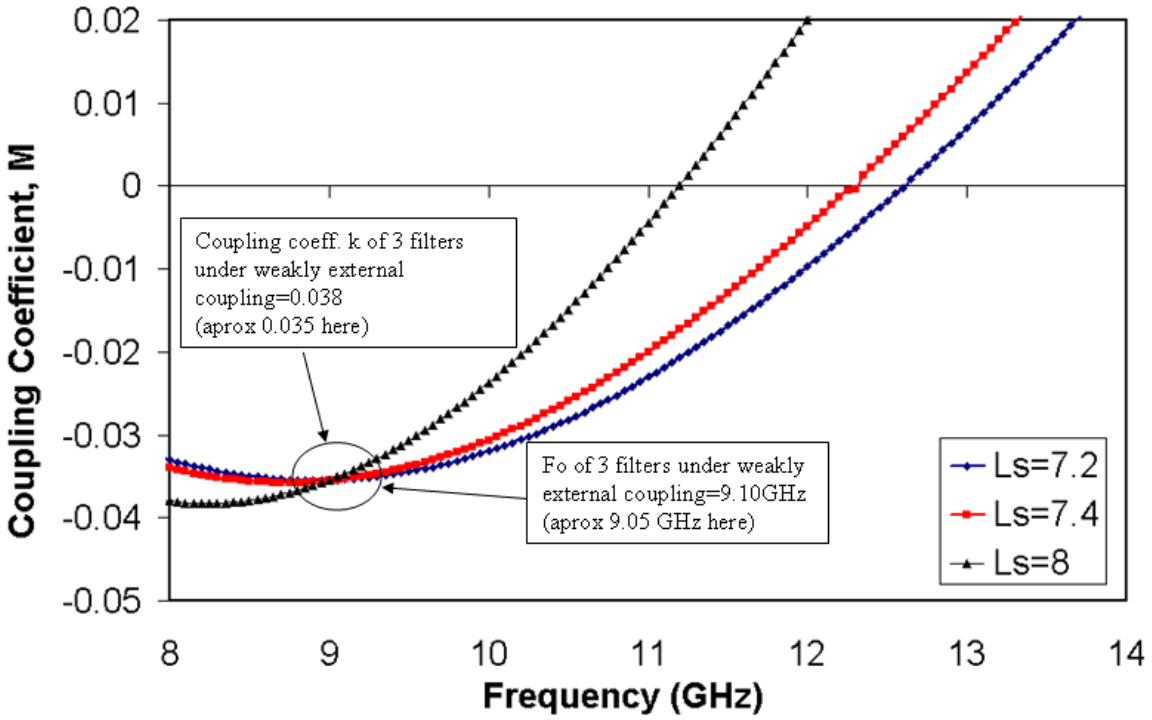

Fig. D-1. Coupling coefficient vs frequency response considering 3 filter prototypes from Fig. 3 (7.2, 7.4 and 8).

From this results we can extract the following conclussions:

- The transmission zeros produced by the parallel coupled ridge WG structure (Fig. 4-11) are located at 11, 12 and 12.3 GHz, while 9.3, 9.6 and 9.7 GHz frequencies are approximately the locations of the TZ produced by the final second order filter structure (Fig. 4-10). Indeed, from the transition of Fig 4-2 (structure producing TZ)

to Fig. 4-10 (filter), should be expected a shift on the TZ location, mainly related to the physical length of the resonators.

- The superimposed functions of Fig D-4 cross at the same point, 8.9 GHz, which is approx. the center frequency chosen to design the prototypes of Fig. 4-7. That center frequency f_0 point is independent of the dispersion, cutoff or impedance of the TE mode in the RCWG section, provided the cross section of the RCWG is the same for all three prototypes, which in this case it is.
- Negative sign of the coupling coefficient M was introduced under the assumption that at frequencies below the TZ the coupling is predominately inductive and associated with the TEM mode, while at higher frequencies of the TZ the coupling is predominately capacitive and associated with the TE mode.
- The normalized coupling M (D-2) are produced taking into account the relative proportions of the bandwidth (bw) comparing the three prototypes selected from Fig. 4-12a:

  bw (prototype 7.2)=1.1bw (prototype 7.4)= 1.5bw (prototype 8).

APPENDIX E. MAIN FORTRAN SUBROUTINE EMPLOYED TO CALCULATE FIELDS OF THE TEM MODE IN THE RCWG

This appendix reproduces one of the main subroutines wrote in Fortran as part of the program to characterize the TEM mode of a RCWG. Similar subroutines are employed for the TE and TM mode.

```
SUBROUTINE Coefficients()

C     This PROGRAM will solve the characteristic BigMatrix equation:
C     will produce the coefficients for the first region A1(k) and then will solve
C     the pair of linear equations which relate them with the A2(m),A3(l) coefficientss

C          ------------------------ D E C L A R A T I O N S -------------------------------

      USE NUMERICAL_LIBRARIES                                    ! IMSL Libraries

      IMPLICIT NONE
```

```
C       Common variables

        REAL(8) b,c1,c2,s_1,s_2,e,t,pi,a                        ! Dimensions
      COMMON /DIMENSIONS/ b,c1,c2,s_1,s_2,e,t,pi,a              ! Common Dimensions

        INTEGER M1,M2,M3                                        ! Number ofExpansion Terms
        COMMON /EXP_TERM/ M1,M2,M3                              ! CommoN Limits of loops


C       Local variables

      REAL V

        INTEGER k,m,n,l,J

      INTEGER IPATH

        PARAMETER (IPATH=1)
      REAL(8) BM(M1,M1)                 !BigMatrix Term
        REAL(8) C(M1)                   !Free terms of the BM Equation
        REAL(8) A1(M1),A2(M2),A3(M3)    !Coeficients
        REAL(8) BM2(M1,M1),BM3(M1,M1)       !2nd and 3rd term of the BigMatrix
        REAL(8) DE11(M1),DE2(M2),DE3(M3)    !DiagMatrix electric field BC
        REAL(8) JE2(M2,M1),JE3(M3,M1)
      REAL(8) DM1(M1),DM2(M2),DM3(M3)
        REAL(8) JM2(M1,M2),JM3(M1,M3)
        REAL(8) NT1,NT2,NT3,NT,pot,lan
        REAL(8) eps,mu
      eps=8.85421878e-12
      mu=1.256637e-6
        V=1

C     Output coefficients for matlab Fields plotting


c       open(21,status='unknown',file='c:/MyProjects/TEMPORAL/RCW(2)/
c     &A1.dat')
c      open(22,status='unknown',file='c:/MyProjects/TEMPORAL/RCW(2)/
c     &A2.dat')
c      open(23,status='unknown',file='c:/MyProjects/TEMPORAL/RCW(2)/
c     &A3.dat')
c      open(24,status='unknown',file='c:/MyProjects/TEMPORAL/RCW(2)/
c     &lan.dat')


C     ------------------------VECTOR DE1--------------------------


      DO k=1, M1

          DE11(k)=(pi*k/2)*(dexp(-pi*k*t/(2*b))-dexp(pi*k*((t/2)-a)/b))

        ENDDO

C     ------------------------END OF VECTOR DE11-------------------------------


C       --------------------BIGMATRIX TERM---------------------------------
C     This part will PRODUCE the characteristic bigmatrix A=BM
```

```
C     BM=DE11-BM2+BM3


      CALL JE2_Integral(JE2)          !Callings of the subroutines for
           CALL DE2_Vector(DE2)             !BigMatrix algebra, 2nd gap
           CALL DM2_Vector(DM2)
           CALL JM2_Integral(JM2)
           CALL DM1_Vector(DM1)

      DO n=1,M1
                    DO l=1,M1
        BM2(n,l)=0
                          DO m=1,M2

                          BM2(n,l)=BM2(n,l)+JE2(m,n)*DE2(m)*DM2(m)*JM2(l,m)*DM1(l)

                          ENDDO
                    ENDDO
           ENDDO


           CALL JE3_Integral(JE3)          !Callings of the subroutines for
           CALL DE3_Vector(DE3)             !BigMatrix algebra, 2nd gap
           CALL DM3_Vector(DM3)
           CALL JM3_Integral(JM3)
           CALL DM1_Vector(DM1)


      DO n=1,M1
                    DO l=1,M1
        BM3(n,l)=0
                          DO m=1,M3

                        BM3(n,l)=BM3(n,l)+JE3(m,n)*DE3(m)*DM3(m)*JM3(l,m)*DM1(l)

                          ENDDO
                    ENDDO

           ENDDO

           DO k=1,M1
                    DO m=1,M1

                          BM(k,m)=-BM2(k,m)-BM3(k,m)

                    ENDDO
           BM(k,k)=DE11(k)+BM(k,k)
           ENDDO


C     ----------END OF BIGMATRIX TERM----------

C     ----------SYSTEM OF EQUATIONS----------

C     The subroutine is LSARG is called to solve the bigmatrix equation;
C     (BM)A1=C     that is to produce the A1(k) coeficients

      CALL C_Vector(C)
           CALL DLSARG (M1, BM, M1, C, IPATH, A1)
```

```
C       Usage
C       CALL LSARG (N, A, LDA, B, IPATH, X)

C       Arguments
C       N— Number of equations. (Input)
C       A— N by N matrix containing the coefficients of the linear system.(Input)
C       LDA—Leading dimension of A exactly as specified in the dimension statement
C       of the calling program. (Input)
C       B—Vector of length N containing the right-hand side of the linear system.
C       (Input)
C       IPATH— Path indicator. (Input)
C       IPATH = 1 means the system AX = B is solved.
C       IPATH = 2 means the system A7X = B is solved.
C       X—Vector of length N containing the solution to the linear system(Output)


C       Once produced de A1(k) coeficients the A2,A3 are solved by linear equations


        CALL DM1_Vector(DM1)

    CALL JM2_Integral(JM2)
    CALL DM2_Vector(DM2)


    DO m=1,M2
        A2(m)=0
                DO k=1,M1
                A2(m)=A2(m)+DM2(m)*JM2(k,m)*DM1(k)*A1(k)

                ENDDO
        ENDDO

    CALL DM1_Vector(DM1)
    CALL JM3_Integral(JM3)
    CALL DM3_Vector(DM3)

        DO l=1,M3
        A3(l)=0
                DO k=1,M1
          A3(l)=A3(l)+DM3(l)*JM3(k,l)*DM1(k)*A1(k)
                ENDDO
        ENDDO

C    ----------------------POWER NORMALISATION----------------------------


    NT1=0
    DO J=1,M1
    NT1=NT1+A1(J)*A1(J)*J*(exp(-2*J*pi*t/(2*b))
   &-exp(2*J*pi*((t/2)-a)/b))
    enddo

    NT2=0
    DO J=1,M2
    NT2=NT2+A2(J)*A2(J)*J*sinh(2*J*pi*t/(2*s_1))
    enddo
```

```
      NT3=0
      DO J=1,M3
      NT3=NT3+A3(J)*A3(J)*J*sinh(2*J*pi*t/(2*s_2))
      enddo

      NT1=NT1*pi/2
      NT2=NT2*pi
      NT3=NT3*pi

      NT=2*sqrt(eps/mu)*
     &(t*V*V/(2*s_1)+t*V*V/(2*s_2)+NT1+NT2+NT3)

      lan=1/NT

C     ---------- DATA OUTPUT ----------

            do k=1,M1

               write(21,*) A1(k)  ! Coefficients data output

            end do

      do k=1,M2

               write(22,*) A2(k)  ! Coefficients data output

            end do

      do k=1,M3

               write(23,*) A3(k)  ! Coefficients data output

            end do

               write(24,*) lan                !Pot related with coeffs

c           CLOSE(21)
c           CLOSE(22)
c           CLOSE(23)
c           CLOSE(24)

      PRINT*,A1,' TEM Coeficients produced'
            print*,lan,' characteristic impedance'

      STOP
            END

C     ----------
```

References

[1] Konishi, Y.; Uenakada, K.; , "The Design of a Bandpass Filter with Inductive Strip Planar Circuit Mounted in Waveguide," *IEEE Transactions on Microwave Theory and Techniques,* , vol. 22, pp. 869- 873, October 1974.

[2] Vahldieck R., Bornemann J., Arndt F., Grauerholz D., "W-Band Low-Insertion-Loss E-Plane Filter", *IEEE Transactions on Microwave Theory and Techniques*, vol. 32, pp. 133 -135, January 1984.

[3] Yi-Chi Shih; , "Design of Waveguide E-Plane Filters with All-Metal Inserts," *IEEE Transactions on Microwave Theory and Techniques*, vol.32, pp. 695- 704, July 1984.

[4] Vahldieck, R.; Hoefer, W.J.R.; , "Finline and Metal Insert Filters with Improved Passband Separation and Increased Stopband Attenuation," *IEEE Transactions on Microwave Theory and Techniques* , vol. 33, pp. 1333- 1339, December 1985.

[5] Goussetis, G.; Budimir, D.; , "Compact ridged waveguide filters with improved stopband performance," *2003 IEEE MTT-S International Microwave Symposium Digest,* , vol. 2, pp. 953- 956, 8-13 June 2003.

[6] Xiao-Peng Liang; Zaki, K.A.; Atia, A.E.; "Dual mode coupling by square corner cut in resonators and filters ," *IEEE Transactions on Microwave Theory and Techniques* , vol. 40, pp. 2294-2302, December 1992.

[7] Guglielmi, M.; Molina, R.C.; Melcon, A.A.; , "Dual-mode circular waveguide filters without tuning screws," *IEEE Microwave and Guided Wave Letters*, vol. 2, pp. 457-458, November 1992.

[8] Hunter, I.C.; Billonet, L.; Jarry, B.; Guillon, P.; , "Microwave filters-applications and technology," *IEEE Transactions on Microwave Theory and Techniques*, vol. 50, pp. 794-805, March 2002.

[9] Mazumdar, J.; , "A Method for the Study of TE and TM Modes in Waveguides of Very General Cross Section," *IEEE Transactions on Microwave Theory and Techniques*, vol. 28, pp. 991- 995, September 1980.

[10] Israel, M.; Miniowitz, R.; , "An Efficient Finite Element Method for Nonconvex Waveguide Based on Hermitian Polynomials," *IEEE Transactions on Microwave Theory and Techniques*, vol. 35, pp. 1019- 1026, November 1987.

[11] Christopoulos, C.; "The historical development of TLM [transmission line modelling]," *IEE Colloquium on Transmission Line Matrix Modelling - TLM*, pp.1/1-1/4, October 1991.

[12] Sorrentino R., *Numerical Methods for Passive Microwave and Millimeter Wave Structures, IEEE Press*, 1989, ISBN 9780879422493.

[13] Itoh T., *Numerical Techiques for Microwave and Millimeter-Wave Passive Structures, Wiley Interscience*, 1989, ISBN 9780471625636.

[14] Tajima, Y.; Sawayama, Y.; , "Design and Analysis of a Waveguide-Sandwich Microwave Filter (Short Papers)," IEEE *Transactions on Microwave Theory and Techniques*, vol. 22, no. 9, pp. 839- 841, September 1974.

[15] Nguyen, C.; Chang, K.; , "Millimetre-wave low-loss finline lowpass filters," *Electronics Letters* , vol. 20, no. 24, pp.1010-1011, November 22 1984.

[16] Mizuno, H.; Verver, C.J.; Douville, R.J.; Stubbs, M.G.; , "Propagation in Broadside-Coupled Suspended-Substrate Stripline in E-Plane," *IEEE Transactions on Microwave Theory and Techniques*, vol. 33, no.10, pp. 946- 950, Oct 1985.

[17] G. Goussetis, A.P. Feresidis and P. Kosmas, “Efficient Analysis, Design and Filter Applications of EBG Waveguide with Periodic Resonant Loads,” *IEEE Transactions on Microwave Theory and Techniques*, vol. 54, no. 11, pp. 3885-3892, November 2006.

[18] Yi-Chi Shih, Itoh T. “E-Plane Filters with Finite-Thickness Septa”, *IEEE Transactions on Microwave Theory and Techniques*, vol. 83, pp. 1009-1013, Dec 1983.

[19] Vahldieck R., Bornemann J., Arndt F., Grauerholz D., “W-Band Low-Insertion-Loss E-Plane Filter”, *IEEE Transactions on Microwave Theory and Techniques*, pp. 133 -135, vol. 32, Issue 1, Jan 1984.

[20] Yi-Chi Shih; , "Design of Waveguide E-Plane Filters with All-Metal Inserts," *IEEE Transactions on Microwave Theory and Techniques,* vol. 32, no. 7, pp. 695-704, July 1984.

[21] Vahldieck, R.; Hoefer, W.J.R.; , "Finline and Metal Insert Filters with Improved Passband Separation and Increased Stopband Attenuation," *IEEE Transactions on Microwave Theory and Techniques,* , vol.33, no.12, pp. 1333-1339, December 1985.

[22] Bornemann, J.; , "Selectivity-improved E-plane filter for millimetre-wave applications," *Electronics Letters* , vol. 27, no. 21, pp. 1891-1893, October 1991.

[23] Budimir, D.; Goussetis, G.; , "Design of asymmetrical RF and microwave bandpass filters by computer optimization," *Microwave Theory and Techniques, IEEE Transactions on* , vol. 51, no. 4, pp. 1174- 1178, April 2003.

[24] Goussetis, G.; Budimir, D.; , "Integration of Lowpass Filters in Bandpass Filters for Stopband Improvement," *32nd European Microwave Conference*, pp.1-3, 23-26, September 2002.

[25] V.E. Boria, B. Gimeno, “Waveguide filters for satellites,” *IEEE Microwave Magazine*, vol. 8 , no. 5, pp. 60-70, 2007.

[26] Hongsheng Chen, Lixin Ran, Jiangtao Huangfu, Xianmin Zhang, and Kangsheng Chen *“*Left-handed materials composed of only S-shaped resonators*”. Physical Review E*, vol. 70, no. 5, pp. 1-4, November 2004.

[27] Suntheralingam, N.; Budimir, D.; , "Compact S-shaped resonator loaded waveguide bandpass filters," *Antennas and Propagation Society International Symposium, 2009. APSURSI '09. IEEE* , pp.1-4, 1-5 June 2009.

[28] Vahldieck, R.; , "Quasi-planar filters for millimeter-wave applications," *IEEE Transactions on Microwave Theory and Techniques*, vol. 37, no. 2, pp. 324-334, February 1989.

[29] Omar, A.S.; Schunemann, K.; , "Realizations and Design of Fin-Line Bandstop Filters," *Microwave Conference, 1983. 13th European* , pp. 157-162, 3-8 September 1983.

[30] Amari, S.; Bornemann, J.; , "Using frequency-dependent coupling to generate finite attenuation poles in direct-coupled resonator bandpass filters," IEEE *Microwave and Guided Wave Letters*, vol. 9, no. 10, pp. 404-406, Octobre 1999.

[31] Young, D.; Hunter, I.C.; , "Integrated E-Plane Filters with Finite Frequency Transmission Zeros," *Microwave Conference, 1994. 24th European* , vol. 1, pp. 460-465, 5-9 September 1994.

[32] Ofli E., Vahldieck R. and Amari S., “Compact E-plane and Ridge Waveguide Filters/Diplexers with Pseudo-Elliptic Response”, *IEEE MTT International Microwave Symposium Digest*, pp. 949-952, Philadelphia 2003.

[33] Ofli, E.; Vahldieck, R.; Amari, S.; , "Novel E-plane filters and diplexers with elliptic response for millimeter-wave applications," *IEEE Transactions on Microwave Theory and Techniques*, vol. 53, no. 3, pp. 843- 851, March 2005.

[34] Goussetis, G.; Feresidis, A.P.; Budimir, D.; Vardaxoglou, J.C.; , "A 3rd order ridge waveguide filter with parallel coupled resonators," *Microwave Symposium Digest, 2004 IEEE MTT-S International* , vol. 2, pp. 595- 597, vol. 2, 6-11 June 2004.

[35] L. Gruner, "Characteristics of Crossed Rectangular Coaxial Structures," *IEEE Transactions on Microwave Theory and Techniques*, vol. 28, no. 6, pp. 622-627, 1980.

[36] Crawford, "Generation of Standard EM Fields Using TEM Transmission Cells", *IEEE Transactions on Electromagnetic compatibility*, vol.16, November 1974.

[37] Crawford, "Mesurement of EM Radiation from Electronic Equipment using TEM Transmission Cells", NBSIR 73-306, February 1973.

[38] O.R. Cruzan and R.V Garner, "Characteristic Impedance of Rectangular Coaxial Transmission Lines," *IEEE Transactions on Microwave Theory and Techniques*, pp. 488-495, 1964.

[39] S.B. Cohn, "Properties of Ridge Wave Guide", Proc IRE, vol.35, pp. 783-788, vol. 15, pp. 483-485, August 1947.

[40] L. Gruner, "Higher order modes in Rectangular Coaxial Structures," *IEEE Transactions on Microwave Theory and Techniques*, vol. MTT-15, pp. 483-485, August 1967.

[41] K. Garb and R. Kastner, "Characteristic Impedance of a Rectangular Double-Ridge TEM Line," *IEEE Trans. Microwave Theory and Techniques*, vol. 45, no. 4, pp. 554-557, 1997.

[42] G.Goussetis, D.Budimir, Bandpass filters with improved stopband performance, *2000 Asia-Pacific Microwave Conference*, pp. 529–532, December 2000.

[43] G. Goussetis, D. Budimir, A. Feresidis and J.C. Vardaxoglou, "A 3rd Order Ridge Waveguide Filter with Parallel Coupled Resonators", *IEEE MTT-S International Microwave Symposium*, Fort-Worth, Texas, USA, 6-10 June 2004.

[44] M.A. Ruiz-Bernal, M. Valverde-Navarro, G. Goussetis, J. L. Gómez-Tornero and A. P. Feresidis, "Higher Order Modes of the Ridged Coaxial Waveguide," *European Microwave Conference 2006, Manchester*, 10-15 September 2006.

[45] J. Schwinger , "Discontinuities in waveguides" , Gordon and Breach Sc. Publ., New York, 1968, ISBN 978-0677018409.

[46] Montgomery J., "On the complete eigenvalue solution of ridged waveguide", *IEEE Transactions on Microwave and Theory and Techniques*, MTT-19, 457-555, 1971.

[47] Hunter I., Theory and Design of Microwave Filters, IEE Press, London 2001, ISBN 978-0852967775.

[48] Collin R., *Foundations of Microwave Engineering*, 2nd editions, IEEE Press, New York 2001, ISBN 978-0780360310.

[49] Itoh T., *Numerical Techiques for Microwave and Millimeter-Wave Passive Structures*, Wiley Interscience, 1989, ISBN 978-0471625636.

[50] High Frequency Structure Simulator, Ansoft corp., Pittsburgh, USA.

[51] R. J. Cameron, C. M. Kudsia, R. R. Mansour, *Microwave Filters for Communication Systems*, Wiley, 2007, ISBN 978-0471450221.

[52] A. E. Atia, A. E. Williams, and R. W. Newcomb, "Narrow-band multiple-coupled cavity synthesis," *IEEE Trans on Circuits Systems*, vol. 21, no. 5, pp. 649–655, September 1974.

[53] R. Levy, “Filters with single transmission zeros at real or imaginary frequencies,” *IEEE Trans. On Microwave Theory and Techniques*, vol. MTT-21, no. 4, pp. 172–181, April 1976.

[54] R. J. Cameron, “General coupling matrix synthesis methods for Chebyshev filtering functions,” *IEEE Trans. on Microwave Theory and Techniques*, vol. 47, no. 4, pp. 433–442, April 1999.

[55] J.-S. Hong and M. J. Lancaster, “Couplings of microstrip square open-loop resonators for cross-coupled planar microwave filters,” *IEEE Trans. on Microwave Theory and Techniques*, vol. 44, no. 12, pp. 2099–2109, December 1996.

[56] J.-S. Hong and M. J. Lancaster, *Microstrip Filters for RF/Microwave Applications*, New York: Wiley, 2001, ISBN 978-0471388777.

[57] S. Amari, “On the Maximum Number of Finite Transmission Zeros of Coupled Resonator Filters with a Given Topology,” *IEEE Microwave Guided Wave Letters*, vol. 9, no. 9, pp. 354-356, September 1999.

[58] U. Rosenberg and S. Amari, “Novel coupling schemes for microwave resonator filters,” *IEEE Transactions on Microwave and Theory Techniques.*, vol. 50, no. 12, pp. 2896–2902, December 2002.

[59] R. J. Cameron, “Advanced coupling matrix synthesis techniques for microwave filters,” *IEEE Transactions on Microwave Theory and Techniques.*, vol. 51, no. 1, pp. 1–10, January 2003.

[60] L. Q. Bui, D. Ball, and T. Itoh, “Broad-band millimeter-wave E-plane bandpass filters,” *IEEE Transactions on Microwave and Theory Techniques*, vol. MTT-32, no. 12, pp. 1655–1658, December 1984.

[61] Ofli, E.; Vahldieck, R.; Amari, S.; , "Analysis and design of mass-producible cross-coupled, folded E-plane filters," *2001 IEEE MTT-S International Microwave Symposium Digest,* vol.3, pp.1775-1778, 2001.

[62] Q. Zhang, T. Itoh, “Computer-aided design of evanescent-mode waveguide filter with non touching E-plane fins,” *IEEE Transasctions on Microwave Theory and Techniques*, vol. 36, no. 2, pp. 404-412, February 1988.

[63] J. Bornemann, F. Arndt, “Transverse Resonance, Standing Wave, and Resonator Formulations of the Ridge Waveguide Eigenvalue Problem and Its Application to the Design of E-Plane Finned Waveguide Filters,” *IEEE Transactions on Microwave Theory Techniques*, vol. 38, no. 8, pp. 1104-1113, August 1990.

[64] J. Bornemann, “Selectivity-improved E-plane filter for millimeter-wave applications,” *IEEE Electronics Letters*, vol. 27, no. 21, pp. 1891–1893, 1991.

[65] D. Budimir, “Optimized E-plane bandpass filters with improved stopband performance,” *IEEE Trans. Microwave Theory and Techniques*, vol. 45, no. 2, pp. 212-220, February 1997 .

[66] G. Goussetis and D. Budimir, “Novel Periodically Loaded E-plane Filters”, *IEEE Microwave and Wireless Components Letters*, pp 193-195, Vol.13, No. 6, June 2003.

[67] E. Ofli, R. Vahldieck, S. Amari, “Novel E-plane filters and diplexers with elliptic response for millimeter-wave applications,” *IEEE Transactions Microwave Theory and Techniques*, vol. 53, no. 3, 1, pp. 843-851, March 2005.

[68] R. Lopez-Villarroya, G. Goussetis, J.S. Hong, J.L. Gomez-Tornero, “E-plane Filters with Selectively Located Transmission Zeros” 38th *European Microwave Conference Proc*, pp. 763-766, October 2008.

[69] Zysman, G.I., Johnson, A.K., "Coupled Transmission Line Networks in an Inhomogeneous Dielectric Medium," *IEEE Transactions on Microwave Theory and Techniques,* vol. 17, no. 10, pp. 753-759, October 1969.

[70] C.-M. Tsai, S.-Y. Lee, H.-M. Lee, "Transmission-line filters with capacitively loaded coupled lines," *IEEE Transactions on Microwave Theory and Techniques*, vol.51, no.5, pp. 1517-1524, May 2003.

[71] H.-M Lee, C.-M. Tsai, "Improves Coupled-Microstrip Filter Design Using Effective Even-Mode and Odd-Mode Characteristic Impedances," *IEEE Transactions on Microwave Theory and Techniques*, vol. 53, no. 9, pp. 2812-2818, September 2005.

[72] Q.-X. Chu, H. Wang, "A Compact Open-Loop Filter With Mixed Electric and Magnetic Coupling," *IEEE Transactions on Microwave Theory and Techniques*, vol. 56, no. 2, pp. 431-439, February 2008.

[73] H. Wang, Q.-X. Chu, "An Inline Coaxial Quasi-Elliptic Filter With Controllable Mixed Electric and Magnetic Coupling," *IEEE Transactions on Microwave Theory and Techniques,* vol. 57, no. 3, pp. 667-673, March 2009.

[74] J. Ness, "A Unified Approach to the Design, Measurement, and Tuning of Coupled-Resonator Filters," *IEEE Transactions on Microwave Theory and Techniques* pp. 343-351, vol. 46, no. 4, April 1998.

[75] L. Q. Bui, D. Ball, and T. Itoh, "Broad-band millimeter-wave E-plane bandpass filters," *IEEE Transactions on Microwave Theory and Techniques*, vol. MTT-32, no. 12, pp. 1655–1658, Decembre 1984.

[76] Q. Zhang, T. Itoh, "Computer-aided design of evanescent-mode waveguide filter with non touching E-plane fins," *IEEE Transactions Microwave Theory and Techniques*, Vol. 36, No. 2, pp. 404-412, February 1988.

[77] J. Bornemann, "Selectivity-improved E-plane filter for millimeter-wave applications," *IEEE Electronic Letters*, vol. 27, no. 21, pp. 1891–1893, 1991.

[78] J. Bornemann, "Comparison between different formulations of the Transverse Resonance Field-Matching Technique for the three-dimensional analysis of metal-finned waveguide resonators", *International Journal of Numerical Networks, Devices and Fields*, vol. 4, pp. 63-73, 1991.

[79] Levy R., "A Generalised Design Technique for Practical Distributed Reciprocal Networks", *IEEE Transactions on Microwave Theory and Techniques,* vol. 21, no 8, pp. 519-526, August 1973.

[80] K.E. Peterson, D.Q. Nacilla, J.B. Barner, "Slow-wave structure for ridge waveguide," *US patent* no 7,023,302, April 2006.

[81] K.E. Peterson, D.Q. Nacilla, J.B. Barner, "Method for making a slow-wave ridge waveguide structure," *US patent* no 7,263,760, September 2007.

[82] D. Pozar, *Microwave Engineering. Reading*, MA: Addison-Wesley, 1993. ISBN 978-0470631553.

[83] R. Lopez-Villarroya, G. Goussetis, "Novel topology for low-cost dual-band stopband filters," *Asia-Pacific Microwaves Conference 2009*, pp.933-936, December 2009.

[84] Uher, Bornemann, and Rosenberg, *Waveguide Components for Antenna Feed Systems: Theory and CAD* Norwood, MA: Artech House, 1993. ISBN 9780890065822.

[85] D. Kajfez**,** Q Factor, Publisher: Vector fields, 1994, ISBN-13: 9780930071066

[86] Cameron, R.J.; Ming Yu; Ying Wang, "Direct-coupled microwave filters with single and dual stopbands," *IEEE Transactions on Microwave Theory and Techniques*, vol.53, no.11, pp. 3288-3297, Nov. 2005.

[87] Yng-Huey Jeng; Chang, S.-F.R.; Hsiao-Kuang Lin, "A high stopband-rejection LTCC filter with multiple transmission zeros," *IEEE Transactions on Microwave Theory and Techniques*, vol.54, no.2, pp. 633-638, February 2006.

[88] Cheng-Chung Chen, "Dual-band bandpass filter using coupled resonator pairs," *IEEE Microwave and Wireless Components Letters*, vol.15, no.4, pp. 259-261, April 2005.

[89] Mokhtaari, M.; Bornemann, J.; Amari, S., "Coupling-Matrix Design of Dual/Triple-Band Uni-Planar Filters," *IEEE MTT-S International Microwave Symposium Digest, 2006*, pp.515-518, 11-16 June 2006.

[90] Mokhtaari, M.; Bornemann, J.; Amari, S., "New Reduced-Size Step-Impedance Dual-Band Filters with Enhanced Bandwidth and Stopband Performance," *IEEE MTT-S International Microwave Symposium Digest,* pp.1181-1184, 11-16 June 2006.

[91] Zhewang Ma; Kobayashi, Y., "Novel design and implementation methods of high-performance RF/microwave planar filters using composite resonators," *Asia-Pacific Microwave Conference, APMC 2006.*, vol., no., pp.1818-1826, 12-15 December 2006.

[92] Zhewang Ma; Kikuchi, K.; Kobayashi, Y.; Anada, T.; Hagiwara, G., "Novel microstrip dual-band bandstop filter with controllable dual-stopband response," *Asia-Pacific Microwave Conference, APMC 2006*, vol., no., pp.1174-1177, 12-15 December 2006.

[93] Meier, P.J., "Integrated Fin-Line Millimeter Components," *IEEE Transactions on Microwave Theory and Techniques* , vol.22, no.12, pp. 1209-1216, December 1974.

[94] Cheng, X, "A Microfluidic device for practical label-free CD4+ T Cell Counting of HIV-Infected Subjects", *Lab on a Chip*, vol. 7 (2007), pp. 170-178.

[95] Cheng, X, "Cell Detection and Counting Through Cell Lysate Impedance Spectroscopy in Microfluidic Devices", *Lab on a Chip,* vol. 7 (2007), pp. 746-755.

[96] Weigl, B H, Bardell, R L, and Cabrera, C R, "Lab-on-a-chip for Drug Development", *Adv. Drug Del. Rev.,* Vol. 55, Issue 3 (2003), pp. 349-377.

[97] The Global Diabetes Community, Guide to Blood Glucose Meters, www.diabetes.co.uk

[98] Schwan, H P, "Electrical Properties of Tissues and Cell Suspensions: Mechanisms and Models", *Engineering in Medicine and Biology Society,* vol. 1, pp. A70-A71, 1999.

[99] Epilog Legend Elite Series Laser, Epilog Laser, www.epiloglaser.com

[100] Juncker, D, et al., "Autonomous Microfluidic Capillary System", *Anal. Chem.,* vol. 74 (2002), pp. 6139-6144.

[101] Birol, H, Maeder, T, and Ryser, P, "Low Temperature Co-fired Ceramic (LTCC) Technology: General Processing Aspects and Fabrication of 3-D Structures for Microfluidic Devices", *Sintering,* 2005, pp. 3b6, 216-219.

[102] Budniewski, K, et al., "Microchamber PCR device in LTCC – Modelling and Preliminary Experiments", *Proceedings of the VI Optoelectronic And Electronic Sensors Conference,* 2004, pp.90-93.

[103] Gongor-Rubio, M,R, et al., “LTCC manifold for heavy metal detection system in biomedical and environmental fluids”, *Proceedings of the XVII Conference in Eurosensors,* 2003, pp.823-826.

[104] Smetana, W, et al., “Processing Procedures for the Realization of fine Structured Channel Arrays and Bridging Elements by LTCC Technology, *Microelectronics Reliability,* vol. 49, 2008, Isssue 6, pp.592-599.

[105] G. Matthaei, L. Young, and E.Jones, Microwave Filters, *Impedance Matching Networks, and Coupling Structures*. Norwood, MA: Artech House, 1980 ISBN 978-0890060991.

[106] R. Vahldieck and B. V. de la Filolie, “Computer aided-design of parallel connected milimeter-wave diplexers/multiplexers”, *IEEE-MTT-S International Microwave Symposium Digest*, 2001, pp. 435-438.